Stability and Aggregation Studies of Immature Superoxide Dismutase

by

Helen Ruthann Broom

A thesis
presented to the University of Waterloo
in fulfilment of the
thesis requirement for the degree of
Doctor of Philosophy
in
Chemistry

Waterloo, Ontario, Canada, 2015

Author's Declaration

I hereby declare that I am the sole author of this thesis. This is a true copy of the thesis, including any required final revisions, as accepted by my examiners.

I understand that my thesis may be made electronically available to the public.

Abstract

Amyotrophic Lateral Sclerosis is a devastating neurological disease with no known cure. In 1993, a genetic link was established between ALS and mutant forms of Cu, Zn-superoxide dismutase (SOD1), an antioxidant enzyme that catalyzes the dismutation of the damaging free radical superoxide anion (O^{2-}) to hydrogen peroxide (H_2O_2) and dioxygen (O_2). The inheritable form of ALS (fALS) accounts for ~10% of all ALS cases and so SOD1 mutations comprise ~1.5-2% of all ALS cases, but nevertheless represent a major known cause of the disease. Furthermore, the clinical symptoms of fALS and sALS are similar, although fALS patients with SOD1 mutations have an earlier age of disease onset than sALS (by ~10 years). A major hypothesis in the field of ALS research is that mutations decrease the stability and increase the aggregation propensity of SOD1, causing motor neuron degeneration. Attempts to identify relationships between the effects of the mutations and ALS characteristics have shown that these effects are highly complex and not correlated with disease characteristics in a simple way. SOD1 undergoes various *in vivo* modifications (notably disulfide bond formation and metal binding) and the form of SOD1 that is relevant to ALS toxicity is unknown. Recently, attention has focused on the immature forms of SOD1, which lack metal and/or disulfide bonds, because these forms are more destabilized by ALS-associated mutations compared to the mature, metal-bound, disulfide oxidize (holoSS) form.

A powerful approach to uncovering the mechanisms of SOD1 misfolding and aggregation is to investigate the how mutations affect the global and local stability of SOD1 under physiological conditions. Here, the stability of disulfide-oxidized (SS), metal free (apo) SOD1 has been investigated by combining isothermal titration and differential scanning calorimetry techniques (ITC and DSC, respectively) to break down changes in global stability

into dimer interface and monomer stability components. First, ITC was used to assess the thermodynamics of dimer dissociation for pWT and 13 ALS-associated mutants and the results were confirmed using size exclusion chromatography (SEC). Together these experiments reveal that all mutations investigated, even those far removed from the interface, promote dissociation. Furthermore, apo SOD1 dissociation is characterized by large ΔC_p, ΔH and ΔS changes, far larger than expected based on theoretical calculations of surface area changes estimated from the crystal structure. This finding suggests that large conformation changes accompany dissociation and that monomeric apo SOD1 is fairly malleable, a finding that suggests dimerization may play an important role in the maturation of SOD1, by preventing the buildup of partially unfolded, aggregation-protein species. Subsequent to these studies, total unfolding (ie. folded dimer to unfolded monomer) for the same set of mutants was characterized using DSC, and the data fit to a 3-state folding mechanism with monomer intermediate. Due to the complexity of this model, numerous DSC experiments for the same mutant were globally fit, with the energetics of the first transition fixed to values obtained by ITC, thus reducing the uncertainty in the fitted parameters that define monomer unfolding. The results from this approach reveal that mutations have variable effects on apoSS monomer stability. In most cases, apoSS monomers are only marginally stable; accordingly, mutations greatly elevate the levels of unfolded protein under physiological conditions. In contrast, two mutations, while decreasing dimer interface stability, actually increase monomer stability. These experiments show that mutations have markedly different effects on the populations of folded and unfolded monomers *in vivo* and disclose important implications for disease-relevant aggregation.

We have also characterized the stability of the most immature form of SOD1 (apoSH SOD1), which lacks both disulfide bonds and metals. This form of the protein is mainly

monomeric, with marginal stability that is greatly affected by ALS-associated mutations. Surprisingly however, we find that this form of SOD1 is remarkably resistant to aggregation under physiological-like conditions. Static and dynamic light scattering (SLS and DLS, respectively) as well as analytical ultracentrifugation (AUC) reveal higher-order interactions are present, but of the 12 mutants invested, only one showed evidence of aggregate formation. Increased protein concentrations or the addition of salt promote aggregation of some SOD1 mutants and the mechanism(s) of aggregation have been characterized using light scattering, atomic force microscopy (AFM), and Thioflavin-T (ThT) binding. Under conditions that enhance aggregation, DLS and AFM experiments reveal that some mutants form small fibrils ranging from ~20-100 nm in length, or ~2-100 monomers. Other mutants aggregate less, but the aggregates that do form are longer (greater than 1000 nm). Furthermore, ThT binding experiments suggest that the aggregates contain different degrees of β-structure. Mutations appear to have complex effects on the energy landscape of apoSH SOD1, promoting different aggregation pathways. This complexity may help explain the different disease phenotypes associated with different mutants.

By characterizing both folding and aggregation of different forms of immature SOD1, we have employed a powerful approach to untangling the role of toxic aggregation in the syndrome of ALS.

Acknowledgements

First of all I would like to thank all the past and present members of the Meiering group for all the support, the interesting discussions, and words of wisdom. I have learned so much from you all. In particular I would like to thank Sarah Holyoak, Heather Primmer, Ming Sze Tong, Dr. Gracie Hwang, and Dr. Kenrick Vassall who were so generous with their help and truly invaluable when I began this work. As well, Dr. Jessica Rumfeldt and Colleen Doyle, whose interesting insights have been vital for this project. You have all been amazing friends throughout this journey.

I would also like to thank my wonderful husband, Aron Broom, for being my rock and my partner in all things, for supporting me during the difficult times and for celebrating with me during the good times. And to my brother, Dan Stubbs, thank you for keeping a smile on my face. To my parents, Gwen McCutcheon and Andrew Stubbs, thank you for always encouraging me to follow my dreams, for your faith in me, for always giving me your unwavering support, and for your unconditional love. I would also like to thank my father who took the time to thoroughly edit this work. And to all other members of my extended family, including Bob and Ruth Broom, I am so grateful for all the good times and laughter we have shared together.

Finally, I would like to thank my supervisor, Dr. Elizabeth Meiering, for the opportunity to work on this project, for always encouraging me to take on new challenges, and for teaching me to think deeply and critically. I would also like to thank the members of my Ph.D. advisory committee, Dr. Richard Manderville, Dr. Jean Duhamel, and Dr. Zoya Leonenko. Thank you all for your insight and helpful suggestions.

Dedication

To my parents, Gwen McCutcheon and Andrew Stubbs.

And to my grandma, Ruth Guthrie, I will strive to live inside your vision of what is possible. You are sorely missed.

Table of Contents

List of Figures

Chapter 1

Chapter 2

Chapter 3

Chapter 4

Chapter 5

Chapter 6

List of Tables

Chapter 2

Chapter 3

Chapter 4

Chapter 5

List of Abbreviations

A ..... intercept of the folded baseline
A ..... the absorbance at radius x in an AUC experiment
A_o ..... the absorbance at reference radius x_o AUC experiment
α ..... the extent of the unfolding reaction
α1AT α1-antitrypsin
AFM ..... atomic force microscopy
ALS ..... amyotrophic lateral sclerosis
ALS-FTLD ..... amyotrophic lateral sclerosis with frontotemporal lobe degeneration
apoSH ..... metal free, disulfide reduced, superoxide dismutase
apoSS ..... metal free, disulfide oxidized, superoxide dismutase
AUC ..... analytical ultracentrifugation
$ASA_{monA\text{-}np}$ ..... non-polar solvent accessible surface area of the folded monomer A
$ASA_{monA\text{-}p}$ ..... polar solvent accessible surface area of the folded monomer A
$ASA_{monB\text{-}np}$ ..... non-polar solvent accessible surface area of the folded monomer B
$ASA_{monB\text{-}p}$ ..... polar solvent accessible surface area of the folded monomer B
$ASA_{dimer\text{-}np}$ ..... non-polar solvent accessible surface area of the folded dimer
$ASA_{dimer\text{-}p}$ ..... polar solvent accessible surface area of the folded dimer
ΔASA ..... change in solvent accessible surface area
ΔASA_{np} ..... change in non-polar solvent accessible surface area
ΔASA_{p} ..... change in polar solvent accessible surface area
B ..... slope of the folded baseline
$\beta 1$ and $\beta 2$ ..... $\Delta H_{vH}/\Delta H_{cal}$ multiplied by the molecular weight of the cooperative unfolding unit
C ..... intercept of the monomer intermediate baseline
CEST ..... Chemical Exchange Saturation Energy Transfer
CCS ..... copper chaperone for superoxide dismutase
CD ..... circular dichroism
C_{mid} ..... the concentration of urea at the midpoint of the denaturation curve
CPMG ..... Carr-Purcell-Meiboom-Gill
Cu or Cu^{2+} ..... copper
Cys ..... cysteine
ΔC_p ..... specific heat capacity
$\Delta C_{p,d}$ or $\Delta C_{p,N_2\leftrightarrow 2M}$ ..... change in specific heat capacity of dimer dissociation
$\Delta C_{p,M\leftrightarrow U}$ ..... change in specific heat capacity of monomer unfolding
$\Delta C_{p,N_2\leftrightarrow 2U}$ ..... change in specific heat capacity of total unfolding
D ..... slope of the monomer intermediate baseline
D_c ..... translational diffusion coefficient
D_h ..... hydrodynamic diameter
$D_{h,I}$ ..... D_h values determined by the intensity distribution
$D_{h,N}$ ..... D_h values determined by the number distribution
DLS ..... dynamic light scattering
DSC ..... differential scanning calorimetry
E ..... intercept of the unfolded baseline
EDTA ..... ethylenediaminetetraacetic acid

ER ..... endoplasmic reticulum
F ..... slope of the unfolded baseline
fALS ..... familial amyotrophic lateral sclerosis
FAP ..... familial amyloid polyneuropathy
f_m ..... fraction of monomer
f_U ..... fraction of unfolded monomer
ΔG ..... change in Gibbs free energy
$\Delta\Delta G$ ..... ΔG of pWT minus ΔG of mutant
ΔG_d or $\Delta G_{N_2 \leftrightarrow 2M}$ ..... change in Gibbs free energy of dimer dissociation
GdmCl ..... guanidinium chloride
G_f ..... free energy of the folded state
$\Delta G_{M \leftrightarrow U}$ ..... change in Gibbs free energy of monomer unfolding
$\Delta G_{N_2 \leftrightarrow 2U}$ ..... change in Gibbs free energy of total unfolding (folded dimer to unfolded monomer)
G_u ..... free energy of the unfolded state
ΔG_{ref} ..... change in Gibbs free energy at reference temperature
g(τ) ..... autocorrelation of $I(t)$ as a function of delay time (τ)
HEPES ..... 4-(2-hydroxyethyl)-1-piperazineethanesulfonic acid
HgS ..... mutant hemoglobin
holoSS ..... copper and zinc bound, disulfide oxidized, superoxide dismutase
ΔH ..... change in enthalpy
Δh_{cal} ..... specific calorimetric enthalpy
ΔH_{cal} ..... calorimetric enthalpy
ΔH_{ref} ..... change in enthalpy at the reference temperature
ΔH_{vH} ..... van't Hoff enthalpy
$\Delta h_{0.5,M \leftrightarrow U}$ ..... specific enthalpy change for monomer unfolding
ΔH_d or $\Delta H_{N_2 \leftrightarrow 2M}$ ..... change in enthalpy of dimer dissociation
$\Delta H_{M \leftrightarrow U}$ ..... change in enthalpy of monomer unfolding
$\Delta H_{N_2 \leftrightarrow 2U}$ ..... change in enthalpy of total unfolding (folded dimer to unfolded monomer)
I ..... intermediate state
I_o ..... the baseline offset in an AUC experiment
$I(t)$ ..... light scattering intensity at time (t)
ITC ..... isothermal titration calorimetry
K ..... Boltzmann constant
K_d or $K_{d,N_2 \leftrightarrow 2M}$ ..... equilibrium constant for dimer dissociation
$K_{M \leftrightarrow U}$ ..... equilibrium constant for monomer unfolding
M ..... monomer intermediate state
$[M_i]$ ..... concentration of apo SOD1 monomer in the ITC cell after injection i
$[M_{i-1}]$ ..... concentration of apo SOD1 monomer in the ITC cell after injection i-1
$[M]_o$ ..... total concentration of apo SOD1 in units of mol monomer L^{-1}
$m_{M \leftrightarrow U}$ ..... the dependence of the monomer stability on urea concentration
$m_{N_2 \leftrightarrow 2M}$ ..... the dependence of the dimer interface stability on urea concentration
MW_{obs} ..... the fitted molecular weight of the protein in an AUC experiment
n ..... molecularity
N ..... native state
N^* or M^* ..... native-like state

NaCl ..... sodium chloride
Na_2SO_4 ..... sodium sulphate
NaH_2PO_4 ..... sodium phosphate
NE ..... neutrophil elastase
NMR ..... nuclear magnetic resonance
ρ ..... the density of the solvent in an AUC experiment
PAR ..... 4-(2-pyridylazo)rescorcinol
PDB ..... protein data bank
PDI ..... polydispersity index
P_{dimer} ..... protein concentration in mol dimer L^{-1}
PrP ..... prion protein
pWT ..... pseudo wild type superoxide dismutase
q ..... light scattering vector
q_i ..... heat associated with each injection in an ITC experiment
q_{dil} ..... the heat associated with sample dilution unrelated to dissociation in an ITC experiment
R ..... universal gas constant
RCL ..... reactive centre loop within α1-antitrypsin
sALS ..... sporadic amyotrophic lateral sclerosis
SEC ..... size exclusion chromatography
serpins ..... serine protease inhibitors
SDS-PAGE ..... sodium dodecyl sulfate polyacrylamide gel electrophoresis
SLS ..... static light scattering
SOD1 ..... superoxide dismutase 1
SOD2 ..... superoxide dismutase 2
SOD3 ..... superoxide dismutase 3
S_N ..... the dependence of the native protein signal on the concentration of urea
S_U ..... the dependence of the unfolded protein signal on the concentration of urea
SPIP ..... Scanning Probe Image Processor
Sup35 ..... yeast prion protein
ΔS ..... change in entropy at the reference temperature
ΔS_{ref} ..... change in entropy at the reference temperature
ΔS_d or $\Delta S_{N_2 \leftrightarrow 2M}$ ..... change in entropy of dimer dissociation
$\Delta S_{M \leftrightarrow U}$ ..... change in entropy of monomer unfolding
$\Delta S_{N_2 \leftrightarrow 2U}$ ..... change in entropy of total unfolding (folded dimer to unfolded monomer)
T ..... temperature
t_{avg} ..... the average value of $t_{0.5}$ for all apo SOD1 variants
TCEP-HCl ..... tris(2-carboxyethyl)phosphine hydrochloride
T_{exp} ..... experimental temperature
T_{ref} ..... reference temperature
ThT ..... thioflavin-T
TTR ..... transthyretin
$T_{0.5}$ ..... the temperature in Kelvin at which half of the protein is unfolded
$t_{0.5}$ ..... the temperature in °C at which half of the protein is unfolded
$t_{0.5,app}$ ..... the temperature in °C at the maximum C_p
$t_{0.5,M \leftrightarrow U}$ ..... temperature midpoint for monomer unfolding
T_1 ..... the temperature at which the thermodynamics of dimer dissociation were measured by ITC

T_2 ..... the temperature at which the equilibrium constant $K_{M\leftrightarrow U}$ is equal to 1
t_0 ..... 0 hours of incubation
t_{22} ..... 22 hours of incubation
t_{143} ..... 143 hours of incubation
t_{300} ..... 300 hours of incubation
U ..... unfolded state
v ..... volume of each injection in an ITC experiment
$\bar{\upsilon}$ ..... the partial specific volume of the protein
V ..... ITC reaction cell volume
VADAR ..... Volume, Area, Dihedral Angle Reporter
V_e ..... elution volume in a SEC experiment
V_M ..... elution volume of the apo SOD1 monomer
VMD ..... Visual Molecular Dynamics
V_{N_2} ..... elution volume of the apo SOD1 dimer
ω ..... the angular velocity of the rotor in an AUC experiment
WT ..... wild type superoxide dismutase
Y_{obs} ..... the observed optical signal in a CD experiment
Y_N° ..... optical signal of the native protein in the absence of urea
Y_U° ..... optical signal of the unfolded protein in the absence of urea
z_d ..... Z-average
Zn or Zn^{2+} ..... zinc
σ ..... PDI width
η ..... viscosity
Θ ..... light scattering angle
λ ..... wavelength of light

Chapter 1

Introduction

Author Contributions

Some of the material presented in this chapter has been published previously. Section 1.3.1 was adapted from Broom *et al.*, 2011 (1) and Broom *et al*., 2014 (2); Section 1.3.2 was obtained from Broom *et al*., 2011 (1); and Sections 1.3.5-1.3.6 were obtained from Broom *et al*., 2014 (2). I have been granted permission from *In Tech* and *Portland Press* for the inclusion of this work in my doctoral thesis.

1.1 Amyotrophic Lateral Sclerosis

Amyotrophic lateral sclerosis (ALS) is a heterogeneous disorder characterized as either a proteinopathy, ribopathy, or both (3). ALS affects upper motor neurons in the motor cortex as well as lower motor neurons in the brainstem and spinal cord, leading to muscle weakness, atrophy, spasticity, and involuntary muscle contraction (3–5), with eventual failure of the respiratory muscles underlying the fatal event in most cases (5, 6). In 1993, a genetic link was established between ALS and mutant forms of Cu, Zn-superoxide dismutase (SOD1) (7, 8), and since then ALS-linked mutations have been found in more than 25 genes affecting many different aspects of protein homeostasis and RNA processing (3, 6, 9). Like many other neurodegenerative diseases (10), the majority of ALS cases are not inherited (ie., sporadic (sALS)), and a small proportion (~10%) are familial (fALS) (8). It is now believed that ALS-linked mutations disrupt normal cellular function through both gain-of-function and loss-of-function mechanisms that ultimately lead to progressive failure of the motor neuron, characterized by protein aggregation, mitochondria stress, endoplasmic reticulum (ER) and Golgi malfunction, and disruption in axon transport, eventually leading to axon retraction and denervation of the lower motor neurons and muscles (3, 6, 11, 12). Similar to other neurodegenerative diseases, ALS pathogenesis progresses from an initial region to adjacent sites through mechanisms not well understood (10). The onset and duration of disease is highly variable, even among patients with the same mutation, indicating that multiple factors may modulate disease (3, 13). The onset of symptoms is typically during middle age and juvenile ALS is very rare; thus, ALS is thought to be associated with aging (3). It has been proposed that the natural decline of proteostatic mechanisms associated with aging plays a role in increasing the propensity of proteins to accumulate and aggregate (14, 15). Disease symptoms become

evident during the first stage of motor neuron death, at which point axon connections are disrupted due to axon retraction. Initially, denervation can be compensated for by a process referred to as "sprouting," whereby axons from motor neurons more resistant to degeneration in the surrounding area re-establish lost connections. Over time however, this mechanism is not sufficient to prevent disease progression, which is usually rapid (~2-5 years) (3). The factors that contribute to motor neuron vulnerability and degeneration are not well understood but relate to the cell's response to stress, regeneration potential, and susceptibility to glutamate-induced exocitotoxicity (3, 16, 17). Furthermore, what defines the actual onset of disease, referred to as the biological onset, is unknown, but is likely determined within the motor neuron. Disease duration may depend on other factors, such as the neuroinflammatory response to degeneration (3), and/or the mechanism by which motor neuron pathology is spread (10, 14). It is possible that the disease may start early in life, perhaps during embryonic development, and become apparent only later in life.

Recent research has increasingly recognized distinguishing pathological features among subsets of patients, but also overlapping symptoms with other neurodegenerative disorders as disease progresses (3, 18, 19). Neurons in the prefrontal and temporal cortex can be affected to varying extents in ALS, resulting in simultaneous development of frontal temperal dementia (FTD), referred to as ALS with frontotemporal lobe degeneration (ALS-FTLD) (3). Thus, it has been proposed that ALS and FTD exhibit two ends of a single-disease spectrum. Furthermore, numerous genes have been linked to ALS, and there is evidence for differences in pathology related to both genetic and environmental factors (3, 20). Therefore, ALS may best be described as a syndrome and not as a single disease (20).

While the cause or causes of ALS remain unknown, a leading hypothesis is that toxic protein misfolding plays a role, as is the case in other neurodegenerative diseases (21). While many misfolding diseases involve the formation of a particular type of fibrillar aggregate known as amyloid, it is not clear to what extent protein aggregation in ALS resembles amyloid formation (22). Amyloidoses are characterized histopathologically using the dye Congo Red, which exhibits green-gold birefringence upon binding to unbranched amyloid fibres containing a highly protease resistant cross-β-structure core, with β-strands oriented perpendicular to the fibre axis (23) (refer to section 1.2.1). Congo Red birefringence is not observed in ALS (22); nevertheless, the observations of fibrillar aggregates and a proximal pattern of cell death (3, 24–26) suggest that ALS has similar disease mechanisms to amyloidoses.

SOD1 mutations comprise ~1.5-2% of all ALS cases, but nevertheless represent a major known cause of the disease (3, 6). Furthermore, the clinical symptoms of fALS and sALS are similar; yet, fALS patients with SOD1 mutations have an earlier age of disease onset than sALS (by ~10 years) (4). Misfolded SOD1 is targeted for degradation via the ubiquitin pathway, and mutations in SOD1 may disrupt this process and in turn impair the proteasomal degradation pathway (27, 28). As these regulatory systems fail, protein oligomers and then aggregates can accumulate in the cytosol, causing cellular stress and eventual death. Mutant SOD1 is the main component of intracellular aggregates found in fALS patients with SOD1 mutations (29). These SOD1 aggregates have been classified morphologically as Lewy-body-like hyaline inclusions which are composed of granule coated fibrils 15-25 nm in diameter (26). Other components include ubiquitin (30), phosphorylated neurofilaments (31), the copper chaperone for SOD1 (CCS) (32), and other folding chaperones (17, 29). While it was originally thought that aggregation of SOD1 was limited to fALS (22), other studies have shown that aggregated SOD1

is present in some sALS aggregates as well (19, 33). The differences in the reported detection of aggregated SOD1 may be accounted for by differences in the binding properties of different anti-SOD1 antibodies. It is possible, therefore, that loss of stabilizing post-translational modifications or aberrant covalent modifications may induce conformational changes in wild type SOD1, similar to the effects of mutations, that result in harm to the cell (19, 33–35), and that SOD1 may serve as a link between a subset of sALS and fALS cases (33).

In ALS and a number of diseases such as Parkinson's, Alzheimer's, and Huntington's, neurodegeneration spreads through interconnected regions of the central nervous system (10, 15). This phenomenon may be explained by the discovery that a diverse number of misfolded and/or aggregated proteins released from one cell via exocytosis or cell lysis can penetrate neighbouring cells and form a structural template (ie. an aggregate "seed") for aggregation of the endogenous protein (10, 14, 24, 36). This finding has led to the hypothesis that the pathogenic mechanism observed in prion diseases may be more pervasive than previously thought (24). In prion diseases, the infectious agent, a misfolded protein, can spread from cell to cell and induce misfolding and aggregation of the endogenous protein (37). The key difference between prion diseases and other protein misfolding diseases, however, lies in the potency of induced aggregation (14). Currently, there is no evidence, with the exception of prion proteins, that misfolded protein can be spread between animals and/or humans; and thus, protein misfolding diseases where infectivity has not been demonstrated are now classified as prion-like diseases or prioniods (24).

Like many other misfolded proteins associated with neurodegenerative diseases, SOD1 has been shown to exhibit seeded aggregation in vitro and in vivo (14, 36, 38–40). SOD1 is largely present in the cytoplasm (70%) (41); however, both wild type and mutants have been

detected in the cerebrospinal fluid of healthy individuals as well as fALS patients (42, 43). Formerly, it was suggested that secretion of SOD1 may be a cellular protective mechanism, preventing intracellular inclusion formation; it now appears more likely that this process is harmful to the central nervous system as a whole (36). It has been shown that SOD1 can be excreted via a variety of distinct pathways, one of which is through association with chromogranins, the major components of secretory granules. This association is specific to mutant SOD1, and can trigger cell death (44). Furthermore, immunization targeting extracellular SOD1 was found to increase the lifespan of transgenic mice expressing mutant SOD1 (45). Once transported to the extracellular environment, misfolded SOD1 conformers and/or SOD1 aggregates less than 0.4 μm in diameter (10, 40) can be taken up by neighbouring cells and seed aggregation of endogenous wildtype and mutant SOD1 (39). Differences in the rate of cell to cell transfer of these aggregate seeds may underlie the rate of disease progression and partially account for the differences in pathology observed (40). Interestingly, human SOD1 seeds are only able to induce aggregation of human SOD1. Expression of human SOD1 in murine models does not cause aggregation of mouse SOD1, perhaps owing to differences in the N-terminal region of the proteins (39). Thus, seeded aggregation of SOD1 is highly sequence and perhaps structurally specific.

A remaining challenge for ALS research lies in uncovering the initial event(s) that lead to disease and the toxic species, misfolded or oligomeric protein, responsible for disease onset. While ALS may best be described as a syndrome, similar disease mechanisms likely underlie sporadic and familial cases, and discovering the common links between different versions of the disease will have a powerful impact on the therapeutic approaches to fighting and eventually curing the disease.

1.2 Protein Folding and Misfolding and Aggregation

Since 1961, when it was discovered that proteins could fold in the absence of the cellular environment, it has been known that a protein's primary sequence contains all the necessary information for protein folding (46); yet predicting the pathway by which proteins fold into their respective functional, native states remains a central problem in molecular biology, despite decades of progress. Because the number of possible conformations a polypeptide can adopt is so large, it would take an extremely long time for folding to occur if the polypeptide were to sample all possible arrangements in a systemic process prior to finding the native structure. Instead, it is believed that the inherent fluctuations of an unfolded protein allow it to make many initial contacts, enabling regions of the sequence to come together (47). In general, native-like interactions tend to be more stable than non-native interactions, and so lower the energy of the system once they form (48). Eventually, through these stochastic conformational fluctuations, the native state is found, a process that has been shown to be highly efficient for proteins that have survived evolution (47). In general, protein folding can be described by a nucleation-condensation mechanism, whereby the protein undergoes a series of conformational changes that eventually lead to compaction of the polypeptide chain and sequestration of the hydrophobic residues within the protein core. In this compact state, the polypeptide can sample fewer conformations, eventually acquiring a native-like structure that can serve as the folding nucleus around which the rest of the structure condenses to form the lowest energy native state (47, 49). The lowest energy state is not a static conformation, however, and local structural fluctuations are common for most protein folds (50). It is often assumed that the functional state of a protein is the most stable state under biological conditions (51), yet recent work has shown that most if not all proteins are able to form amyloid fibrils, structures that have even higher stability (52,

53). During folding, a polypeptide chain may encounter a number of energetic barriers caused by topology, proteins with large contact order fold more slowly, polypeptide inflexibility, improper disulfide bond formation, and aberrant intramolecular or intermolecular interactions (51). The native state, therefore, may reflect the conformation energetically accessible from the unfolded state and low enough in energy to be highly populated.

When proteins fold in an aqueous environment, roughly 85 percent of the non-polar side chains become buried in the core (54). These hydrophobic interactions are believed to be the driving force behind protein folding (55). When a protein is unfolded in an aqueous environment, the water molecules form hydration shells around the hydrophobic regions of the polypeptide (56). When favourable hydrophobic interactions within the core of a protein are formed, these structures are disrupted and water is released to the surrounding environment, an entropically favourable process despite the reduced conformational freedom of the polypeptide chain (57, 58). Mutations that introduce a cavity within the hydrophobic core of the protein decrease the number of van der Waals interactions and can largely reduce protein stability (54, 59). Hydrogen bonds also make very important contributions. In the native state, approximately 1.1 hydrogen bonds are formed per residue; 65 percent of those bonds occur between peptide groups, 23 percent occur between peptide groups and amino acid side chains, and only 11 percent occur between side chains (54). Thus, the polypeptide backbone forms the majority of the stabilizing hydrogen bonds in the native state. Hydrogen bonds and electrostatic interactions have also been found in the core of proteins, where they are stronger due to the lower dielectric constant in the hydrophobic core. In such cases, the residues involved in these interactions tend to be highly conserved (54).

A central aspect in understanding protein misfolding diseases is knowledge of the protein structural states that are relevant to pathology and their respective stabilities and mechanisms of formation. The populations of different states are determined by their relative stabilities. Protein stability can be thought of in two ways: thermodynamic and kinetic stability. Thermodynamic stability defines the populations of different states at equilibrium, while kinetic stability describes the rates of interconversion between states (Fig. 1.2A). Thus, thermodynamic and kinetic measurements provide complementary approaches for determining the conformations a protein is likely to adopt. Decreased protein stability is associated with increased unfolding, either from folded to less folded states, or within the ensemble of conformers that comprise a given state. Different conformers can vary greatly in their propensity to form aggregates (53). For the purposes of interpreting this work, the focus of this introduction will be on thermodynamic stability.

Thermodynamic stability, or the Gibbs free energy of folding (ΔG), is defined as the difference in energy between the unfolded and folded states when the system has reached equilibrium.

$$\Delta G = G_u - G_f \qquad \text{(Eq. 1.1)}$$

Thermodynamic stability (ΔG) is also related to both the change in enthalpy (ΔH) and entropy (ΔS) with temperature (T) by the Gibbs-Helmholtz equation (equation 1.2).

$$\Delta G = \Delta H - T\Delta S \qquad \text{(Eq. 1.2)}$$

Favourable reactions, such as protein folding, proceed spontaneously with negative (ΔG) values, while processes that are not energetically favourable have positive (ΔG) values. The thermodynamic stability (ΔG), enthalpy (ΔH), and entropy (ΔS), must always be determined with respect to a reference state according to the following equations.

$$\Delta H = \Delta H_{ref} + \Delta C_p(T - T_{ref}) \quad \text{(Eq. 1.3)}$$

$$\Delta S = \Delta S_{ref} + \Delta C_p \ln(\frac{T}{T_{ref}}) \quad \text{(Eq. 1.4)}$$

ΔH_{ref} and ΔS_{ref} refer to the enthalpy and entropy at the reference temperature (T_{ref}), respectively, and ΔC_p refers to the change in specific heat capacity for the process. Once these three values are known, the ΔG of folding/unfolding can be determined at all temperatures according to equation 1.5, which is a combination of equations 1.2, 1.3 and 1.4.

$$\Delta G = \Delta H_{ref} - T\Delta S_{ref} + \Delta C_p(T - T_{ref} - Tln(\frac{T}{T_{ref}}) \quad \text{(Eq. 1.5)}$$

Extrapolating ΔG, ΔH, and ΔS from the reference temperature requires an accurate ΔC_p. The first models of protein folding assumed no change in ΔC_p upon protein folding (ie., $\Delta C_p = 0$), implying that ΔH and ΔS are temperature independent variables. Given that protein folding involves the sequestration of hydrophobic residues, and that the heat capacity of a solution increases with hydrophobic hydration (58, 60), it is now believed that this early assumption is inaccurate (61). For protein folding/unfolding, the temperature dependence of ΔH and ΔS is in fact quite large (Fig. 1.1A). Furthermore, the ΔC_p for thermal denaturation of most proteins is positive, and usually can be considered constant for a given temperature range (56, 59). Given these characteristics, the ΔG of protein folding/unfolding varies non-linearly with temperature, and is referred to as a stability curve (Fig. 1.1). Owing to the curvature of this plot, there is a characteristic temperature range where ΔG is positive (ie., $G_u > G_f$ and protein unfolding is not favourable) and a temperature where the protein is most stable. The temperatures where the stability curve crosses the x-axis, corresponds to the melting temperatures of the protein. In most cases, there are two melting temperatures; the lower melting temperature is often below the freezing point of water and is usually not observed. Furthermore, the larger the ΔC_p, the larger the curvature, and the smaller the temperature range where ΔG is positive (59) (Fig. 1.1B).

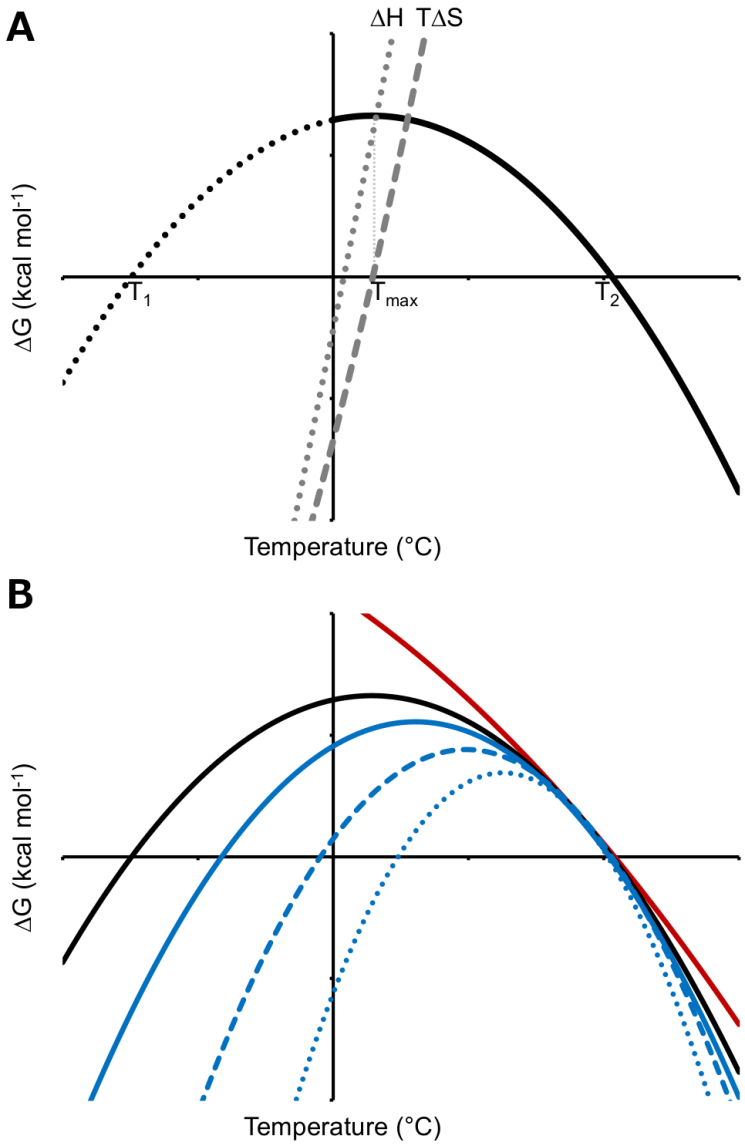

Figure 1.1 Protein Stability Curves. The stability curves represented here were constructed using data obtained for SOD1 mutant V148I in the fully metallated, holo, state (holoSS) (Broom and Meiering, unpublished data). **(A)** ΔG versus temperature is a non-linear function with negative curvature. T_1 and T_2 indicate the melting temperatures of the protein (ie., where ΔG=0, and for monomeric proteins that unfold/fold via a 2-state pathway, where half the protein is unfolded). T_{max} indicates the temperature of maximum stability (ie., where ΔS=0). **(B)** The magnitude of ΔC_p determines the curvature of the ΔG versus temperature function. If the ΔC_p is small, the temperature of maximum stability is not well defined (red curve), and the stability curve approaches linearity. As ΔC_p increases, the curvature of the function increases and cold-unfolding occurs at higher temperatures (ie. T_1 increases). For holo SOD1, ΔC_p is 2.75 kcal mol-1 °C^{-1} (black curve) (60). The red and blue lines were constructed with differing ΔC_p values: 1 kcal mol^{-1} °C^{-1} (red curve), 3.5 kcal mol^{-1} °C^{-1} (solid blue curve), 5 kcal mol^{-1} °C^{-1} (dashed blue curve), and 7.5 kcal mol^{-1} °C^{-1} (dotted blue curve). Both Fig. 1.1A and 1.1B are adapted from Becktel and Schellman, 1987 (59).

Destabilization of proteins by chemical modifications or by mutations favours an increase in the population of partially folded species that may possess a higher degree of aggregation propensity owing to the exposure of the hydrophobic groups, or hydrogen bonding ligands, that are normally buried in the protein core (Fig. 1.2B). This exposure can promote the formation of non-native intermolecular contacts between proteins which leads to formation of aggregates. Thus, the propensity of a given globular protein to aggregate depends on how energetically feasible it is for the protein to access locally, partially, or fully unfolded aggregation-prone state(s) (Fig. 1.2B). Interestingly, subtle decreases in global protein stability are often accompanied by local destabilization, which may only subtly alter the protein structure but nevertheless increase the aggregation propensity of the protein. As more light is shed on the various aggregation mechanisms, it is clear that there is evidence of aggregate formation from native-like species that have undergone much more restricted unfolding (53, 62). Examples of aggregate formation from native-like states include various proteins associated with disease such as mutant lysozyme (53), β2-microglobulin (53), and SOD1 (63). Various mechanisms of protein aggregation have been proposed, including formation of a cross-β spine, end to end stacking, and domain swapping, and in some cases protein aggregation may involve more than one of these mechanisms (64). These mechanisms will be explored further in sections 1.2.1 and 1.2.2, as they relate to amyloid and non-amyloid aggregation.

In addition to protein stability and structure, many other factors, such as physicochemical properties of amino acids within a protein sequence and solution conditions, can affect protein aggregation. Hydrophobicity, β-sheet propensity, and charge of a polypeptide sequence have been shown to modulate the formation of amyloid aggregates by unfolded proteins (65). Interestingly, these properties are also important for facilitating correct protein folding,

suggesting that while similar forces contribute to both processes, different key residues are involved in forming the initial contacts that drive native protein folding and aggregation (66). In many cases, the overall aggregation propensity of a protein increases if the primary sequence contains short stretches of amino acids with properties that favour aggregation, for example low net charge, extensive hydrophobicity, and/or a tendency to form a β-sheet over an α-helix (67). Taken together, these studies indicate that aggregation is at least partially controlled by the physicochemical properties of amino acid residues within a polypeptide sequence (65, 67).

Solution conditions are another important factor that can modulate the stability, conformation, and the intermolecular interactions of a protein, and thereby influence the rate of protein aggregation and the type of aggregate structure formed (68, 69). Importantly, variations in solution conditions can cause the same protein to aggregate by fundamentally different mechanisms (70–72). Temperature, pH, macromolecular crowding, agitation, and ionic strength are all variables that can influence both the type of aggregation observed (amorphous versus fibrillar) and the extent to which this process occurs (68, 69, 73, 74). A number of studies have used different solution conditions (increased temperature, decreased pH, increased ionic strength, sonication or agitation) to promote the formation of fibrillar amyloid aggregates by various forms of SOD1 (75–78). Other studies have demonstrated soluble oligomer and small aggregate formation by various forms of SOD1 in quiescent, physiologically relevant solution conditions (63, 79). Thus, it is becoming increasingly evident that multiple factors can greatly influence protein folding and aggregation and that these factors must be considered when investigating the molecular mechanisms of protein aggregation and the relevance of these mechanisms to disease.

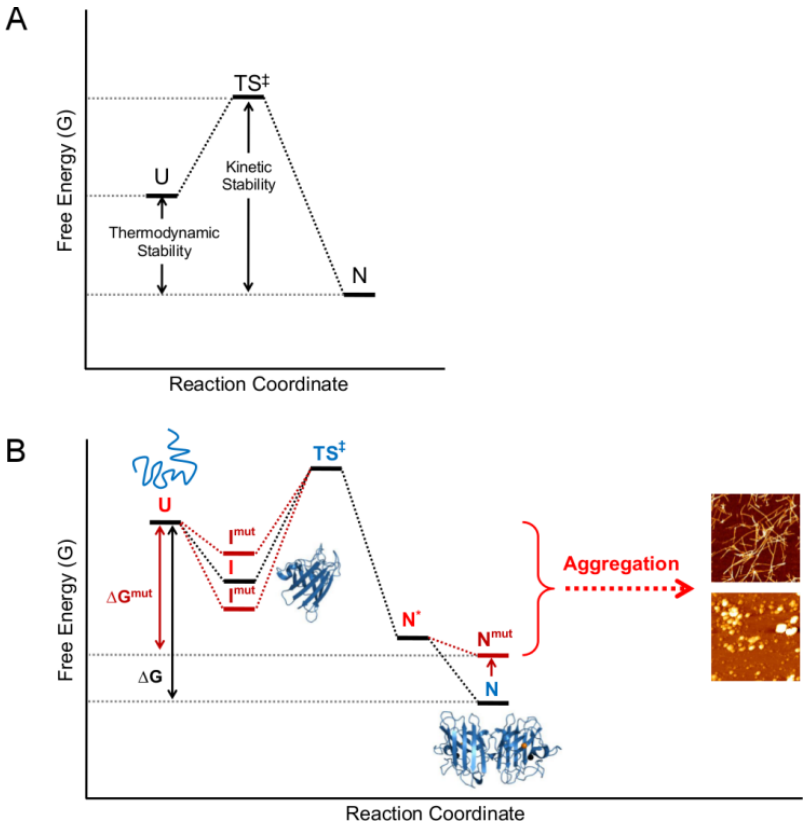

Figure 1.2 Reaction Coordinate Diagrams for Protein Folding. (A) Thermodynamic stability is defined as the energy difference between the folded native state (*N*) and the unfolded state (*U*). The higher the stability, the more populated the *N* state at equilibrium. Kinetic stability is defined as the difference in energy between the folded, native state (*N*) and the transition state (*TS*), which represents the main energetic barrier to folding. For proteins with high kinetic stability, the transition state is less energetically accessible, and proteins will spend more time in the native conformation. **(B)** The effects of native state (*N*) destabilization by mutation on the population of locally unfolded, native-like (*N**), partially folded intermediate (*I*), and fully unfolded (*U*) states are shown. Aggregation may occur from *N**, *I* or *U*, and the morphology of the aggregates formed may depend on the conformation of the protein prior to aggregation. Mutations that destabilize *N* (destabilization is indicated by the red arrow), decrease the energy difference between the *N* and the more unfolded states (*N**, *I* or *U*), and thereby promote aggregation. Note that destabilization of *N*, does not necessarily imply destabilization of *I*. Mutations that destabilize *N* may stabilize or destabilize *I*, resulting in a large increase or decrease, respectively, in the population of *I* compared to levels observed in the native folding pathway. Panel B was obtained from Broom *et al*., 2011 (1), and originally adapted from Chiti and Dobson 2009 (53).

1.2.1 Amyloid Aggregates

Amyloid has traditionally been defined by pathologists as extracellular fibrils that give rise to a cross-β X-ray diffraction pattern and cause green birefringence upon binding congo red (23, 62, 64, 80). Currently, extracellular deposition of classical amyloid aggregates has been identified in approximately 25 syndromes defined clinically as amyloidosis (81). The definition of amyloid however, is evolving and has become controversial, as fibrils resembling amyloid have been discovered intracellularly, in diseases not traditionally considered amyloidosis (23, 64, 82), and numerous biophysical studies have identified structural heterogeneity in amyloid fibrils (23, 82, 83).

From a biophysical perspective, the fundamental feature of amyloid fibrils is the cross-β spine core; yet, these fibrils can differ widely, in the size of the fibril spine (ie., how much of the protein forms the amyloid core), the arrangement of β-strands (parallel or antiparallel) and the degree to which these β-strands align (23, 62, 84). Despite these differences, the β-sheet is the strongest repeating unit of the amyloid fibril. Most structural studies of amyloid fibrils have revealed that the β-strands run perpendicular to the fibril axis, stabilized by hydrogen bonds between main chain atoms arranged parallel to the fibril axis, and the side chains face above and below the sheet (23). Other structural studies of amyloid fibrils formed from out-of-register β-sheets have revealed that the β-strands are arranged at an angle, with repeating weak and strong interfaces, stabilized by two and six hydrogen bonds, respectively. The stability of these fibrils is lower than that of fibrils formed from in-register β-sheets, possibly due to hydrogen bonding donor and acceptor groups left unsatisfied at the ends of the β-strands (84). Each β-sheet is typically referred to as a protofibril, and the number and orientation of the protofibrils add further variation to the amyloid theme. The protofibrils can be oriented face to face, or face to

back, and they can pack together with the same or opposite edge strands at each end. The amyloid core is referred to as a dry steric zipper due to the highly packed side chains and the release of water upon formation. Due to this release of water, the hydrophobic effect contributes stability to the fibril (23).

Most of what is known about the amyloid structure derives from structural studies of small amyloidogenic peptides that form the amyloid core through side-chain interactions of self-complementary sequences (62, 82). One example is the peptide GNNQQNY, derived from the yeast prion protein Sup35p (Fig. 1.3A). In the amyloid state, the peptide side chains interact in the core such that the glutamine (Q) and asparagine (N) are tightly interlocked (80). More complex cores can form from sequences that are not self-complementary, but nevertheless interact in favourable ways. Remarkably, several different amyloid forming proteins have been shown to form numerous distinct dry steric zippers, most notably the amyloid-β peptide, which can form diverse fibrils with 13 different dry steric zippers under different solution conditions (23, 62, 85).

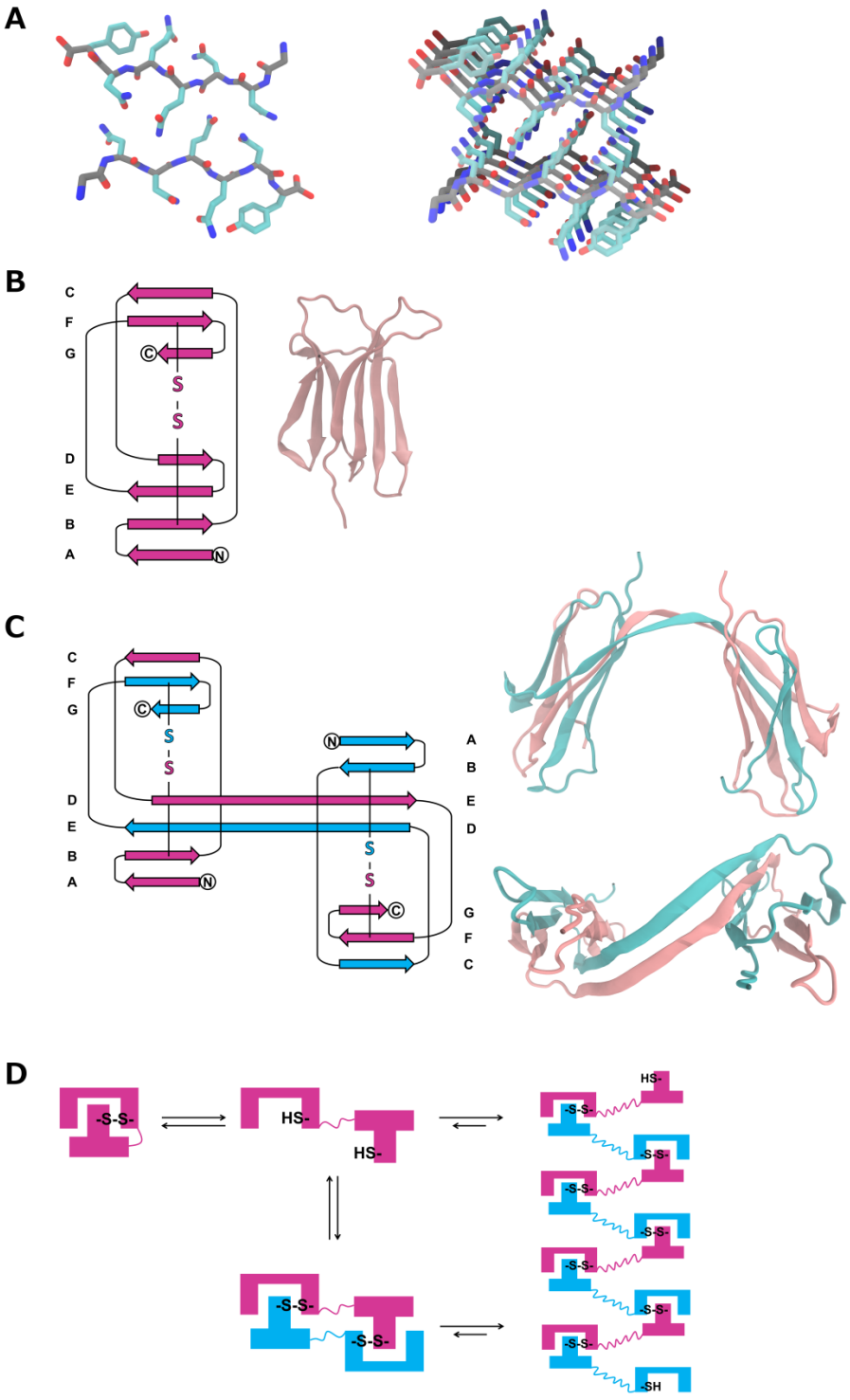

Figure 1.3 Modes of Amyloid Formation. **(A)** The amyloidogenic peptide GNNQQNY, derived from the yeast prion protein Sup35p, is shown interacting with an identical peptide. The polypeptide backbone carbon atoms are shown in grey, the side chain carbon atoms in cyan, oxygen atoms in red, and nitrogen atoms in blue. Interactions between side chain residues form the steric zipper amyloid core. As peptides add to the fibril, the growing β-sheet extends from the page, as shown on the right. Panels B through D depict β2-microglobulin misfolding and

run-away domain-swapping leading to dimerization and formation of amyloid fibrils. In each panel, the different subunits within the domain-swapped structure are coloured either blue or pink. These panels were recreated from Liu et. al., 2011 (83). **(B)** The native structure of monomeric β2-microglobulin forms a β-sandwich that is stabilized by one disulfide bond that links the two sheets formed by strands A, B, D, E and C, F, G. A schematic representation of the native state fold is shown on the left, while the crystal structure is shown on the right (PDB code 1LDS) (86). **(C)** A domain swapped dimer forms when the disulfide is reduced and β-strands E, F, and G are exchanged between the subunits, creating two new intermolecular interfaces. One is identical to the original contacts made in the monomer, while the other interface is formed by the hinge loop, corresponding to the original loop 4, which connects the swapped domains. This hinge loop region contains an amyloidogenic sequence and can form the steric zipper amyloid core. Disulfide shuffling also accompanies dimer formation, where the original intramolecular disulfide bond becomes an intermolecular disulfide bond, adding stability to the dimer structure. A schematic representation of the domain-swapped dimer is shown on the left, while two views of the crystal structure are shown on the right. The higher and lower images show the frontal and top-down views of the domain-swapped dimer (PDB code 3LOW) (83). **(D)** Run-away polymerization of β2-microglobulin can occur if domain swapping is not reciprocal. Disulfide reduction can promote dimerization and oligomerization, and the self-association of the hinge loop region transforms the oligomers into amyloid fibrils. Disulfide bonds reformed between the interacting subunits promote aggregation (83).

It is generally believed that most proteins can form amyloid under destabilizing conditions, which exposes sites within the protein that can interact non-natively; yet, it is becoming increasingly evident that amyloid formation can arise from states that closely resemble the native state (53, 64, 83, 87). In fact, it was recently demonstrated that protein activity was preserved within an amyloid fibril, indicating that the active site is mainly intact despite fibrillation of the protein (64, 88). For proteins with extensive β-sheet secondary structure, amyloid formation may arise from subtle changes to the protein fold that expose edges of the native β-sheets, allowing for end-to-end stacking of the protein (64, 89). Such a mechanism has been proposed for SOD1; however, it is unclear whether these aggregates are truly amyloid (90). Amyloid formation can also be promoted by domain swapping between proteins (23, 64, 83, 89). Domain swapping can be reciprocal, where no unsatisfied domains are exposed, or it can be open-ended, where at least one or more unsatisfied domains exist at each end, resulting in propagation of a domain-swapped oligomer (Fig. 1.3B-D). In the latter case, interdomain interactions are identical to those found in the native state; thus, aggregation can be promoted by exposure of any segment free to interact with an identical partner (64, 83). Some amyloidogenic proteins, notably prion proteins, contain frustrated regions, where residues do not adopt the most favoured β-strand secondary structure. Domain swapping causes structural changes that alleviate this frustration (64, 91). Domain swapping can also facilitate non-amyloid fibrillation, as discussed in the following section.

Amyloid fibrils form via nucleation-dependent kinetics characterized by a lag phase corresponding to the time required to form the initial nucleus, the template upon which aggregates can grow (87, 92). For fibrils formed from small amyloidogenic peptides, approximately three peptides are required to form the template (93). Once formed, additional

peptides can join the fibril by exposing sequences that can interact with the template (23, 94). Due to the specific rotamer conformations the side chains must adopt in the fibril core, β-sheets within each protofibril form faster than the protofibrils can pair. For small peptides, the loss of entropy in the side chains creates a barrier to fibril formation (80). For full length proteins, however, the barrier may mainly be due to local and/or global unfolding processes that expose amyloidogenic side chains and/or the backbone amide N-H and C=O groups, which can form non-native hydrogen-bonding interactions (23, 87).

It can be seen, therefore, that the term amyloid can refer to a variety of fibrils with a similar core motif, but with a great deal of variety and structural complexity. Numerous studies reveal that amino acid sequences are not the singular determinant of fibril structure, as specific amyloidogenic sequences can form fibrils that differ in, for example, diameter, twist period, and stability (82); and it has been proposed that the heterogeneity observed in amyloid structures may account for the phenotypic diversity observed in amyloid-associated diseases (10). Furthermore, the observation that certain amyloid seeds can induce aggregation of some amyloidogenic proteins but not others may depend on, for instance, sequence complementarity, the size of the amyloid core, and the number of protofibrils wound together (23). In general, it is believed that the larger the amyloidogenic sequence, the more complex the aggregation pathway, and the more difficult it may be to determine which species are toxic (95). It was recently demonstrated that two distinct amyloid fibrils, formed from the same protein, displayed different degrees of toxicity. Furthermore, the toxicity of one fibril was increased after fragmentation, while the toxicity of the other decreased, thus indicating the smaller aggregates are not always more toxic (96). In another study, it was shown that fibrils formed from out-of-register β-sheets were more toxic than those formed from in-register β-sheets, owing to the former's lower stability and

increased likelihood of fragmentation (84). The cellular response to different amyloid conformations is highly complex; it is becoming increasingly clear that the pathways that lead to protein aggregation are highly diverse (95). Biophysical studies of amyloid fibrils are important, given that amyloid architecture appears to underlie fibril toxicity (97). Many studies of amyloid structure and formation have helped to explain why amyloid fibrils are associated with so many diseases and to distinguish the particular biophysical properties of the toxic fibrils from the benign ones.

1.2.2 Non-amyloid Aggregates

Non-amyloid protein aggregation has been observed in a number of protein conformational diseases, as well as in vitro (64, 98–105), albeit in general this type of protein aggregation is less well characterized than amyloid aggregation. Examples of disease-relevant proteins that form non-amyloid aggregates include hemoglobin, in cases of sickle-cell anemia, members of the superfamily of serine protease inhibitors (serpins), in a number of diseases generalized as the serpinopathies, and the crystallins, associated with the onset of cataracts. In the first example, hemoglobin forms ordered helical fibrils (Fig. 1.4A, B), while the serpins form an assembly of β-sheets that differ from amyloid in that they lack the characteristic cross-β spine (Fig. 1.4 C) (64). In the final example, it is currently believed that aggregation of crystallin results in the formation of non-structured aggregates referred to as amorphous (104, 106).

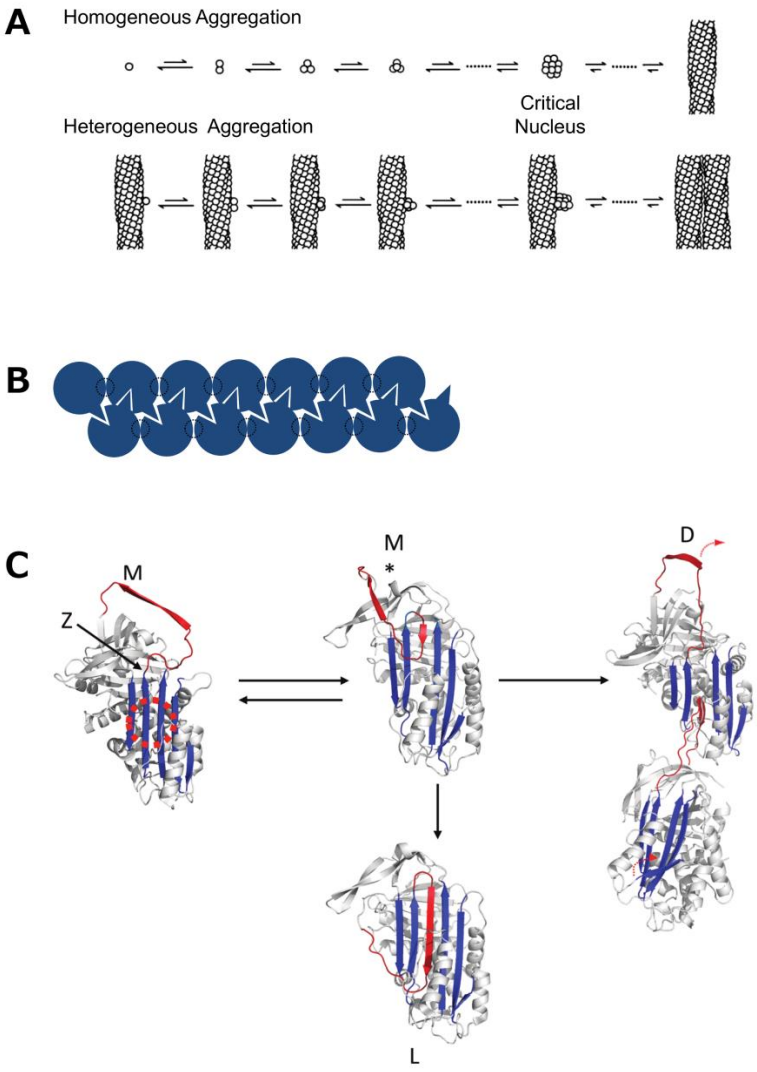

Figure 1.4 Modes of Non-amyloid Aggregation. Here two different modes of non-amyloid aggregation are shown. **(A)** Mutant hemoglobin (HgS) forms helical aggregates via a double nucleation mechanism whereby fibrils form de novo, through homogeneous nucleation, and grow by addition of monomers to a preformed fibril, through heterogeneous nucleation. In each case, the critical nucleus represents the thermodynamic turning point in the aggregation pathway whereby further aggregate growth becomes favourable. This figure was obtained from Ferrone, 2004 (103). **(B)** The HgS fibril is composed of double stranded HgS polymers that associated via interactions between β6 valine and the hydrophobic pocket of an additional HgS monomer. In this schematic representation, β6 valine is depicted as a protruding triangle. Interactions between β6 valine residues are not reciprocal and facilitate further higher order assembly of HgS molecules. A secondary interaction site exists between HgS monomers within the fibril, indicated by the black circle; however, these interactions are not well characterized. This figure was adapted from Wang et. al., 2013 (107). **(C)** Domain swapping underlies aggregation of α1-antitrypsin, a member of the serpin superfamily. A common cause of α1-antitrypsin deficiency arises when individuals inherit the Z allele of the gene, which contains a mutation at the beginning of the reactive centre loop (RCL, the location of this mutation is indicated by a Z). The RCL loop is indicated in red. Others inherit mutations in β-sheet A, indicated in blue,

referred to as the shutter region, and indicated by a red circle. These inherited mutations disrupt β-sheet A, promoting formation of an aggregation-prone native-like state (M*), which allows the insertion of the RCL into β-sheet A, adding an additional strand. If this process occurs intramolecularly, α1-antitrypsin forms a more stable latent monomer (L), but if the RCL of one molecule inserts into the β-sheet of another, dimerization (D) and later polymerization can occur. This figure was obtained from Lomas, 2013 (100).

Aggregation of mutant hemoglobin (HbS) underlies the pathology of sickle cell anemia (108). Hemoglobin contains four subunits, two denoted as α, and two as β. Individuals with sickle cell anemia contain mutations at the sixth position within the two β chains, that replace a glutamic acid with a valine, resulting in the introduction of two hydrophobic residues at the surface of the protein (109). When hemoglobin is in the deoxygenated state, the β6 valine residue can interact with a hydrophobic pocket within the β-chain of an adjacent molecule, leading to polymerization at high enough concentrations (Fig. 1.4A, B) (102, 103, 110). A salt bridge situated within this hydrophobic pocket underlies the pH dependence of HbS polymerization (103). The β6 valine contact site, which lies at a diagonal with respect to the fibril axis and is referred to as the lateral interaction site, combined with a secondary contact site, which does not contain the site of mutation and lies along the fibril axis, form the important interactions that underlie the double stranded fibril that is the fundamental unit of the helical polymer. The polymer structure has been shown to contain seven of these fibril pairs (111, 112). As the HbS fibrils grow, they distort the structure of the red blood cell, causing it to move more slowly through the venous capillaries, resulting in damage that is associated with the clinical symptoms of sickle cell anemia (110).

Aggregation of HbS proceeds through a double nucleation mechanism (Fig. 1.4A) (103). The initial contacts made between HbS molecules are not favourable and form only through stochastic structural fluctuations that lead to temporary association between HbS molecules (103, 110). The critical nucleus is thought to consist of a small segment of the 14-strand polymer; however, the structural details of this species are unclear. The nucleus is considered to be the thermodynamic turning point, and its properties may vary with HbS concentration and pH, as well as other variables (103). Once the critical nucleus forms, polymer growth becomes

thermodynamically favourable. Additionally, the surface of the polymer supports further nucleation, forming branching sites where additional HbS molecules can add on to the fibril (103, 110).

The serpin superfamily includes a large number of proteins, approximately 1500, with varied functions (113, 114). Members of the serpin superfamily include serine and cysteine protease inhibitors, dual class inhibitors, as well as non-inhibitory proteins. These proteins are important regulators of proteolysis, and play key roles in coagulation, inflammation, and fibrinolysis (100, 113, 115). While the primary sequences of serpin proteins differ, these proteins share a core structure composed of approximately 400 amino acids (113, 114). This core consists of three β-sheets and nine α-helices, conventionally named A-C and A-I respectively (100, 113). The most common and thoroughly studied member of the serpin superfamily is α1-antitrypsin (α1AT), which functions as an inhibitor of neutrophil elastase (NE), a protease involved in the inflammatory response (116). Through a combination of loss-of-function and gain-of-function mechanisms, mutations in α1AT cause α1AT deficiency, and result in increased levels of NE, in turn leading to emphysema, and intracellular aggregation of α1AT, causing liver disease (100, 113, 115). The general mechanism by which serpin inhibitors carry out their function demands a great deal of structural flexibility; thus, these proteins are only marginally stable in their native conformations (101, 113, 114). In the native state, these proteins expose a large loop, designated the reactive centre loop (RCL), which contains the cleavage site for the target protease. Following proteolytic cleavage, the RCL inserts into β-sheet A, a more stable conformation, adding an additional β-strand. Because the target protease is covalently bound to the RCL, this movement drags the protease from one end of the protein to the other, inactivating both the serpin and protease. Because the inactive state is more stable

than the native state, the energy gained from insertion of the RCL into β-sheet A provides a driving force for inactivation (101, 113–115).

A number of disease-associated mutations have been identified in cases of α1AT deficiency (100, 113, 116). Mutations destabilize the protein, resulting in slower folding into a native state that contains an opening in β-sheet A, and an unraveled α-helix F. These structural alterations predispose the protein to forming an expanded β-sheet A, as the reactive loop can then insert into the middle of β-sheet A. This conformational change can result in the formation of an inactive monomer, if the RCL inserts into its own β-sheet A, or an inactive domain-swapped dimer, if the RCL from another monomer inserts into β-sheet A. Propagation of this dimer leads to polymerization (100, 101, 113–115). It was originally believed that polymerization of the serpin proteins occurred via a unified mechanism, but it is now well established that the reactive loop can insert into different positions within β-sheet A, or even add to another β-sheet, depending on the solution conditions (115). In some cases, the aggregates formed were identical to those observed in disease; in other cases, they were only observed *in vitro* (117).

Protein association can also involve formation of aggregates that are far less structured and this type of aggregation is referred to as amorphous. Amorphous protein aggregation is associated with a number of processes, such as production of wine haze and the development of cataracts, and is a common problem during purification of recombinant proteins (118, 119), frequently observed when proteins are incubated at their isoelectric pH (120). In cataracts, proteins within the ocular lens accumulate age-related damage, due to oxidative stress and exposure to UV light, resulting in protein destabilization and consequently aggregation. These aggregates scatter light and cause blurred vision and eventually blindness if left untreated (121). This process is believed to begin with the crystallin proteins, notably α-crystallin, which

functions as a folding chaperone, binding to proteins in the molten globule state to prevent aggregation, though in later stages of the disease other cytoskeletal proteins are also recruited (104, 106, 121). These aggregates are resistant to 8 M urea, yet are dissolved with the addition of reducing agent and thus are enriched in cross-linked protein (122). Cross-linking is thought to occur between cysteine residues; lens proteins undergo cysteine, methionine and tryptophan oxidation over time, but can also occur through non-disulfide covalent bonds involving dehydroalanine for example (104, 106, 123). It is important to note that the structure of aggregates formed within the ocular lens during cataract development remains controversial; both amyloid and amorphous aggregation of crystalline proteins has been observed under different conditions (124).

Few mathematical models exist to describe the mechanism of amorphous aggregation; yet, it has been characterized as a disordered process whereby monomers add to a growing aggregate in any direction. As the surface area of the aggregate grows, so does the rate of aggregation (125). Various modes of amorphous aggregation may differ, however, depending on the initial conformation of the aggregating protein and the degree of residual structure within the aggregate.

While other modes of protein assembly exist, these examples reflect how multifaceted protein aggregation processes are. Furthermore, single mutations have the potential to significantly alter the aggregation mechanism of many proteins. It may not be surprising, given the complexity and diversity of native protein structures, that various modes of protein assembly are possible; and with further progress being made each year toward uncovering the mechanisms and structural characteristics of protein aggregates, more strategies will be developed to combat protein aggregation in cases where it is inconvenient or toxic.

1.3 Cu, Zn-Superoxide Dismutase

1.3.1 Cu, Zn-Superoxide Dismutase Structure

Cu, Zn-Superoxide Dismutase (SOD1) is a paradigm for understanding protein structure and function as well as folding and misfolding in disease, and has been studied extensively (1, 2, 126). Human SOD1 is a member of the SOD family of proteins, which all function as antioxidant metalloenzymes, yet differ in their cellular localization, quaternary structure, and active site metal (127). SOD1 is a homodimer, while SOD2 and SOD3 are homotetramers; however, all catalyze the dismutation of superoxide to form hydrogen peroxide and oxygen (see section 1.3.2). SOD1 is located mainly in the cytosol and to a small extent in the intermembrane space of the mitochondria, whereas SOD2 and SOD3 are located in the mitochondria matrix and the extracellular space, respectively (127). To date, only SOD1 has been implicated in ALS pathogenesis (3, 33).

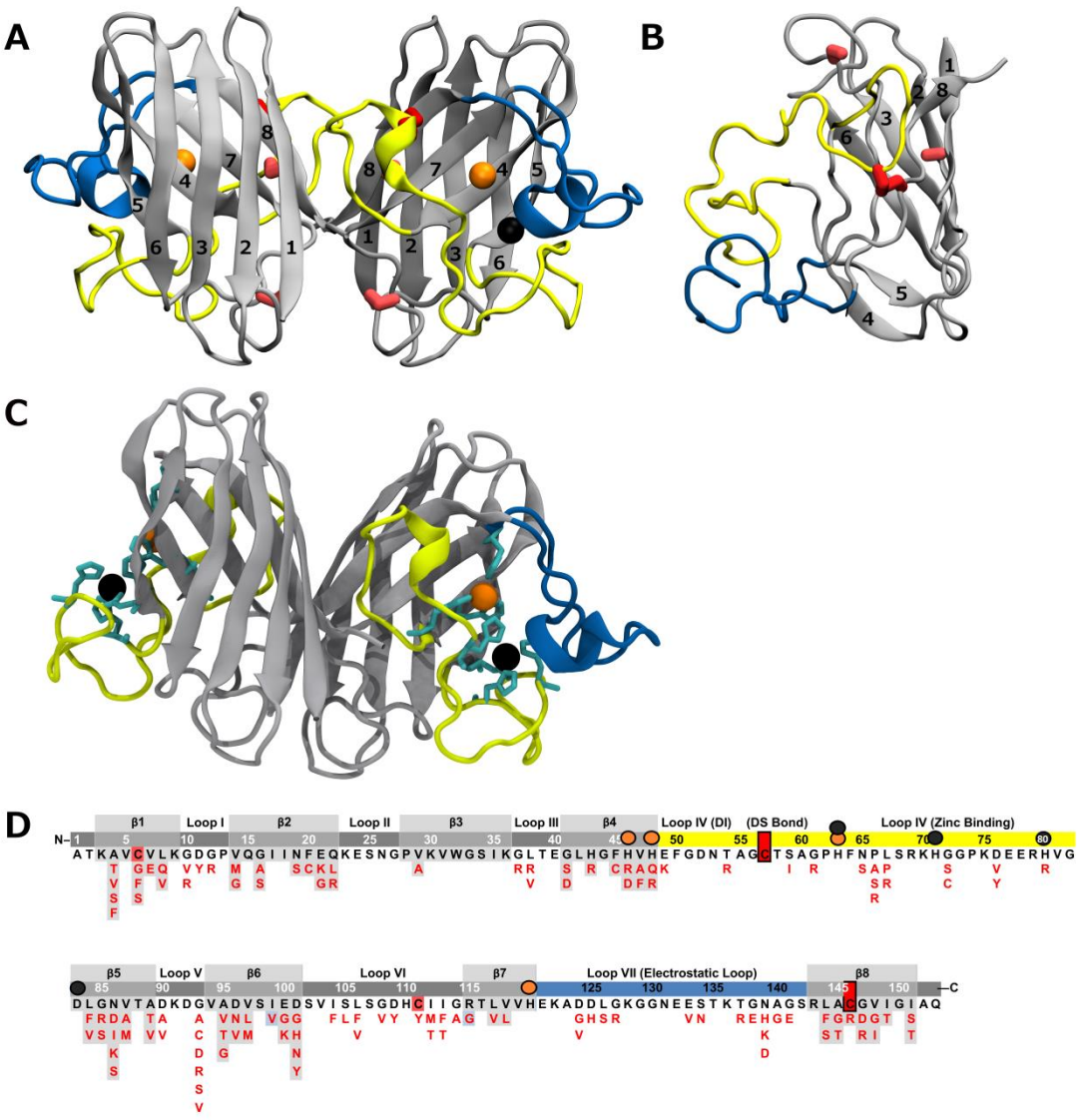

Figure 1.5 Structures of human SOD1 and variants associated with ALS. The structures of two different forms of SOD1 highlight how post-translational modifications have major effects on the structure of the protein. FALS-associated mutations are located throughout the protein and may promote misfolding in different ways. **(A)** Crystal structure of holoSS SOD1 (pdb 1HL5) with the protein backbone represented as a ribbon. HoloSS is a homodimer of 153 amino acid subunits, which adopt a Greek key β-barrel structure consisting of 8 β-strands and connecting loops. Each subunit binds one zinc (black sphere) and one copper (orange sphere), contains a highly conserved intramolecular disulfide bond between Cys 57 and 146 (red ball and stick), and is naturally N-acetylated (not shown). SOD1 also contains two free cysteines at positions 6 and 111 (pink ball and stick). The longest loops are the zinc-binding loop (Loop IV, yellow) and the electrostatic loop (Loop VII, blue). The zinc-binding loop contains residues that form the Zn-binding site, as well as one of the cysteines involved in the intrasubunit disulfide bond, which attaches this loop to β-strand 8. In addition, the zinc-binding loop contains residues involved in forming the dimer interface. Zinc binding, disulfide bond formation, and dimerization constrain the flexibility of the zinc-binding loop and markedly increase protein

stability. **(B)** Solution structure of apoSS monomer variant of SOD1 (PDB 1RK7). The colour scheme is identical to Panel A. The structure of the monomer is less defined than in mature holoSS. **(C)** Crystal structure of holoSS SOD1 (PDB 1HL5) with metal binding ligands shown in cyan. Zinc is coordinated by four histidines, His 63, 71, and 80, as well as Asp 83, while copper is coordinated by His 46, 48, 63 and 120, as well as one water molecule (not shown). The colour scheme for the rest of the molecule is identical to panels A and B. **(D)** Primary sequence of the SOD1 monomer and mis-sense mutations associated with fALS (adapted from Broom *et al*., 2014 (2). The secondary structural elements are listed above the primary sequence and coloured as in A and B. FALS-associated mutations are listed vertically in red below the wild type amino acid in black. The black and orange spheres indicate zinc and copper-coordinating residues, respectively.

The fully mature, holo form of SOD1 (holoSS) has a melting temperature of ~92 °C (128) and can maintain enzymatic activity in strongly denaturing conditions (129). The high stability of holoSS can be attributed to the highly compact dimeric structure (Fig. 1.5A, C), composed of two identical monomers, each consisting of 153 amino acid residues that bind one copper and one zinc ion, contain one intramolecular disulfide bond between Cys 57 and 146, and two free cysteines at positions 6 and 111. Each monomer folds into a Greek key β-barrel, consisting of two, four-stranded antiparallel β-sheets, connected by 7 loops of differing size. These two β-sheets are oriented in a cross conformation, such that the four strands of each β-sheet lie at an angle with respect to one another (130). The longest loops, the zinc-binding loop (Loop IV) and the electrostatic loop (Loop VII), are highly important for SOD1 stability and function (126). The zinc-binding loop contains residues that form the zinc-binding site, as well as one of the cysteines involved in the intrasubunit disulfide bond, which attaches this loop to β-strand 8. In addition, the zinc-binding loop contains residues involved in forming the dimer interface (126, 130). Thus, zinc binding, disulfide bond formation, and dimerization constrain the flexibility of the zinc binding loop and markedly increase protein stability (131). The electrostatic loop is composed of charged residues that are essential for guiding the superoxide anion from the surface of the protein into the active site where the redox active copper ion sits (132, 133). Both zinc-binding and electrostatic loops contain more hydrogen bonding and hydrophilic side chain interactions than the β-barrel, and these interactions are thought to play an essential role in stabilizing the loop conformations by providing a network of connections between the loops and the metal binding sites (130). Furthermore, the zinc and copper-binding sites are linked by His 63, functioning as a ligand for both metals, as well as by Aso 124 within the electrostatic loop, which forms hydrogen bonds with copper-ligand His 46 and zinc-ligand His 71 (126, 130).

Metal free disulfide oxidized (apoSS) and disulfide reduced (apoSH) SOD1 have markedly reduced stability, and melt at 60 °C and 48 °C, respectively (98, 131, 134). When the disulfide bond is formed, metal free SOD1 (apoSS) is a dimer (135). While the long loops have increased conformational flexibility (90, 136–139), the disulfide bond fixes the zinc-binding loop to the β-barrel, thereby ensuring that many of the dimer interface residues are in place. When the disulfide bond is reduced, dimerization is much less favourable, and the monomer remains the only populated form of SOD1 under physiological conditions (Fig. 1.5B) (98, 140).

In summary, each holoSS monomer consists of a β-barrel scaffold with two large loops projecting from this scaffold, forming the functional regions of the protein. The network of stabilizing interactions that forms when both metals are bound to SOD1 constrains the motion of the zinc-binding and electrostatic loops, the result of which is a highly stable, compact structure. In the absence of metal, SOD1 is much less stable (98, 131, 134), and the large loops gain conformational freedom. Therefore, the functional regions of SOD1 may be the Achilles heel of the protein, enabling aberrant interactions to take place if metal binding is compromised (see section 1.3.6).

Over 170, predominantly missense, mutations are associated with ALS, giving rise to ~20% of fALS cases (http://alsod.iop.kcl.ac.uk/). The mutations are associated with characteristic average disease durations, which vary greatly, for example from ~1 year for the dimer interface mutation A4V, the most common mutation in North America, to ~18 years for H46R, a metal binding mutant. Over the years, a great deal of attention has been focused on elucidating the structural characteristics of different SOD1 variants to account for differing disease phenotypes. While the most abundant form of SOD1 in vivo is generally holoSS (126), conditions such as mutation or aging may promote increased population of undermetalled or

disulfide reduced, less stable forms of the protein; and the form(s) of SOD1 most relevant to pathology in different ALS cases remain(s) unknown.

1.3.2 Pseudo-WT Cu,Zn-Superoxide Dismutase

In recent years, systematic analyses of the effects of fALS-associated mutations on the stability and folding of various forms of SOD1 have been reported (1, 2). Human SOD1 contains two free cysteine residues at amino acid positions 6 and 111 (Fig. 1.5A), and these free cysteine residues inhibit reversible unfolding of SOD1 *in vitro* by forming intramolecular and intermolecular non-native disulfide bonds, which promote SOD1 aggregation (141, 142). Reversible unfolding is a prerequisite for thermodynamic analysis, and so to overcome this limitation, pseudo-wild type (pWT) constructs lacking these free cysteines have been used extensively for *in vitro* studies of SOD1. In the most widely used pWT construct, the free cysteines are mutated to alanine and serine at positions 6 and 111, respectively (1, 98, 128, 134, 141, 143–146); however, other mutations at these positions have also been used (most notably C6A and C111A) (147–149). Not only are these chemically and structurally conservative mutations, but a serine at position 111 is found in most other mammalian SOD1, and alanine at position 6 is observed in other non-mammalian organisms (150). Mutating the free cysteines results in highly reversible unfolding of pWT, while having very minimal effects on structure, function, and stability (98, 130, 141, 142). The pWT construct also makes it easier to study modes of aggregation not catalyzed by cysteine oxidation. The use of pWT SOD1 constructs has provided valuable insights into the mechanism of SOD1 folding and misfolding and aggregation. Unless otherwise stated, all SOD1 variants studied in this work contain C6A and C111S mutations.

1.3.3 Cu, Zn-Superoxide Dismutase Function

The zinc and copper ions lie in close proximity and share the metal binding residue, His 63 (Fig. 1.5C). This interaction is essential since it limits the redox activity of the copper ion, preventing harmful reactions from damaging essential cellular molecules. Zinc is coordinated by His 63, 71, 80, and Asp 83, while copper is coordinated by His 46, 48, 63, and 120 and one water molecule (126, 130). The mechanism by which superoxide is converted to hydrogen peroxide and oxgyen is performed through oxidation and reduction cycles between the substrate and the catalytic copper ion. The first step of the SOD1 catalyzed reaction is superoxide reduction, immediately followed by reduction of a second superoxide molecule and reoxidation of copper. This two-step reaction is presented below:

Step 1: $O_2^- + Cu^{2+} \rightarrow O_2 + Cu^{1+}$

Step 2: $O_2^- + 2H^+ + Cu^{1+} \rightarrow H_2O_2 + Cu^{2+}$

Overall: $2O_2^- + 2H^+ \rightarrow O_2 + H_2O_2$

Upon reduction, the copper ion shifts 1.3 Å and releases His 63 and the water ligand. This release changes the conformation of the copper-binding site from a five-coordinated structure to a trigonal planar, three-coordinated arrangement, while the arrangement of zinc-coordinating residues remains unchanged. Reoxidation of the copper ion regenerates the five-coordinated structure of the copper-binding site (126).

1.3.4 Cu, Zn-Superoxide Dismutase Maturation In Vivo

SOD1 requires a number of posttranslational modifications before achieving full activity; and these modifications are regulated by oxygen and copper levels in a many Eukaryote cells (151–154). It has been shown that SOD1 activity rapidly increases in yeast cells grown under

anaerobic conditions with increases in copper and oxygen concentrations (154), and similar results were mirrored in animal models (155). Studies in yeast also suggest that regulation of SOD1 activity occurs at both the transcription and translation levels (153, 154, 156). It has been proposed that the first response to increased oxidative stress involves rapid activation of a pre-existing pool of immature SOD1, followed by increased expression of antioxidant enzymes (153, 157). The metal content of immature SOD1 awaiting activation, and whether or not this mechanism is relevant in more complex organisms, remains unknown. It appears possible, though, that SOD1 can exist in a number of different states within the cell, depending on different conditions (151). In addition to metal binding, intrasubunit disulfide bond formation, and dimerization, the polypeptide undergoes methionine cleavage at the N-terminus followed by acetylation of the adjacent alanine residue (126).

The most immature form of the polypeptide is the apo reduced form (apoSH), which lacks all modifications. While the mechanism(s) of zinc acquisition *in vivo* remain unknown, the steps that facilitate copper binding to SOD1 have been the focus of numerous studies over the past decade and are now understood in greater detail. Copper can be harmful to cellular components; therefore, homeostatic levels are under tight regulatory control and virtually no free copper exists in Eukaryote cells (158). Copper acquisition and distribution to various cellular compartments and copper chaperones involves a highly complex set of metabolic pathways which are still the focus of extensive investigation (159, 160). It is believed that copper enters the cell in the Cu^{1+} state through high affinity copper transporters or specific, lower affinity permeases, and is subsequently passed to copper chaperones responsible for delivery to cytosolic enzymes or to membrane transports for delivery to other cellular compartments. Transport from one site to another is facilitated by specific protein-protein interactions and increasing copper-affinity

gradients (160). Human SOD1 acquires its copper cofactor mainly through direct interaction with the copper chaperone for superoxide dismutase (CCS), a homodimeric protein composed of monomers consisting of three unique domains (151, 152, 161, 162). SOD1 can also acquire copper through a CCS-independent pathway through interaction between electrostatic residues in Loop VI with glutathione (163). This mechanism is poorly understood, but likely plays only a minor role in SOD1 activation (158, 162). Most studies on CCS have focused on the yeast and human forms of CCS, which differ slightly in sequence, quaternary structure, and metal binding capabilities, but nevertheless likely activate SOD1 through a similar mechanism, since it has been shown that human CCS can activate yeast SOD1 (151, 152, 162, 164). As the focus of this thesis is human SOD1, only what is known about human CCS will be discussed in detail.

The first domain of human CCS is homologous to the family of Atx1 metallochaperones, forming a βαββαβ ferrodoxin fold that contains a highly conserved MXCXXC copper binding domain located in a surface exposed loop (165). In general, Atx1 metallochaperons interact with their targets through structural complementarity, either electrostatic or hydrophobic interactions, facilitating target recognition and correct orientation of the copper-coordinating residues (166). Copper is transferred from Atx1 chaperones to their target proteins through a series of two and then three-coordinate intermediates that involve the Atx1 copper-coordinating cysteines and a pair of reduced cysteines close to or within the target recognition site (Fig. 1.6A) (166). While SOD1 is not a typical binding partner for Atx1 metallochaperones, domain one of CCS is accessible to SOD1 Cys 57 and 146 upon heterodimer formation (161, 165). It is of further note that SOD1 constructs with alanine mutations at residues 57 and 146 showed decreased ability to become activated by CCS; therefore, Cys 47 and 146 may mediate delivery of copper from domain one of CCS to the SOD1 active site (165). While previous studies showed that domain

one was only essential for activation of SOD1 when copper was limiting (162, 164), more recently it has been demonstrated that the absence of domain one abolishes the ability of CCS to transfer copper to SOD1 (161). In the current model, therefore, domain one is considered the copper-delivery domain; however, it is possible that domain three may also bind copper either independently or through interactions with domain one under certain conditions. It has been shown that CCS from various species can bind more than one equivalent of copper (158), and may adopt different conformations to protect the copper binding site during transfer to SOD1, as has been previously proposed (162). Transfer from the cysteine ligands within CCS to the histidine ligands within Cu,Zn-SOD also suggests a change in the copper redox state from Cu^{+1} to Cu^{+2}, since nitrogen donor ligands more readily bind Cu^{2+} than Cu^{1+}, while the opposite is true for sulphur donating ligands (159). Therefore, a change in copper redox state may enable a change in copper ligand. It has been shown that SOD1 CCS-dependent activation relies on the presence of oxygen (153, 154), suggesting that oxygen may play a role in the oxidation of copper, in turn facilitating ligand switching.

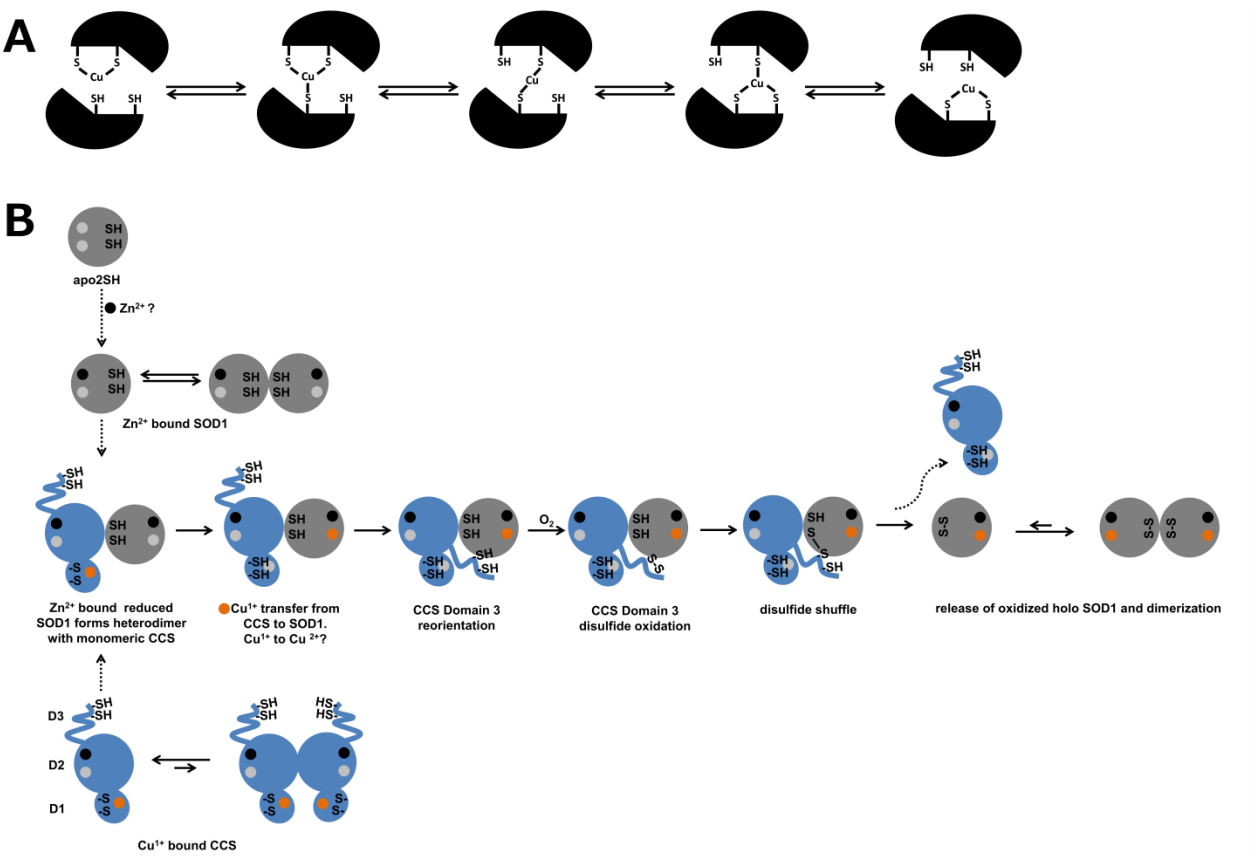

Figure 1.6 Maturation of SOD1. **(A)** A schematic representation of copper transfer from an Atx1 chaperone to its target protein through a series of two and then three-coordinate intermediates that involve the Atx1 copper-coordinating cysteines and a pair of reduced cysteines close to or within the target recognition site. It is possible that copper transfer from CCS domain one to SOD1 occurs through a similar interaction between cysteine residues. This figure was adapted from Bertini et al. 2007 (166). **(B)** A proposed mechanism of SOD1 maturation. Here SOD1 is indicated in grey and CCS in blue. Copper and zinc are shown as orange and black spheres respectively. Disulfide status is indicated as SH for reduced and S-S for oxidized. The three CCS domains are labelled D1, D2, and D3. Heterodimer formation between CCS and SOD1 is facilitated by interactions between the native SOD1 interface and the SOD1-like interface within CCS domain two. Copper transfer involves domain one and disulfide oxidation domain three. Following copper transfer and disulfide oxidation, SOD1 is released from CCS and can dimerize, forming the active enzyme. This figure was adapted from Banci et al., 2012 (161).

Domain two resembles monomeric SOD1, both structurally and in terms of sequence. It forms a Greek-key β-barrel with both large loops corresponding to the zinc-binding and electrostatic loops, as well as six of the seven metal binding residues found in SOD1 (167). Human CCS binds one zinc ion, which is required for function (168), at the site analogous to the SOD1 zinc binding site, while being unable to bind copper as it is missing one of the metal-binding histidine residues (167). It has been proposed, therefore, that domain two is not involved in copper transfer to SOD1, but rather is involved in target recognition (151, 152, 161, 169, 170). The similarity of CCS domain two and SOD1 suggests that the SOD1-CCS heterodimer may form through interactions of residues important for homodimerization, and in fact the crystal structure of yeast CCS-SOD1 heterodimers reveals that the heterodimer interface is very similar to the homodimer interface (170). Furthermore, mutations introduced into the dimer interface abolish CCS activation of SOD1 in yeast (157). Zinc binding to SOD1 likely precedes interaction with CCS, as it has been shown to be a requirement for copper transfer from CCS to SOD1 (161, 169), although heterodimer formation is possible with apo SOD1 and CCS (161). This discovery indicates that the conformational changes of some key residues, notably disulfide bonding region, which occur upon zinc-binding to SOD1 and subsequent stabilization of the zinc-binding loop, are a prerequisite for copper transfer (161). If heterodimer formation between SOD1 and CCS is facilitated by interactions between residues in the homodimer interfaces, efficient transfer of copper from SOD1 to CCS would require significant population of monomeric forms of both proteins. Interestingly, disulfide oxidation of SOD1, which would promote dimerization, has been reported to inhibit CCS-dependent activation, further suggesting that the SOD1 dimer is not a well-matched target for CCS (161). It is worth noting, however, that other Greek key β-barrel dimers can rapidly exchange monomers under physiological

conditions (171). Given the similarity between CCS domain two and SOD1, it is possible that heterodimer formation is under kinetic control (162).

The third domain of CCS is a short polypeptide, ~40 amino acids in length, with little secondary structure and a highly conserved CXC copper-binding motif (151, 170). Previous work has shown that copper can bind to both domains 1 and 3; but, only domain 3 is able to deliver copper to the SOD1 active site (162, 164). More recently however, experiments with different CCS constructs, missing one or two of the three domains, have revealed that copper transfer to the SOD1 active site is possible in the absence of domain 3. It is now generally believed that domain 3 is primarily responsible for SOD1 disulfide bond formation, which can only occur when domains one and two are present (161). Disulfide bond formation between SOD1 Cys 57 and 146 involves an oxygen-dependent disulfide shuffle, which begins with the formation of an intermolecular disulfide bond between CCS Cys 244 and SOD1 Cys 57, which is subsequently transferred to SOD1, resulting in oxidation of Cys 57 and 146 (151–153).

There are still questions regarding the mechanism of SOD1 CCS-dependent activation. It is unclear how copper is oxidized to Cu^{2+}, how the disulfide shuffle is initiated, and how these step(s) are regulated by oxygen levels. The emerging model for CCS-dependent activation of SOD1 involves a series of stages that require coordination of all three CCS domains. First, zinc binding occurs, possibly-independent of CCS, followed by heterodimer formation between CCS and SOD1. This step facilitates copper transfer, mediated by SOD1 Cys 57 and 146, and transfer of the intersubunit disulfide bond between CCS domain 3 and SOD1 to the intrasubunit disulfide bond within SOD1. The final step of SOD1 activation is dimerization, which has been shown to be regulated by COMMD1, which acts downstream of CCS, inhibiting dimerization when there is excess copper and CCS (156). It appears, therefore, that each post-translational modification

of SOD1 is regulated by the demands of the cell, ensuring that there is no excess of activated SOD1.

1.3.5 Cu, Zn-Superoxide Dismutase Stability and Folding

As discussed at the beginning of this introduction (section 1.2), protein folding can depend very strongly on solution conditions, in particular protein concentration, denaturant concentration, and temperature, and these can be varied to characterize different structural transitions (2, 172, 173). Most proteins in nature, including SOD1, consist of more than one subunit, and as a consequence their folding inherently depends on protein concentration (173). Denaturant- and temperature-induced unfolding of SOD1 have been fit to 2- or 3-state mechanisms. For monomeric apoSH, reversible unfolding fits a 2-state transition between folded (*M*) and unfolded (*U*) monomers ($M \leftrightarrow U$). At low protein concentrations, dimeric apoSS and holoSS exhibit 3-state equilibrium transitions between folded dimers (N_2), *M* and *U* ($N_2 \leftrightarrow 2M \leftrightarrow 2U$). Increasing protein concentration decreases the proportion of *M* such that only a net 2-state process ($N_2 \leftrightarrow 2U$) is observed at equilibrium, although inter-conversion among all 3 states may still be observed kinetically.

In its most immature form, apoSH, pseudo wild-type (pWT) SOD1 adopts a folded, but highly dynamic monomeric structure (Chapters 4 and 5) (174). This form of SOD1 has marginal stability, with ~95% of the protein being folded at physiological temperature and pH. Kinetic studies further show that disulfide reduction decreases stability by increasing the rate of unfolding (147). Accordingly, the stability of apoSH is relatively low compared to other globular proteins (1), and far lower than more mature forms of SOD1. In general, mutations have the largest effects on the stability of the apoSH form, ranging from slightly increasing to,

more often, greatly decreasing its melting temperature to below 37 °C. Thus, mutations can markedly alter the populations of folded and unfolded conformations (98).

Disulfide bond formation stabilizes both the folded monomer and the dimer interface of SOD1, such that 3-state folding can be analyzed by equilibrium chemical (134) and in some cases thermal denaturation (refer to Chapter 2), as well as by kinetics. In contrast to apoSH, pWT and mutant apoSS are very predominantly folded under physiological conditions (98, 134). Nevertheless, based on equilibrium denaturation and molecular dynamics simulations, it has been proposed that the effects of mutations propagate extensively through the protein structure and disrupt the dimer interface (98, 175). Kinetic experiments have shown that mutations can increase the rate of dissociation and/or monomer unfolding (176, 177). Thus, in apoSS, mutations generally have destabilizing effects, resulting in increased native-state structural fluctuations and small increases in population of folded and unfolded monomers. Until now, however, the dimer interface stability has not been calculated directly (refer to Chapter 2).

Metal binding strongly stabilizes SOD1 and reduces its dynamics. The overwhelming majority of mutations characterized to date decrease the stability of holoSS (1, 143, 146), but because the folded dimer is extremely stable, the absolute increases in the amounts of unfolded species (*M* and *U*) are extremely small, and hence are unlikely to directly impact aggregation. Rather, increased local structural fluctuations tend to promote metal loss and/or disruption of the dimer interface, and so expose regions that are normally buried (99). Various covalent modifications have similar destabilizing effects. For example, oxidation of active site histidine residues destabilizes holoSS, promotes monomerization, increases exposure of hydrophobic residues, and leads to metal loss (178). Metal binding also increases the kinetic stability of SOD1; pWT holoSS unfolds extremely slowly *via* formation of a folded monomer, which has

weakened metal binding compared to the dimer (146). Various mutations increase the unfolding rates of holoSS, and increase the accessibility of misfolded species, notably mis-metallated monomers. Collectively, these studies have revealed that mutations and covalent modifications increase structural fluctuations and misfolding in the otherwise extremely stable holoSS.

1.3.6 Modes of Cu,Zn-Superoxide Dismutase Aggregation

A key theme emerging from the folding studies of SOD1 is that mutations have differing effects on the amounts of unfolded and misfolded species that may be populated in disease. This suggests that aggregation may arise from multiple, very different initial conformations. Enhanced aggregation has been reported for many species of SOD1, including mutant and/or modified protein, with formation of diverse structures, ranging from amorphous to various kinds of fibrils (Fig. 1.7). It must be emphasized that varying experimental conditions strongly influence observed aggregation mechanisms and structures, which have different aberrant interactions, for example between the edges of the β-barrel, exposed hydrophobic groups, and improper loop interactions.

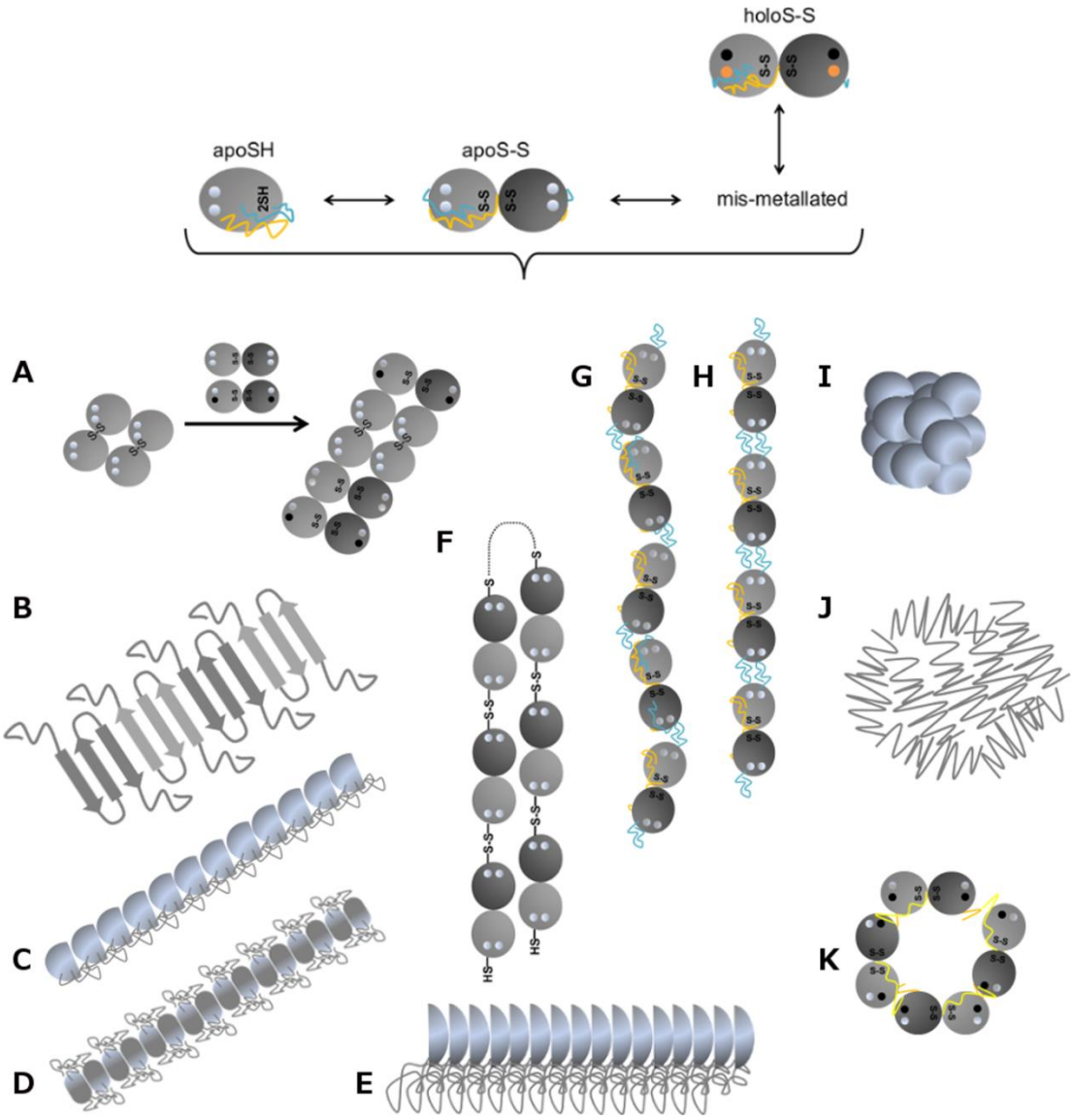

Figure 1.7 Mechanisms of SOD1 aggregation. Some of the many reported misfolded/aggregated structures of SOD1 are illustrated schematically **(A-K)**. These structures may depend strongly on the conformation of the various possible precursor SOD1 species. Soluble, natively folded SOD1 is represented by grey spheres. Copper and zinc ions are indicated by orange and black spheres respectively and disulfide status is indicated as SH for reduced and S-S for oxidized. **(A)** Under agitation, apoSH forms a nucleus containing intermolecular disulfide bonds involving Cys 57 and Cys 146, which then recruit more stable apo and part metallated SS forms of SOD1. The resulting fibres bind the fluorescent dye, Thioflavin-T (ThT), and exhibit twisted morphologies by atomic force microscopy (AFM) (76). **(B)** Destabilizing and/or agitation conditions result in fibres with features of classic amyloid (75, 179, 180), as is frequently observed when proteins aggregate from a globally unfolded state (179). Such "classic" fibrils have a protease-resistent cross-β spine, cause large enhancements in ThT fluorescence, exhibit green-gold birefringence upon binding the dye Congo Red, and have fibril diameters of ~5-20 nm (75, 179). **(C-E)** Amyloid-like aggregates showing polymorphism

due to a protease-resistant fibril core (shaded shapes) are formed by different fragments of the SOD1 sequence, such as the N-terminal ~60 amino acids **(C)**, centre of the protein forms the core **(D)**, C-terminal region **(E)**. Protease sensitive parts are shown as grey coils. The structures of the cores are not known and may include cross β-strands (181). **(F)** Dimers of apoSS linked through disulfide linkages, which involve normally reduced Cys 6 and Cys 111 (182, 183). **(G, H)** Amyloid-like fibrils formed as a result of non-native interactions between apoSS dimers (90, 137, 138). Exposure of the edge of the β-barrel in apoSS due to disorder in the zinc-binding and electrostatic loops results in a zig-zag packing of dimers when the edge is partially exposed **(G)** or linear packing when the edge is fully exposed **(H)**. **(I, J)** Different types of amorphous aggregates formed by structured **(I)** and unstructured **(J)** protein respectively (35, 99). **(K)** Amyloid pores formed by zinc-bound SS dimers. The zinc-binding loop, indicated in yellow, of one dimer interacts with the β-barrel of another dimer at angle. The zinc-binding loop forms an additional β-strand, the result of which is an extended β-sheet that spirals around the long axis (90).

In recent years, there has been extensive research on the aggregation of apoSH, as this unstable form of SOD1 has been proposed to be particularly likely to aggregate in disease (1, 98, 131). *In vitro*, the extent and type of aggregation for apoSH varies greatly with experimental conditions (Fig. 1.7). Thermal denaturation has been shown to be highly reversible for apoSH pWT and some mutants, suggesting resistance to aggregation from partially or fully unfolded states, although other mutations show evidence of misfolding and aggregation (98). In contrast, other conditions strongly enhance aggregation of even wild type (WT) apoSH. Agitation of both WT and mutant apoSH solutions can cause formation of various amyloid-like fibres (76, 184). Mutations modulate the structural features of the fibres, resulting in distinct, or common, protease-resistant cores under different conditions (181, 185). Intriguingly, such structural polymorphisms may be analogous to different "strains" observed in prion aggregation (23). Furthermore, under agitation conditions, small amounts of apoSH can seed the aggregation of more stable forms of SOD1 (76, 185). It is well established that amyloid can form quite readily from highly unfolded sections of proteins. Also, agitation induces aggregation of many proteins through mechanisms that are not well understood but may involve unfolding at air-water or water-solid interfaces and/or disulfide shuffling (186, 187). Recent studies have shown that various forms of metal-free SOD1 can make amyloid-like fibres with smooth, unbranched morphologies under agitation conditions; and this occurs from the globally unfolded rather than the folded state (188). In contrast, under quiescent solution conditions, both WT and pWT apoSH show little tendency to aggregate, and different apoSH mutants form different sizes of aggregates at different rates (98) (refer to Chapter 5). These varying results suggest that the mode(s) of apoSH aggregation are particularly diverse, and sensitive to varying conditions, due to the marginal stability, and hence easily altered conformational properties.

Due to the higher stability of apoSS compared to apoSH, more strongly destabilizing and/or disulfide oxidizing/shuffling conditions are generally required to induce aggregation on an experimentally tractable time scale (75, 78, 144, 182, 189). For apoSS, different destabilizing conditions result in multiple aggregate structures, ranging from amorphous to non-amyloid and amyloid fibrils, in varying proportions (75, 144). Destabilization of apoSS can also cause disulfide shuffling between the normally reduced free cysteines (Cys 6 and 111) and those normally forming the disulfide bond (Cys 57 and 146) (Fig. 1.5) (189). Furthermore, under non-destabilizing, oxidizing conditions, aberrant disulfide bonding involving the free cysteines is required for the formation of amyloid-like fibrils (Fig. 1.7) (182). The roles of aberrant disulfide bonding for misfolding and aggregation are complex and not fully clear in both *in vitro* and *in vivo* studies; in disease models, early roles are uncertain, but they are likely to be significant as disease progresses due to increasingly oxidizing cellular conditions (190). Alternatively, apoSS can form other amyloid-like fibres, without aberrant disulfide bonds. These fibres are composed of native-like dimers undergoing local unfolding, forming non-native intermolecular interactions involving the zinc-binding and electrostatic loops and exposed β-barrel edge strands (90, 138). Crystallographic studies of undermetallated and mismetallated SOD1 variants have revealed numerous structural changes that occur upon metal loss that enable formation of these assemblies of SOD1 dimers. Various interactions between the zinc binding and electrostatic loops are lost in the absence of metal, the result of which is increased disorder in these loops (90, 136–138). When zinc is bound in its proper site, His 46 (a copper binding ligand) and 71 (a zinc binding ligand) form hydrogen bonds with Asp 124 in the electrostatic loop (136, 191). Zinc binding further stabilizes the electrostatic loop by capping the negatively charged end of the short α-helix within this loop, which sits above the zinc binding site (Fig. 1.5) (191). When the zinc binding

and electrostatic large loops are in place, charged residues Asp 76 and Glu 77 act as "gatekeepers," preventing exposure of the β-barrel edge strands; but when the conformation of these loops is lost, the edge strands are exposed and SOD1 dimers can assemble in a linear or zig-zag fashion, depending on the degree of loop disorder (90). These structural studies show that the SOD1 dimer is finely tuned for proper metal binding, and the conformational freedom of zinc binding and electrostatic loops is highly influenced by the numerous interactions formed in the presence of metal. Consequently, aggregation of apoSS may progress from various locally or globally unfolded conformations, with or without aberrant disulfide linkages.

The highly stable holoSS form of SOD1 is generally thought to be highly resistant to aggregation (35, 76, 144, 192). Nevertheless, agitation of holoSS, in combination with strongly destabilizing solution conditions, results in fibril formation (76, 78); prolonged quiescent incubation of both WT and mutant holoSS under physiological temperature and pH, eventually results in formation of amorphous aggregates (99). Lag phases are characteristic of unfavourable nucleation-rapid elongation aggregation mechanisms, and have been observed for many disease-linked amyloid-forming proteins. Similar to these proteins, for SOD1 various mutations may decrease the length of the lag phase, possibly due to enhanced metal loss and/or dimer dissociation (99, 193). In cells, these structural changes may in turn promote disulfide reduction (194). Increased population of various misfolded forms of SOD1 due to these changes could also contribute to aggregation in ALS. Of note, loss of all bound metals was not required for amorphous aggregation (99), and crystallographic studies found that part-metallated SS SOD1 can form helical fibrils via non-native loop and β-barrel interactions (90). In addition, the oxidation of various residues has been implicated in misfolding/aggregation. For example, oxidation of active site histidine residues promotes amorphous aggregation of metallated SS

SOD1 (178). Thus, mutation and/or other covalent changes to holoSS can also give rise to misfolded, aggregation-prone species. Taken together, the above-described findings provide evidence for multiple possible aggregation processes, which may play various contributive roles in disease.

1.4 Research Objectives

A long standing theory in the field of ALS research is that the immature, metal free, forms of SOD1 are the most relevant to disease due to their lower stability, and consequently heightened aggregation propensity (52). There has been a great deal of speculation that these species, notability apoSH, represent the common denominator in various cases of familial and sporadic ALS (76, 135, 147, 180, 184, 195). Monitoring SOD1 aggregation is difficult however, and many of these studies were performed *in vitro*, under non-physiological conditions, in order to accelerate the rate of aggregation to aid with experimental tractability. Interpreting these results in relation to disease characteristics is therefore difficult.

Previous studies in the Meiering lab have focused on characterizing the stability of various apoSS SOD1 variants (128, 134). The work presented herein is an elaboration of these studies. In particular, using a combination of isothermal titration calorimetry (ITC) and differential scanning calorimetry (DSC), instead of reporting on just total dimer stability, the thermodynamics of apoSS dimer dissociation and monomer unfolding have been separately characterized (Chapter 2 and 3). Using this approach, we have found that the common effect of all fALS-associated mutations investigated is that they weaken the dimer interface, while exerting different effects on the stability of the apoSS monomer. Our experiments also reveal that dimer dissociation is accompanied by extensive unraveling of the structure resulting in the formation of poorly packed and malleable monomers. These findings provide key information for understanding the mechanisms and energetics underlying normal maturation of SOD1, as well as toxic SOD1 misfolding pathways associated with disease.

Earlier DSC experiments in the Meiering lab also revealed that fALS-associated mutations have the largest effects on the stability of apoSH, in some cases decreasing the melting

temperature of the protein to below 37 °C; thus, a significant fraction of the protein is unfolded at physiological temperature (174). Whether or not this decrease in stability promotes aggregation under physiological conditions was largely unknown. Here we have expanded these studies to additional apoSH variants to more fully appreciate how the different structural contexts of the mutations impact the thermodynamics of unfolding. We have also characterized how fALS-associated mutations impact the aggregation propensity of apoSH under physiological conditions (Chapter 4). Aggregation was assessed using a combination of complimentary biophysical techniques, such as light scattering, atomic force microscopy (AFM), and Thioflavin-T (ThT) binding, with the goal of reporting on aggregation behaviour, not induced by extreme conditions that cause the marginally stable apoSH form to unfold. We also accounted for the effects of removing the free cysteines (Cys 6 and 111) on the folding and aggregation behaviour of apoSH (Chapter 4). We find that under physiological conditions, apoSH is fairly resistant to aggregation. Low levels of small oligomers do form, but the concentration of these oligomers remains too low to support extensive aggregation. We therefore explored other mild conditions that enhance the intermolecular interactions between apoSH and encourage aggregation. Interestingly, at higher protein concentration and/or in the presence of salt, we observe very different aggregation propensities of diverse apoSH variants that do not appear to correlate with differences in stability (Chapter 5).

The goal of these in depth biophysical analysis of metal free stability and aggregation propensity has been to provide valuable insight into various ways metal free SOD1 may misfold and aggregate and inevitably contribute to disease.

Chapter 2

Destabilization of the dimer interface is a common consequence of diverse ALS-associated mutations in metal free SOD1

Author Contributions

This chapter has been accepted for publication in *Protein Science* with the following authors: Helen R. Broom, Jessica A.O. Rumfeldt, Kenrick A. Vassall, Elizabeth M. Meiering. This manuscript was written by mainly by Helen R. Broom with contributions from Jessica A. O. Rumfeldt and Elizabeth M. Meiering. Isothermal titration calorimetry experiments were designed by Helen R. Broom and Kenrick A. Vassall, and performed by Helen R. Broom. Size exclusion chromatography experiments were performed by Jessica A. O. Rumfeldt. Also I am grateful to Aron Broom and Colleen Doyle for all the insightful discussions and assistance with data interpretation.

Overview

Neurotoxic misfolding of Cu,Zn-superoxide dismutase (SOD1) is implicated in causing amyotrophic lateral sclerosis, a devastating and incurable neurodegenerative disease. Disease-linked mutations have been proposed to promote misfolding and aggregation by decreasing SOD1 stability and increasing the proportion of less folded forms of the protein. Here we report direct measurement of the thermodynamic effects of chemically and structurally diverse mutations on the stability of the dimer interface for metal free (apo) SOD1 using isothermal titration calorimetry and size exclusion chromatography. Remarkably, all mutations, even ones that are distant from the dimer interface, decrease interface stability and increase the population of monomeric SOD1. The thermodynamic analyses show that substantial structural perturbations accompany dimer dissociation, resulting in formation of poorly packed and malleable dissociated monomers. These findings provide key information for understanding the mechanisms and energetics underlying normal maturation of SOD1, as well as toxic SOD1 misfolding pathways associated with disease.

2.1 Introduction

Amyotrophic lateral sclerosis (ALS) is a common, rapidly progressive motor neuron disease, for which there is no cure, and treatment options are very limited (3). Mutations in homodimeric Cu, Zn superoxide dismutase (SOD1) (Fig. 2.1) account for ~20% of familial and 3-5% of sporadic ALS cases (fALS and sALS, respectively) (3), and an increasing body of research suggests a role also for the wild-type SOD1 in disease (33). Clinical symptoms are similar in fALS and sALS (3); thus, studies on SOD1 are critical for understanding the molecular mechanisms of disease.

Many, predominantly missense, mutations distributed throughout SOD1 have been associated with fALS (http://alsod.iop.kcl.ac.uk/home.aspx), and confer a toxic gain-of-function to the protein (3). A characteristic feature of ALS is the formation of protein aggregates in motor neurons (21), and SOD1 is a component of aggregates in SOD1-linked fALS and in some sALS cases (26), as well as in animal models of the disease (196). Thus, a prominent hypothesis is that ALS is caused by protein misfolding and aggregation, analogous to toxic misfolding of other proteins in various neurodegenerative diseases such as Huntington's, Alzheimer's and prion disorders (52). The mechanisms by which SOD1 forms aggregates, however, remain poorly understood (2).

Extensive research indicates that an increased population of unmetallated (apo) monomeric forms of SOD1 may promote toxic aggregation (134, 143, 175, 193, 197–199). Folding and thermodynamic stability measurements of SOD1 can reveal if and how mutations create instability and so favour misfolding and aggregation (2). In previous studies, we observed moderately destabilizing effects of several mutations on the highly stable metal-bound (holo) SOD1, owing mainly to decreases in monomer stability, and mutations that weaken metal

binding tend to have the largest destabilizing effects on holo monomers (143). For the apo protein, the mutations tend to decrease both dimer interface and monomer stability to a larger extent than for the holo protein (134). Measurements of the kinetics of unfolding and refolding have similarly indicated that some mutations weaken the apo SOD1 dimer interface; however, these experiments have high uncertainties due to long extrapolations (176, 177, 200), and the assumption of invariance in the underlying rate constant for dimer association (176, 200). Molecular dynamic simulations have also predicted that the large majority of mutations weaken the dimer interface of apo SOD1 (175, 201, 202). Collectively, these studies suggest that some fALS-associated mutations weaken the apo SOD1 dimer interface, but until now direct experimental measurement of these effects has been very limited and further experimental studies are needed to ascertain the effects of mutations on dimerization.

Here, we report direct quantitative measurements of the thermodynamics of dimer dissociation for 13 chemically and structurally diverse ALS-associated mutations distributed throughout the SOD1 structure (Fig. 2.1) by isothermal titration calorimetry (ITC) and size exclusion chromatography (SEC). ITC is a powerful, yet little explored, tool for characterizing the thermodynamics of protein-protein association using measurements of the heat changes that accompany binding (203). A single ITC experiment can define the dissociation equilibrium constant (K_d) and enthalpy (ΔH_d), from which the Gibbs free energy (ΔG_d) and entropy of dissociation (ΔS_d) can be determined. In addition, using measurements of ΔH_d as a function of temperature, the change in the specific heat capacity for dissociation ($\Delta C_{p,d}$) can be obtained. Using ITC to analyze the thermodynamics of apo SOD1 dimer dissociation at physiological temperature and pH, as well as parallel measurements of dissociation using SEC, we obtain the striking result that diverse mutations decrease dimer interface stability and increase formation of

structurally disrupted monomers. The ITC and SEC give valuable information on the energetics and mechanism of SOD1 subunit association for understanding natural protein maturation and disease.

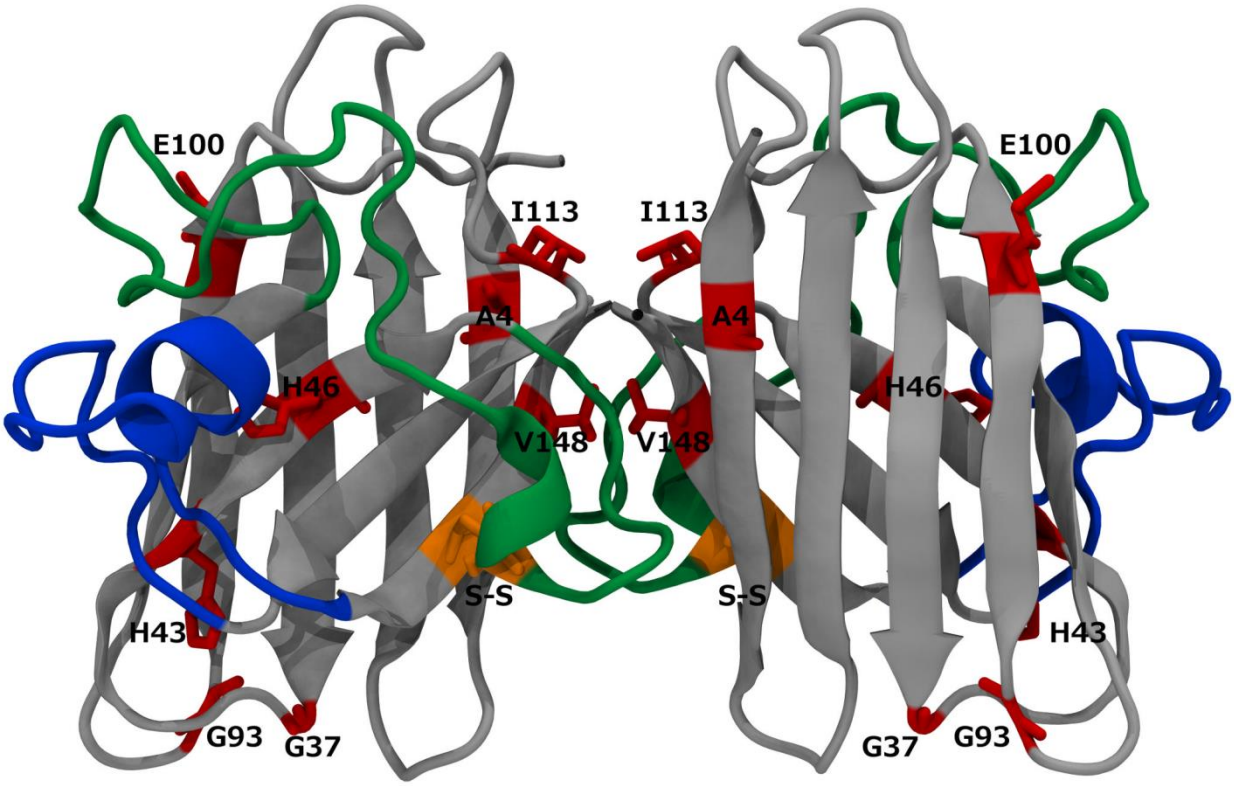

Figure 2.1 Structural features of apo SOD1. SOD1 is a homodimeric metalloenzyme. Each monomer forms a Greek key β-barrel and contains a single disulfide bond (orange). In the absence of bound metals, loops IV (green) and VII (blue) are disordered and the structure is more flexible than the metal-bound (holo) protein (135, 136). The sites of ALS-associated mutations characterized herein are shown in red sticks (PDB code 1HL4).

2.2 Materials and Methods

2.2.1 Recombinant SOD1 expression and purification

The human pWT SOD1 (pseudo wild-type with nonconserved Cys 6 and Cys 111 replaced by Ala and Ser, respectively) (1, 98, 141) and mutant SOD1 were expressed using the plasmid vector pHSOD1ASlacI1 (204) in *E. coli* cells, purified and demetallated by dialysis against ethylenediaminetetraacetic acid (EDTA) as described previously (128, 205). Protein concentration was determined by absorbance at 280 nm using an extinction coefficient of 10,800 M^{-1} cm^{-1} for the SOD1 dimer (206).

2.2.2 Isothermal titration calorimetry (ITC)

ITC experiments measuring the heat of dissociation of the apo SOD1 dimer (N_2) to folded monomers (M), $N_2 \leftrightarrow 2M$, governed by the dissociation constant (K_d), were performed as described (207, 208) using a Microcal Isothermal Titration Calorimetry 200 instrument (Microcal Inc, Northampton, MA, USA). Measurements were performed at 37 °C, where dissociation is increased compared to previous measurements at lower temperatures (134, 177, 193, 197), and below the transition temperature of thermal denaturation experiments (128, 134). Highly concentrated apoSS SOD1 (0.35-1 mM total dimer), buffered in 20 mM 4-(2-hydroxyethyl)-1-piperazineethanesulfonic acid (HEPES), pH 7.8, was diluted into the identical buffer in the ITC reaction cell in successive small volume (0.3-0.5 μL) injections. Dilution artefacts were minimized by injecting the protein directly into flow-through collected during concentration by ultrafiltration of the high protein concentration solution. The heat associated with each injection (q_i) was determined by integrating the power *versus* time trace. Data were fit to a dimer dissociation model (207, 208) according to Eq. 2.1:

$$q_i = V\Delta H_d \left([M_i] - [M_{i-1}] \left(1 - \frac{v}{V}\right) - f_m [M_o] \frac{v}{V} \right) + q_{dil} \quad \text{(Eq. 2.1)}$$

where ΔH_d is the enthalpy change of dissociation from native dimer to two monomers, calculated per mol monomer. $[M]_o$ is the total concentration of apo SOD1 (monomer units) in the syringe, $[M_i]$ and $[M_{i-1}]$ are the concentrations of apo SOD1 monomer in the ITC cell after injection *i* and *i*-1, respectively, *v* is the volume of each injection, *V* is the ITC reaction cell volume, q_{dil} is a correction factor for the heat associated with sample dilution unrelated to dissociation, and f_m is the fraction of protein in the syringe that exists as free monomer, which can be expressed as:

$$f_m = \frac{1}{4[M_0]} \left(-K_d + \sqrt{{K_d}^2 + 8K_d[M_o]} \right) \quad \text{(Eq. 2.2)}$$

The data were fit using Microcal Origin 7.0 (Microcal Inc, Northampton, MA, USA) with ΔH_d, K_d and q_{dil} as floating parameters. At the experimental temperature, T_{exp}, $\Delta G_d(T_{exp})$ was calculated from $K_d(T_{exp})$ using Eq. 2.3:

$$\Delta G_d(T_{exp}) = -RT_{exp} ln K_d(T_{exp}) \quad \text{(Eq. 2.3)}$$

where *R* is the universal gas constant. ITC experiments were performed at temperatures ranging from 18 to 37 °C to obtain the temperature dependence of ΔH_d, the $\Delta C_{p,d}$, for mutants where dissociation was measureable at lower temperatures (Fig. 2.3A). Values of $\Delta G_d(T)$ at other temperatures can be calculated using Eq. 2.4 (128).

$$\Delta G_d(T) = \left[\Delta H_{d,exp} + \Delta C_{p,d}(T - T_{exp})\right] - T\left[\Delta S_{d,exp} + \Delta C_{p,d} \ln\left(\frac{T}{T_{exp}}\right)\right] \quad \text{(Eq. 2.4)}$$

2.2.3 Size Exclusion Chromatography (SEC)

SEC was performed on a Bio-Rad BioLogic DuoFlow system with a prepacked Superose 12 10/300 GL (GE Healthcare) analytical gel filtration column. The mobile phase was 20 mM HEPES, 150 mM NaCl, pH 7.8, with a flow rate of 1 mL min^{-1}. Experiments were conducted at

ambient temperature (~23 °C) and sample injection volumes were 25 µL. Linear calibration curves of elution time versus log of molecular weight were obtained using standards: bovine serum albumin (66 kDa), myoglobin (16.9 kDa), and cytochrome C (12.6 kDa). Dilution of the sample on the column was determined once daily by using the peak width at half height of the myoglobin standard (~800 µL) and dividing by the volume loaded (25 µL). This dilution factor (~32) was used to calculate the total concentration of the SOD1 when eluted from the column.

The elution volume of each sample (V_e) plotted against total protein concentration in dimer equivalents $[N_2]_o$ was fit to Eqs. 2.5 and 2.6 (209) using Origin Software:

$$V_e = V_M - \left[\frac{(V_M - V_{N_2})\left(\log\left(\frac{1+\%N_2}{100}\right)\right)}{log2}\right] \quad \text{(Eq. 2.5)}$$

$$\%N_2 = \left[\frac{(8[N_2]_o + K_d) - \sqrt{{K_d}^2 + 16K_d[N_2]_o}}{0.08[N_2]_o}\right] \quad \text{(Eq. 2.6)}$$

where $\%N_2 = [N_2]/[N_2]_o * 100$ and V_M and V_{N_2} are the elution volumes of the monomer and dimer, respectively. For dimers with a K_d in the range of 1 to 10 µM, the data could be fit to Eqs. 2.5 and 2.6 to obtain parameters V_M , V_{N_2} and K_d (210). On average, the fitted V_M was 1.2 mL greater than V_{N_2} indicating the hydrodynamic volume of the dissociated monomers is increased ~ 10% relative to the associated monomers (211). For dimers with a K_d in the range of 0.001 to 0.01 µM, values of V_{N_2} were well defined by the data; detection limits at 280 nm precluded obtaining V_e at lower protein concentrations for determination of V_M and so this was set to a value based on the dimers with larger K_d values. Linear transformations of the data were generated using V_e and fitted values according to Eqs. 2.7-2.10:

$$\%N_2 = 100 \times 2^{\frac{V_M - V_e}{V_M - V_{N_2}}} - 1 \quad \text{(Eq. 2.7)}$$

$$K_d = \frac{0.04[N_2]_o(100 - \%N_2)^2}{\%N_2} \quad \text{(Eq. 2.8)}$$

$$\log\left[\frac{\%N_2}{0.04(100-\%N_2)^2}\right] = \log[N_2]_o - \log[K_d] \quad \text{(Eq. 2.9)}$$

$$Y = \frac{\%N_2}{0.04(100-\%N_2)^2} \quad \text{(Eq. 2.10)}$$

A plot of log Y versus log $[N_2]_o$ yields a straight line with a slope of 1; when Y = 1, $K_d = [N_2]_o$ (Fig. 2.4).

2.3 Results and Discussion

2.3.1 Apo SOD1 dissociation is endothermic and strongly dependent on temperature

ITC experiments were conducted for pWT (pseudo wild-type) apoSS SOD1 and fALS-associated mutants (Figs. 2.1, 2.2), yielding K_d and associated thermodynamic properties (Fig. 2.2C, Table 2.1). Previous measurements by analytical ultracentrifugation (AUC), SEC and chemical denaturation conducted at lower than physiological temperature found that the wild-type apo SOD1 dimer is quite stable (e.g. K_d ~1 nM at neutral pH, temperature range 5-25 °C) (134, 177, 193, 197). Here, we report measurements at a physiological temperature of 37 °C, where we find dissociation is markedly increased, with K_d values larger than ~67 nM (Figs. 2.2C, S2.1). Furthermore, SOD1 dissociation is endothermic (Figs. 2.3A, C, *vide infra*), with a large positive $\Delta C_{p,d}$ (Fig. 2.3A). Thus, the dissociation enthalpy is strongly temperature-dependent, and dissociation is increasingly favorable and measurable by ITC at higher temperature due to the increased heat of dissociation. Owing to relatively larger heats of dissociation being observed for some mutants (A4V, H43R, I113T and V148G), their dissociation is also measurable at 25 °C (Figs. 2.3A, B). Measurements of K_d using SEC (Figs. 2.4, S2.2) are in excellent agreement with ITC (Fig. 2.3B and Table 2.1).

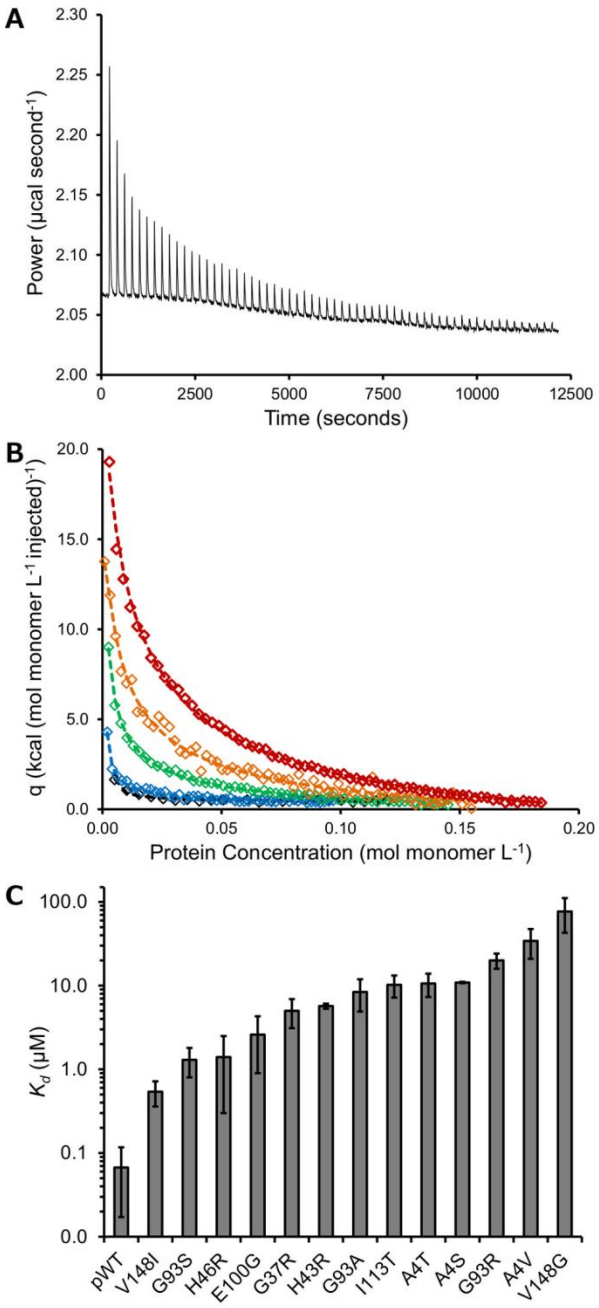

Figure 2.2 Isothermal titration calorimetry reveals decreased dimer stability for SOD1 mutants. **(A)** Raw ITC data for I113T mutant at 37 °C. Each peak corresponds to the heat measured for a small volume injection of protein solution into the ITC sample cell. The endothermic heats of dissociation decrease for successive injections due to the increase in protein concentration in the cell and the accompanying shift of the equilibrium towards native dimer. **(B)** Integrated heats at 37 °C for each injection (diamonds) are shown for pWT (black), E100G (blue), I113T (green), A4V (orange) and V148G (red), in order of increasing values of K_d. The dashed lines are the fits of the data to a dimer dissociation model (Eq. 2.1) with fitted values shown in Figs. 2.2C, 2.3 and summarized in Table 2.1. **(C)** For all mutants, the K_d is increased relative to the pWT as measured by ITC at 37 °C.

2.3.2 fALS-associated mutations weaken the apo SOD1 dimer interface

The ITC and SEC measurements clearly demonstrate a common effect of weakening of the apo SOD1 dimer interface by diverse ALS-associated mutations that are distributed throughout the protein structure (Fig. 2.1). The ITC data for all the apo SOD1 variants are well fit by a 2-state dimer dissociation model ($N_2 \leftrightarrow 2M$) (see Experimental Procedures, Fig. 2.2B). The ΔH_d and K_d values from the fits and the corresponding ΔG_d values are summarized in Figs. 2.2C, 2.3B, C, and Table 2.1. At 37 °C, the pWT apo SOD1 dimer interface still has a relatively high affinity, with a K_d of 67 nM and ΔG_d of 10.3 kcal (mol dimer)$^{-1}$. All mutations increase the K_d at 25 and 37 °C but to different extents (Figs. 2.2C, S2.1), corresponding to decreases in interface stability of 1.3-4.3 kcal (mol dimer)$^{-1}$ at 37 °C (Fig. 2.3B, Table 2.1).

Notably, the effects of mutations on the integrity of the dimer interface cannot be predicted readily based on the different structural contexts of the mutations (Fig. 2.1). The dimer interface stability is considerably weaker at 37 °C than measured previously at lower temperature and the mutations are more destabilizing at 37 °C resulting in a significant proportion of monomer at physiological temperature and protein concentration (~ 40 μM (212); ~2% for pWT to ~50% for V148G). In general, mutations in or near the dimer interface, such as A4V, I113T and V148G, tend to be the most destabilizing, but distant mutations, notably G93R, can also markedly weaken the interface (Figs. 2.1, 2.2C). Thus, a key finding here is that the effects of fALS-associated mutations commonly propagate through the protein and weaken the dimer interface of apo SOD1. Additional support for the generality of this result is provided by simulations of additional mutants and more limited experimental measurements of stability under non-physiological conditions (134, 175–177). Similar long range effects of mutations on interfaces have been reported for some other oligomeric proteins (213–215). Notably, inherited

mutations in transthyretin (TTR) are proposed to cause familial amyloid polyneuropathy (FAP) by inducing conformational changes that promote dissociation of the native tetramer, leading to formation of partially folded monomers that can self-assemble into amyloid fibrils (215). For SOD1, the finding that all the mutations studied destabilize the interface is especially significant in light of antibody binding studies that identified exposure of the SOD1 dimer interface in aggregates from ALS patients (22, 216), implicating dimer dissociation as a common occurrence in disease.

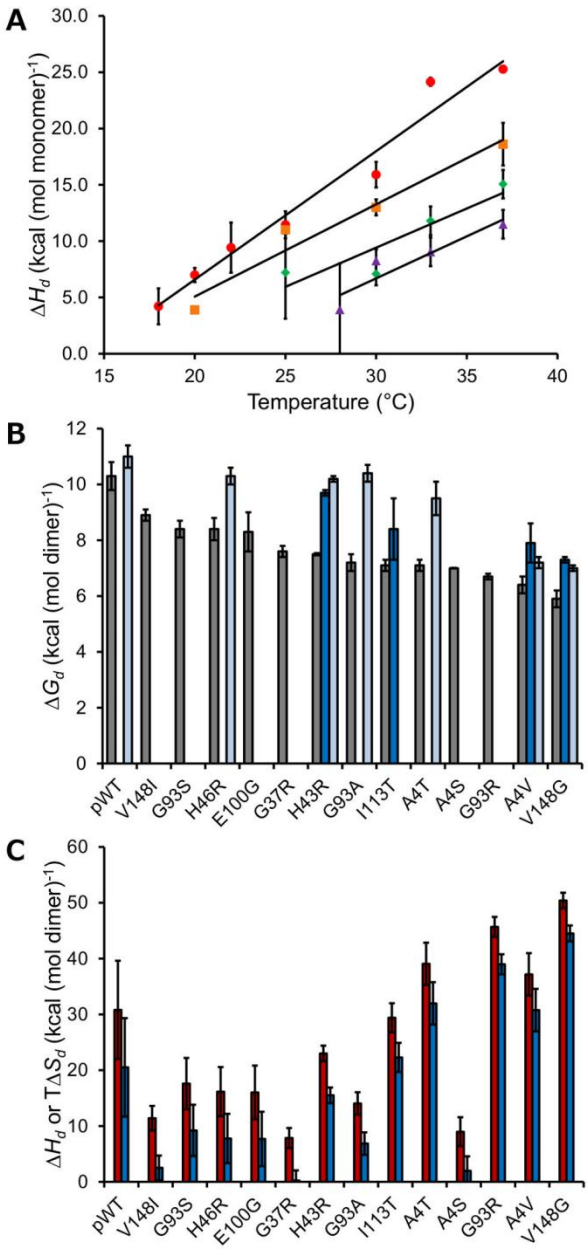

Figure 2.3 Thermodynamics of apo SOD1 dimer dissociation. **(A)** Kirchoff plot of ΔH_d versus temperature. The $\Delta C_{p,d}$ is determined from the temperature dependence of ΔH_d and is similar for diverse mutants. For V148G (red circles), A4V (orange squares), I113T (green diamonds), and H43R (purple triangles), the $\Delta C_{p,d}$ is 1.1 ± 0.1, 0.8 ± 0.1, 0.7 ± 0.2, and 0.8 ± 0.2 kcal (mol monomer)$^{-1}$ °C^{-1}, respectively. Thus, the average $\Delta C_{p,d}$ is ~0.9 kcal (mol monomer)$^{-1}$ °C^{-1} (1.7 ± 0.2 (kcal (mol dimer)$^{-1}$ °C^{-1})). **(B)** ΔG_d determined by ITC at 37 °C and 25 °C (left bar, grey; middle, dark blue, respectively), and by SEC at ~23 °C (right, light blue). The expected difference in ΔG_d at 25 and 23 °C calculated using Eq. 2.4 (Experimental Procedures) is less than 0.1 kcal (mol dimer)$^{-1}$. **(C)** ΔH_d (red) and $T\Delta S_d$ (blue) determined by fitting heats of dissociation at 37 °C. Error bars reflect the standard deviation of multiple (3-10) ITC experiments. The determined values are summarized in Table 2.1.

Table 2.1 Dimer interface stability of apo SOD1 variants measured by ITC and SEC.

SOD1 variant	ΔH_d (kcal (mol dimer)$^{-1}$)) ITC (37 °C)[a]	K_d (μM) ITC (37 °C)[a]	ΔG_d (kcal (mol dimer)$^{-1}$)) ITC (37 °C)[a,b]	$\Delta\Delta G_d$ (kcal (mol dimer)$^{-1}$)) ITC (37 °C)[c]	ΔG_d (kcal (mol dimer)$^{-1}$)) ITC (25 °C)[a,b]	ΔG_d (kcal (mol dimer)$^{-1}$)) SEC (23 °C)[b,d]
pWT	30.8 ± 8.8	0.067 ± 0.050	10.3 ± 0.5	na	nd	11.0 ± 0.4
V148I	11.4 ± 2.2	0.5 ± 0.2	8.9 ± 0.2	1.3	nd	nd
G93S	17.6 ± 4.6	1.3 ± 0.5	8.4 ± 0.3	1.8	nd	nd
H46R	16.2 ± 4.4	1.4 ± 1.1	8.4 ± 0.4	1.9	nd	10.3 ± 0.3
E100G	16.0 ± 4.8	2.6 ± 1.7	8.0 ± 0.4	2.3	nd	nd
G37R	7.8 ± 1.8	5.0 ± 1.9	7.6 ± 0.2	2.7	nd	nd
H43R	23.0 ± 1.4	5.7 ± 0.4	7.5 ± 0.0	2.7	9.7 ± 0.1	10.2 ± 0.1
G93A	14.0 ± 2.0	8.4 ± 3.5	7.2 ± 0.3	3.0	nd	10.4 ± 0.3
I113T	30.2 ± 2.5	10.2 ± 3.0	7.1 ± 0.2	3.1	8.4 ± 1.1	9.5 ± 0.6
A4T	39.2 ± 3.8	10.6 ± 3.3	7.1 ± 0.2	3.1	nd	nd
A4S	9.0 ± 2.6	10.9 ± 0.2	7.0 ± 0.0	3.1	nd	nd
G93R	45.6 ± 1.8	20.0 ± 4.1	6.7 ± 0.1	3.5	nd	nd
A4V	37.2 ± 3.8	34.2 ± 13.3	6.4 ± 0.3	3.8	7.9 ± 0.7	7.2 ± 0.2
V148G	50.6 ± 1.4	76.8 ± 34.0	5.9 ± 0.3	4.3	7.3 ± 0.1	7.0 ± 0.1

na = not applicable.

nd = not determined.

[a]Values for each mutant are derived from fitting integrated raw ITC data to a dimer dissociation model (Eq. 2.1, Fig. 2.2B) and are an average and standard deviation of 3-10 experiments.

[b]ΔG_d values were obtained from K_d values using Eq. 2.3.

[c]$\Delta\Delta G_d = \Delta G_{d,pWT} - \Delta G_{d,mutant}$; positive values indicate a decrease in interface stability for the mutant relative to pWT.

[d]Data obtained by SEC. For pWT, G93A and H46R, heats of dissociation at 25 °C were too small to be measurable by ITC, thus K_d at this temperature was measurable only by SEC. Values are the average of 3-6 experiments and error bars represent the 95% confidence intervals.

SEC data was obtained and analyzed by Jessica A. O. Rumfeldt.

2.3.3 Thermodynamics show that apo SOD1 dimer dissociation is accompanied by extensive disruption of structure and explain the particular sensitivity of the dimer interface to mutation

The thermodynamic data provide insights into structural changes accompanying apo SOD1 dissociation. The measured enthalpies (Fig. 2.3C, Table 2.1) are much (up to 20-fold) larger than expected values calculated using empirical models based on surface area changes between the crystal structure of the SOD1 dimer and its constituent monomer (217, 218). In addition, the value of $\Delta C_{p,d}$ (1.7 ± 0.2 kcal (mol dimer)$^{-1}$ °C^{-1}, Fig. 2.3A) is relatively large; the large values of ΔH_d and $\Delta C_{p,d}$ indicate a substantial increase in exposure of hydrophobic residues upon dissociation (219). For protein folding, ΔC_p can be calculated fairly accurately based on changes in solvent accessible surface area (217, 218). Applying this approach, and assuming no structural change in the monomer upon dissociation, the estimated $\Delta C_{p,d}$ for SOD1 is ~0.5 kcal (mol dimer)$^{-1}$ °C^{-1}, again, much lower than the experimental value. Notably, large ΔH_d and $\Delta C_{p,d}$ values have been reported for some other proteins, and were explained by significant conformational changes and/or changes in solvent binding upon dissociation (203, 218, 220). The total ΔC_p for unfolding of the apo SOD1 dimer to unfolded monomers, $\Delta C_{p,N_2 \leftrightarrow 2U}$, has been measured previously as 3.3 ± 0.8 kcal (mol dimer)$^{-1}$ °C^{-1} (128); combining this value with $\Delta C_{p,d}$, the change in heat capacity for monomer unfolding, $\Delta C_{p,M \leftrightarrow U}$ (= $\Delta C_{p,N_2 \leftrightarrow 2U}$ - $\Delta C_{p,d}$)/2), can be calculated as 0.8 ± 0.4 kcal (mol monomer)$^{-1}$ °C^{-1}. These values of $\Delta C_{p,d}$ and $\Delta C_{p,M \leftrightarrow U}$ are consistent with measurements of the denaturant-dependence of dimer dissociation and monomer unfolding for apo SOD1 which, similar to changes in heat capacity, are roughly correlated with changes in solvent exposed surface area (134). Thus, the relatively large $\Delta C_{p,d}$ and small $\Delta C_{p,M \leftrightarrow U}$ reveal significant disruption of the compact structure of the apo SOD1 dimer upon dissociation to form less well packed monomers (discussed further below).

Additional mechanistic insights into the process of consolidation of the dimer interface during SOD1 maturation may be obtained from further consideration of the dissociation thermodynamics combined with structural and folding studies. For all the SOD1 variants, dimer dissociation is enthalpically unfavorable and entropically driven at 37 °C (Fig. 2.3C), suggesting increased protein entropy upon dissociation overcomes the loss of solvent entropy due to increased exposure of hydrophobic residues (221). The solution NMR structure of an engineered monomeric apo SOD1 variant containing multiple mutations in the interface that abolish dimerization shows substantial disruption of structure compared to the dimer (222). Also, chemical denaturation *m* values indicate that the pWT apo SOD1 monomer involves lower than typical burial of solvent exposed surface area upon folding, and the monomer becomes considerably more compact in the presence of stabilizing Na_2SO_4 (134). Moreover, most of the substantial stability of dimeric apo SOD1 originates from the formation of the dimer interface, which is only slightly less stable than in the holo form of the protein (134, 143). Other indirect measures using chemical denaturants found the isolated apo SOD1 monomer has only marginal thermodynamic stability (134, 177). Thus, the direct measurements of thermodynamics of dissociation determined here are consistent with previous results obtained under non-physiological conditions, and provide strong evidence for extensive structural disruption upon dissociation of apo SOD1. The thermodynamic results also provide information on the mechanisms underlying the natural maturation of SOD1. Due to the loose packing of the apo monomer, dimerization confers strong stabilization as well as protection against aggregation by structuring regions of the protein that are highly dynamic in the monomer.

The particular sensitivity of the SOD1 dimer interface to disruption by mutations as demonstrated here is consistent with the structural and dynamic features of the interface. The

SOD1 interface is not evolutionarily conserved (223), is relatively small (~10% of monomer surface area) and has high hydrophobicity (~80% nonpolar residues) (173). The small size and high hydrophobicity of the interface suggest a low extent and selectivity of monomer-monomer interaction so that association may be easily perturbed by mutation. Indeed, significant changes in the interface were observed in structural studies of A4V and I113T (198). Furthermore, due to the small size of the interface there may be little variation possible for stable orientations of monomers (224). Computational studies have shown that the dimer interface and metal binding sites in SOD1 are highly connected (225), and have identified coupled motion between SOD1 monomers that is lost in A4V, G37R and H46R dimers (226, 227). Taken together, these computational studies point to long-range structural effects caused by mutations that may disrupt proper interface contacts. Furthermore, the network of stabilizing interactions that form when metals are bound to SOD1 constrains the flexibility of loops IV and VII (Fig. 2.1); but, in the absence of metal these loops gain conformational freedom (135, 136, 165), and have been proposed to create energetic frustration in the apo form of the protein (148). These regions of enhanced dynamics, notably in Loop IV which forms part of the dimer interface, may be easily perturbed by mutations leading to compromised dimer interface stability. Thus, the common weakening of the dimer interface of apo SOD1 with temperature and mutation as characterized here rationalizes a range of experimental and computational results and demonstrates the susceptibility of the interface to disruption by modest changes in the covalent structure of the protein. This disruption may occur not only due to fALS-associated mutations but also upon covalent modifications of wild-type SOD1 observed in sALS (19).

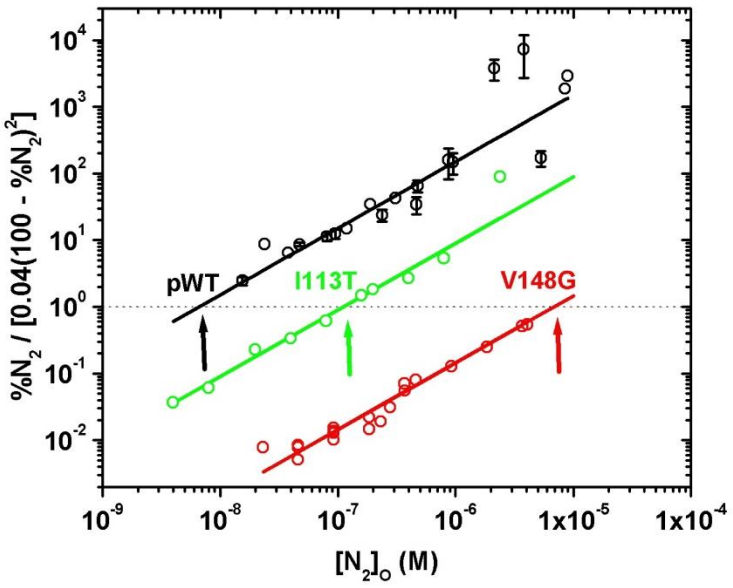

Figure 2.4 Size exclusion chromatography reveals decreased dimer stability for SOD1 mutants. SEC data were measured as a function of total dimer concentration, $[N_2]_o$. The linear transformation of the data (Experimental Procedures, Eq. 2.9) gives the fitted K_d values (Table 2.1) at Y=1 as indicated by the arrows. Symbols with error bars represent the average and 95% confidence intervals for 3-6 SEC measurements. SEC data was obtained and analyzed by Jessica A. O. Rumfeldt.

2.3.4 Conclusions

In summary, we report here ITC and SEC measurements that reveal common destabilization of apo SOD1 caused by diverse mutations whose effects manifest at the dimer interface. To date, relatively few homodimeric proteins have been characterized by ITC, and predicting the energetics and mechanisms of protein binding remains challenging (203, 218, 220). Such predictions are particularly difficult when association also involves significant protein conformational changes (228). The results here show how quantitative analysis of protein interface stability by ITC can provide valuable data both for fundamental understanding and modelling of protein-protein interactions and for understanding disease.

Many studies have attempted to correlate various properties of mutant SOD1 with ALS characteristics. A correlation between total protein stability (i.e. combined monomer and dimer interface stability) and disease duration has been reported; however, the data are very scattered (200, 229, 230). Thus, mutational effects on total stability are only part of the story. Our results show that dimerization and monomer stabilities are additional key characteristics to consider for unravelling the origins of toxic effects of SOD1 in ALS.

2.4 Supplementary Information

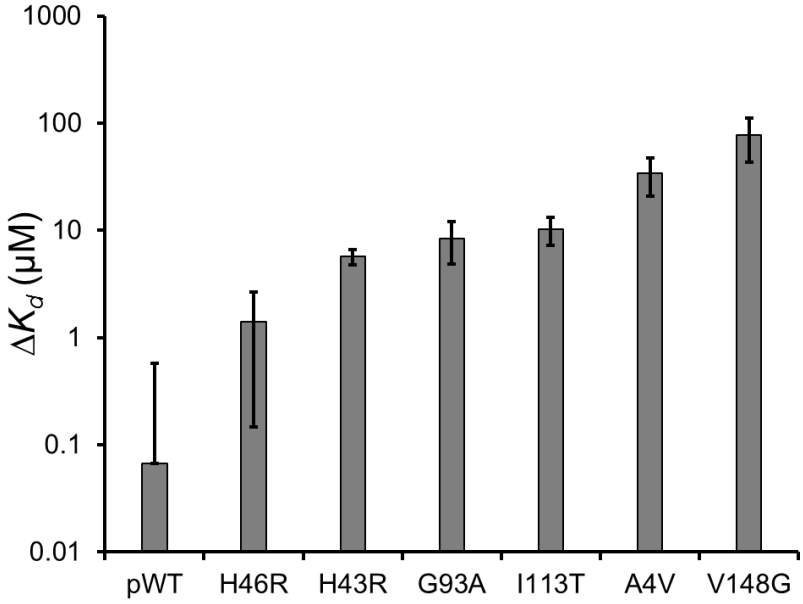

Figure S2.1 Change in dimer interface affinity with increasing temperature. The grey bars represent the increase in the K_d at 37 °C relative to 25 °C ($\Delta K_d = K_d(37) - K_d(25)$). SEC and ITC experiments at ~23 °C and 25 °C, respectively, were performed for H43R, I113T, A4V, and V148G. Extrapolating $\Delta G_d(25)$ values determined by ITC to $\Delta G_d(23)$ using Eq. 2.4 and a $\Delta C_{p,d}$ of 1.7 kcal (mol dimer)$^{-1}$ °C^{-1} results in very little change in ΔG_d (0.03-0.09 kcal (mol dimer)$^{-1}$) and K_d (0.02-0.6 μM), which are smaller than the experimental uncertainties. Thus, the $K_d(25)$ values were calculated as the average of the ITC and SEC values. For pWT, H46R, and G93A, the heat of dissociation was too small at 25 °C to be measurable by ITC, and so the SEC values were used. Error bars reflect the standard deviation of multiple measurements of $K_d(37)$ and $K_d(25)$.

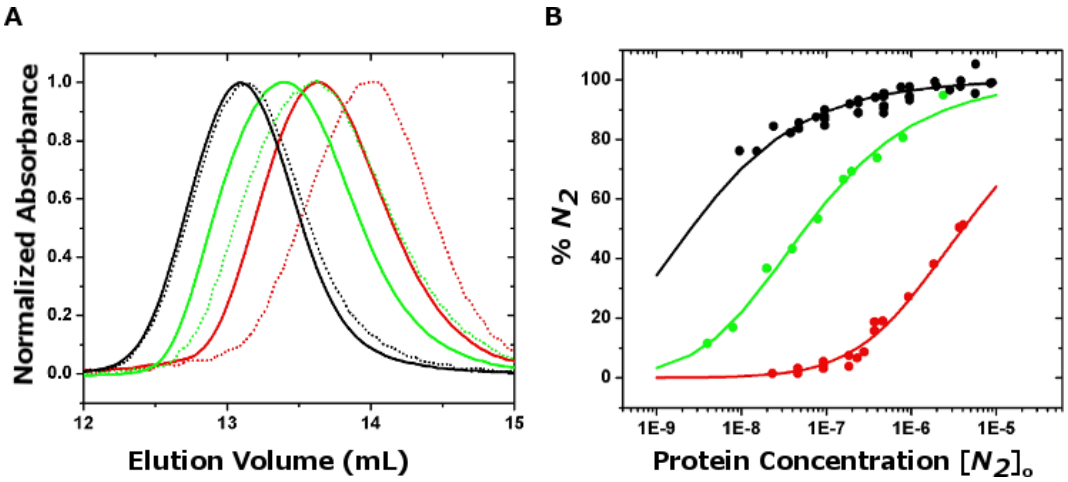

Figure S2.2 Decreased dimer stability of SOD1 mutants measured by SEC at ambient temperature (23 °C). (A) SEC elution profile for pWT (black), I113T (green), and V148G (red) at 0.9 and 0.2 μM dimer, shown as solid and dotted lines, respectively. **(B)** Percent native dimer (N_2) as a function of protein concentration (M dimer). Data points are calculated from experimental elution volumes and fitted parameters using Eq. 2.7. Solid lines were generated using Eq. 2.6 and fitted values of K_d (Table 2.1).

Chapter 3

Combined calorimetry techniques reveal complex effects of fALS-associated mutations on the stability of metal free SOD1

Author Contributions

This chapter will be submitted for publication with the following authors: Helen R. Broom, Kenrick A. Vassall, Jessica A.O. Rumfeldt, Ming Sze Tong, Julia M. Bonner, and Elizabeth M. Meiering. The manuscript was written mainly by Helen R. Broom with contributions from Kenrick A. Vassall, Jessica A.O. Rumfeldt, and Elizabeth M. Meiering. The ITC data were obtained by Helen R. Broom (Chapter 2); the DSC data were obtained by Helen R. Broom, Kenrick A. Vassall, Jessica A.O. Rumfeldt, Ming Sze Tong, and Julia M. Bonner, as well as previously published data acquired by Peter B. Stathopulos (128); chemical denaturation of apo pWT SOD1 was performed by Jessica A.O. Rumfeldt; dimer 2-state data fitting was performed by Helen R. Broom, Kenrick A. Vassall, and Jessica A. O. Rumfeldt; monomer 2-state data fitting was performed by Helen R. Broom and Kenrick A. Vassall, and 3-state data fitting using was performed by Helen R. Broom.

Overview

Neurotoxic aggregation of mutant Cu, Zn-superoxide dismutase (SOD1) has been implicated in causing amyotrophic lateral sclerosis (ALS), a devastating neurodegenerative disease. It has been proposed that ALS-associated mutations in SOD1 promote the formation of neurotoxic aggregates by enhancing dissociation of mutant SOD1 homodimers to form aggregation-prone monomers. We have previously investigated the thermodynamic effects of chemically and structurally diverse mutations on dimer interface stability for unmetallated (apo) SOD1 using isothermal titration calorimetry (ITC) and shown that the effects of the mutations generally propagate through the structure and compromise the strength of the dimer interface. Here we use these measurements of dimer interface stability combined with measurements of total unfolding by differential scanning calorimetry (DSC) and urea denaturation to assess the effects of mutations on both dimer interface and monomer stability. We find that although all mutations characterized herein decrease the stability of the dimer interface, they have varying effects on the monomer stability ranging from slightly stabilizing to moderately destabilizing. These values reflect the true stability of the apo monomer; previous experiments commonly used a monomer construct with mutations in the dimer interface to assess the effects of disease-associated mutations. Using stability parameters to calculate the population of folded dimer, folded monomer intermediate, and unfolded monomer reveals that the mutations increase the population of a monomers at physiological temperature and pH. Since apo monomers have an increased propensity to aggregate, these results are particularly pertinent for understanding toxic aggregation pathways involved in neurodegeneration.

3.1 Introduction

Cu, Zn-superoxide dismutase (SOD1), a dimeric metalloenzyme, has become a model for understanding protein structure and function as well as folding and misfolding associated with disease (126). In 1993, a genetic link was established between ALS and mutant forms of SOD1 (8). A characteristic feature of ALS is the presence of protein aggregates in motor neurons (21) and SOD1 has also been identified as a component of aggregates in SOD1-linked familial ALS and some sporadic ALS patients (26, 29, 231). To date, over 170 predominantly missense mutations distributed throughout the protein have been linked to familial ALS (http://alsod.iop.kcl.ac.uk/home.aspx). These mutations have an autosomal dominant pattern of inherence, and it is generally accepted that the mutations confer a toxic gain of function to SOD1, although the mechanisms of toxicity remain unclear (232). Due to similarities in the clinical symptoms of fALS and sALS, common mechanisms are proposed for both forms of the disease (33, 233). Thus, a major hypothesis in the field of ALS research is that mutations promote aggregation of SOD1, analogous to toxic misfolding of other proteins associated with various neurodegenerative diseases such as Huntington's, Alzheimer's, and prion disorders (52), leading to a cascade of toxic events that culminate in motor neuron death (3). However, attempts to identify relationships between the effects of the mutations and ALS characteristics have shown that these effects are highly complex and not correlated with disease characteristics in a simple way (98, 229).

The fully mature form of SOD1 (holoSS) is a homodimer that binds one zinc and one copper ion per subunit, has a very high melting temperature (~92 °C (128)), and can maintain enzymatic activity under strongly denaturing conditions (129). Yet, while mature SOD1 is highly stable against denaturation, ALS-associated mutants have an increased tendency to be

metal deficient (99), which increases the dynamics of the protein (135). Folding and thermodynamic stability analyses of mutant SOD1 proteins can reveal whether the mutations have adverse effects on protein stability and alter folding such that misfolding and aggregation become more favorable. We have previously used differential scanning calorimetry (DSC) and chemical denaturation to determine the stability and unfolding mechanism of metallated (holo) and unmetallated (apo) disulfide oxidized (SS) pWT SOD1, and identified complex effects of several fALS-associated mutations (134, 143). These studies and others have suggested that increased population of unmetallated monomeric forms of SOD1 may initiate toxic aggregation (99, 144, 193, 197–199, 226, 234, 235), implicating metal loss and dimer dissociation as key steps in the SOD1 aggregation pathway.

ITC is an attractive method for analyzing binding energetics (203, 236). In addition, combining ITC with DSC provides a method for dissecting the effects of mutations on dimer interface and monomer stability. Strikingly, ITC data clearly show that diverse mutations all weaken dimer interface (Chapter 2). In this chapter we expand on these findings and show that mutations have varying effects on monomer stability. For most mutations, the effects on monomer stability are moderately to highly destabilizing, while some mutations actually increase monomer stability. Thus, point mutations can have very different effects on the component stabilities of the SOD1 dimer. These results highlight the importance of understanding not just total protein stability, but both interface and monomer stability, as it is the interplay between these two properties that determines whether or not a monomer intermediate is populated, and thus able to nucleate aggregation under physiological conditions.

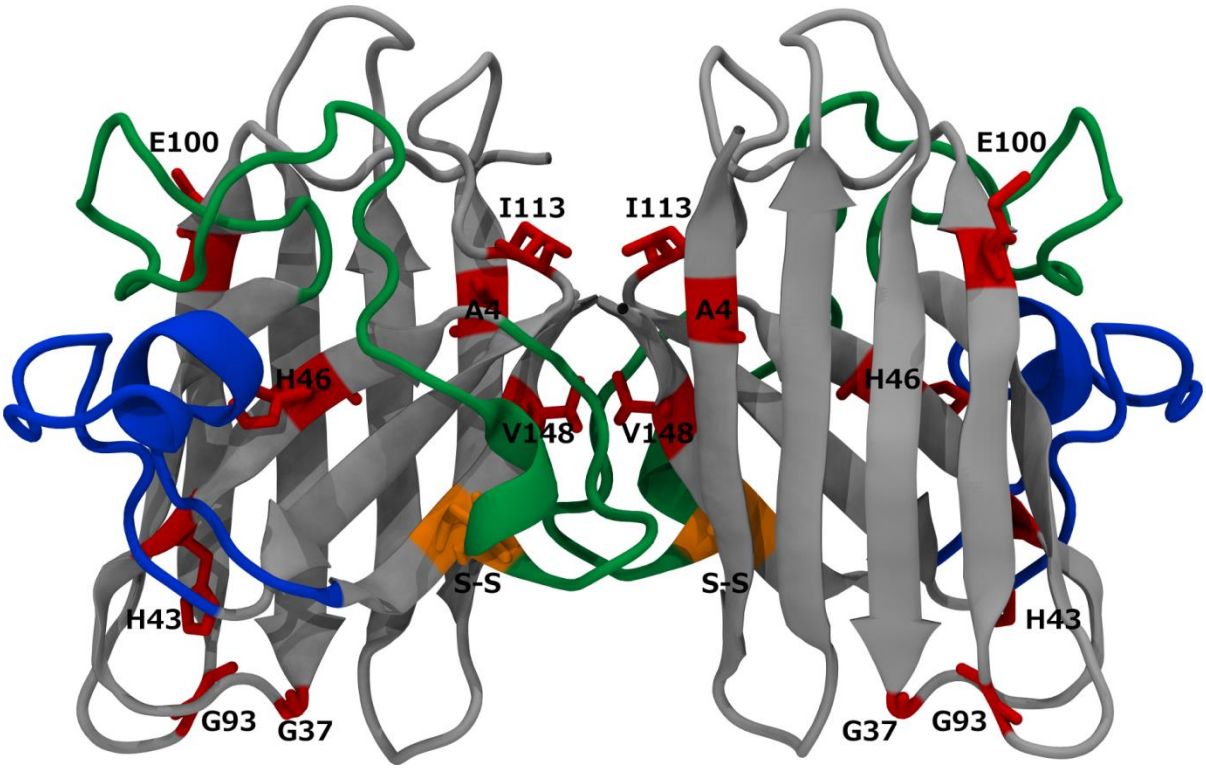

Figure 3.1 Structural features of apo SOD1. SOD1 is a homodimeric metalloenzyme. Each monomer forms a Greek key β-barrel and contains a single disulfide bond (orange). Structural studies have shown that in the absence of metal, zinc-binding loops (loop IV, green) and electrostatic loops (loop VII, blue) are disordered, and the protein is more flexible compared to the metal-bound form (135, 136). The sites of ALS-associated mutations characterized herein are shown in red (PDB code 1HL4).

3.2 Materials and Methods

3.2.1 Recombinant SOD1 expression and purification

The human pWT SOD1 (pseudo wild-type with nonconserved Cys 6 and Cys 111 replaced by Ala and Ser, respectively) (1, 98, 141) and mutant SOD1 were expressed using the plasmid vector pHSOD1ASlacI1 (204) in *E. coli* cells, purified and demetallated by dialysis against EDTA as described previously (128, 205). Protein concentration was determined by absorbance at 280 nm using an extinction coefficient of 10,800 M^{-1} cm^{-1} for the SOD1 dimer (206).

3.2.2 Differential Scanning Calorimetry

DSC experiments were performed as described previously (128), using a LLP VP DSC (MicroCal Inc., Malvern Instruments Ltd.). Samples contained ~0.05-3 mg mL^{-1} of protein in 20 mM HEPES, pH 7.8. Buffer versus buffer thermograms were subtracted from protein versus buffer thermograms and data were normalized to units of cal g^{-1} °C^{-1} before fitting. As in previous studies (128, 134), the reversibility of unfolding for the apo SOD1 mutants was assessed by heating the sample to the end of the unfolding endotherm, followed immediately by cooling and subsequent re-scanning. Reversibility was quantified by calculating the area under the unfolding endotherm for the first scan and second scan. Samples were scanned at a rate of 1 °C $minute^{-1}$, unless otherwise specified.

3.2.3 Isothermal Titration Calorimetry

ITC experiments measuring the heat associated with apo SOD1 dimer (N_2) dissociation to folded monomers (M), $N_2 \leftrightarrow 2M$, as governed by the dissociation constant ($K_{d,N_2 \leftrightarrow 2M}$), were

performed and data analyzed as described (207, 208) (Chapter 2). For pWT and all SOD1 mutations, experiments were performed at 37 °C where we found dissociation was increased relative to dissociation at room temperature (~23 °C). Some mutations were sufficiently destabilizing that dissociation was also measureable at 25 °C, and in such cases the data could be readily compared with SEC measurements of dissociation. Data from both ITC and SEC were in good agreement (Chapter 2).

3.2.4 Analysis of calorimetry data

Calorimetry data were analyzed using 2-state and 3-state models with various combination of parameters defined as fixed or fitted. A 2-state unfolding model describing the transition from native folded dimer to unfolded monomers with no intermediate, $N_2 \leftrightarrow 2U$, and a 3-state model with the formation of a monomer intermediate, $N_2 \leftrightarrow 2M \leftrightarrow 2U$ (143, 237, 238) (Tables 3.1, 3.2) were used. For the 2-state model, individual thermograms were fit as described previously for apo SOD1 to Eq. 3.1 (128, 134):

$$C_p = (A + BT)(1 - \alpha) + (E + FT)\alpha + \frac{\beta \Delta h_{cal}^2(T_{0.5})}{RT^2} \frac{\alpha(1-\alpha)}{2-\alpha} \quad \text{(Eq. 3.1)}$$

where C_p is the total specific heat capacity at temperature T (in Kelvin); A and B are the intercept and slope of the folded baseline, respectively; E and F are the intercept and slope of the unfolded baseline, respectively; R is the universal gas constant; β is the ratio of the van't Hoff enthalpy (ΔH_{vH}) to calorimetric enthalpy (ΔH_{cal}) multiplied by the molecular weight (MW) of the SOD1 dimer; $\Delta h_{cal}(T)$ is the specific calorimetric enthalpy (ΔH_{cal} divided by the molecular weight) of unfolding at T; α is the extent of the unfolding reaction and $T_{0.5}$ (or $t_{0.5}$) is the temperature in Kelvin (or °C) at which half of the protein is unfolded (i.e α = 0.5). Values of molecularity, n, were calculated using Eq. 3.2:

$$n = \frac{-\Delta H_{vH}}{slope * R} + 1 \quad \text{(Eq. 3.2)}$$

where ΔH_{vH} is from the 2-state fit for a given thermogram and slope is the slope of a plot of $\ln P_{dimer}$ versus $1/T_{0.5}$, where P_{dimer} is the protein concentration in M dimer (128, 239). For each variant, the slope was determined using the data at all protein concentrations. Representative plots of $\ln P_{dimer}$ versus $1/T_{0.5}$ are shown in Fig. S3.1.

For the dimer 3-state with monomer intermediate model, the data were fit to Eq. 3.3:

$$C_p = \left(\frac{\beta_1 \Delta h_{cal,N_2 \leftrightarrow 2M}(T_1') + \alpha_2 \beta_2 \Delta h_{cal,M \leftrightarrow U}(T_1')}{RT^2}\right) \Delta h_{cal,N_2 \leftrightarrow 2M}(T_1') \frac{\alpha_1(1-\alpha_1)}{2-\alpha_1} +$$

$$\left(\left(\frac{\beta_1 \Delta h_{cal,N_2 \leftrightarrow 2M}(T_1') + \alpha_2 \beta_2 \Delta h_{cal,M \leftrightarrow U}(T_1')}{RT^2}\right) \frac{\alpha_1 \alpha_2 (1-\alpha_1)}{2-\alpha_1} + \frac{\beta_2 \Delta h_{cal,M \leftrightarrow U}(T_2')}{2RT^2} \alpha_1 \alpha_2 (1-\alpha_2)\right)$$

$$\Delta h_{cal,M \leftrightarrow U}(T_2') + (1-\alpha_1)(A+BT) + \alpha_1(1-\alpha_2)(C+DT) + \alpha_1 \alpha_2 (E+FT) \quad \text{(Eq. 3.3)}$$

In Eq. 3.3, the subscripts 1 and 2 refer to the first transition, $N_2 \leftrightarrow 2M$, and second transition, $M \leftrightarrow U$, respectively, both defined per M of dimer. T_1' was set to 310 K (37 °C), corresponding to the temperature at which the thermodynamics of dimer dissociation were measured by ITC, thus allowing for these values to be fixed during data fitting (*vide infra*) (Fig. S3.2); T_2' was defined as the temperature at which the equilibrium constant, $K_{M \leftrightarrow U}$, is equal to 1, and is thus independent of protein concentration; C and D are the intercept and slope, respectively, of the monomer intermediate baseline. Due to the additional parameters in the 3-state model compared to the 2-state model, fitting individual thermograms to Eq. 3.3 resulted in high uncertainties in the fitted values. Accordingly, multiple datasets obtained for different protein concentrations were fit globally with various parameters shared across the datasets as follows. The slopes of the monomeric intermediate and unfolded monomer baselines were set equal to that of the native baseline (i.e., B=D=F; commonly normalized per M dimer), making the common assumption

that ΔC_p of unfolding is temperature independent (Fig. S3.3) (219). The intercepts of the intermediate and unfolded baselines were defined relative to the intercept of the native baseline according to temperature-independent values for $\Delta C_{p,N_2 \leftrightarrow 2M}$ (change in heat capacity upon dimer dissociation to monomeric intermediate) and $\Delta C_{p,M \leftrightarrow U}$ (change in heat capacity upon monomeric intermediate unfolding):

$$C = \Delta C_{p,N_2 \leftrightarrow 2M} + A \quad \text{(Eq. 3.3a)}$$

$$E = \Delta C_{p,N_2 \leftrightarrow 2M} + \Delta C_{p,M \leftrightarrow U} + A \quad \text{(Eq. 3.3b)}$$

$\Delta C_{p,N_2 \leftrightarrow 2M}$ was set to 1.7 kcal (mol dimer)$^{-1}$ °C^{-1}, the average value determined by Kirchoff analysis of ITC data for four SOD1 variants for which the enthalpy of dimer dissociation was measured as a function of temperature (Chapter 2, Fig. 2.3A). Since $\Delta C_{p,N_2 \leftrightarrow 2M} + \Delta C_{p,M \leftrightarrow U} = \Delta C_{p.N_2 \leftrightarrow 2U}$ (total ΔC_p upon unfolding of apo SOD1 from folded dimer to unfolded monomers), the value of $\Delta C_{p,M \leftrightarrow U}$ was set by subtracting $\Delta C_{p,N_2 \leftrightarrow 2M}$ from a $\Delta C_{p,N_2 \leftrightarrow 2U}$ of 3.30 kcal (mol dimer)$^{-1}$ °C^{-1}, which gives a value of 1.6 kcal (mol dimer)$^{-1}$ °C^{-1} (0.8 kcal (mol monomer)$^{-1}$ °C^{-1}). $\Delta C_{p,N_2 \leftrightarrow 2U}$ of 3.30 kcal (mol dimer)$^{-1}$ °C^{-1} was determined previously for apo SOD1 from Kirchoff analysis, structure-based calculations, and DSC data fitting of SOD1 variants (128). This approach is supported by the observation that the average $\Delta C_{p,N_2 \leftrightarrow 2U}$ values for apo SOD1 variants are close to 3.30 kcal (mol dimer)$^{-1}$ °C^{-1} (Table 3.2) (128, 134), and mutations typically cause minimal changes in ΔC_p (240, 241) (Chapter 2). For a more thorough discussion of our approach to 3-state fitting, refer to section 3.3.4. All global fitting was performed using Matlab R2013b (The MathWorks Inc.).

3.2.5 Calculation of thermodynamic parameters using fitted values for 2-state and 3-state models

Values for ΔG, ΔH, and ΔS were calculated from fitted DSC parameters according to the following equations:

$$\Delta G(T) = \Delta H(T) - T\Delta S(T) \quad \text{(Eq. 3.4)}$$

$$\Delta H(T) = \Delta H(T_{ref}) + \Delta C_p(T - T_{ref}) \quad \text{(Eq. 3.5)}$$

$$\Delta S(T) = \Delta S(T_{ref}) + \Delta C_p \ln(\frac{T}{T_{ref}}) \quad \text{(Eq. 3.6)}$$

$$\Delta S(T_{ref}) = \frac{\Delta H(T_{ref}) - \Delta G(T_{ref})}{T_{ref}} \quad \text{(Eq. 3.7)}$$

where T_{ref} is the reference temperature, $T_{0.5}$ (or $t_{0.5}$) for DSC 2-state fitting; for DSC 3-state fitting T_{ref} = 310.15 K for dimer dissociation and $T_{0.5}$ (or $t_{0.5}$) for monomer unfolding; and $\Delta H(T_{ref})$, $\Delta S(T_{ref})$, and $\Delta G(T_{ref})$ are the corresponding enthalpy, entropy, and free energy, respectively, at the reference temperature. $\Delta G(T_{ref})$ was calculated using Eq. 3.8.

$$\Delta G(T_{ref}) = -RT_{ref} lnK(T_{ref}) \quad \text{(Eq. 3.8)}$$

For calculating stabilities obtained from 2-state and 3-state fitting, ΔC_p values were set to the same temperature-independent values discussed above (Section 3.2.4). For such calculations, ΔC_p is commonly taken to be temperature-independent (219), and this assumption has been shown to be reasonable, particularly over short temperature ranges (58, 128, 242). Accordingly, thermodynamic values were calculated at 51.2 °C (the average of all the $t_{0.5}$ values in Table 3.1, t_{avg}) and at physiological temperature, 37 °C. Extrapolation errors are decreased when considering differences in stability, $\Delta\Delta G_{N_2 \leftrightarrow 2U}$ = ($\Delta G_{N_2 \leftrightarrow 2U,WT}$ - $\Delta G_{N_2 \leftrightarrow 2U,mut}$), from values obtained using the same ΔC_p (128, 243). The calculated thermodynamic parameters were also

used to determine the fractions of different species (N_2, M and U) (Fig. 3.7), as described previously (143, 173).

3.2.6 Equilibrium urea denaturation curves at 37 ℃

Denaturation curve experiments were performed at 37 ℃ in 1 mM EDTA, 20 mM HEPES, pH 7.8. Stock solutions of apo pWT were diluted 10-fold into different concentrations of urea and equilibrated at 37 ℃ for 10 hours. Fluorescence was measured using a Fluorolog3-22 spectrofluorometer (Horiba-Jobin-Yvon Spex Inc.) equipped with a thermostated cuvette holder with excitation and emission wavelengths of 282 and 360 nm, respectively. Thermodynamic parameters were obtained by globally fitting denaturation curves at 0.2, 0.8, 3, 10, and 25 μM dimer using a 3-state dimer with a monomeric intermediate model as described in (143) using Microcal Origin 6.0 (Microcal Inc, Northampton, MA, USA). Baselines were analyzed as follows and fixed during the global fitting. The slope and intercept of the folded baseline were determined by linear regression using data between 0.3 and 1.8 M urea for the 25 μM denaturation curve, where the population of native dimer is the largest. These values were then normalized according to protein concentration. The unfolded baseline slope and intercept were also determined individually for all protein concentrations by linear regression. The fluorescence of the intermediate was determined by systematically changing the magnitude of the fluorescence to identify the value that corresponded to the lowest χ^2, similar to previous denaturation curve analyses of apo pWT in guanidinium hydrochloride (134). More specifically, the fluorescence of the intermediate was fixed to a value between 10 and 80% of the total amplitude of the transition. The change in fluorescence of the intermediate with urea concentration was set to a value between that of the folded and unfolded protein according to the

magnitude of the intermediate signal; for example, when the fluorescence was set to 50% of the way through the transition, the slope of the intermediate was half way between the values for the folded and unfolded baselines. In the global fitting for each intermediate fluorescence value, the four parameters $\Delta G_{N_2 \leftrightarrow 2M}$, $\Delta G_{M \leftrightarrow U}$, and the dependence of the dimer interface and monomer stability on urea concentration ($m_{N_2 \leftrightarrow 2M}$ and $m_{M \leftrightarrow U}$, respectively) were shared across all protein concentrations and were allowed to float. The lowest χ^2 value for the fit was obtained with intermediate fluorescence and slope corresponding to 30% of the total amplitude of the transition.

3.3 Results

3.3.1 DSC reveals generally destabilizing but also some stabilizing effects of mutations on the total stability of apo SOD1 mutants

DSC was used to measure the energetics of total protein unfolding. Thermodynamic analysis requires reversibility of thermal unfolding. As was seen for other apo SOD1 variants (128, 134), when scanning to the end of the unfolding endotherm, cooling and rescanning (Fig. 3.2A), unfolding of the mutants studied here is highly reversible, generally 85-95%. Additionally, the DSC thermograms were not significantly affected by scan rate, which is evidence for equilibrium unfolding behaviour (Table 3.1) (128, 244). Apo pWT SOD1 has a melting temperature, $t_{0.5}$ (temperature at which half of the protein is unfolded), of ~59 °C (128), while the mutants generally have $t_{0.5}$ values ranging from 10 to 15 °C lower than pWT, indicating marked destabilization (Table 3.1, Fig. 3.2). Notable exceptions are H46R and V148I, which are slightly more stable than pWT with $t_{0.5}$ values that are ~2 °C higher. A similar change in the

apparent $t_{0.5}$ has been reported previously for the irreversible unfolding of H46R in the WT SOD1 background (see Section 1.3.2) (245).

3.3.2 Fitting of apo SOD1 thermal unfolding to dimer 2-state model

Under constant pressure, heat flow is equal to the enthalpy of a system and, thus, can be directly measured using calorimetric techniques. Enthalpy can also be determined indirectly by van't Hoff analysis whereby the equilibrium constant for a given process (K) is determined at different temperatures to yield enthalpy (246, 247). In simple cases, a plot of ln$K$ versus 1/T is linear with a slope related to the enthalpy, referred to as the van't Hoff enthalpy (ΔH_{vH}). This type of analysis relies on a specific and appropriate model to define K correctly; thus, comparing the ΔH_{vH} to the enthalpy directly measured by calorimetry (ΔH_{cal}) can provide a way to assess the accuracy of the model used. A common approach to analyzing the validity of a particular model is to calculate the $\Delta H_{vH}/\Delta H_{cal}$, which should be 1 if the model is correct. However, we have found from many scans of different apo SOD1 variants that uncertainties in protein concentration (usually ~10%) and small amounts of protein aggregation can have a large impact on ΔH_{cal}, which in turn can lead to some scatter in the $\Delta H_{vH}/\Delta H_{cal}$ values. A better approach to investigating the possibility of monomer formation during unfolding is by calculating the number of subunits in the cooperatively unfolding homo-oligomer, also known as the molecularity, n, which is related to ΔH_{vH} (Materials and Methods Eq. 3.2, Fig. S3.1) (128, 239). ΔH_{vH} is relatively insensitive, compared to ΔH_{cal}, to errors in protein concentration (128, 244, 248, 249).

Furthermore, we have shown previously that the effects of aggregation on the thermodynamic analysis can be effectively eliminated by excluding high temperature data (i.e. excluding data at temperatures where exothermic aggregation can in some cases be significant),

and by calculating thermodynamic quantities using ΔH_{vH}. We are confident in the validity of this approach given that the average values for $\Delta C_{p,N_2\leftrightarrow 2U}$ determined from the 2-state fits for all mutants, except A4V and V148G, are similar to the value of $\Delta C_{p,N_2\leftrightarrow 2U}$ of 3.30 kcal (mol dimer)$^{-1}$ °C^{-1} determined for pWT using multiple experimental methods (Table 3.1, Materials and Methods) (128); exothermic aggregation would decrease the values of $\Delta C_{p,N_2\leftrightarrow 2U}$. The lower value of $\Delta C_{p,N_2\leftrightarrow 2U}$ for A4V and V148G is likely related to increased monomer formation, which is most pronounced for these mutants (*vide infra*). Furthermore, while aggregation might in principle affect the shape of the endotherm at high temperatures, fitting different extents of the endotherm has very little effect on the determined total stability, described previously for dimer 2-state fits (128), and for 3-state fits, described further below.

The DSC data for the mutants were fit initially to a dimer 2-state unfolding model ($N_2\leftrightarrow 2U$), as done previously for pWT and other ALS-associated mutants (128, 134). Representative fits are shown in Fig. 3.2B, with fitted parameters summarized in Table 3.1. At higher protein concentrations the data for most mutants are well fit by a dimer 2-state model, and the data follow similar trends to those reported for apo pWT and mutant SOD1 (Fig. 3.3) (128, 134). Furthermore, there is good agreement between stability measured by calorimetry and chemical denaturation for pWT (*vide infra* and Table 3.3) (134, 176, 177, 200).

But at lower protein concentrations, clear deviations from 2-state behavior are observed. Increases in *n* from lower values at low protein concentration to ~2 at higher protein concentration, the value expected for 2-state unfolding of a dimeric protein, suggests that for most variants there is some formation of monomer at low protein concentrations due to mass action (Table 3.1). For A4V, H46R, and V148G, the *n* values are considerably lower than 2 at all protein concentrations, indicating that the size of the cooperative unfolding unit is smaller for

these variants. Thus, dimer dissociation and monomer unfolding occur over a broader temperature range, which points to non-2-state behavior (Fig. S3.2).

Protein concentration dependence of $t_{0.5}$ can further define when formation of monomer is occurring. For various mutants, the $t_{0.5}$ values increase with protein concentration as expected for a dimer 2-state transition. The expected protein concentration dependence of $t_{0.5}$ can be determined from the intersection of plots of ΔG versus t and $-RT\ln 2P_{dimer}$ versus t, where R is the universal gas constant, P_{dimer} is the total dimer concentration in mol L^{-1}, T is the temperature in Kelvin and t is the temperature in °C (Fig. 3.3) (128, 250). In Fig. 3.3, representative ΔG versus t plots are shown in the upper left panel for pWT, A4T, and A4S, while plots of the predicted $t_{0.5}$ versus protein concentration for various mutants compared to the fitted $t_{0.5}$ values are shown in the remaining panels.

For pWT, A4S, A4T, and V148I, the fitted $t_{0.5}$ values show close agreement with predicted $t_{0.5}$ values, while the fitted $t_{0.5}$ values for A4V, H46R, V148G, and to some extent G37R change less with protein concentration than predicted (128, 134). Thus, for A4V, H46R and V148G, several observations point to a relatively high population of folded monomer during DSC scans. Taken together, it can be seen that the 2-state model is accurate for many apo variants at higher protein concentration. But at low protein concentration, and for some mutants other, more complex, unfolding models are required to characterize the energetics of apo SOD1 unfolding (*vide infra*).

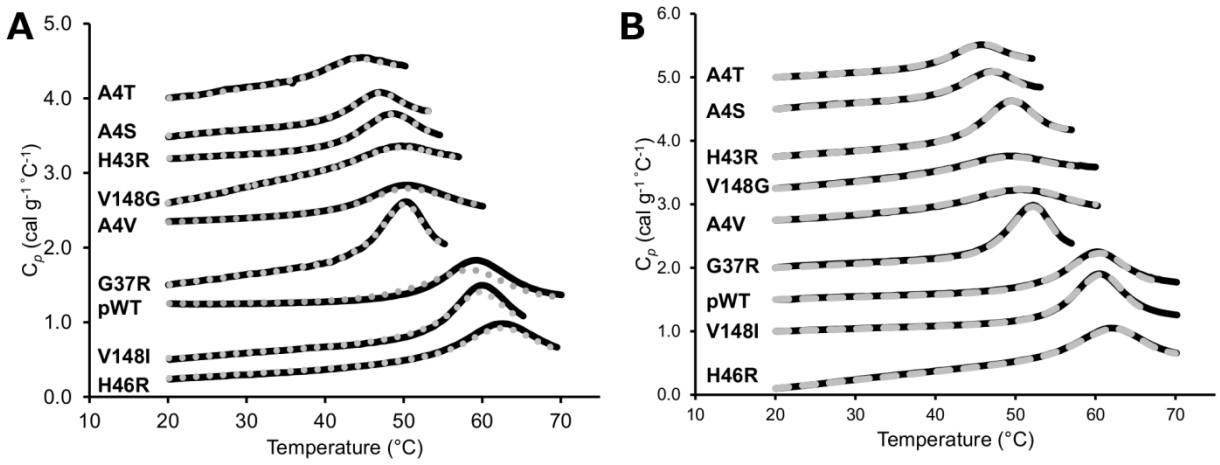

Figure 3.2 Fits of reversible unfolding for apo SOD1 variants to a dimer 2-state unfolding model. In a typical DSC experiment, the protein sample is heated at a constant rate and the heat capacity (C_p) is monitored. The temperature where half of the protein is unfolded is referred to as the melting temperature ($t_{0.5}$). After the first scan, the sample is cooled and rescanned to assess the reversibility of unfolding, a requisite for thermodynamic analysis of the process. **(A)** The reversibility of the unfolding transitions was determined by performing two consecutive scans. The second scan (grey dashed line) was obtained immediately after cooling the sample following completion of the first scan (black solid line). The reversibility, determined by integrating the area under the endotherm (ΔH_{cal}) for the first scan and the second scan after subtraction of the baselines, is 95% or greater for all mutants except for A4V where it is ~85%. The native baseline was subtracted and datasets offset for purposes of comparison. **(B)** Typical DSC thermograms with corresponding dimer 2-state fits for apo pWT SOD1 and a representative subset of mutants. Data are presented as black solid lines while the corresponding dimer 2-state fits are presented as grey dashed lines. Parameters obtained from the fits are summarized in Table 3.1. Datasets were offset for purposes of comparison. In both panels, the data were normalized for protein concentration (0.12-1.25 mg mL^{-1}) and SOD1 variants are arranged from right to left in order of decreasing $t_{0.5}$.

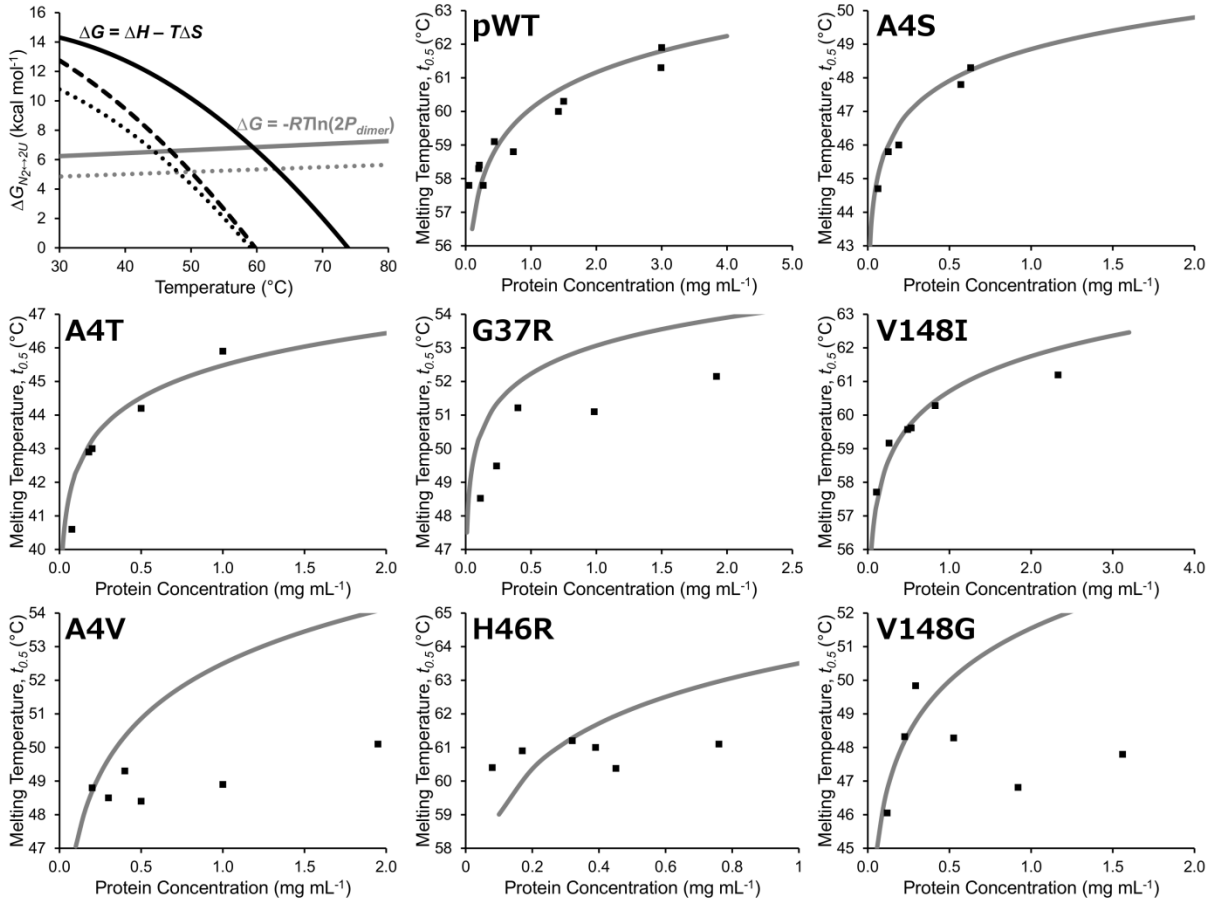

Figure 3.3 Predicted $t_{0.5}$ for thermal unfolding of apo pWT and a subset of mutants. In the top left panel, predicted values for $t_{0.5}$ were calculated from the intersection of $-RT\ln(2P_{dimer})$ versus t (grey lines) and ΔG versus t (black lines) for pWT (solid black line), A4S (dashed black line), and A4T (dotted black line) (128, 250). The line generated for 0.5 mg mL^{-1} (solid grey line) intersects each ΔG versus t plot at a lower temperature than the line generated for 5 mg mL^{-1} (dotted grey line). The ΔG values were calculated using the average fitted parameters for the 2-state dimer unfolding (Table 3.1). Predicted $t_{0.5}$ values (solid grey lines) from these calculations were then plotted as a function of protein concentration and compared to the actual fitted $t_{0.5}$ values (filled black squares) from Table 3.1.

Table 3.1 Thermodynamic parameters for dimer 2-state unfolding of apo SOD1.

SOD1 variant	[SOD1] (mg mL^{-1})	$t_{0.5}$[f] (°C)	$\Delta C_{p,N_2\leftrightarrow 2U}$[g] (kcal (mol dimer)$^{-1}$ °C^{-1})	$\Delta H_{vH}(t_{0.5})$[f] (kcal (mol dimer)$^{-1}$)	$\Delta G_{N_2\leftrightarrow 2U}$[g,h] (kcal (mol dimer)$^{-1}$) t_{avg}	$\Delta G_{N_2\leftrightarrow 2U}$[g] (kcal (mol dimer)$^{-1}$) 37 °C	n[i]
pWT[a]	0.05	57.8 ± 0.6	3.71	106.5 ± 18.9	10.1	12.3	1.60
pWT[a]	0.20	58.3 ± 0.1	2.95	112.8 ± 6.7	9.4	11.9	1.64
pWT[a]	0.21	58.4 ± 0.1	3.74	116.8 ± 9.1	9.5	12.1	1.66
pWT[a]	0.27	57.8 ± 0.0	3.85	115.4 ± 2.7	9.1	11.8	1.65
pWT	0.40	58.6 ± 0.2	2.20	121.7 ± 6.3	9.3	12.1	1.69
pWT[a]	0.44	59.1 ± 0.2	4.25	137.6 ± 9.4	9.7	13.1	1.78
pWT	0.50	59.1 ± 0.0	3.32	130.0 ± 3.1	9.4	12.5	1.74
pWT	0.50	59.2 ± 0.1	2.73	137.0 ± 6.6	9.6	13.0	1.78
pWT	0.50	59.5 ± 0.0	2.23	129.7 ± 2.7	9.5	12.6	1.74
pWT	0.52	58.4 ± 0.0	3.51	127.6 ± 2.8	9.2	12.3	1.72
pWT	0.60	59.0 ± 0.1	1.08	127.0 ± 2.8	9.2	12.2	1.72
pWT	0.73	59.4 ± 0.0	2.82	136.7 ± 1.9	9.5	12.8	1.78
pWT[a]	0.73	58.8 ± 0.0	4.30	144.1 ± 2.5	9.4	13.2	1.82
pWT[a]	1.42	60.0 ± 0.0	4.38	163.6 ± 2.4	9.9	14.3	1.93
pWT[a]	1.50	60.3 ± 0.0	5.11	164.4 ± 4.0	10.0	14.4	1.93
pWT[a]	2.99	61.3 ± 0.0	5.10	178.5 ± 1.4	10.4	15.3	2.01
pWT[a]	3.00	61.9 ± 0.0	3.93	183.3 ± 1.9	10.8	15.8	2.04
AVG[c]	**n/a**	**n/a**	**3.48 ± 0.5**	**n/a**	**10.6 ± 0.4**	**15.6 ± 0.5**	**n/a**
A4S	0.06	44.7 ± 0.1	2.81	132.2 ± 5.8	5.1	10.6	1.98
A4S	0.13	45.8 ± 0.4	1.67	156.3 ± 11.6	4.7	11.1	2.16
A4S	0.19	46.0 ± 0.3	2.85	140.8 ± 8.1	4.9	10.5	2.04
A4S	0.57	47.8 ± 0.0	2.53	155.4 ± 0.9	4.9	10.9	2.15
A4S	0.63	48.3 ± 0.0	4.45	159.0 ± 1.0	5.0	11.2	2.18
AVG[c]	**n/a**	**n/a**	**2.86 ± 0.88**	**n/a**	**4.9 ± 0.1**	**10.9 ± 0.3**	**n/a**
A4T	0.08	40.6 ± 0.2	6.77	76.0 ± 6.0	4.7	8.3	1.77
A4T	0.18	42.9 ± 0.1	3.98	116.3 ± 5.7	3.9	9.0	2.18
A4T	0.20	43.0 ± 0.4	1.20	127.7 ± 18.9	3.6	9.2	2.29
A4T	0.50	44.2 ± 0.3	2.34	133.9 ± 9.4	3.5	9.1	2.36
A4T	1.00	45.9 ± 0.1	2.94	145.7 ± 2.1	3.7	9.6	2.48
AVG[c]	**n/a**	**n/a**	**3.45 ± 1.85**	**n/a**	**3.7 ± 0.5**	**9.2 ± 0.5**	**n/a**
A4V	0.20	48.8 ± 1.6	-0.22	81.5 ± 17.2	6.6	9.2	1.43
A4V	0.30	48.5 ± 0.1	1.73	82.4 ± 1.9	6.3	9.0	1.43
A4V	0.40	49.3 ± 0.1	0.54	86.7 ± 3.5	6.3	9.0	1.46
A4V	0.50	48.4 ± 0.1	2.50	77.5 ± 1.6	6.0	8.5	1.41
A4V[d]	0.52	48.2 ± 0.1	3.46	78.1 ± 2.5	5.9	8.4	1.41
A4V[e]	0.52	49.5 ± 0.2	1.24	80.1 ± 4.7	6.2	8.7	1.42
A4V	1.00	48.9 ± 0.2	2.21	93.9 ± 3.5	5.5	8.7	1.50
A4V	1.95	50.1 ± 0.0	1.88	120.6 ± 2.2	5.4	9.5	1.64
AVG[c]	**n/a**	**n/a**	**1.67 ± 0.80**	**n/a**	**6.0 ± 0.5**	**9.0 ± 0.4**	**n/a**
E100G	0.20	49.5 ± 0.0	1.82	184.7 ± 10.2	6.4	12.2	2.19

E100G	0.50	51.0 ± 0.0	2.18	163.6 ± 0.9	6.6	12.4	2.24
E100G	1.20	53.0 ± 0.0	2.40	156.9 ± 0.8	7.2	13.6	2.40
AVG[c]	**n/a**	**n/a**	**2.13 ± 0.30**	**n/a**	**6.7 ± 0.4**	**12.8 ± 0.8**	**n/a**
G37R	0.11	48.5 ± 0.1	3.01	168.6 ± 2.5	6.2	12.7	2.12
G37R	0.24	49.5 ± 0.0	2.64	171.3 ± 1.5	6.2	12.7	2.14
G37R	0.40	51.2 ± 0.0	3.81	173.5 ± 0.4	6.8	13.1	2.16
G37R	0.98	51.1 ± 0.0	3.59	180.8 ± 1.0	6.2	12.8	2.21
G37R	1.92	52.2 ± 0.0	3.16	182.9 ± 0.5	6.3	12.9	2.22
AVG[c]	**n/a**	**n/a**	**3.25 ± 0.47**	**n/a**	**6.4 ± 0.3**	**12.8 ± 0.2**	**n/a**
G93A[a]	0.10	45.6 ± 0.2	2.99	119.8 ± 8.3	5.4	10.2	1.96
G93A[a]	0.12	46.6 ± 0.1	3.60	123.1 ± 8.3	5.6	10.4	1.99
G93A[a]	0.50	49.1 ± 0.2	3.81	148.2 ± 5.0	5.6	11.1	2.18
G93A[a]	0.50	49.0 ± 0.0	2.77	150.3 ± 2.4	5.5	11.2	2.20
G93A[a]	0.50	49.0 ± 0.0	3.82	147.2 ± 0.9	5.6	11.1	2.18
G93A[a]	0.50	48.0 ± 0.0	3.92	138.1 ± 2.1	5.2	10.4	2.10
G93A[a]	1.00	49.1 ± 0.1	3.25	149.7 ± 2.1	5.1	10.8	2.19
AVG[c]	**n/a**	**n/a**	**3.53 ± 0.44**	**n/a**	**5.4 ± 0.2**	**10.7 ± 0.3**	**n/a**
G93R[a]	0.21	47.0 ± 0.1	6.14	115.4 ± 3.7	5.5	9.9	2.39*
G93R[a]	0.21	47.3 ± 0.0	5.73	123.7 ± 2.7	5.6	10.3	2.50*
G93R[a]	0.40	48.7 ± 0.0	4.36	144.0 ± 2.4	5.6	11.0	2.74*
AVG[c]	**n/a**	**n/a**	**5.39 ± 0.97**	**n/a**	**5.6 ± 0.0**	**10.4 ± 0.5**	**n/a**
G93S[a]	0.25	49.6 ± 0.1	2.60	146.4 ± 7.8	6.3	11.6	2.80*
G93S[a]	0.29	50.0 ± 0.0	3.48	149.8 ± 4.1	6.4	11.8	2.84*
G93S[a]	0.40	50.8 ± 0.0	2.13	158.6 ± 2.5	6.5	12.2	2.94*
AVG[c]	**n/a**	**n/a**	**2.74 ± 0.69**	**n/a**	**6.4 ± 0.1**	**11.9 ± 0.3**	**n/a**
H43R	0.21	46.9 ± 0.1	3.60	123.1 ± 2.5	5.5	10.2	2.12*
H43R	0.23	47.3 ± 0.0	2.80	120.6 ± 2.0	5.6	10.2	2.10*
H43R	0.39	48.1 ± 0.0	3.07	128.8 ± 1.7	5.5	10.3	2.18*
AVG[c]	**n/a**	**n/a**	**3.16 ± 0.46**	**n/a**	**5.5 ± 0.1**	**10.2 ± 0.1**	**n/a**
H46R	0.08	60.4 ± 0.3	4.81	90.0 ± 11.4	9.9	11.0	1.17
H46R	0.17	60.9 ± 0.1	2.56	107.8 ± 2.0	10.0	11.8	1.21
H46R	0.32	61.2 ± 0.0	3.31	120.2 ± 2.1	10.0	12.4	1.23
H46R	0.39	61.0 ± 0.0	0.74	128.6 ± 2.1	10.1	12.9	1.25
H46R	0.76	61.1 ± 0.0	5.18	139.2 ± 1.8	9.8	12.5	1.27
AVG[c]	**n/a**	**n/a**	**3.32 ± 1.57**	**n/a**	**10.0 ± 0.1**	**12.1 ± 0.7**	**n/a**
I113T	0.08	43.4 ± 0.5	4.91	68.7 ± 16.8	5.8	8.7	1.53
I113T[c]	0.10	45.3 ± 1.0	1.86	105.3 ± 18.1	5.6	9.8	1.82
I113T	0.15	44.9 ± 0.4	3.03	94.4 ± 9.0	5.4	9.1	1.73
I113T	0.21	45.0 ± 0.2	4.17	110.2 ± 5.8	4.9	9.3	1.85
I113T[b]	0.40	46.0 ± 0.1	2.44	106.2 ± 4.0	4.9	9.1	1.82
I113T[b]	0.50	47.1 ± 0.1	2.79	129.0 ± 4.1	4.9	9.9	2.00
I113T[b]	0.75	46.4 ± 0.1	4.75	118.0 ± 3.9	4.5	9.1	1.91
I113T	1.20	47.8 ± 0.0	3.35	138.5 ± 2.0	4.6	9.9	2.07
AVG[c]	**n/a**	**n/a**	**3.41 ± 0.76**	**n/a**	**4.8 ± 0.3**	**9.6 ± 0.5**	**n/a**
V148G	0.12	46.1 ± 0.2	5.55	76.6 ± 5.6	6.2	9.0	0.71

V148G	0.23	48.3 ± 0.1	1.26	89.1 ± 0.7	6.3	9.3	0.59
V148G	0.29	49.8 ± 0.0	-2.00	104.6 ± 2.0	6.6	10.0	0.64
V148G	0.53	48.2 ± 0.0	0.07	91.5 ± 2.1	5.8	8.9	0.66
V148G	0.92	46.8 ± 0.0	2.47	81.7 ± 2.9	5.1	8.0	0.73
V148G	1.56	47.8 ± 0.3	-2.44	99.0 ± 1.0	4.8	8.4	0.70
AVG[c]	**n/a**	**n/a**	**0.82 ± 3.0**	**n/a**	**5.6 ± 0.7**	**8.8 ± 0.5**	**n/a**
V148I	0.11	57.7 ± 0.1	6.67	108.8 ± 6.7	9.6	12.0	1.56
V148I	0.26	59.2 ± 0.1	3.01	137.7 ± 3.0	10.1	13.5	1.71
V148I	0.49	59.6 ± 0.1	6.37	141.4 ± 5.9	9.9	13.4	1.73
V148I	0.53	59.6 ± 0.0	3.75	152.1 ± 1.7	10.1	14.1	1.78
V148I	0.83	60.3 ± 0.0	3.38	166.9 ± 1.8	10.5	15.0	1.86
V148I	2.33	61.2 ± 0.0	3.99	182.6 ± 1.1	10.6	15.7	1.94
AVG[c]	**n/a**	**n/a**	**4.53 ± 1.58**	**n/a**	**10.1 ± 0.4**	**13.9 ± 1.3**	**n/a**

n/a = not applicable.

Unless otherwise specified, all data were obtained at a scan rate of 1.0 °C minute^{-1}. Data for individual scans were fit to Eq. 3.1 as described in Materials and Methods.

[a]Data reported previously (128).

[b]Data reported previously (134).

[c]Values are averages and standard deviations calculated using thermograms with $n \sim 2$ or more.

[d] Scan rate of 0.75 °C minute^{-1}.

[e] Scan rate was 1.5 °C minute^{-1}.

[f] Error estimates for individual thermograms are from the fitting program.

[g]Uncertainties were estimated from the standard deviations in the values obtained from the individual thermograms.

[h]t_{avg} is 51.2 °C, the average value of $t_{0.5}$ for all apo SOD1 variants.

[i]Molecularity values determined using Eq. 3.2 and Figure S3.1, as described in Materials and Methods.

*Molecularity values are determined from the slope of a line with only three data points, and thus have a high level of uncertainty.

Unpublished experiments were performed and the data analyzed by Helen R. Broom, Kenrick A. Vassall, Jessica A. O. Rumfeldt, Ming Sze Tong, and Julia M. Bonner.

3.3.3 ITC reveals that all mutations decrease the stability of the apo dimer interface.

ITC was used to determine the thermodynamics of dimer dissociation, providing values for $\Delta H_{N_2 \leftrightarrow 2M}$, $K_{d,N_2 \leftrightarrow 2M}$, and corresponding $\Delta G_{N_2 \leftrightarrow 2M}$. In this chapter the ITC results have been combined with the DSC results, and so pertinent points from the ITC analyses will be summarized here before continuing with the combined analyses in the following sections. While the effects of mutations on total stability range from highly destabilizing to moderately stabilizing, ITC experiments reveal that all mutations weaken the dimer interface (Chapter 2). ITC was also used to determine the temperature dependence of $\Delta H_{N_2 \leftrightarrow 2M}$, $\Delta C_{p,N_2 \leftrightarrow 2M}$, and both the magnitude of $\Delta H_{N_2 \leftrightarrow 2M}$ and $\Delta C_{p,N_2 \leftrightarrow 2M}$ were shown to be much higher than predictions based on surface area exposure upon dissociation would suggest (217, 218) (Chapter 2). The $\Delta C_{p,N_2 \leftrightarrow 2M}$ and $\Delta C_{p,M \leftrightarrow U}$ were found to be similar, 1.7 ± 0.2 and 1.6 ± 0.8 kcal (mol dimer)$^{-1}$ °C^{-1}, respectively, suggesting that there is considerable structural rearrangement upon dimer dissociation. This interpretation is supported by the solution structure of the apo monomer variant, which contains mutations in the dimer interface that prevent dimerization. This construct shows high levels of disorder in one half of the β-barrel and the largest loops (IV and VII, ~35 % of the sequence), and adopts what is referred to as an "open clam" structure (222). Chemical denaturation as a function of temperature under equilibrium and kinetic conditions has been performed on the apo monomer variant. From these experiments the $\Delta C_{p,M \leftrightarrow U}$ was found to be even higher than what we have reported, 2.27 ± 0.69 kcal (mol dimer)$^{-1}$ °C^{-1} (251). In this method, the $\Delta G_{M \leftrightarrow U}$ versus *t* curve obtained from these experiments was fit to a modified Gibbs-Helmholtz equation to extract $\Delta H_{M \leftrightarrow U}$ and $\Delta C_{p,M \leftrightarrow U}$. This approach will result in larger uncertainties in these parameters compared to the direct measurements reported herein.

Differences between the two $\Delta C_{p,M\leftrightarrow U}$ values may also be related to the effects of the added dimer interface mutations in the monomer variant construct used for comparison.

Furthermore, our values for ΔC_p are consistent with chemical denaturation experiments, where the denaturant dependence of $\Delta G_{N_2\leftrightarrow 2M}$ and $\Delta G_{M\leftrightarrow U}$, also related to changes in exposed surface area, was determined to be 2.7 and 2.6 kcal (mol dimer)$^{-1}$, respectively (134). Addition of a stabilizing salt, Na_2SO_4, resulted in compaction of the monomer intermediate and an increase in the denaturant dependence of $\Delta G_{M\leftrightarrow U}$ from 2.6 to 3.5 kcal (mol dimer)$^{-1}$ (134). Thus, there is substantial evidence that dimer dissociation is accompanied by a considerable amount of structural disruption, accounting for the high value of $\Delta C_{p,N_2\leftrightarrow 2M}$.

3.3.4 Fitting to 3-state dimer with monomeric intermediate model

Given the evidence for non-2-state unfolding behavior in the DSC experiments (Fig. 3.3), and that ITC dilution experiments show measurable endothermic heats associated with dimer dissociation (Chapter 2, Fig. 2.2A), dimer dissociation and monomer unfolding appear decoupled quite prominently for a number of SOD1 variants, and to some extent for all variants at low protein concentrations. The DSC data for all apo SOD1 variants were, therefore, also fit to a bimolecular 3-state dimer unfolding model with a monomeric intermediate ($N_2\leftrightarrow 2M\leftrightarrow 2U$). Fitted data is shown in Fig. 3.4 and values obtained are summarized in Tables 3.2 and S3.1.

For comparison, DSC data for apo A4V, H46R, and V148G, which exhibited the most pronounced 3-state unfolding behavior, were also fit to a unimolecular 2-state monomer unfolding model ($M\leftrightarrow U$), which would be applicable if the transition temperatures for each step in the 3-state mechanism were very different and if the majority of the heat effects reflected monomer unfolding (250, 252). Fitting the DSC data for these three mutants to the 2-state

monomer unfolding model returned ΔH_{vH} values that increased significantly with protein concentration, a finding that is inconsistent with unimolecular 2-state monomer unfolding (237) (Supplementary Methods, Section 3.5.1.1 and Table S3.2). Thus, a 3-state model is more appropriate for describing apo unfolding.

Fitting apo DSC data to a 3-state model with monomer intermediate allows the thermodynamics of both dimer dissociation and monomer unfolding to be quantified (Figs. 3.4, 3.6, Table 3.2). In order to define the larger number of parameters in this model, all data for a given apo variant were fit simultaneously, fixing the parameters for dimer dissociation, $K_{d,N_2\leftrightarrow 2M}$ and $\Delta h_{cal,N_2\leftrightarrow 2M}$, at 37 °C, to the values measured by ITC (Table 2.1) and the values for ΔC_p to experimental values determined independently (Sections 3.2.4 and 3.3.3). To allow for uncertainties in the concentration of protein undergoing thermal unfolding due to protein concentration measurements (~10%) and possible presence of small amounts of aggregated protein (128), the β_1 and β_2 were set equal to each other and allowed to vary, as was done previously for the 2-state fits (128, 134). Thus, in fitting data to Eq. 3.3, the globally shared fitted parameters were T_2', $\Delta h_{cal,M\leftrightarrow U}(T_2')$, $\beta_1 = \beta_2$, and parameters defining the slope and intercept of the native baselines. The data for all mutants are generally well fit using this method (Fig. 3.4, Table 3.2). As a control, mutants with more than 3 datasets were also globally fit without constraints from the ITC data (i.e., with $\Delta h_{cal,N_2\leftrightarrow 2M}$ and $K_{d,N_2\leftrightarrow 2M}$ at 37 °C also globally shared) and β_1 and β_2 fixed to the molecular weight of the dimer. Using this method, the uncertainty in all values increased substantially. Nevertheless, $K_{d,N_2\leftrightarrow 2M}$, and thus $\Delta G_{N_2\leftrightarrow 2M}$, values converged to those obtained by ITC (Table S3.1). The agreement between fitted and experimentally determined $\Delta h_{cal,N_2\leftrightarrow 2M}$ and $K_{d,N_2\leftrightarrow 2M}$ is particularly good for the few cases (I113T, A4V, and

V148G.) where this latter method resulted in low uncertainty in the fitted values. Thus, our approach of fixing parameters defining dimer dissociation to those obtained by ITC is valid.

In addition, a number of extra measures were used to assess the uncertainty in monomer stability as well as total protein stability. In general, mutations have been found to have little effect on the ΔC_p of global protein unfolding ($\Delta C_{p,N_2 \leftrightarrow 2U}$) (128, 219, 240, 241). Similarly, ITC experiments show that the ΔC_p of dimer dissociation, $\Delta C_{p,N_2 \leftrightarrow 2M}$, varies little upon mutation of SOD1 (Chapter 2, Fig. 2.3A). Highly non-conservative substitutions at buried positions of hydrophobic residues by hydrophilic residues or vice versa have, however, been reported to change ΔC_p by up to ~40% (253), and for one SOD1 variant, V148G, the $\Delta C_{p,N_2 \leftrightarrow 2M}$ was found to be slightly larger than the values obtained for the three other mutants analyzed (Chapter 2, Fig. 2.3). Because the $\Delta C_{p,N_2 \leftrightarrow 2M}$ could not be measured for all SOD1 variants, the data were also fit with the maximum $\Delta C_{p,N_2 \leftrightarrow 2M}$ obtained (2.2 kcal (mol dimer)$^{-1}$ °C^{-1}), corresponding to the estimated upper limits of mutational effects, to evaluate how changes in ΔC_p impact monomer stability. Increasing $\Delta C_{p,N_2 \leftrightarrow 2M}$ by ~0.6 kcal (mol dimer)$^{-1}$ °C^{-1} had small effects on $\Delta G_{M \leftrightarrow U}$ determined at t_{avg} (on average ±0.1 kcal (mol monomer)$^{-1}$) and at 37 °C (on average ±0.2 kcal (mol monomer)$^{-1}$). Because dimer stability was determined at 37 °C, changes in $\Delta C_{p,N_2 \leftrightarrow 2M}$ had no effect on $\Delta G_{N_2 \leftrightarrow 2M}$ (37 °C), but decreased $G_{N_2 \leftrightarrow 2M}$ (t_{avg}) by 0.2 kcal (mol dimer)$^{-1}$. Thus, for 3-state fitting of DSC data it is reasonable to treat ΔC_p as a constant, and changes appear to have no significant impact on monomer stability.

The effects of aggregation at high temperature on $\Delta G_{N_2 \leftrightarrow 2U}$ were assessed by fitting varying amounts of data beyond the peak of the unfolding endotherm, from a maximum of the apparent end of the endotherm peak to a minimum of ~25% of the decreasing side of the

endotherm. In the dimer 2-state fits, where $\Delta C_{p,N_2 \leftrightarrow 2U}$ is calculated from floating parameters that define the native and unfolded baselines, fitting the whole endotherm, including the post-transition baseline can result in systematically low or negative $\Delta C_{p,N_2 \leftrightarrow 2U}$ values. However, fitting various amounts of the endotherm to the 3-state model has very little impact on total stability, ±0.5-1.0 kcal (mol dimer)$^{-1}$ at 37 °C and ±0.2-0.4 kcal (mol dimer^{-1}) at t_{avg}. Furthermore, similar stability values were obtained when ΔH_{vH} and ΔH_{cal} were set equal to each other (Table S3.1). Based on these observations, effects of aggregation can be eliminated by excluding the high temperature data from the fit, and so aggregation at high temperature has little effect on measured stability. The agreement between the DSC and ITC, as well as DSC and urea denaturation (*vide infra*), further supports the validity of our data fitting method (Tables 3.2, 3.3).

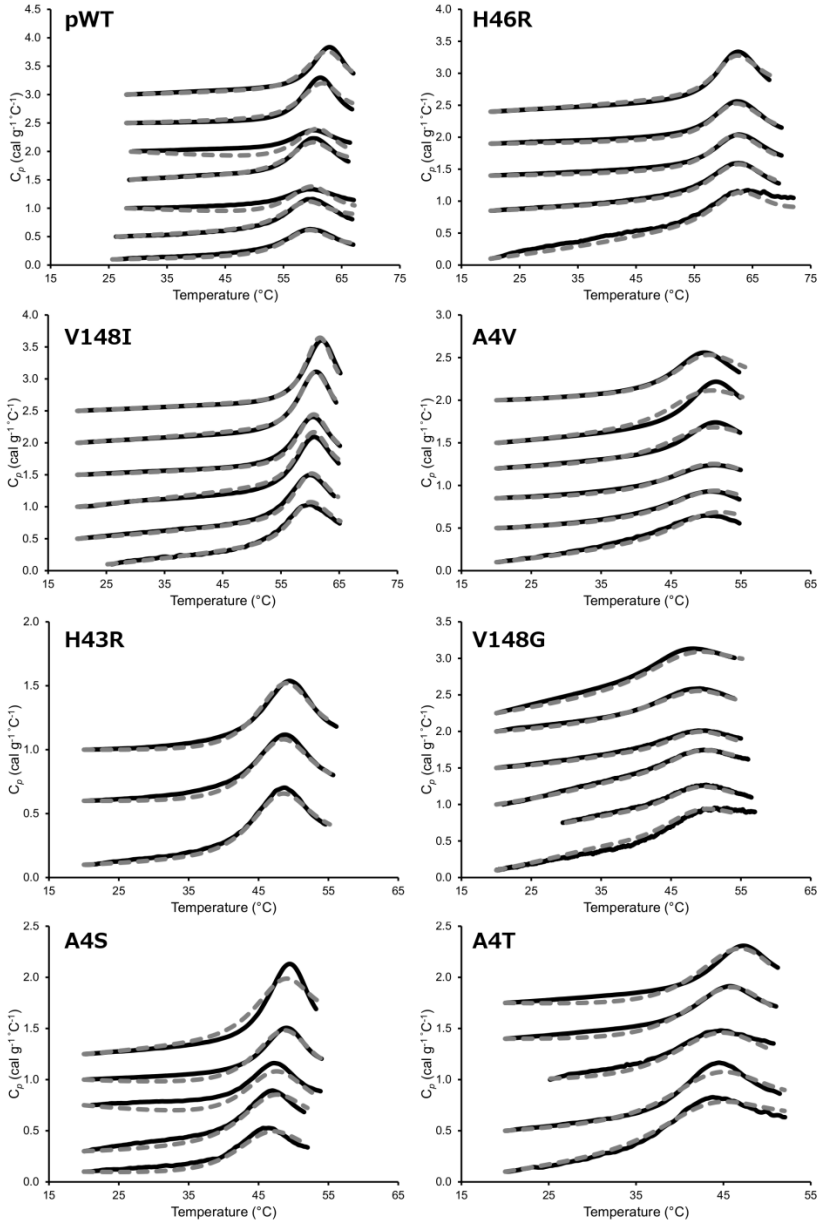

Figure 3.4 Global fitting of apo SOD1 DSC data to the 3-state model. Representative global fits of thermograms to the dimer 3-state with monomer intermediate model are shown. The black solid lines represent the data, while the grey dashed lines correspond to the fit. In each panel, scans at different protein concentrations are offset for clarity, with low concentrations at the bottom and high at the top. The protein concentrations for each experiment are listed in Table 3.1, and the parameters obtained from the global fits of all mutants are summarized in Tables 3.2 and S3.1.

Table 3.2 Summary of thermodynamic parameters for apo SOD1 determined from global 3-state fits of DSC data.

SOD1 variant[a]	$\Delta H_{N_2 \leftrightarrow 2M}$ (kcal (mol dimer)$^{-1}$) 37 °C[b]	$\Delta G_{N_2 \leftrightarrow 2M}$ (kcal (mol dimer)$^{-1}$) 37 °C[b]	$t_{0.5,\, M \leftrightarrow U}$ (°C)[c]	$\Delta H_{M \leftrightarrow U}$ (kcal (mol monomer)$^{-1}$) t_{avg}[c,d]	$\Delta G_{M \leftrightarrow U}$ (kcal (mol monomer)$^{-1}$) 37 °C[e,f]	$\Delta G_{M \leftrightarrow U}$ (kcal (mol monomer)$^{-1}$) t_{avg}[d, f]	$\Delta\Delta G_{M \leftrightarrow U}$ (kcal (mol monomer)$^{-1}$) t_{avg}[d,g]
pWT[c,h]	n/a	10.2 ± 0.7	n/a	n/a	3.4 ± 0.5	n/a	n/a
pWT	(30.8 ± 8.8)	(10.3 ± 0.5)	59.5 ± 0.9	44.0 ± 2.0	2.8 ± 0.6	1.2 ± 0.4	n/a
V148I	(11.4 ± 2.2)	(8.9 ± 0.2)	60.1 ± 0.2	84.0 ± 1.2	5.7 ± 0.8	2.3 ± 0.4	-1.2
G93S	(17.6 ± 4.6)	(8.4 ± 0.3)	49.2 ± 1.1	58.3 ± 3.7	2.0 ± 0.3	-0.4 ± 0.2	1.5
H46R	(16.2 ± 4.4)	(8.4 ± 0.4)	62.5 ± 0.1	71.2 ± 1.1	5.3 ± 0.4	2.6 ± 0.2	-1.4
E100G	(16.0 ± 4.8)	(8.0 ± 0.4)	48.0 ± 0.7	53.3 ± 8.4	1.6 ± 0.3	-0.5 ± 0.1	1.7
G37R	(7.8 ± 1.8)	(7.6 ± 0.2)	50.3 ± 0.1	84.1 ± 2.8	3.2 ± 0.8	-0.2 ± 0.0	1.4
H43R	(23.0 ± 1.4)	(7.5 ± 0.0)	47.6 ± 0.4	59.5 ± 5.2	1.7 ± 0.1	-0.7 ± 0.0	1.8
G93A	(14.0 ± 2.0)	(7.2 ± 0.3)	47.4 ± 0.3	58.9 ± 4.7	1.7 ± 0.1	-0.7 ± 0.1	1.9
I113T	(30.2 ± 2.5)	(7.1 ± 0.2)	46.7 ± 0.2	53.2 ± 3.7	1.4 ± 0.2	-0.7 ± 0.1	1.9
A4T	(39.2 ± 3.8)	(7.1 ± 0.2)	43.6 ± 0.4	48.9 ± 9.6	0.8 ± 0.3	-1.1 ± 0.1	2.3
A4S	(9.0 ± 2.6)	(7.0 ± 0.0)	46.3 ± 0.4	61.1 ± 10.0	1.5 ± 0.3	-0.9 ± 0.2	2.1
G93R	(45.6 ± 1.8)	(6.7 ± 0.1)	49.1 ± 0.2	87.8 ± 7.7	3.1 ± 0.1	-0.6 ± 0.0	1.7
A4V	(37.2 ± 3.8)	(6.4 ± 0.3)	50.9 ± 0.2	59.2 ± 3.4	2.3 ± 0.1	-0.1 ± 0.1	1.2
V148G	(50.6 ± 1.4)	(5.9 ± 0.3)	48.6 ± 0.0	67.8 ± 0.5	2.2 ± 0.1	-0.5 ± 0.0	1.7

[a]For each mutant, the scans at different protein concentrations used in the global fitting are those listed in Table 3.1, with the exception of pWT, where concentrations 0.20, 0.21, 0.40, 0.44, 0.85, 1.50, and 3.0 were fit; I113T where concentration 0.21 mg mL^{-1} was omitted; A4V where concentration 0.52 mg mL^{-1} was omitted; and G93R mg mL^{-1} where concentration 0.21 was omitted.

[b]Numbers in the brackets were determined by ITC (Table 2.1) and fixed in the DSC 3-state fits.

[c]Errors determined from the fit.

[d]t_{avg} is 51.2 °C, the average of all $t_{0.5}$ values obtained from the 2-state fits.

[e]$\Delta G_{M \leftrightarrow U}$ values calculated at physiological temperature.

[f]Error estimates were determined from the differences in values obtained from fits allowing $\Delta H_{vH}/\Delta H_{cal}$ to deviate from unity, compared to values obtained when ΔH_{vH} and ΔH_{cal} were set equal, and values obtained using a higher $\Delta C_{p,N_2 \leftrightarrow 2M}$ (2.2 kcal (mol dimer)$^{-1}$ °C^{-1}) (Table S3.1).

[g]$\Delta\Delta G = \Delta G_{pWT} - \Delta G_{mutant}$, a positive value indicates lower stability of the mutant relative to pWT; values are calculated at t_{avg}.

[h]$\Delta G_{N_2 \leftrightarrow 2M}$ and $\Delta G_{M \leftrightarrow U}$ were also determined by globally fitting urea denaturation curves at 37 °C to a 3-state model with monomeric intermediate.

3.3.5 Equilibrium urea denaturation at 37 ℃ of apo pWT

In order to obtain an independent measure of stability, urea denaturation curves were determined for pWT at 37 °C as a function of protein concentration (Fig. 3.5). We have used this approach previously for pWT at 25 °C to measure the total stability, $\Delta G_{N_2 \leftrightarrow 2U}$, dissected into constituent $\Delta G_{N_2 \leftrightarrow 2M}$ and monomer stability, $\Delta G_{M \leftrightarrow U}$; similar analyses cannot be performed for mutants, however, owing to their lower stability (134). The values of stability measured for pWT at 37 °C (Table 3.2) are consistent with values obtained previously by chemical denaturation at lower temperatures (134, 147, 177, 254), and with values determined at 37 °C by calorimetry (Tables 3.2, 3.3, S3.1). The dimer interface stability is weakened at increased temperature, resulting in significant population of monomer at physiologically relevant temperature and pH (*vide infra*).

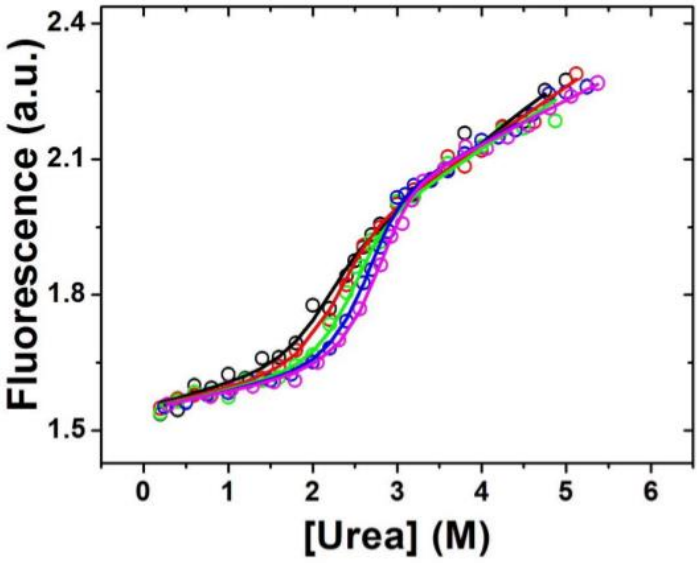

Figure 3.5 Equilibrium denaturation of apo pWT. Equilibrium urea denaturation curves for apo pWT at dimer concentrations of 25 μM (pink circles), 10 μM (blue circles), 3 μM (green circles), 0.8 μM (red circles), and 0.2 μM (black circles). Fluorescence data are scaled to aid comparison. Solution conditions were 37 °C, 1 mM EDTA, 20 mM HEPES, pH 7.8. Solid lines represent the global fit of all protein concentrations using the fluorescence value of the intermediate set to 30% of the total amplitude of the transition (see Materials and Methods) with fitted values of $\Delta G_{N_2 \leftrightarrow 2M}$, $\Delta G_{M \leftrightarrow U}$, $m_{N_2 \leftrightarrow 2M}$, and $m_{M \leftrightarrow U}$ of 10.2 ± 0.7 kcal (mol dimer)$^{-1}$, 3.4 ± 0.4 kcal (mol monomer)$^{-1}$, 0.4 ± 0.4 kcal (mol dimer)$^{-1}$ (M urea)$^{-1}$, and 1.8 ± 0.2 kcal (mol monomer)$^{-1}$ (M urea)$^{-1}$, respectively. Changing the fluorescence of the intermediate from 10% to 50% of the total amplitude changes the values of $\Delta G_{N_2 \leftrightarrow 2M}$, $\Delta G_{M \leftrightarrow U}$, $m_{N_2 \leftrightarrow 2M}$ and $m_{M \leftrightarrow U}$ by ± 1.0 kcal (mol dimer)$^{-1}$, ± 0.1 kcal (mol monomer)$^{-1}$, ± 0.41 kcal (mol dimer)$^{-1}$ M^{-1}, and ± 0.1 kcal (mol monomer)$^{-1}$ M^{-1}, respectively. Experiments were performed and data analyzed by Jessica A. O. Rumfeldt.

3.3.6 Comparing monomer, dimer and total stabilities of apo SOD1 determined from 2-state and 3-state fitting

Total protein stability and the constituent dimer and monomer stabilities obtained from the 3-state fits were compared to values for total stability obtained from the dimer 2-state fits at the t_{avg} (Fig. 3.6A) and at physiological temperature (37 °C), and these results are summarized in Table 3.3. For total unfolding, generally $\Delta G_{N_2 \leftrightarrow 2U}$ values for the 2-state fits with *n* values of ~2 are similar to the values of $\Delta G_{N_2 \leftrightarrow 2M \leftrightarrow 2U}$ from the global 3-state fits (Fig. 3.6A, Table 3.3). This agreement between the 2-state and 3-state fits indicates that there is relatively little formation of monomer for pWT, A4S, A4T, E100G, G37R, G93S, G93A, H43R, and I113T and that 2-state fitting gives a reasonably accurate measure of stability (Fig. 3.6A). The advantage of 3-state fitting though, even for apo variants that form low levels of monomer, is that the data can be used to dissect total stability into constituent dimer interface and monomer stabilities (Tables 3.2, 3.3) and this method returns values for monomer stability that are consistent with previous measurements (Table 3.2) (176, 177, 188). When the population of monomer is significant, as occurs when including DSC data at lower protein concentrations or when mutations either highly weaken the dimer interface (A4V, G93R, and V148G) or increase monomer stability (H46R and V148I), larger discrepancies in the stability determined by the dimer 2-state and 3-state fits are evident (Fig. 3.6A). In these cases, fitting the data to a 2-state model will give inaccurate values.

The total stabilities determined from the 3-state fits of the different apo SOD1 mutants vary greatly. All the apo SOD1 mutants are destabilized relative to pWT, with total $\Delta\Delta G_{N_2 \leftrightarrow 2M \leftrightarrow 2U}$ values on the order of ~4.3 to 8.9 kcal (mol dimer)$^{-1}$, except for H46R and V148I, which are stabilized by 1.5 and 1.9 kcal (mol dimer)$^{-1}$ (Table 3.3). The contributions of dimer interface and monomer stability to overall changes in stability also vary markedly. All the

mutations weaken dimerization, although to different extents (Chapter 2, Fig. 2.2), while the effects on monomer stability range from being significantly stabilizing for H46R and V148I to slightly or significantly destabilizing for the other mutants (Table 3.2). Except for H46R and V148I, the destabilizing effects of mutations on monomer stability are relatively high, from ~1.5 to 2.3 kcal (mol monomer)$^{-1}$. The molecular origin of the altered monomer stabilities likely varies considerably among the mutants. The low monomer stability of H43R, G37R, the G93 mutants, and E100G may be related to significant disruptions in beta sheet packing (255, 256), while for the dimer interface mutants A4S, T and V, and I113T, the low monomer stability could be the result of a combination of unfavorable burial of the polar moieties of serine and threonine into the hydrophobic core of the protein and steric effects (Fig. 3.1). The other dimer interface mutations, V148G and V148I, have very different effects on monomer stability. For the former, monomer stability is decreased, potentially owing to a loss of stabilizing interactions when valine is truncated to a glycine; while for the latter, the monomer is stabilized relative to pWT, which could be due to additional favourable hydrophobic interactions. The increased stability for H46R relative to pWT is reminiscent of the stabilizing effects of mutations in functional residues within active sites of other proteins (257). In the crystal structure of apo H46R (138), the guanidinium group of the arginine lies within the copper binding site and may stabilize the apo protein by mimicking, to some extent, the stabilizing effect of copper binding.

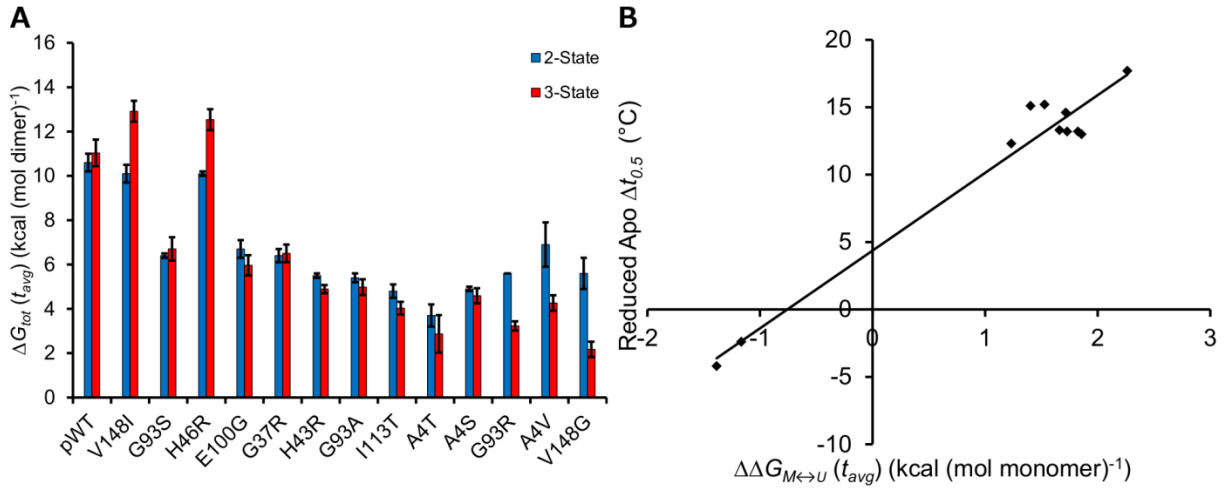

Figure 3.6 Comparing stabilities obtained from 3-state fitting of apo SOD1 variants. (A) Total stability at t_{avg} determined from 2-state (blue bars) and 3-state (red bars) fits of DSC data (Table 3.1 and Table 3.3). Errors bars for total stability determined from 2-state fits are the standard deviation of multiple experiments at different protein concentrations (Table 3.1). Error bars for total stability obtained from the 3-state fits were determined from the uncertainty in dimer interface stability, as determined by the standard deviation of multiple ITC experiments and monomer stability, as determined by different approaches to 3-state fitting (Table 3.2). **(B)** Changes in monomer stability upon mutation are highly correlated (R=0.98) with changes in the $t_{0.5}$'s of the disulfide reduced apo form of the protein. Therefore, 3-state fitting returns reasonable values for $\Delta G_{M\leftrightarrow U}$. Disulfide reduction has a large effect on the stability of the apo dimer interface, and thus this form of the protein is monomeric under physiological conditions. Limited stability data are available for reduced apo SOD1, owing to the irreversibility of unfolding for a number of mutations, but the $\Delta t_{0.5}$'s are a good indicator of the destabilizing effects of mutations (Chapter 4) (174).

Table 3.3 Comparisons of global stability determined from dimer 2-state and 3-state fits of apo SOD1.

SOD1 variant	$\Delta G_{N_2 \leftrightarrow 2U}$ (kcal (mol dimer)$^{-1}$) 37 °C[a]	$\Delta G_{N_2 \leftrightarrow 2U}$ (kcal (mol dimer)$^{-1}$) t_{avg} °C[a]	$\Delta G_{N_2 \leftrightarrow 2M \leftrightarrow 2U}$ (kcal (mol dimer)$^{-1}$) 37 °C[b]	$\Delta G_{N_2 \leftrightarrow 2M \leftrightarrow 2U}$ (kcal (mol dimer)$^{-1}$) t_{avg} °C[b]	$\Delta\Delta G_{N_2 \leftrightarrow 2U}$ (kcal (mol dimer)$^{-1}$) t_{avg} °C[c]	$\Delta\Delta G_{N_2 \leftrightarrow 2M \leftrightarrow 2U}$ (kcal (mol dimer)$^{-1}$) t_{avg} °C[c]
pWT[d]	n/a	n/a	17.0 ± 1.2	n/a	n/a	n/a
pWT	15.6 ± 0.5	10.6 ± 0.4	15.8 ± 1.3	11.0 ± 1.3	n/a	n/a
V148I	13.9 ± 1.3	10.1 ± 0.4	20.2 ± 1.6	12.9 ± 1.0	0.5	-1.9
G93S	11.9 ± 0.3	6.4 ± 0.1	12.3 ± 0.7	6.7 ± 0.7	4.2	4.3
H46R	12.1 ± 0.7	10.1 ± 0.1	18.9 ± 0.9	12.5 ± 0.8	0.5	-1.5
E100G	12.8 ± 0.2	6.7 ± 0.4	11.1 ± 0.7	6.0 ± 0.6	3.9	5.1
G37R	12.8 ± 0.2	6.4 ± 0.3	13.9 ± 1.6	6.5 ± 0.2	4.2	4.5
H43R	10.2 ± 0.1	5.5 ± 0.1	18.9 ± 0.2	4.9 ± 0.0	5.1	6.1
G93A	10.7 ± 0.4	5.4 ± 0.2	10.5 ± 0.4	5.0 ± 0.5	5.2	6.1
I113T	9.6 ± 0.5	4.8 ± 0.3	9.8 ± 0.4	4.0 ± 0.4	5.8	7.0
A4T	9.2 ± 0.5	3.7 ± 0.5	8.7 ± 0.6	2.9 ± 0.4	6.9	8.2
A4S	10.9 ± 0.3	4.9 ± 0.1	10.1 ± 0.6	4.6 ± 0.4	5.7	6.7
G93R	10.4 ± 0.5	5.6 ± 0.0	12.8 ± 0.2	3.2 ± 0.1	5.0	7.8
A4V	9.0 ± 0.4	6.0 ± 0.5	10.9 ± 0.4	4.3 ± 0.5	4.6	6.8
V148G	8.8 ± 0.5	5.6 ± 0.7	10.2 ± 0.4	2.2 ± 0.3	5.0	8.9

n/a = not applicable.

[a]Uncertainties are the standard deviation of $\Delta G_{N2 \leftrightarrow 2U}$ values obtained from 2-state fits of the individual thermograms (Table 3.1).

[b]Uncertainties are calculated from uncertainties in dimer interface stability, determined by ITC, and monomer stability, determined by averaging the values obtained by various fitting methods (Tables 3.2, S3.1).

[c]$\Delta\Delta G = \Delta G_{pWT} - \Delta G_{mutant}$, a positive value indicates lower stability of the mutant relative to pWT; values are calculated at t_{avg}.

[d]$\Delta G_{N_2 \leftrightarrow 2M \leftrightarrow 2U} = \Delta G_{N_2 \leftrightarrow 2M} + 2\Delta G_{M \leftrightarrow U}$. $\Delta G_{N_2 \leftrightarrow 2M}$ and $\Delta G_{M \leftrightarrow U}$ were determined by globally fitting urea denaturation curves at 37 °C to a 3-state model with monomeric intermediate. Uncertainties are from the fitting program.

3.3.7 Populations of N_2, M, and U for apo SOD1 variants

With knowledge of the dimer interface and monomer stabilities for different apo variants (Table 3.2), the fractions of N_2, *M* and *U* can be calculated as a function of temperature for a given protein concentration (Fig. 3.6) (143, 173). It is noteworthy that folded monomer is not significantly populated for pWT (<2%) at physiologically relevant temperature (37 °C), pH, and protein concentration (~40 μM (212)). But, all of the mutants have markedly increased populations of folded monomer, ranging from 6% for V148I to 52% for V148G, and all but H46R and V148I have increased populations of unfolded monomer, ranging from 3% for V148G to 6% for A4T. These results are of interest because monomeric species have been implicated in giving rise to toxic aggregates (see Discussion).

Inspection of the populations of different species also provides insight into the different thermal unfolding mechanisms observed by DSC for the mutants. The differences are a consequence of the relative effects of mutations both on dimer dissociation and on monomer stability (Table 3.2). The observation of a monomer intermediate occurs when the dimer interface stability is low and/or the monomer stability is high. For example, V148G has the most destabilized dimer interface, whereas H46R has significantly increased monomer stability. Thus, for both of these mutants, there is a high population of monomer intermediate throughout the thermal unfolding transition (Fig. 3.7). Although the other mutants examined also show a weakened dimer interface, the corresponding monomer stabilities are also substantially decreased and consequently the monomer intermediate is not as highly populated in DSC scans.

Protein concentration also plays a role in the observation of monomer formation. The relatively high concentrations required for DSC experiments result in decreased population of monomeric intermediate (as a percentage of total protein) and apparent 2-state unfolding (Fig.

3.7). In contrast, monomer is more readily observed by ITC or chemical denaturation, both of which are typically performed at lower protein concentrations, which favour monomer formation (Chapter 2). Therefore, it is important to consider the interplay between the interface and monomer stabilities in addition to solution conditions such as protein concentration as these will influence the observation of intermediate states.

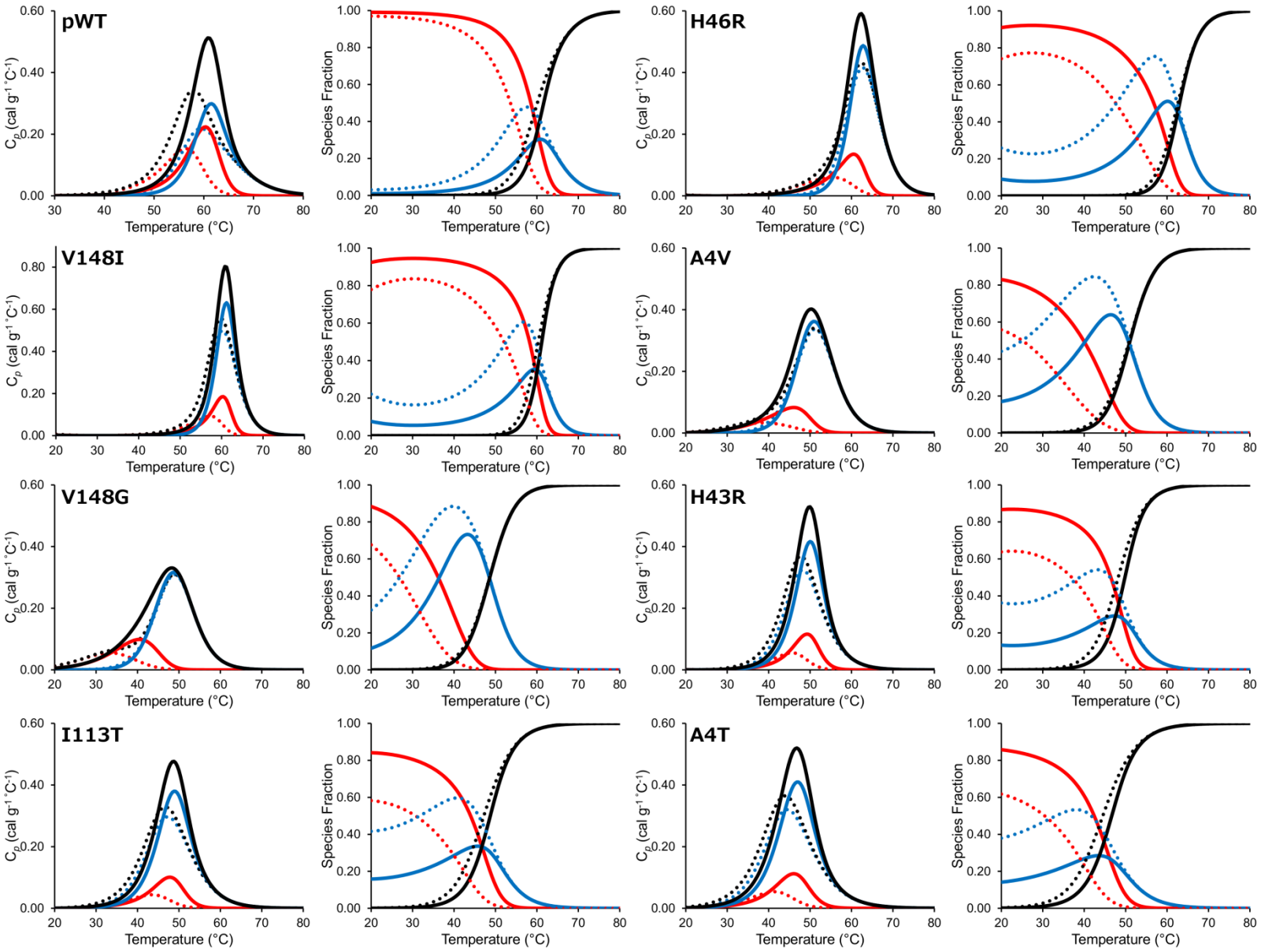
pWT
H46R
V148I
A4V
V148G
H43R
I113T
A4T
C_p (cal g^{-1} °C^{-1})
Species Fraction
Temperature (°C)

Figure 3.7 Fractional populations of N_2, M and U for apo SOD1 variants as a function of temperature. In the panels on the left side, the total excess heat of unfolding (black lines) is dissected into the contributions from dimer dissociation (red lines) and monomer unfolding (blue lines) at protein concentrations, 0.10 mg mL^{-1} (0.32 μM dimer) (dotted lines) and 1.0 mg mL^{-1} (32 μM dimer) (solid lines). In these panels, the folded and unfolded baselines are subtracted, leaving only the excess specific heat. In the panels on the right side, the populations of the N_2 (red lines), M (blue lines) and U (black lines) were calculated using the thermodynamic parameters obtained from fitting DSC data to a dimer 3-state model with monomeric intermediate with parameters for dimer dissociation determined by the ITC (Table 3.2, Materials and Methods). Solid lines represent the populations at total protein concentrations of 1.0 mg mL^{-1} (32 μM dimer), and dotted lines represent the populations at 0.10 mg mL^{-1} (0.32 μM dimer). As the temperature increases, the fraction of monomer increases, to varying extents, for all variants. 3-state unfolding behaviour is more readily detected when the transition from N_2 to M becomes well resolved from the transition from M to U. At 1.0 mg mL^{-1}, the maximal fraction of monomer is <0.3 for pWT, H43R, and A4T, consistent with measured n values at comparable protein concentrations for these variants (Table 3.1), indicating predominantly dimer 2-state unfolding behaviour. For mutants I113T and V148I, the maximal fraction of monomer is <0.4 at 1 mg mL^{-1}, and the corresponding n values are low for experiments done at lower protein concentrations. Thus, 3-state unfolding is more pronounced at lower protein concentrations. A4V, H46R, and V148G exhibit the most 3-state unfolding behavior, as these mutants show the highest maximal fraction of monomer at 1 mg mL^{-1} (>0.6) and the lowest n-values. At 0.10 mg mL^{-1}, the maximal fraction of monomer is >0.5 for all variants indicating predominately 3-state unfolding behavior at lower protein concentration.

3.4 Discussion

In this study, we have demonstrated a valuable new approach for characterizing ALS-associated apo SOD1 mutants by combining ITC, chemical denaturation and DSC to obtain thermodynamic analyses of total protein stability, as well as constituent dimer interface and monomer stabilities. Relatively few ITC studies have been performed on homodimeric proteins, and ITC has not previously been combined with DSC to dissect the components of total protein stability. Here we show how this can be done, and we validate our approach by comparison to chemical denaturation data.

ITC performed at physiological temperatures, where we find that dissociation is enhanced compared to lower temperatures, allows for accurate direct measurement of thermodynamic parameters ($\Delta H_{N2\leftrightarrow 2M}$ and $\Delta G_{N2\leftrightarrow 2M}$) (Chapter 2). Using ITC data to constrain 3-state global fits of DSC data obtained for a range of protein concentrations then enables more accurate determination of monomer stability and total protein stability when the monomer becomes highly populated during unfolding (Fig. 3.6A, Tables 3.2, 3.3). We find that calculations of molecularity for dimer 2-state fits of DSC scans provide a sensitive tool for monitoring monomer formation (Table 3.1), allowing for previously undetected monomer formation to be taken into account. Molecularity values also provide an explanation for increases in ΔH_{vH} with $t_{0.5}$ (Table 3.1), which should increase linearly with increases in $t_{0.5}$ but are larger than expected for a dimer 2-state model. This observation can be attributed to a shift from ΔH_{vH} values that are systematically low at low protein concentration, due to significant population of monomer, to higher values at higher protein concentrations that correspond to dimer unfolding (Table 3.1). The results reported here provide new insights into the molecular determinants of apo SOD1

folding, and the methods used should be broadly applicable to studying other oligomeric proteins.

3.4.1 Many ALS mutations enhance dimer dissociation of apo SOD1 but have differing effects on monomer stability

Direct analysis of dimer dissociation by ITC reveals that chemically and structurally diverse fALS-associated mutations promote the dissociation of apo SOD1 (Chapter 2). These results are particularly interesting because the effects of mutations on the integrity of the dimer interface cannot be predicted readily based on inspection of the different structural contexts of the mutations. Although the dimer interface mutations tend to have the largest deleterious effects, the consequences of mutations distant from the dimer interface propagate through the protein and weaken the interface.

Previous indirect kinetic and equilibrium analyses of apo SOD1 have been conducted to assess the effects of mutations on dimer interface and monomer stabilities. Together, these studies report similar trends to the results obtained here by calorimetry. Mutations H46R, E100G, H43R, G93A, I113T, G93R, A4V, and V148G all destabilize the dimer interface (134, 176, 177), although the $\Delta G_{N_2 \leftrightarrow 2M}$ of G93A was found to be very marginally increased relative to pWT in one study (177). Consistent with our ITC experiments, A4V and V148G had the largest destabilizing effects on the interface (176, 177); yet, the magnitude of these effects differ. Discrepancies between the different approaches may be due to differences in experimental conditions. Previous experiments were performed at relatively low temperatures (<25 °C) (134, 176, 177), where dissociation is less pronounced and mutational effects are smaller relative to the effects at 37 °C (Chapter 2). Compared to the direct measurements of $\Delta G_{N_2 \leftrightarrow 2M}$ at 37 °C by ITC,

these previous experiments have high uncertainties due to long extrapolations (176, 177, 200), and the assumption of invariance in the rate constant for dimer association (176, 200). The relative monomer stabilities of E100G, I113T, and G93R, determined by equilibrium denaturation at 25 °C, are, however, consistent with the relative monomer stabilities reported here (134), and the effects of mutations on monomer stability at t_{avg} are highly correlated with changes in $t_{0.5}$ of the reduced apo form (Fig. 3.6B), which is monomeric (98). Although, the effects of mutations on the stability of the apo monomer variant, determined by kinetic analysis, were found to be more pronounced (176). Taking into consideration the different SOD1 constructs, experimental methodologies, and conditions, on the whole there is fairly good agreement between the different studies.

It is worth mentioning that comparing mutational effects on stability at different temperatures requires knowledge of the curvature and amplitude of the ΔG versus t function. Mutations can in some cases affect this curvature in complex ways leading to large differences in stability relative to pWT. For example, our studies show that G37R destabilizes the monomer at t_{avg} by 1.4 kcal (mol monomer)$^{-1}$(Table 3.2), but stabilizes the monomer by 0.4 kcal (mol monomer)$^{-1}$ at 37 °C. This large difference in relative stability at the different temperatures is due to the large $\Delta H_{M\leftrightarrow U}$ value, which causes a large increase in the amplitude of the ΔG versus t function relative to pWT, in turn leading to high stability in the lower temperature range. The same behaviour is observed for G93R and V148I mutants. This finding emphasizes the difficulty in comparing relative stabilities obtained using different experimental approaches and measurement conditions. To compare variations in reported relative stabilities, experiments should be performed under as close to identical conditions as possible.

3.4.2 Mutations increase population of monomeric species: implications for aggregation and ALS

Correlations between the properties of SOD1 mutants in vitro and ALS characteristics, such as disease duration and age of onset, have long been sought. A number of studies have attempted to relate various measures of stability with disease duration, and, while there appears to be a correlation between total stability and disease duration for some mutants, there are also many outliers (200, 229, 230). The results obtained here suggest that, rather than considering only total stability for such correlations, it is important also to account for the stabilities and populations of additional SOD1 species. In particular, the fractions of both folded and unfolded monomer may be important, as these species have been suggested to be key precursors for aggregate formation (76, 99, 193, 199, 258). Aggregation is generally enhanced by decreasing global or local protein stability and is thought to arise from fully or partially unfolded states (52). Here we show that the actual folded apo SOD1 monomer intermediate (i.e., not a mutant monomer model) has relatively low stability (Table 3.2) (134, 176, 177, 188). Furthermore, the monomer is usually further destabilized by mutation (Table 3.2), and the expanded structure (Section 2.2.3) of folded monomeric apo SOD1 mutants may more readily allow for propagation of the destabilizing effects of mutations, increasing access to aggregation-prone states.

All the mutants studied increase the fraction of folded monomers under physiologically relevant concentration, temperature, and pH (Fig. 3.7). Since SOD1 aggregation has been reported to occur via a nucleation-dependent mechanism (99), even small increases in malleable monomers, which may promote nucleation, are important for accelerating aggregation. These observations suggest that mutations promote different structural changes that may in turn promote aggregation in different ways (2, 181).

3.4.3 Conclusions

Of central importance in understanding SOD1-mediated ALS is deciphering the mutation-driven mechanisms that may transform this protein into toxic aggregates. Systematic thermodynamic analyses such as those reported herein are valuable not only for determining global stability but also for quantifying the stabilities and populations of species that may be important precursors to aggregation. While many mutations, including ones distant from the dimer interface, decrease interface stability, and promote monomer formation, the effects on monomer stability are more complex. Consequently, the relative amounts of folded and unfolded monomers populated under physiological conditions by different mutants will differ and may account for the complexity of aggregation mechanisms reported (2). The new approach of using ITC combined with protein concentration dependence of DSC, provides detailed quantitative data on total, interface, and monomer stabilities for SOD1 mutants. The results suggest that mutational effects on total stability of SOD1 are only part of the story; monomer and dimer interface stabilities are important additional factors central to understanding the origins of toxic SOD1 aggregation in ALS.

3.5 Supplementary Information

3.5.1 Supplementary Methods

3.5.1.1 Fitting of differential scanning calorimetry data to a 2-state monomer unfolding model

In addition to the dimer 2-state unfolding and dimer 3-state with monomeric intermediate unfolding models, DSC data for apo A4V, H46R, and V148G were analyzed using a monomer 2-state unfolding model describing a reversible transition from folded monomer (*M*) to unfolded monomers (*U*), $M \leftrightarrow U$ (237). Individual thermograms were fit to Eq. S3.1:

$$C_p = (A + BT)(1 - \alpha) + (E + FT)\alpha + \frac{\beta \Delta h_{cal}^2 (T_{0.5}) \alpha (1-\alpha)}{RT^2} \quad \text{(Eq. S3.1)}$$

where C_p is the total specific heat absorbtion at temperature T (in Kelvin); A and E are the intercepts of the folded and unfolded baselines, respectively; B and F are the slopes of the folded and unfolded baselines, respectively; R is the universal gas constant; β is the ratio of van't Hoff to calorimetric enthalpy multiplied by the molecular weight of the SOD dimer; Δh_{cal} is the specific calorimetric enthalpy of unfolding at T; α is the extent of the unfolding reaction; and $T_{0.5}$ is the temperature at which unfolding is half complete (i.e α =0.5). Fitting was performed using Microcal Origin 5.0 (Microcal Inc., Malvern Instruments).

3.5.1.2 Predicting $\Delta C_{p,N_2 \leftrightarrow 2M}$ based on changes in solvent accessible surface area (ΔASA)

The polar and non-polar contributions to ΔASA (ΔASA_p and ΔASA_{np}, respectively) between dimer and dissociated monomers were determined using the crystallographic structures for both apo SOD1 wild-type (1HL4) using:

$$\Delta ASA_p = ASA_{monA\text{-}p} + ASA_{monB\text{-}p} - ASA_{dimer\text{-}p} \quad \text{(Eq. S3.2a)}$$

$$\Delta ASA_{np} = ASA_{monA\text{-}np} + ASA_{monB\text{-}np} - ASA_{dimer\text{-}np} \quad \text{(Eq. S3.2b)}$$

where $ASA_{monA\text{-}p}$ and $ASA_{monB\text{-}p}$ are the polar, $ASA_{monA\text{-}np}$ and $ASA_{monB\text{-}np}$ are the non-polar solvent accessible surface areas of the folded monomers A and B, respectively, which together make up the dimer in the crystal structure, and $ASA_{dimer\text{-}p}$ and $ASA_{dimer\text{-}np}$ are the polar and non-polar respectively, solvent accessible surface areas of the folded dimer. These values were calculated using InterProSurf (259).

The $\Delta C_{p,N_2 \leftrightarrow 2M}$ can be predicted using ΔASA_p and ΔASA_{np} calculated above and the empirically derived equations:

$\Delta C_{p,N_2 \leftrightarrow 2M} = -0.32 \times \Delta ASA_{np} + 0.14 \times \Delta ASA_p$ (260) (Eq. S3.3a)

$\Delta C_{p,N_2 \leftrightarrow 2M} = -0.45 \times \Delta ASA_{np} + 0.26 \times \Delta ASA_p$ (261) (Eq. S3.3b)

$\Delta C_{p,N_2 \leftrightarrow 2M} = -0.28 \times \Delta ASA_{np} + 0.09 \times \Delta ASA_p$ (262) (Eq. S3.3c)

$\Delta C_{p,N_2 \leftrightarrow 2M} = -0.51 \times \Delta ASA_{np} + 0.21 \times \Delta ASA_p$ (263) (Eq. S3.3d)

An average $\Delta C_{p,N_2 \leftrightarrow 2M}$ value of 0.45 ± 0.12 kcal (mol dimer)$^{-1}$ °C^{-1} was determined based on equations S3.3a-S3.3d and using predicted ΔASA_{np} and ΔASA_p of 1262 Å and 258 Å, respectively (173).

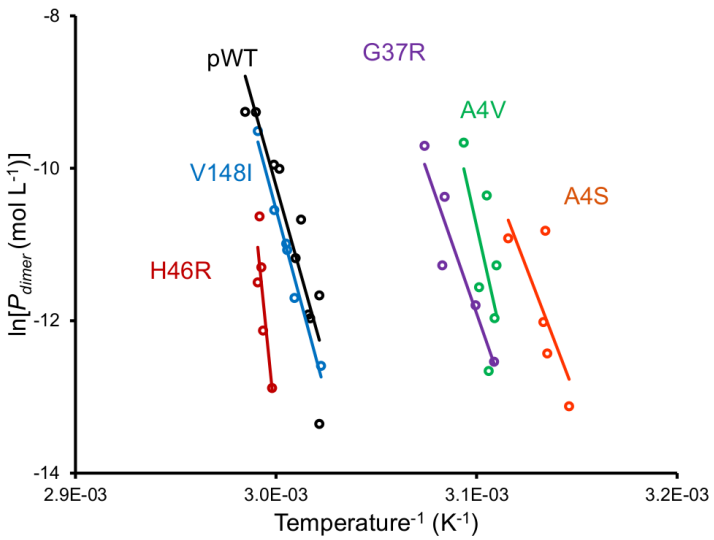

Figure S3.1 Plots of ln*P* versus 1/$T_{0.5}$ used to determine molecularity, *n*, for apo SOD1 variants. Here the lnP_{dimer} values are plotted versus 1/$T_{0.5}$ values from the dimer 2-state fits for a representative set of apo variants (Table 3.1), and fit to a straight line using linear regression. Note that the midpoint of the thermal unfolding transition is a relatively well defined experimental value that is affected little in different unfolding models. Data are plotted for H46R (red), V148I (blue), pWT (black), G37R (purple), A4V (green), and A4S (orange), ordered from most thermally stable to least stable variant and (left to right). The slope values were used to determine *n* (summarized in Table 3.1) using Eq. 3.2, as described in the Material and Methods. Values of *n* are related to the inverse of the *slope* values. Of the representative set of mutants, the data for H46R and A4V have the steepest slopes, and hence the lowest average *n* values of ~1.3 and ~1.6, respectively, consistent with these mutants having higher populations of monomer (Fig. 3.6). The lower slopes for the other variants correspond to higher *n* values approaching ~2, consistent with predominantly dimer unfolding. When molecularities were calculated with ΔH_{cal} there was much more scatter in the data due to there being more experimental error in ΔH_{cal} (128, 244). Taken together, the data are consistent with dimer unfolding with varying levels of monomer, in agreement with trends in $t_{0.5}$ values with protein concentration (Fig. 3.3, Table 3.1).

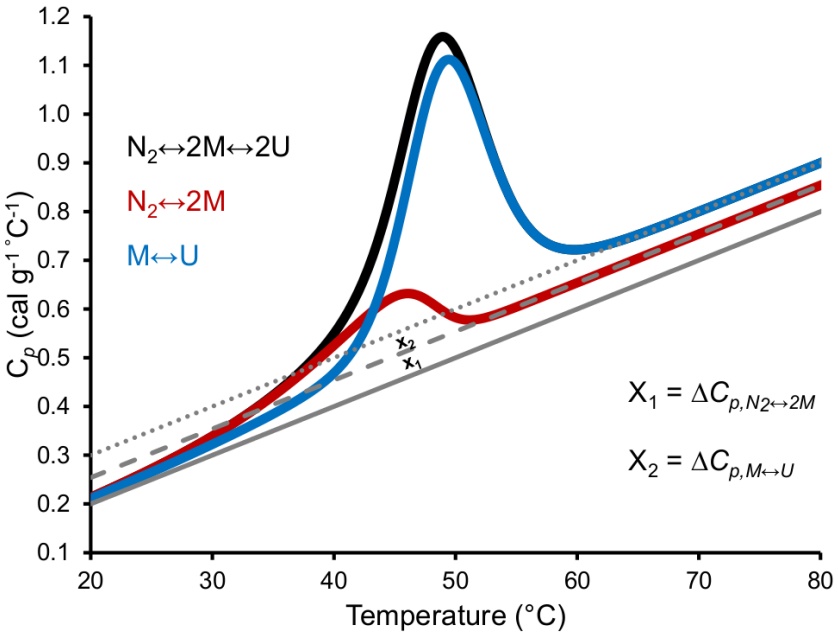

Figure S3.2 3-state thermal denaturation of apo SOD1. The total heat of unfolding (black curve) can be dissected into contributions from dimer dissociation (red curve) and monomer unfolding (blue curve). In the 3-state global fitting approach taken herein, $K_{d,N_2 \leftrightarrow 2M}$ and $\Delta h_{cal,N_2 \leftrightarrow 2M}$, which characterize dimer dissociation, were set to the values determined by ITC at 37 °C. The slopes of the monomeric intermediate and unfolded monomer baselines were set equal to that of the native baseline, making the common assumption that ΔC_p of unfolding is temperature independent (219). The intercepts of the intermediate and unfolded baselines were defined relative to the intercept of the native baseline (solid grey line) according to temperature-independent values for $\Delta C_{p,N_2 \leftrightarrow 2M}$ and $\Delta C_{p,M \leftrightarrow U}$ determined by Kirchoff analysis (Materials and Methods). Thus, the unfolded monomer and dimer baselines, grey dashed and dotted lines respectively, were defined based on $\Delta C_{p,N_2 \leftrightarrow 2M}$ (X_1) and $\Delta C_{p,M \leftrightarrow U}$ (X_2); only T_2', $\Delta h_{cal,M \leftrightarrow U}(T_2')$, $\beta_1 = \beta_2$, and parameters defining the slope and intercept of the native baselines (solid grey line) were set as globally shared floating parameters.

Table S3.1 Thermodynamic parameters for apo SOD1 determined from global 3-state fits.

SOD1 variant[a]	$\Delta H_{N_2 \leftrightarrow 2M}$ (kcal (mol dimer)$^{-1}$) 37 °C[b]	$\Delta G_{N_2 \leftrightarrow 2M}$ (kcal (mol dimer)$^{-1}$) 37 °C[b]	$t_{0.5,\, M \leftrightarrow U}$ (°C)[c]	$\Delta H_{M \leftrightarrow U}$ (kcal (mol monomer)$^{-1}$) t_{avg}[c,d]	$\Delta G_{M \leftrightarrow U}$ (kcal (mol monomer)$^{-1}$) 37 °C[e,f]	$\Delta G_{M \leftrightarrow U}$ (kcal (mol monomer)$^{-1}$) t_{avg}[d,f]	$\Delta\Delta G_{M \leftrightarrow U}$ (kcal (mol monomer)$^{-1}$) t_{avg}[d,g]
pWT[c,i]	n/a	10.2 ± 0.7	n/a	n/a	3.4 ± 0.5	n/a	n/a
pWT	(30.8 ± 8.8)	(10.3 ± 0.5)	59.5 ± 0.9	44.0 ± 2.0	**2.8** (1.9, 3.0)	**1.2** (0.7, 1.3)	n/a
pWT[j]	8.8 ± 13.5	9.0 ± 11.8	58.4 ± 0.9	49.1 ± 6.7	3.0	1.10	n/a
V148I	(11.4 ± 2.2)	(8.9 ± 0.2)	60.1 ± 0.2	84.0 ± 1.2	**5.7** (4.2, 5.7)	**2.3** (1.6, 2.4)	-1.2
V148I[j]	7.5 ± 3.8	7.7 ± 3.2	60.0 ± 0.1	79.9 ± 3.2	5.4	2.18	n/a
G93S	(17.6 ± 4.6)	(8.4 ± 0.3)	49.2 ± 1.1	58.3 ± 3.7	**2.0** (1.5, 2.0)	**-0.4** (-0.6, -0.3)	1.5
H46R	(16.2 ± 4.4)	(8.4 ± 0.4)	62.5 ± 0.1	71.2 ± 1.1	**5.3** (4.7, 5.4)	**2.6** (2.3, 2.6)	-1.4
H46R[j]	25.0 ± 3.0	8.7 ± 3.1	62.8 ± 0.1	70.0 ± 1.9	5.3	2.5	n/a
E100G	(16.0 ± 4.8)	(8.0 ± 0.4)	48.0 ± 0.7	53.3 ± 8.4	**1.6** (2.1, 1.6)	**-0.5** (-0.3, -0.4)	1.7
G37R	(7.8 ± 1.8)	(7.6 ± 0.2)	50.3 ± 0.1	84.1 ± 2.8	**3.2** (3.0, 1.8)	**-0.2** (-0.3, -0.3)	1.4
G37R[j]	42.7 ± 26.5	10.3 ± 15.6	46.7 ± 0.8	55.4 ± 21.6	1.5	-0.8	n/a
H43R	(23.0 ± 1.4)	(7.5 ± 0.0)	47.6 ± 0.4	59.5 ± 5.2	**1.7** (1.9, 1.7)	**-0.6** (-0.6, -0.6)	1.8
G93A	(14.0 ± 2.0)	(7.2 ± 0.3)	47.4 ± 0.3	58.9 ± 4.7	**1.7** (1.7, 1.7)	**-0.7** (-0.7, -0.6)	1.9
G93A[j]	22.0 ± 10.6	8.1 ± 3.8	46.1 ± 0.7	50.8 ± 5.4	1.3	-0.8	n/a
I113T	(30.2 ± 2.5)	(7.1 ± 0.2)	46.7 ± 0.2	53.2 ± 3.7	**1.4** (1.7, 1.5)	**-0.7** (-0.7, -0.6)	1.9
I113T[j]	27.2 ± 4.3	7.8 ± 1.3	45.7 ± 0.4	50.7 ± 1.7	1.2	-0.9	1.9
A4T	(39.2 ± 3.8)	(7.1 ± 0.2)	43.6 ± 0.4	48.9 ± 9.6	**0.8** (1.3, 0.9)	**-1.1** (-1.1, -1.0)	2.3
A4T[j]	13.7 ± 46.3	10.4 ± 17.4	30.0 ± 6.4	42.9 ± 50.2	-0.8	-2.6	n/a
A4S	(9.0 ± 2.6)	(7.0 ± 0.0)	46.3 ± 0.4	61.1 ± 10.0	**1.5** (1.0, 1.1)	**-0.9** (-1.3, -1.2)	2.1
A4S[j]	46.5 ± 14.0	9.0 ± 4.1	45.5 ± 1.7	45.0 ± 6.6	1.1	-0.8	n/a
G93R	(45.6 ± 1.8)	(6.7 ± 0.1)	49.1 ± 0.2	87.8 ± 7.7	**3.1** (2.9, 3.1)	**-0.6** (-0.5, -0.5)	1.7
A4V	(37.2 ± 3.8)	(6.4 ± 0.3)	50.9 ± 0.2	59.2 ± 3.4	**2.3** (2.4, 2.2)	**-0.1** (-0.1, -0.1)	1.2
A4V[j]	35.9 ± 5.4	6.8 ± 2.2	51.0 ± 0.4	55.9 ± 3.6	2.3	0.0	n/a
V148G	(50.6 ± 1.4)	(5.9 ± 0.3)	48.6 ± 0.0	67.8 ± 0.5	**2.2** (2.1, 2.3)	**-0.5** (-0.5, -0.5)	1.7
V148G[j]	54.8 ± 0.4	5.7 ± 0.2	48.6 ± 0.0	65.7 ± 0.3	2.2	-0.5	n/a

[a]For each mutant, the scans at different protein concentrations used in the global fitting are those listed in Table 3.1, with the exception of pWT, where concentrations 0.20, 0.21, 0.40, 0.44, 0.85, 1.50, and 3.0 were fit; I113T where concentration 0.21 mg mL^{-1} was omitted; A4V where concentration 0.52 mg mL^{-1} was omitted; and G93R mg mL^{-1} where concentration 0.21 was omitted.

[b]Numbers in the brackets were determined by ITC and fixed in the DSC 3-state fits.

[c]Errors are the uncertainty in fitted values.

[d]t_{avg} is 51.2 °C, the average of all $t_{0.5}$ values obtained from the 2-state fits.

[e]$\Delta G_{M \leftrightarrow U}$ values calculated at physiological temperature.

[f]Values shown in bold are determined from fits allowing $\Delta H_{vH}/\Delta H_{cal}$ to deviate from unity. Data were also fit with ΔH_{vH} and ΔH_{cal} set equal, and these values are the first values shown in brackets. Monomer stability was also determined using a higher $\Delta C_{p,N_2\leftrightarrow 2M}$ (2.2 kcal (mol dimer)$^{-1}$ °C^{-1}), and these values are the second values shown in brackets. Uncertainties in monomer stability were approximated from the range of values obtained from these 3 different fitting procedures (Table 3.2).
[g]$\Delta\Delta G = \Delta G_{pWT} - \Delta G_{mutant}$, a positive value indicates lower stability of the mutant relative to pWT; values are calculated at t_{avg}, where monomer stability is best defined.
[h]$\Delta G_{N_2\leftrightarrow 2M}$ and $\Delta G_{M\leftrightarrow U}$ were also determined by globally fitting urea denaturation curves at 37 °C to a 3-state model with monomeric intermediate.
[i]$\Delta G_{M\leftrightarrow U}$ values obtained by fitting additional parameters $\Delta H_{N_2\leftrightarrow 2M}$ and $\Delta G_{N_2\leftrightarrow 2M}$ (i.e., not fixing these parameters to the values obtained by ITC) and setting ΔH_{vH} and ΔH_{cal} equal, for mutants with more than 3 datasets. This fitting method returns values with high uncertainty; therefore, the values from the fixed fits give more reliable comparison of relative stabilities.

Table S3.2 Thermodynamic parameters for monomer 2-state unfolding of apo SOD1.

SOD1 variant	[SOD1] mg mL^{-1}	$t_{0.5}$ (°C)[a]	$\Delta C_{p,M\leftrightarrow U}$ (kcal (mol monomer)$^{-1}$)	$\Delta H_{vH}(t_{0.5})$ (kcal (mol monomer)$^{-1}$) [a]
A4V	0.20	51.5 ± 1.4	-1.15	45.5 ± 10.6
A4V	0.30	50.3 ± 0.6	0.02	56.6 ± 7.9
A4V	0.40	50.6 ± 0.3	-0.47	56.9 ± 5.1
A4V	0.50	50.8 ± 0.2	0.29	54.7 ± 2.5
A4V	1.00	50.3 ± 0.4	0.26	65.9 ± 4.4
A4V	1.95	51.5 ± 0.1	-0.18	79.3 ± 2.6
H46R	0.08	61.6 ± 1.3	1.55	73.0 ± 18.8
H46R	0.17	61.9 ± 0.3	0.71	74.6 ± 6.6
H46R	0.32	62.2 ± 0.1	1.01	84.6 ± 2.2
H46R	0.39	62.2 ± 0.2	0.27	86.6 ± 4.7
H46R	0.76	62.2 ± 0.1	1.07	94.9 ± 2.5
V148G	0.12	47.1 ± 0.5	5.19	44.7 ± 4.3
V148G	0.23	51.1 ± 0.1	-1.68	62.3 ± 0.6
V148G	0.29	52.3 ± 0.0	-3.07	52.4 ± 0.3
V148G	0.53	49.8 ± 0.0	-0.76	61.0 ± 0.2
V148G	0.92	49.2 ± 0.0	-0.71	59.2 ± 0.1
V148G	1.56	48.4 ± 0.0	-0.51	55.6 ± 0.8

[a]Errors in fitted parameters are obtained from the fitting program.
For A4V and H46R, data was obtained and fit by Kenrick A. Vassall.

Chapter 4

Decreased stability and increased formation of soluble aggregates by immature SOD1 do not account for disease severity in ALS

Author Contributions

This chapter was published in the *Proceedings of the National Academy of Sciences* in 2010, with the following authors: Kenrick A. Vassall*, Helen R. Broom* (published under my maiden name, Stubbs), Heather A. Primmer, Ming Sze Tong, Sarah M. Sullivan, Ryan Sobering, Sai Praveen Srinivasan, Lee-Ann K. Briere, Stanley D. Dunn, Wilfredo Colòn, and Elizabeth M. Meiering (174), and has been reproduced with permission.

*Kenrick A. Vassall and Helen R. Broom contributed equally to this work.

Kenrick A. Vassall, Helen R. Broom, Heather A. Primmer, Stanley D. Dunn, and Elizabeth M. Meiering designed experiments. Plasmids containing wild type SOD1 (a construct containing the native free cysteines, refer to section 1.3.2), as well as SOD1 mutants with free cysteines were provided by Wilfredo Colòn. Samples were prepared by Kenrick A. Vassall, Helen R. Broom, Heather A. Primmer, Ming Sze Tong, Sarah M. Sullivan and Sai Praveen Srinivasan. Differential scanning calorimetry experiments were mainly performed by Kenrick A. Vassall with a subset being performed by Helen R. Broom; Helen R. Broom performed light scattering experiments; Stanley D. Dunn and Lee-Ann K. Briere performed the analytical ultracentrifugation experiments; Kenrick A. Vassall and Ryan Sobering performed circular-dichroism experiments; and Heather A. Primmer performed the aggregation-prediction analysis. The manuscript was co-written by Kenrick A. Vassall, Helen R. Broom, Heather A. Primmer,

and Elizabeth M. Meiering. We are grateful to Gian Tartaglia for assistance in using Zaggregator.

Overview

Protein aggregation is a hallmark of many diseases, including amyotrophic lateral sclerosis (ALS), where aggregation of Cu, Zn-superoxide dismutase (SOD1) is implicated in causing neurodegeneration. Recent studies have suggested that destabilization and aggregation of the most immature form of SOD1, the disulfide-reduced, unmetallated (apo) protein is particularly important in causing ALS. We report herein in depth analyses of the effects of chemically and structurally diverse ALS-associated mutations on the stability and aggregation of reduced apo SOD1. In contrast with previous studies, we find that various reduced apo SOD1 mutants undergo highly reversible thermal denaturation with little aggregation, enabling quantitative thermodynamic stability analyses. In the absence of ALS-associated mutations, reduced apo SOD1 is marginally stable but predominantly folded. Mutations generally result in slight decreases to substantial increases in the fraction of unfolded protein. Calorimetry, ultracentrifugation, and light scattering show that all mutations enhance aggregation propensity, with the effects varying widely, from subtle increases in most cases, to pronounced formation of 40–100 nm soluble aggregates by A4V, a mutation that is associated with particularly short disease duration. Interestingly, although there is a correlation between observed aggregation and stability, there is minimal to no correlation between observed aggregation, predicted aggregation propensity, and disease characteristics. These findings suggest that reduced apo SOD1 does not play a dominant role in modulating disease. Rather, additional and/or multiple forms of SOD1 and additional biophysical and biological factors are needed to account for the toxicity of mutant SOD1 in ALS.

4.1 Introduction

Mutations in Cu,Zn superoxide dismutase (SOD1) cause familial amyotrophic lateral sclerosis (fALS), a devastating and invariably fatal neurodegenerative disease. Although accounting for only a small percentage of all ALS cases, SOD1 mutations represent one of the main known causes of the disease. The similar symptoms and pathology of familial and sporadic ALS suggest common disease mechanisms and the potential for related therapeutic strategies (196, 232, 264). The mechanisms by which mutant SOD1 cause ALS are not known; however, extensive evidence supports a toxic gain of function due to increased aggregation of mutant protein. Misfolding and aggregation of diverse proteins are observed in numerous diseases, including other neurodegenerative diseases such as Alzheimer's, Huntington's and prion diseases (196, 264). Amyloid is a type of aggregate structure formed by many disease-associated proteins, and perhaps by all proteins, often under destabilizing conditions (265). Although there has been some controversy concerning the amyloid-like nature of large insoluble aggregates in mutant SOD1 mice models of ALS, amyloid aggregates are not observed in ALS patients (22, 26, 266). Here, we characterize the formation of small, soluble, non-amyloid aggregates by mutant SOD1.

In its mature form, SOD1 is a highly stable, homodimeric protein, with each subunit binding one catalytic copper ion and one structural zinc ion, and containing one intramolecular disulfide bond as well as two non-conserved free cysteines (Fig. S4.1A). Numerous in vivo and in vitro studies have shown that various immature, destabilized forms of SOD1 are prone to aggregate, and this is often enhanced by disease-associated mutations (76, 78, 128, 131, 144, 184, 190, 267, 268). Recently, attention has focused on aggregation of the most immature form of SOD1, in which the disulfide bond is reduced and no metals are bound, referred to here as the

reduced apo form. Studies of various mutant-SOD1 ALS mice models have shown that small, soluble, misfolded forms of reduced apo SOD1 are enriched in the spinal cord and may be the common cytotoxic species that cause ALS (269, 270). In addition, cell culture studies suggest that ALS-associated mutations can promote disulfide bond reduction and metal loss (194). Relatively little is known, though, about the properties of reduced apo SOD1, and how mutations affect these properties. In vitro studies have shown that agitation and/or oxidation of reduced apo SOD1 results in the formation of large, insoluble, amyloid aggregates (76, 184). However, the relevance of amyloid formation to ALS is questionable, and recent studies of mutant-SOD1 mice models have shown that formation of aberrant intermolecular disulfide bonds and large insoluble aggregates by SOD1 becomes pronounced only occurs in the final, symptomatic stages of disease (268). There is also extensive evidence that smaller, soluble aggregates are particularly neurotoxic (264). Thus, it is of central importance to elucidate the properties of reduced apo SOD1s, and how these may relate to pathogenic mechanisms.

We report here in depth analyses of the effects of chemically and structurally diverse ALS-associated mutations on the stability and aggregation of reduced apo SOD1, under physiologically relevant quiescent, reducing conditions. The mutations are predominantly destabilizing, causing marked changes in the fraction of protein that is unfolded and increasing the propensity of the protein to form soluble aggregates. However, the formation of these aggregates is not well correlated with disease duration. While the results suggest that aggregation of reduced apo SOD1 may play some role in disease, they do not support increased aggregation of reduced apo mutants as the dominant determinant of ALS duration. Rather, multiple immature or aberrant forms of SOD1 are implicated in playing important roles in modulating disease.

4.2 Materials and Methods

4.2.1 Expression and purification of mutant SOD1

Disulfide-oxidized apo SOD1 proteins were prepared as described previously (134, 271). Reduced apo SOD1 was prepared by first unfolding the protein in 2 M guanidinium chloride (GdmCl), 20 mM HEPES, pH 7.8 for 30 min at ambient temperature with degassing. Tris(2-carboxyethyl)phosphine hydrochloride (TCEP-HCl) was then added to a final concentration of 10 mM with reduction occurring in an anaerobic environment for 1 hr. Finally, samples were exchanged into buffer containing 1 mM TCEP-HCl, 20 mM HEPES pH 7.4 by successive dilutions and reconcentrations using a 3 kDa cutoff Nanosep centrifugal device (Pall Corporation).

4.2.2 Differential scanning calorimetry

DSC scans of apo SOD1 samples were performed as described elsewhere (128). After subtraction of buffer versus buffer scans from protein versus buffer scans, disulfide-reduced apo SOD1 data were fit to a 2-state monomer unfolding model after normalizing for protein concentration (Supplementary Methods, Section 4.5.1).

4.2.3 Analytical ultracentrifugation

Sedimentation velocity and equilibrium experiments were conducted in the Biomolecular Interactions & Conformations Facility (Shuclich School of Medicine & Dentistry, University of Western Ontario) using an Optima XL-A Analytical Ultracentrifuge (Beckman Coulter Inc.) with an An60Ti rotor and 2/6-channel cells with Epon-charcoal centerpieces. Centrifugation was carried out at 20 °C with absorbance detection at either 252 or 280 nm. Equilibrium data were

collected in radial step sizes of 0.002 cm and averaged over 10 readings. Equilibrium data were fit to a single ideal species model (Supplementary Methods, Sections 4.5.3 and 4.5.4) using Prism 5 (GraphPad Software).

4.2.4 Light scattering measurements

Time average dynamic light scattering measurements were performed using a Zetasizer Nano ZS (Malvern Instruments Ltd.). Particle size was determined from an average of 3 correlation functions, each being the average of 5 consecutive 10 second data accumulations. Particle size was analyzed by the CONTIN method using Malvern software. Samples were initially measured daily and then at increasing time intervals.

4.3 Results

For most experiments herein, we employed a well-established pseudo wild-type (pWT) construct in order to facilitate measurements of stability and aggregation of reduced apo SOD1s and avoid complications caused by aberrant disulfide bond formation (76, 78, 126, 128, 144, 255, 272). In pWT, the nonconserved free cysteines at residues 6 and 111 are replaced by alanine and serine respectively, while the highly conserved cysteines at residues 57 and 146 are retained (Fig. S4.1A). Cysteines 57 and 146 form a disulfide bond in mature forms of SOD1 but are reduced in the current study. pWT is a suitable background because its activity, structure and stability are extremely similar to wild-type, and use of this background formerly enabled thermodynamic stability analyses for disulfide oxidized holo and apo SOD1s (128, 134, 143, 144). In various in vivo and in vitro studies, the free cysteines are frequently but not always observed to form aberrant disulfide bonds in aggregates, and they have been suggested to also play subtle roles in modulating noncovalent interactions during aggregation (76, 78, 131, 183, 190, 267, 268). These effects were controlled for here by analyzing the properties of mutations relative to the pWT background in the absence of disulfide bond formation. In addition, we conducted some experiments using the wild-type (WT) background containing cysteines 6 and 111; the results obtained are consistent with those obtained using pWT.

All experiments on reduced apo SOD1s were conducted under physiologically relevant conditions of pH (20 mM HEPES, pH 7.4) and protein concentration (~30-60 μM monomer, 0.5-1.0 mg mL^{-1}) (131, 273), under reducing conditions (1 mM TCEP), with no agitation and sample incubation under anaerobic conditions. The reduced status of the protein throughout all experiments was confirmed by iodoacetamide modification of the reduced cysteines followed by sodium dodecyl sulfate polyacrylamide gel electrophoresis (SDS-PAGE) (Fig. S4.1B) (131).

4.3.1 In the absence of ALS-associated mutations, reduced apo SOD1 unfolds with high reversibility at well above physiological temperature

The stability of reduced apo pWT and WT SOD1 were measured by differential scanning calorimetry (DSC) (Figs. 4.1A, B, 2D, Table S4.1), which shows that the temperature of maximum heat capacity (C_p), $t_{0.5,app}$, is ~48 °C for both constructs. The $t_{0.5,app}$ for reduced apo SOD1 is markedly lower compared to those for the more mature disulfide-oxidized apo and holo forms (Fig. 4.1A) (128, 144). However, despite being significantly less stable, reduced apo pWT thermally unfolds with high reversibility, typically ~95 % (Fig. 4.1B), comparable to the reversibility for disulfide-oxidized forms of SOD1 (128, 134, 143). The reversibility for the WT (Fig. 4.2D) is somewhat lower, at ~75%, likely due to the presence of the free thiols that have been shown previously to decrease reversibility due to the formation of aberrant disulfide bonds (141). To minimize inaccuracies due to irreversibility, pWT was used for most of the further analyses.

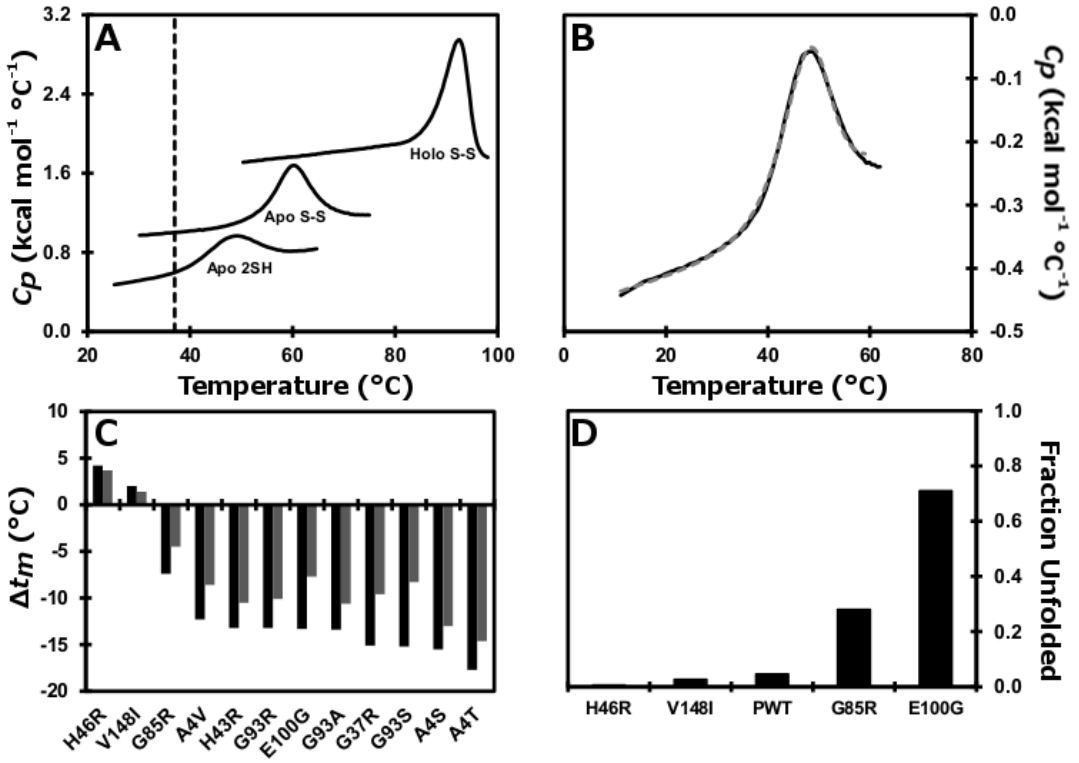

Figure 4.1 Reversible thermal unfolding of reduced apo pWT SOD1. **(A)** DSC scans of pWT SOD1 in the reduced apo form in 20 mM HEPES, 1 mM TCEP, pH 7.4 and the disulfide-oxidized apo and holo forms in 20 mM HEPES, pH 7.8. The dashed black line indicates physiological temperature of 37 °C. **(B)** Consecutive thermal unfolding traces of disulfide-oxidized apo pWT SOD1 in which the sample was heated (solid black line), cooled and heated again (dashed grey line). **(C)** Change in apparent $t_{0.5}$ of apo SOD1 in the disulfide-oxidized form (light shaded bars) and the disulfide-reduced form (dark shaded bars). In all cases the mutations have a larger effect on the apparent $t_{0.5}$ in the reduced apo form. **(D)** Fraction of unfolded reduced apo mutant SOD1 at 37 °C. The fraction of unfolded protein was calculated using the thermodynamic parameters (Table 4.1 and Supplementary Methods, Section 4.5.1).

4.3.2 Thermodynamic analysis under physiologically-relevant conditions shows reduced apo SOD1 undergoes a monomer 2-state unfolding transition and is predominantly folded

High reversibility of unfolding is a prerequisite for thermodynamic analysis, which has not been reported previously for reduced apo SOD1. In previous studies, we showed that disulfide-oxidized apo and holo pWT SOD1 thermally unfold with high reversibility according to a 2-state dimer unfolding mechanism (128); however, reduction or mutation of the disulfide bond in apo SOD1 greatly weakens the dimer interface (147, 197, 273). Measurements of thermal unfolding for reduced apo pWT are consistent with a monomer unfolding transition, showing no systematic shift in $t_{0.5,app}$ over ~20-fold range in protein concentration (7-152 μM, 0.1-2.4 mg mL^{-1}) (Fig. S4.2A). The unfolding data for pWT are well fit using a 2-state monomer unfolding model (Table 4.1, Supplementary Methods, Section 4.5.1), with an average van't Hoff to calorimetric enthalpy ratio ($\Delta H_{vH}/\Delta H_{cal}$) of 1.1 ± 0.2 (Table 4.1, Table S4.1) further confirming the applicability of the 2-state monomer model (237). Similar fits are obtained for WT (Fig. 4.2E, Tables 4.1, S4.1).

Calculation of the temperature dependence of stability requires knowledge of the change in heat capacity upon unfolding, ΔC_p (Supplementary Methods, Section 4.5.2), which was determined by Kirchoff analysis (274) to be 1.1 ± 0.1 kcal mol^{-1} °C^{-1} for reduced apo pWT (Fig. S4.2B, C). This value is relatively low compared to that expected for a protein of this size, ~2 kcal mol^{-1} °C^{-1} (262, 275), suggesting that the reduced apo monomer may be less structured than a typical globular protein. The Gibbs free energy of unfolding, ΔG, calculated from the thermodynamic parameters is 3.5 ± 0.1 and 1.8 ± 0.1 kcal mol^{-1} at 25 °C and 37 °C, respectively (Table 4.1). Similar values were obtained for WT and are given in Table 4.1.

An independent measure of ΔG was obtained for pWT using CD-monitored equilibrium urea chemical denaturation and renaturation curves (Fig. S4.2D, E, Table 4.1). These data are also well fit by a 2-state monomer unfolding transition, giving a ΔG of 4.0 ± 0.2 kcal mol^{-1} at 25 °C, which is in reasonable agreement with the value obtained by DSC, and previous chemical denaturation experiments for reduced apo WT at pH 6.3 (147).

Knowledge of ΔG enables calculation of the fraction of protein that is unfolded, f_U (Supplementary Methods, Section 4.5.1). For pWT at 37 °C, f_U is ~0.05 (Fig. 4.1D), showing that the protein is predominantly (95 %) folded. However, owing to the relatively low value of ΔG, f_U is very sensitive to small perturbations in stability caused by mutation, as described below.

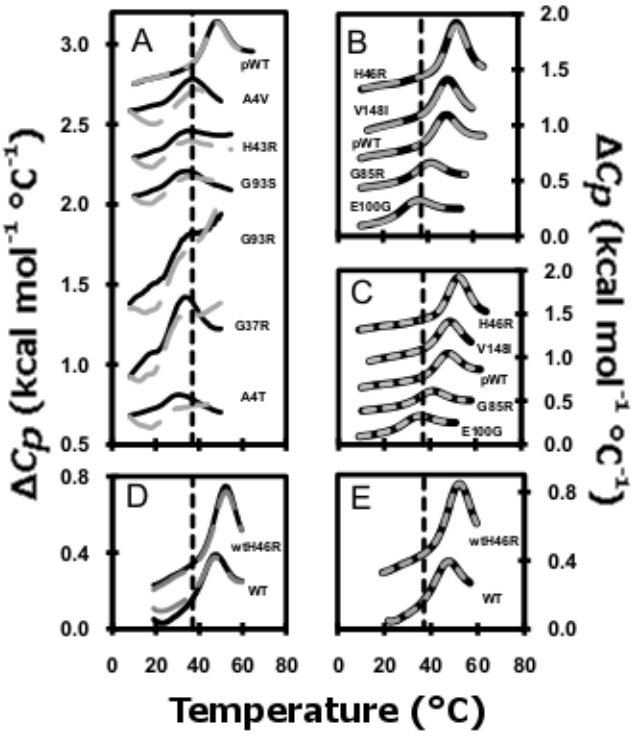

Figure 4.2 Reversibility and data fitting of reduced apo mutants. The dashed black line indicates physiological temperature of 37 °C. **(A)** Consecutive thermal unfolding endotherms of reduced apo mutants with low unfolding reversibility and **(B)** with high unfolding reversibility (scan one-solid black line; rescan-dashed grey line). **(C)** DSC data fitting of the reduced apo mutants and pWT. Typical thermograms (solid black lines) with corresponding 2-state monomer fits (dashed grey lines) are shown. **(D)** Consecutive thermal unfolding endotherms of WT and $H46R^{wt}$ (scan one-solid black line; rescan-dashed grey line). **(E)** DSC data fitting of WT and $H46R^{wt}$ SODl. Thermograms (solid black lines) with corresponding two-state monomer fits (dashed grey lines) are shown. In each panel, the datasets are offset for clarity.

4.3.3 DSC reveals complex effects of ALS-associated mutations on the stability and aggregation propensity of reduced apo SOD1

The effects of chemically and structurally diverse ALS-associated SOD1 mutations on both the disulfide-oxidized and reduced apo forms of the protein were also analyzed by DSC. The mutations include: A4V, T and S, and V148I, located in the dimer interface; G37R and H43R, affecting the packing of residues in the beta barrel; metal binding mutants H46R and G85R; G93R, S, A and D at a mutational hot-spot within a tight turn; and E100G located at the end of strand 6, which eliminates a salt bridge with K30 (Fig. S1A). All of the mutants produced measurable thermograms (Figs. 4.2A, B, Table S4.2), except G93D.

Based on lower $t_{0.5,app}$ values, the mutants are generally destabilized relative to pWT, except for H46R and V148I which have slightly increased stabilities (Fig. 4.1C, Table S4.2). Furthermore, in the reduced apo form all mutants except H46R, V148I and G85R have $t_{0.5,app}$ values at or below 37 °C (Tables 4.1, S4.2). This is in contrast to the more mature disulfide-oxidized apo form where the mutants all have $t_{0.5,app}$ values significantly higher than 37 °C (128, 134). Although it is difficult to directly compare the effects of the mutations on the thermodynamic stability of the oxidized to the reduced apo forms due to the change in quaternary structure, it is noteworthy that the changes in melting temperature are larger in the reduced apo form compared to the oxidized apo form (Fig. 4.1C, Table S4.2). Similarly, the effects of mutations in non-metal binding mutants are larger in the oxidized apo forms than in the holo (metallated) forms (128), suggesting that the effects of mutations in SOD1 tend to propagate more as the protein becomes increasingly destabilized and folding becomes less cooperative. Overall, the propensity of most reduced apo SOD1s to misfold/aggregate is evident

from the decreased reversibility of thermal unfolding traces (Fig. 4.2A), which is generally most pronounced in the significantly destabilized mutants.

Nevertheless, the reversibility of thermal unfolding is remarkably high for several mutants: H46R, V148I, G85R, and E100G, enabling thermodynamic analysis using the 2-state monomer unfolding model (Figs. 4.2B, and C, Tables 4.1, S4.1). Similar results were also obtained for H46R in the WT background ($H46R^{wt}$, Figs. 4.2D and E, Tables 4.1 and S4.1). The stability of pWT and H46R was also measured using chemical denaturation, again giving results consistent with those obtained by DSC (Figs. S4.2D and E, Table 4.1). Using the fitted thermodynamic parameters, f_U at 37 °C is calculated to be 0.05, 0.007, 0.03, 0.28, and 0.71 for pWT, H46R, V148I, G85R and E100G respectively (Fig. 4.1D, Supplementary Methods, Section 4.5.1). Thus, at physiological temperature the slightly stabilizing H46R and V148I mutants are predominantly folded (in fact, more so than pWT), but the proportion of unfolded protein is markedly increased for the other destabilizing mutants, with E100G being more unfolded than folded. This differs significantly from the effects of the mutations in the disulfide-oxidized apo form where the proteins remain very predominantly folded (Table S4.2) (134).

Table 4.1 Summary of thermodynamic parameters for reduced apo SOD1s.

Apo Reduced SOD1[a]	$t_{0.5}$ (°C)	ΔH_{vH}(37 °C) (kcal mol^{-1})	$\frac{\Delta H_{vH}}{\Delta H_{cal}}$	ΔC_p (kcal mol^{-1}°C^{-1})	ΔG(25 °C) (kcal mol^{-1})[b,c]	ΔG(37 °C) (kcal mol^{-1})	$\Delta\Delta G$(37 °C) (kcal mol^{-1})[d]
pWT	47.6 ± 0.5	50.5 ± 1.6	1.14 ± 0.15	0.72 ± 0.57	3.5 ± 0.1 *4.0 ± 0.2*	1.8 ± 0.1	N/A
H46R	52.6 ± 0.5	56.1 ± 4.2	0.95 ± 0.08	-0.42 ± 0.84	4.9 ± 0.1 *5.1 ± 0.1*	3.1 ± 0.1	1.3
V148I	51.0 ± 1.1	58.4 ± 2.6	0.93 ± 0.04	-2.62 ± 1.19	3.6 ± 0.1	2.2 ± 0.0	0.4
G85R	40.7 ± 0.4	46.9 ± 1.8	1.06 ± 0.36	-0.11 ± 0.34	2.1 ± 0.1	0.6 ± 0.0	-1.2
E100G	33.2 ± 1.2	47.3 ± 2.0	1.27 ± 0.06	0.79 ± 0.32	1.0 ± 0.1	-0.6 ± 0.2	-2.4
WT	46.8 ± 0.4	57.2 ± 1.1	1.49 ± 0.27	1.01 ± 0.67	3.0 ± 0.0	1.6 ± 0.0	N/A
H46R^{wt}	52.7 ± 2.5	57.4 ± 5.4	0.76 ± 0.22	-1.59 ± 3.18	3.8 ± 0.5	2.4 ± 0.4	0.8

N/A, not applicable

All values are averages and standard deviations from at least three samples (Table S4.1), excluding WT and V148I, which are averages from two samples. DSC experiments for pWT, H46R, G85R, and E100G were performed by Kenrick A. Vassall; DSC experiments for V148I, WT, and H46R^{wt} were performed by Helen R. Broom.

[a]All mutants are in the pWT background unless otherwise specified.

[b]Values are calculated using the thermodynamic parameters obtained from the monomer two-state model and a temperature independent ΔC_p of 1.1 ± 0.1 kcal mol^{-1} °C^{-1} (Fig. 4.2C).

[c]Values in italics are from monomer two-state unfolding fits of equilibrium urea chemical denaturation curves (Figs. S4.2D, E). These experiments were performed by Kenrick A. Vassall and Ryan E. Sobering.

[d]$\Delta\Delta G = \Delta G_{mutant} - \Delta G_{pWT}$

Although the thermal unfolding of these reduced apo SOD1s is highly reversible, there is some evidence in the DSC fitted parameters for increased aggregation propensity (128). H46R, G85R and V148I have relatively low, mostly negative, fitted ΔC_p's, with average values of 0.42 ± 0.84, -2.62 ± 1.19 and -0.11 ± 0.34 kcal mol^{-1} °C^{-1} respectively (Table 4.1). The negative average ΔC_ps for H46R and V148I are pronounced and consistent, suggesting the occurrence of exothermic aggregation as these mutants thermally unfold (128). In contrast, E100G does not exhibit unusually low ΔC_p values; however, the $\Delta H_{vH}/\Delta H_{cal}$ ratios tend to be larger than 1 (1.3 ± 0.1 on average), suggesting a larger cooperative unfolding unit, i.e. presence of aggregates (244). Overall, the DSC data are suggestive of subtle increases in aggregation of all mutant SOD1s.

4.3.4 Analytical ultracentrifugation shows that reduced apo SOD1s are predominantly monomeric, and mutations slightly increase protein-protein interactions

In order to further investigate the tendency of reduced apo SOD1s to aggregate, analytical ultracentrifugation (AUC) sedimentation velocity and equilibrium experiments were performed (Supplementary Methods, Sections 4.5.3 and 4.5.4). Sedimentation velocity experiments can assess sample heterogeneity with high sensitivity. Analysis of the velocity data for pWT and H43R revealed species with sedimentation coefficients of 1.5-2 S (Fig. S4.3), very similar to the values reported previously for reduced apo WT SOD1 (197). The plots of boundary fraction versus sedimentation coefficient show only a modest slope, indicating no significant population of dimers or larger aggregated species for either pWT or H43R in these experiments.

Sedimentation equilibrium experiments at several rotor speeds (20,000, 25,000, 30,000 and 35,000 rpm) were also performed to analyze the molecular weights (MWs) of the species present in solution. Fitting of the equilibrium data for pWT, H43R, A4V, and E100G to a single

species model gave highly reproducible results (Table S4.3). For the pWT protein, the fitted MW at lower rotor speeds is generally close to 15 kDa, just under the calculated mass of ~ 15.8 kDa. In contrast to the pWT, the fitted MWs for the A4V and E100G mutants are intermediate between monomer and dimer, while fits for the mutant H43R tend to give values closer to what would be expected for a dimer. Additionally, fitted MW values for all mutants markedly decrease with increased rotor speed (Table S4.3). These results clearly indicate increased intermolecular association of the mutant proteins. Attempts to fit the data to 2-state models for monomer/dimer, monomer/trimer and monomer/tetramer transitions gave poor fits with non-random residuals, indicating that the association is likely more complex than a simple 2-state process. Overall, the sedimentation equilibrium data indicate that the pWT protein remains predominantly monomeric during the lengthy period required for these studies, but that the mutants have an increased tendency to form small aggregated species. These findings are consistent with the results of the DSC experiments.

4.3.5 Light scattering reveals markedly differences in aggregation of mutants upon prolonged incubation

Dynamic light scattering (DLS) was used to monitor the size of particles in solution upon incubating samples at 37 °C (Figs. 4.3, S4.4 and S4.5A). It is important to note that light scattering intensity is proportional to the sixth power of the diameter of the scattering particle, thus this technique is extremely sensitive to aggregate formation (276). DLS analyses showed that all reduced apo SOD1 solutions were initially monodisperse, with a single species of hydrodynamic diameter ~5-6 nm. This diameter is intermediate between those expected for a protein the size of SOD1 in the fully folded and unfolded states (277), consistent with the

relatively low ΔC_p (see above), and suggesting that the folded reduced apo SOD1 may have an expanded structure.

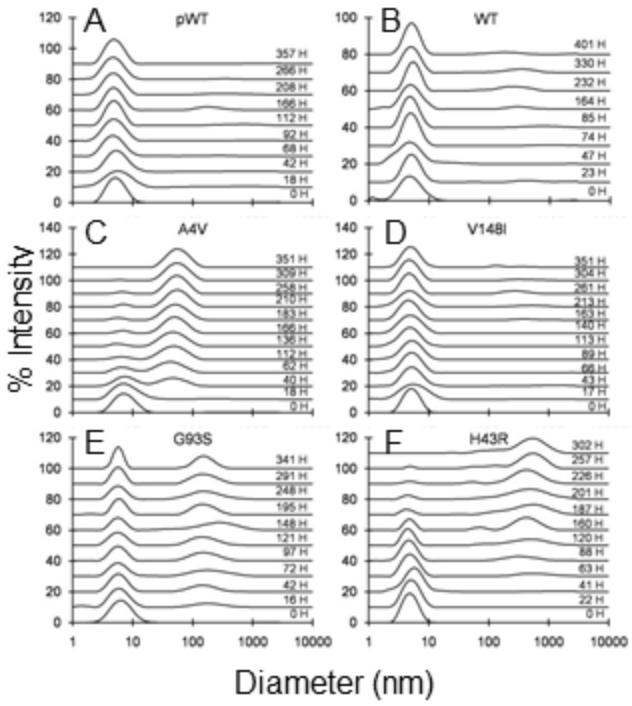

Figure 4.3 Dynamic Light Scattering (DLS) data for reduced apo pWT and mutant SOD1. Particle size distributions for reduced apo pWT and mutants at 37 °C, pH 7.4, measured by dynamic light scattering over time, as indicated in hours (H).

Upon prolonged incubation, gradual formation of small amounts of soluble aggregates was observed, with distinct differences between mutants (Figs. 4.3, S4.4 and S4.5). At one extreme, H46R and V148I show only very slight evidence for aggregation, with more than 99 % of the protein remaining as reduced monomers after ~300 hrs of incubation (Figs. 4.3D, S4.4D). In contrast, A4V, and H43R show the most pronounced evidence of soluble aggregates species (Figs. 4.3C, F). A4V forms aggregates with hydrodynamic diameters of 40-60 nm within ~15 hrs of incubation, and these approximately double in diameter and increase in abundance over ~2 weeks. H43R forms 100-1000 nm species within ~60 hours, which also increase in abundance with time. For both mutants, at long incubation times the larger species dominate the scattering and the soluble monomers can no longer be observed. However, the total intensity of scattered light continues to increase, indicating continued aggregation (Fig. S4.5B). In general, the extent of aggregation of different mutants, as shown by the prominence of large species in the size distributions (Figs. 4.3, S4.4, 4.5A), is consistent with the extent of aggregation as indicated by total light scattering intensity (Figs. S4.5B-D). Both observations give similar indications of the relative aggregation propensities of different mutants. It should be noted, however, that lack of observation of the monomer peak does not indicate a predominantly aggregated sample. If one considers a hypothetical mixture containing only 5 and 50 nm species, due to the dependence of light scattering intensity on the sixth power of the diameter, when 99 % of the intensity arises from the 50 nm species, this species will account for only 0.1 % by mass of the total protein in solution (276). Therefore, the DLS data indicate only slight to moderate formation of soluble aggregates by reduced apo SOD1 variants, consistent with the DSC and centrifugation data.

4.4 Discussion

The biophysical analyses conducted here show that ALS-associated mutations have the most pronounced effects on stability in the reduced apo form of SOD1, and enhance the formation of soluble aggregates. These represent the first in depth analyses of reduced apo SOD1 stability and aggregation, and have important implications for understanding mechanisms of SOD1 aggregation that may be involved in ALS, considered further below.

4.4.1 In the absence of ALS-associated mutations, reduced apo SOD1 is predominantly folded and has low aggregation propensity under physiologically relevant conditions

The unfolding of pWT measured here by DSC and chemical denaturation is well fit by a reversible 2-state monomer unfolding transition, based on multiple DSC and chemical denaturation criteria (Figs. 4.2C, S4.2D,E, Table 4.1), and comparable results are obtained by DSC for WT (Fig. 4.2E, Table 4.1). These results reveal that the ΔG of unfolding for reduced apo SOD1 at 37 °C, which has not been reported previously, is 1.8 ± 0.1 kcal mol^{-1} for pWT and 1.6 ± 0.0 kcal mol^{-1} for WT. Thus, at physiological temperature and pH the protein is predominantly folded, and shows very little tendency to aggregate.

The very minimal aggregation observed here for monomeric reduced apo pWT and WT is particularly noteworthy given that previous studies have reported monomerization and loss of metals greatly enhance, or are required for, aggregation (76, 193). Moreover, several studies have reported observations of amyloid formation by apo SOD1 in which the intramolecular disulfide bond was reduced or removed by mutagenesis (76, 78, 184). A key difference between these and the current studies is their use of agitation rather than quiescent solution conditions. It is well established that agitation promotes the aggregation of many proteins, often as amyloid

(76, 278, 279). This is not well understood but likely involves interface effects and perhaps also accelerated oxidation of free thiols.

The relevance of the formation of amyloid aggregates in previous studies of reduced apo SOD1 to ALS disease mechanisms is not clear. Other forms of SOD1 have also been shown previously to form amyloid under destabilizing conditions caused by denaturant, sonication, trifluoroethanol or low pH (75, 76, 78, 255), and formation of intermolecular disulfide bonds (183). In contrast, other studies under less extreme conditions have also reported evidence for distinct aggregation processes from native-like states (90, 99, 280). Protein aggregation is generally strongly dependent on solution conditions, and many destabilizing and often non-physiological conditions can result in the formation of amyloid. In this regard, it should be noted that the amyloid-specific characteristic of green-gold Congo Red birefringence and ThT binding of aggregates is not observed in ALS (22, 266) and the intracellular SOD1-containing aggregates in fALS have a granule-coated rather than the smooth fibrillar structure characteristic of amyloid (26); thus, ALS is not a typical amyloid disease.

A key aspect for in vitro studies of aggregation is to consider their relation to in vivo conditions. Here we have used physiologically relevant conditions of temperature, pH, protein concentration and quiescence. Importantly, the very minimal aggregation of reduced apo pWT and WT is consistent with cell culture and mice studies where wild-type SOD1 shows very little tendency to aggregate and mice do not develop ALS symptoms (268, 269). This differs from observations for mutant SOD1s, which tend to aggregate more than WT in cell culture, and form small aggregated species in mice prior to the onset of symptoms followed by large disulfide-linked aggregates in the final stages of disease (190, 268). In contrast, in previous in vitro studies the comparable wild-type-like constructs not only formed amyloid (76, 78, 184) but in

some cases this was more pronounced than for ALS-associated mutants (184). This suggests fundamentally different aggregation processes are being observed under different conditions.

4.4.2 ALS-associated mutations have complex effects on stability and aggregation

Under the physiologically relevant conditions used herein, we were able to measure the effects of many chemically and structurally diverse ALS-associated mutations on stability and aggregation propensity. The effects on stability range from slightly stabilizing to slightly or significantly destabilizing (Fig. 4.1C, Tables 4.1, S4.2). Consistent with previous studies on apo SOD1 where metal binding mutations had relatively small effects on $t_{0.5,app}$ (245), the metal binding mutants H46R and G85R are among the most stable mutants studied here. In the disulfide-oxidized apo form, all the mutants have $t_{0.5,app}$ values well above physiological temperature; however, in the reduced apo form, most have $t_{0.5,app}$ values close to or lower than 37 °C, indicating that they will be 50% or more unfolded at physiological temperature (Fig. 4.1D, Table S4.2). The observation that decreases in melting temperatures tend to be largest in the reduced apo form implies that substantial increases in the population of unfolded conformations will also occur for many other mutants that have been found to have decreased $t_{0.5,app}$ in the disulfide-oxidized apo form (128, 134, 245). Thus overall, many but not all ALS-associated mutations are likely to significantly increase the population of reduced apo unfolded monomers.

Regardless of stability, the DSC, AUC and DLS experiments indicate that the reduced apo mutants generally have increased propensity to misfold/aggregate. In particular, DLS results indicate that distinct sizes of small, soluble aggregates are observed for different mutants (Figs. 4.3, S4.4, S4.5A). Evidence for structural polymorphism of SOD1 aggregates was also reported

for agitation-induced aggregation (181). These findings are intriguing as variations in aggregate structures may cause different disease phenotypes.

4.4.3 Limited correlations between the properties of reduced apo mutant SOD1s and ALS characteristics implicate multiple forms of SOD1 in modulating disease

Correlations between the properties of mutant SOD1 and ALS disease characteristics have been sought for many years and are critical for deciphering disease mechanisms. Previous studies have reported evidence for a weak inverse correlation between oxidized apo SOD1 stability and ALS disease duration (176, 200, 229), which improves when global or local protein characteristics such as charge (281) or hydrogen bonding (200) are considered. The results for V148I suggest that increased hydrophobicity of the exposed dimer interface may be another significant modulator of aggregation. A weak correlation is observed between reduced apo mutant SOD1 stability and disease duration (Figs. 4.4 and S4.6A), suggesting that the effects of the mutations on the stability of reduced apo SOD1 do not play a more significant role than their effects on oxidized apo in determining disease duration. This implies that factors beyond stability, and multiple forms of SOD1, are important in modulating disease duration.

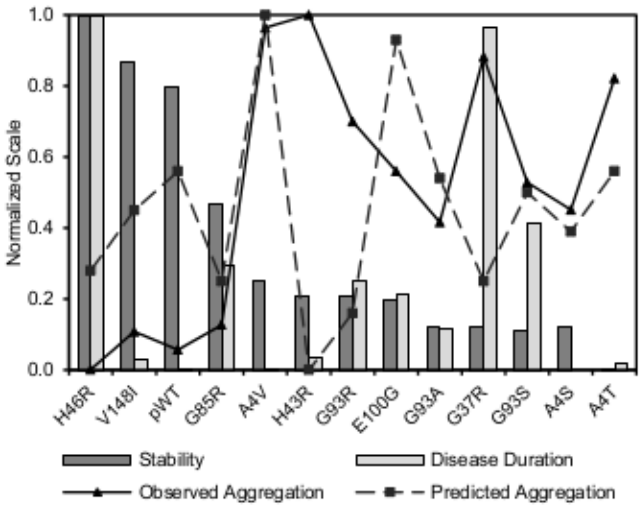

Figure 4.4 A correlation plot representing the relationship between reduced apo SOD1 mutant stability, fALS disease durations, and observed and predicted aggregation. The stability is determined by a change in apparent $t_{0.5}$ of mutants compared to pWT and normalized, from 0 (least stable) to 1 (most stable). Observed aggregation is based on DLS measurements as described in Fig. S4.5A. Predicted aggregation based on the Chiti *et al*. 2003 method (282) was normalized from 0 (lowest propensity) to 1 (highest propensity). Disease duration (229) is normalized from 0 (short) to 1 (long). The aggregation-prediction analysis was performed by Heather A. Primmer.

There is a significant correlation (r = 0.78, Figs. 4.4, S4.6B) between observed aggregation and mutant destabilization, consistent with results of general studies of protein aggregation. This has also been observed for more mature forms of SOD1 which tend to aggregate more readily when destabilized (128, 131, 144, 184). The aggregation observed here is poorly correlated with nine different aggregation prediction models (Fig. S4.6E, SI Text). The lack of correlations may be because most of these aggregation prediction algorithms were developed based on datasets of amyloid forming proteins and peptides. As noted above, amyloid formation may differ significantly from the formation of the soluble, non-amyloid aggregates that are characterized here. There is also no significant correlation between observed aggregation and ALS disease duration (Fig. 4.4, S4.6C). Furthermore, the aggregation propensities of the SOD1 mutants predicted using the preceding methods are also poorly correlated with disease duration (Fig. S4.6D).

Consideration of these correlations points to two key conclusions: neither the association of reduced apo SOD1 mutants into small soluble aggregates nor the predicted aggregation propensities of SOD1 mutants are able to account for fALS disease duration. These key findings have two important implications: i) Multiple forms of SOD1 are likely to modulate disease characteristics and ii) amyloid formation is likely not an important factor in SOD1-associated fALS. Further support for the first point is evidence that mutations enhance the population and aggregation of various immature forms of mutant SOD1, and the observation of multiple forms of SOD1 in aggregates in vivo (90, 126, 128, 196, 268, 280, 283). The second point is further supported by evidence that fALS patient data fails to reveal any support for a role of amyloid in disease (22).

In conclusion, the results reported here provide novel and important data on the stability and soluble aggregate formation by reduced apo SOD1s, which should prove useful for further testing of ALS disease hypotheses. The increased aggregation of reduced apo SOD1 upon mutation suggests that this form of the protein may play a role in causing disease. However, the lack of strong correlations between reduced apo SOD1 stability and disease duration and between measured aggregation and disease duration, imply that the effects of mutations on reduced apo SOD1 are unlikely to be the dominant factor in modulating disease, and that multiple forms of the protein are involved. Unravelling the complex aggregation processes that are likely to contribute to the syndrome of ALS (284) may ultimately lead to new and urgently needed approaches for treating this devastating disease.

4.5 Supplementary Information

4.5.1 Analysis of Differential Scanning Calorimetry (DSC) thermal unfolding data

Thermal unfolding scans for reduced apo SOD1 were fit to a 2-state monomer unfolding model ($N \leftrightarrow U$) using the following Eq. 4.1 (237):

$$C_p(T) = (A + BT)(1 - f_u) + (C + DT)f_u + \frac{\beta \Delta h^2(T) f_u (1 - f_u)}{RT^2} \quad \text{(Eq. 4.1)}$$

where, $C_p(T)$ is the total specific heat capacity, normalized per gram of protein, at temperature, T (in Kelvin), f_U is the fraction of unfolded protein at T, R is the universal gas constant, $\Delta h(T)$ is the specific enthalpy of unfolding at T, A and B are the intercept and slope of the native baseline respectively, whereas C and D are the intercept and slope of the unfolded baseline respectively. β is a temperature-independent constant equal to the molecular weight of the dimer multiplied by the ratio of van't Hoff to calorimetric enthalpies of unfolding, $\Delta H_{vH}/\Delta H_{cal}$. The DSC data were fit to the approximate end of the unfolding transition due to the occurrence of downward sloping post-transition baselines, presumably due to exothermic aggregation of the unfolded protein at higher temperatures.

The baselines for scans obtained in urea for the determination of the change in heat capacity upon unfolding, ΔC_p, had higher variability, which created problems in obtaining consistent fitted values using Eq. 4.1. Accordingly, scans in urea were analyzed using the commonly employed baseline subtraction with linear connect (which effectively removes the influence of the baselines), followed by fitting of the resulting excess specific heat capacity, $C_p(T)$ normalized per mol of protein, to the MN2-state model, Eq. 4.2 (Microcal Origin version 5.0) (128, 285–288):

$$C_p(T) = \frac{\gamma \Delta H^2(T) f_u (1 - f_u)}{RT^2} \quad \text{(Eq. 4.2)}$$

where $\Delta H(T)$ is the enthalpy of unfolding at T, f_U is the fraction of unfolded protein and γ is $\Delta H_{vH}/\Delta H_{cal}$. Fitted parameters for reduced apo pWT datasets acquired in the absence of urea gave fitted parameters that were very similar to those obtained using Eq. 1 (<0.5 °C difference for $t_{0.5}$ (temperature in °C at which $f_U = 0.5$) and <10 % difference for ΔH_{vH} and ΔH_{cal}).

The fraction of unfolded protein can be determined from the equilibrium constant, $K(t)$, at temperature, t (°C) using Eq. 4.3 and Eq. 4.4:

$$f_u = \frac{-1+\sqrt{1+\frac{8}{b}}}{\frac{4}{b}} \quad \text{(Eq. 4.3)}$$

where, $b = \frac{K(t)}{K(t_{0.5})}$ (Eq. 4.4)

4.5.2 Calculation of thermodynamic parameters at 37 °C

$\Delta H(T)$, $\Delta S(T)$ and $\Delta G(T)$ of thermal unfolding were calculated at 37 °C (310.15 K) using a temperature independent ΔC_p as previously described (128) using the following equations:

$$\Delta G(T) = \Delta H(T) - T\Delta S(T) \quad \text{(Eq. 4.5)}$$

$$\Delta H(T) = \Delta H(T_{0.5}) - \Delta C_p(310.15 - T_{0.5}) \quad \text{(Eq. 4.6)}$$

$$\Delta S(T) = \Delta S(T_{0.5}) + \Delta C_p \ln(\frac{310.15}{T_{0.5}}) \quad \text{(Eq. 4.7)}$$

$$\Delta S(T_{0.5}) = \frac{\Delta H(T_{0.5}) + \Delta G(T_{0.5})}{T_{0.5}} \quad \text{(Eq. 4.8)}$$

and $\Delta G(T_{0.5}) = -RT_{0.5}\ln P$ (Eq. 4.9)

where P is the protein concentration of monomer subunits and $t_{0.5}$ is the temperature at which the protein is half unfolded.

4.5.3 Analytical ultracentrifugation

Sedimentation velocity and equilibrium experiments were conducted at the Biomolecular Interactions & Conformations Facility (Shuclich School of Medicine & Dentistry, University of Western Ontario) using an Optima XL-A Analytical Ultracentrifuge (Beckman Coulter Inc.) with an An60Ti rotor and 2/6-channel cells with Epon-charcoal centerpieces. Centrifugation was carried out at 20 °C, 20 mM HEPES, 1mM tris(2-carboxyethyl)phosphine (TCEP), pH 7.4, with absorbance detection at either 252 or 280 nm. Equilibrium data were collected in radial step sizes of 0.002 cm and averaged over 10 readings. Equilibrium data were fit to a single ideal species model (see below) using Prism 5 (GraphPad Software).

4.5.4 Analysis of sedimentation equilibrium data

Data were analyzed according to a single ideal species model as described elsewhere (289), according to Eq. 10:

$$A = A_o exp\left[\frac{\omega^2}{2RT} MW_{obs}(1 - \bar{v}\rho)(x^2 - x_o^2)\right] + I_o \qquad \text{(Eq. 4.10)}$$

where A is the absorbance at radius x, A_o is the absorbance at reference radius x_o, ω is the angular velocity of the rotor, MW_{obs} is the fitted molecular weight of the protein, $\bar{\upsilon}$ is the partial specific volume of the protein, ρ is the density of the solvent, and I_o is the baseline offset.

4.5.5 Chemical renaturation and denaturation

Chemical renaturation and denaturation equilibrium curves of reduced apo SOD1 were prepared as described elsewhere (134), except that urea was used as the denaturant instead of guanidinium chloride. All samples contained 1 mM TCEP, 20 mM HEPES, pH 7.4 and were incubated for 24 hrs at 25 °C in an anaerobic environment before measuring circular dichroism

(CD) at 216 and 231 nm using a J715 spectropolarimeter (Jasco Research Ltd.). Data were fit to a 2-state monomer unfolding model as described (290) according to Eq. 4.11:

$$Y_{obs} = \frac{\{(Y_N^o - S_N[urea]) - [(Y_N^o - S_N[urea]) - (Y_U^o - S_u[urea])]\}e^{\frac{m([urea] - C_{mid})}{RT}}}{1+e^{\frac{m([urea] - C_{mid})}{RT}}} \quad \text{(Eq. 4.11)}$$

where, Y_{obs} is the observed optical signal, Y_N° and Y_U° are the native and unfolded signals respectively, in the absence of urea, and S_N and S_U describe the dependence of the native and unfolded signals with urea respectively. m is a constant that describes the dependence of the free energy of unfolding ΔG_U on urea concentration and C_{mid} is the concentration of urea at the midpoint of the curve, corresponding to the point at which $f_U = 0.5$.

4.5.6 Acquiring predicted aggregation propensities from a variety of known algorithms

In order to further investigate aggregation mechanisms, the following methods were used to compare predicted mutant SOD1 aggregation with observed reduced apo mutant SOD1 aggregation and disease duration: Chiti et al. (282) and Wang et al. (229) methods, and online algorithms including Zyggregator (http://www-vendruscolo.ch.cam.ac.uk) (291), PASTA (http://protein.bio.unipd.it/pasta2/) (292), Waltz (http://waltz.switchlab.org/) (293), TANGO (http://tango.crg.es/) (294), FoldAmyloid (http://bioinfo.protres.ru/fold-amyloid/) (295), and Profile3D (http://services.mbi.ucla.edu/zipperdb/) (296). Predictions were made for pseudo WT (pWT) and all 12 mutants presented in this study. Additionally, 13 extra mutants with disease duration averages based on 5 or more patients (229) were predicted and included in the correlations for disease duration. All results were compared to pWT and no convincing correlations between predicted aggregation propensity and observed aggregation or familial amyotrophic sclerosis (fALS) disease duration were observed.

4.5.7 Supplementary Data

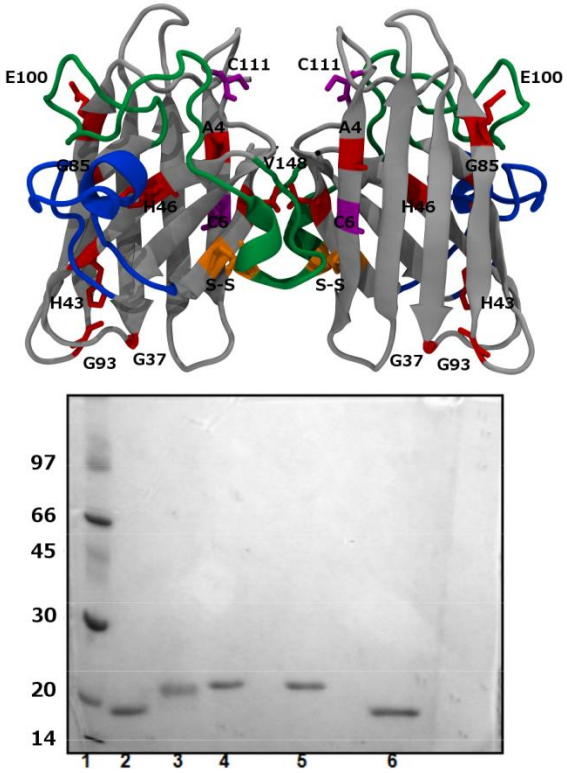

Figure S4.1 (A) Ribbon representation of apo SOD1 (pdb code 1HL4) (139). Each monomer binds one copper and one zinc (metals not shown). The locations of C57 and C146, which form the intramolecular disulfide bond in each monomer, are shown in yellow. The sites of the fALS-associated mutations that were investigated in this study (A4, G37, H43, H46, G85, G93, E100, and V148) are shown in red. The fALS mutations are dispersed throughout the structure of SOD1 and have a range of structural contexts. H46R and G85R (138, 297) alter metal binding, A4S, A4T, A4V, and V148 are located in the dimer interface, G93S, A, and R are in a tight turn, G37R and H43R disrupt packing in the β-barrel (255, 256), and E100G removes a salt bridge with K30 (143). Residues C6 and C111 are mutated to A and S respectively, in the pWT construct and are shown in purple. The figure was rendered using VMD software (http://www.ks.uiuc.edu/). **(B) SDS-PAGE of reduced apo SOD1 before and after DSC experiments.** The gel contained 12% acrylamide and was visualized by staining with Coomassie Blue. Lane 1 is a low molecular weight marker with molecular weights as indicated. Lanes 2 and 6 are disulfide-intact apo SOD1 controls, whereas lane 3 is apo SOD1 with disulfide reduced by β-mercaptoethanol. Lanes 4 and 5 are reduced apo SOD1 in 20 mM HEPES, 1 mM TCEP, pH 7.4 before and after DSC scanning, respectively. These samples were treated with iodoacetamide prior to loading on the gel to prevent free cysteines from being oxidized on the gel (131). Samples, both before and after each experiment, were found to run much closer to the disulfide-reduced control in lane 3 than the oxidized controls in lanes 2 and 6, indicating that the samples remained fully reduced throughout each experiment.

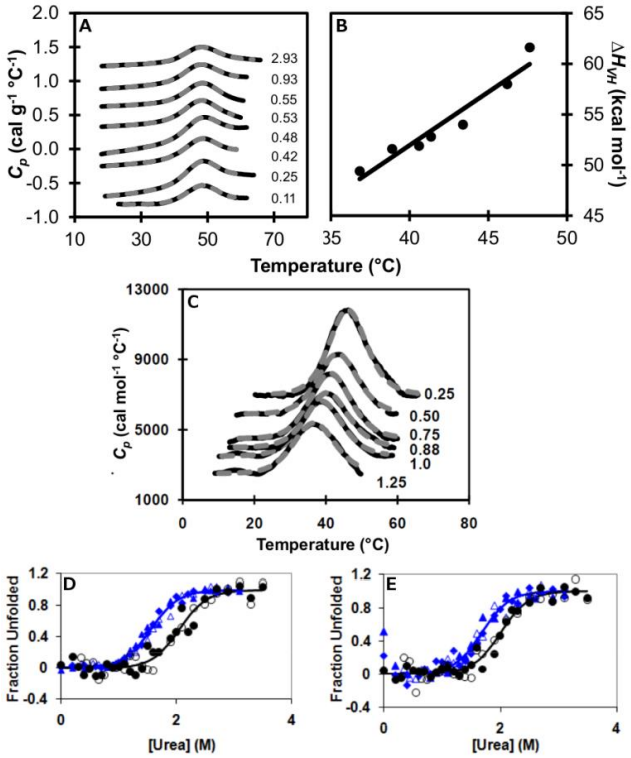

Figure S4.2 (A) Protein concentration dependence of reduced apo pWT thermal unfolding. DSC endotherms were collected in 20mM HEPES, 1mMTCEP, pH 7.4 at different protein concentrations as indicated (in mg mL^{-1}). There is no concentration dependent shift to higher temperatures of unfolding, as expected for a monomer. The data (solid black lines) over the >20-fold concentration range are well fit (broken grey lines) by a monomer two-state unfolding model (Supplementary Methods, Section 4.5.1, Eq. S4.1). Fitted parameters are given in Table S4.1. **(B) Kirchoff plot analysis of ΔC_p.** The ΔH_{vH} values were obtained from two-state monomer fitting of pWT DSC data collected in the presence of urea (see D and E). The ΔH_{vH} data are well fit by linear regression (r = 0.967) giving a ΔC_p value from the slope of 1.1 ± 0.1 kcal mol^{-1} °C^{-1}. **(C) Reduced apo pWT DSC scans in urea.** Baselines generated by the linear connect method in Origin 5.0 (Microcal) were subtracted from raw data and normalized for protein concentration, prior to fitting data to a two-state monomer unfolding model (Supplementary Methods, Section 4.5.1, Eq. S4.1). Fits (broken grey lines) are shown for data (solid black lines) collected in 20 mM HEPES, 1 mM TCEP, pH 7.4 with 0.25, 0.5, 0.75, 0.875, 1, and 1.25 M urea (Top to Bottom) as indicated. ΔH_{vH} values from the fits are plotted in Fig. S2A. **(D and E) Equilibrium urea renaturation and denaturation curves for reduced apo SOD1 at 25 °C.** Data for pWT are shown in blue and data for H46R are shown in black. Protein concentrations for the curves are 8.5 μM (0.13 mg mL^{-1}) (circles), 14 μM (0.22 mg mL^{-1}) (triangles), and 24 μM (0.38 mg mL^{-1}) (diamonds). Denaturation and renaturation data are plotted as closed and open symbols, respectively. CD data for each protein at (D) 216 nm and (E) 231 nm were globally fit to a two-state monomer unfolding model with C_{mid} and m as shared parameters (Supplementary Methods, Section 4.5.5, Eq. S4.11). pWT and H46R yielded similar m values with the average being 2.49 ± 0.30 kcal mol^{-1}, whereas the midpoint of denaturation (C_{mid}) for pWT was 1.63 ± 0.07 M and 2.04 ± 0.04 M for H46R, corresponding to ΔG of 4.0 ± 0.2 kcal mol^{-1} and 5.1 ± 0.1 kcal mol^{-1} for pWT and H46R respectively (Table 4.1).

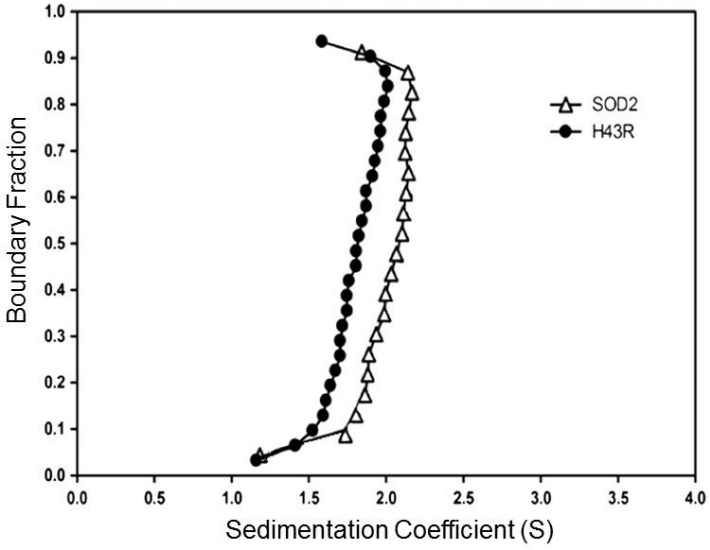

Figure S4.3 Van Holde–Weischet analysis (298) **of sedimentation velocity analytical ultracentrifugation experiments for reduced apo pWT and H43R SOD1.** Experiments were conducted in 20 mM HEPES, 1 mM TCEP, pH 7.4 at 20 °C using an Optima XL-A Analytical Ultracentrifuge (Beckman Coulter Inc.) with an An60Ti rotor and two channel cells with Epon-charcoal centerpieces and absorbance detection at 280 nm. All velocity data were acquired at 50,000 rpm with measurements (average of three readings) collected at radial step sizes of 0.003 cm; scans were taken at 10 minute intervals for a total of 30 scans. Data were analyzed using the program Sedfit (299). The initial absorbances at 280 nm were 0.29 and 0.33 for pWT and H43R respectively.

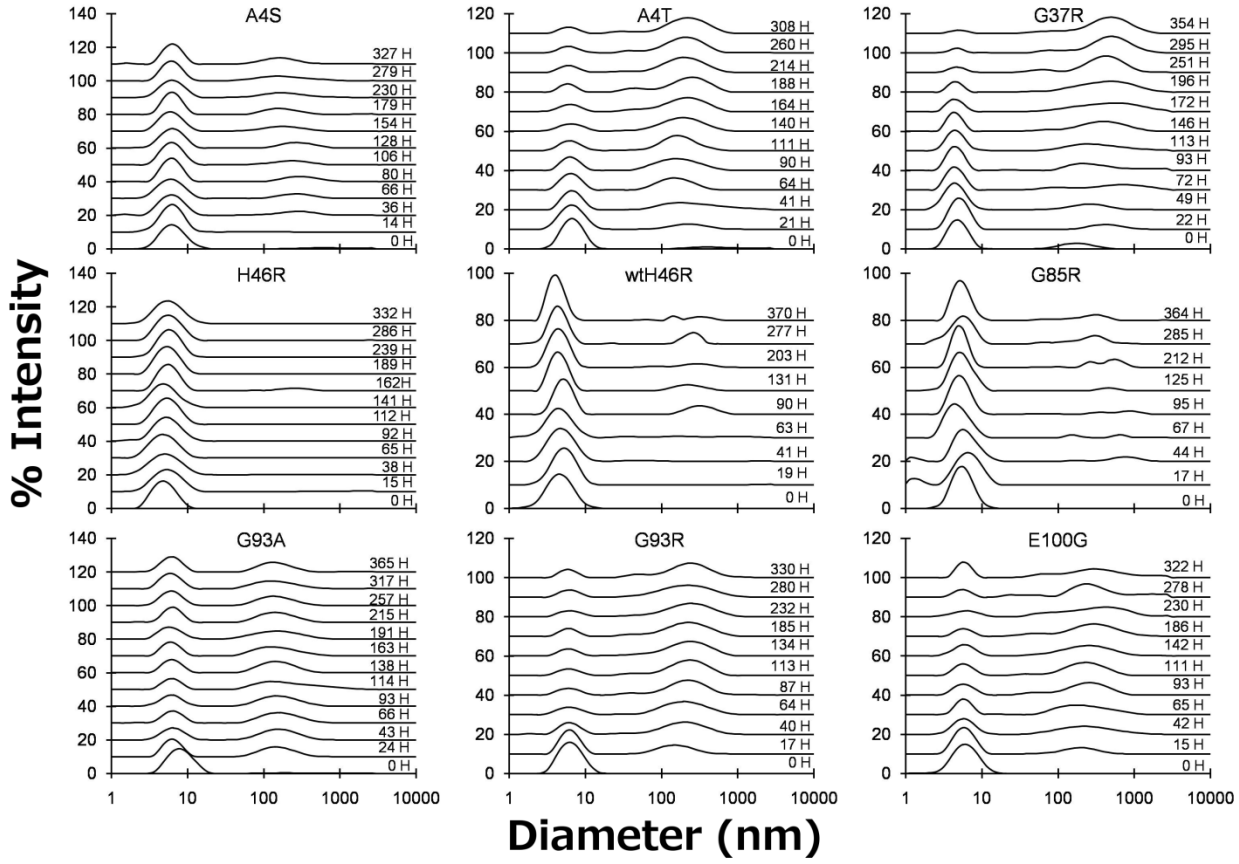

Figure S4.4 Particle size distributions for apoSH A4S, A4T, G37R, H46R, wtH46R, G85R, G93A, G93R, and E100G as a function of incubation time in hours (H). Samples contained 1 mg mL^{-1} protein in 20mM HEPES, 1mM TCEP, pH 7.4. The differing aggregation tendencies of each mutant are shown. The monomer remains the dominant species and after incubating G85R, H46R, and wtH46R for ~300 H, whereas diminished monomer intensity and varying amounts of larger species form after incubating A4S, A4T, G37R, G93A, G93R and E100G under the same conditions. There is no significant difference in the aggregation behavior of H46R in the pWT and WT background.

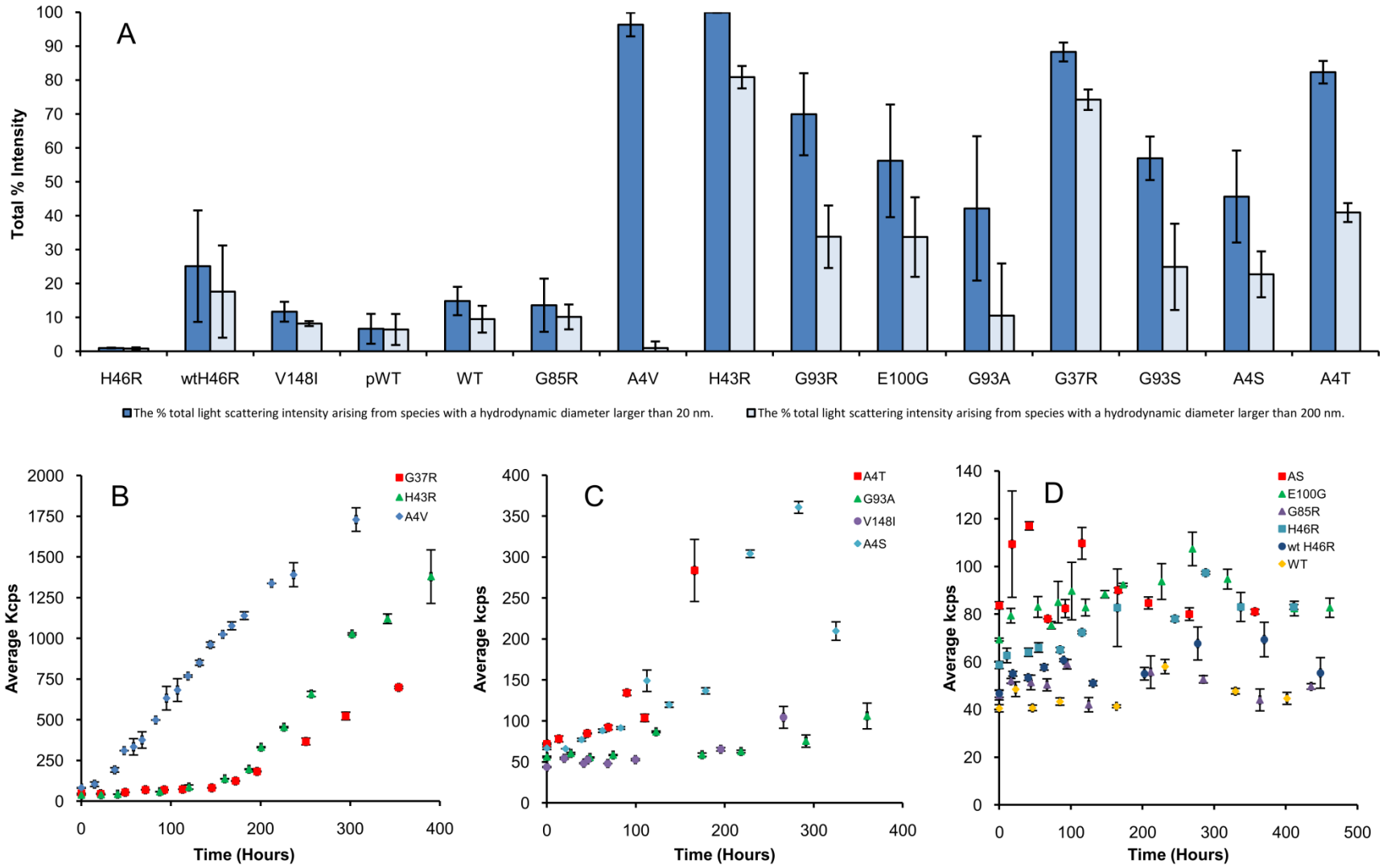
A
Total % Intensity
H46R
wtH46R
V148I
pWT
WT
G85R
A4V
H43R
G93R
E100G
G93A
G37R
G93S
A4S
A4T
The % total light scattering intensity arising from species with a hydrodynamic diameter larger than 20 nm.
The % total light scattering intensity arising from species with a hydrodynamic diameter larger than 200 nm.
B
Average Kcps
Time (Hours)
G37R
H43R
A4V
C
Average kcps
Time (Hours)
A4T
G93A
V148I
A4S
D
Average kcps
Time (Hours)
AS
E100G
G85R
H46R
wt H46R
WT

Figure S4.5 Summary of apoSH aggregation results. (A) To address reproducibility, each DLS experiment was repeated between two and five times and the percent of total light scattering intensity after incubation for ~300 H arising from species with a hydrodynamic diameter larger than 20 nm (dark blue bars) and 200 nm (light blue bars) was compared. The reproducibility of each DLS experiment is reflected by the error bars. **(B–D)** Change in light scattering intensity (in kilocounts per second (kcps)) as a function of incubation time is shown for all mutants studied. All values plotted are an average of three measurements at each time point shown over the duration of the time course. The data acquired for each mutant were categorized into three plots: **(B)** mutants that showed significant aggregation, **(C)** mutants that show evidence for slight to moderate increased aggregation tendencies, and **(D)** mutants that showed very little to no evidence of aggregation.

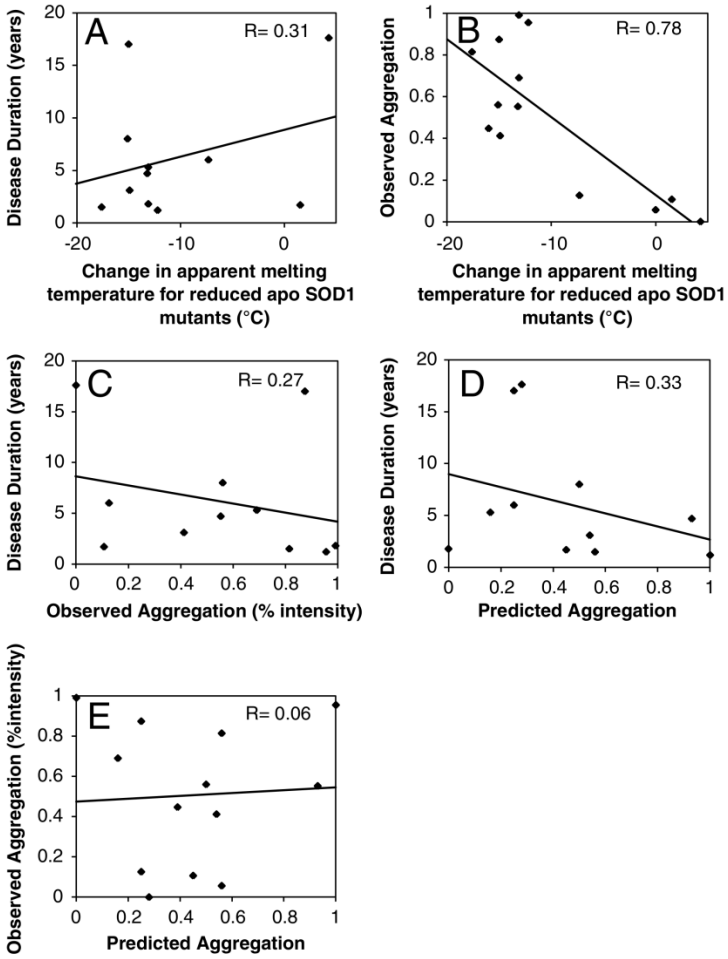

Figure S4.6 A correlation plot of reduced apo SOD1 mutant stability, observed aggregation, predicted aggregation propensity and disease duration. Stability is represented as the change in $t_{0.5,app}$ for reduced apo SOD1 upon mutation. Observed aggregation values are based on light scattering intensity at the end of each mutant SOD1 DLS time course (see Fig. S5A). Predicted aggregation was assessed for SOD1 mutants based on the Chiti *et al.* method (282). Aggregation values are normalized in such a way that 1 represents the most aggregation and 0 represents the least aggregation. Finally, disease duration is based on summarized data by Wang et al. (229) and is normalized so that 1 represents mutants with the longest disease durations and 0 represents mutants with the shortest disease durations. **(A)** A poor correlation is observed between mutant reduced apo SOD1 stability and disease duration. **(B)** Increased observed reduced apo SOD1 aggregation correlates well with a decrease in mutant stability. Disease duration is poorly correlated with observed reduced apo SOD1 aggregation **(C)** and predicted SOD1 aggregation **(D)**. **(E)** There is no correlation between observed and predicted aggregation (refer to Table S4.2).

Table S4.1 DSC monomer 2-state unfolding fitted parameters for disulfide-reduced apo SOD1s.

ApoSH SOD1 variants	[Protein] (mg/mL)	$t_{0.5}$[a] (°C)	$\Delta C_p(t_{0.5})$[b] (kcal (mol)$^{-1}$°C^{-1})	$\Delta H_{vH}(t_{0.5})$[c] (kcal (mol)$^{-1}$)	$\Delta H_{cal}(t_{0.5})$[c] (kcal (mol)$^{-1}$)	$\Delta H_{vH}/\Delta H_{cal}$
pWT	0.11	47.3±0.1	1.12	63.5±1.7	47.9±0.8	1.33
pWT	0.25	47.0±0.5	1.66	60.4±1.1	62.6±0.7	0.96
pWT	0.42	47.4±0.3	0.88	63.2±2.8	52.4±1.9	1.21
pWT	0.48	47.8±0.6	0.80	62.5±5.4	59.4±4.0	1.05
pWT	0.53	47.5±0.0	0.71	60.2±0.6	60.2±0.4	1.00
pWT	0.55	48.8±0.0	-0.27	60.6±0.7	59.8±0.4	1.01
pWT	0.93	47.7±0.3	0.27	62.7±3.2	51.2±1.9	1.22
pWT	2.30	47.5±0.1	0.61	59.8±1.7	44.6±0.8	1.34
AVG[d]		47.6 ±0.5	0.72±0.57	61.6±1.5	54.8±6.6	1.14±0.15
H46R	0.33	52.3±0.1	-0.05	77.1±2.1	75.6±1.2	1.02
H46R	0.48	52.5±0.0	0.17	70.5±0.8	80.9±0.1	0.87
H46R	0.57	53.2±0.2	-1.39	70.5±2.9	73.2±1.6	0.96
AVG[d]		52.6±0.5	-0.42±0.84	72.7±3.8	76.5±4.0	0.95±0.08
V148I	0.74	51.8±0.9	-3.46	56.6±9.4	58.4±3.8	0.97
V148I	0.89	50.3±0.1	-1.77	60.3±1.3	67.0±0.8	0.90
AVG[d]		51.0±1.1	-2.62±1.19	58.4±2.6	62.7±6.1	0.93±0.05
G85R	0.17	40.6±2.0	-0.46	52.2±13.9	74.3±13.2	0.70
G85R	0.38	40.4±0.6	0.22	50.9±3.8	47.1±2.5	1.08
G85R	1.42	41.2±0.2	-0.11	49.3±1.5	35.0±0.7	1.41
AVG[d]		40.7±0.4	-0.11±0.34	50.8±1.5	52.3±20.2	1.06±0.36
E100G	0.43	35.0±0.1	0.32	42.2±1.0	32.8±0.4	1.24
E100G	0.49	32.7±1.1	0.87	45.5±6.8	37.9±4.8	1.20
E100G	0.75	33.0±0.1	0.89	43.4±1.3	32.3±0.7	1.34
E100G	0.80	32.1±0.1	1.07	42.1±1.2	32.6±0.5	1.29
AVG[d]		33.2±1.2	0.79±0.32	43.3±1.4	34.3±2.6	1.27±0.06
WT	0.34	46.5±0.0	0.53	57.9±1.0	34.7±0.25	1.68
WT	0.30	47.1±0.7	1.48	56.4±7.4	43.3±3.75	1.30
AVG[d]		46.8±0.4	1.01±0.67	57.2±1.1	39.0±6.1	1.49±0.27
H46R^{wt}	0.50	50.4±0.0	-1.86	55.5±0.9	64.9±0.63	0.86
H46R^{wt}	0.50	52.5±0.2	-0.40	63.6±1.6	70.9±1.26	0.90
H46R^{wt}	0.50	52.6±0.6	-0.77	64.4±6.0	85.2±5.19	0.76
AVG[d]		51.8±1.3	-1.01±0.76	61.2±4.9	73.7±10.4	0.84±0.07

[a]Errors (±) from the fitting program (Microcal Origin, version 5.0).
[b]Errors from individual fits could not be reliably determined because they are based on uncertainties in five independent variables.
[c]Errors derived using standard procedures (300) from errors in fitted $\Delta h_{cal}(t_{0.5})$ and β returned by the fitting program.

[d]Average and standard deviation.
Data for pWT, H46R, G85R and E100G was obtained by Kenrick A. Vassall. Data for WT, $H46R^{wt}$, and V148I was obtained by Helen R. Broom.

Table S4.2 Stability and aggregation summary for disulfide-reduced apo SOD1s.

ApoSH SOD1	$t_{0.5}$ (disulfide reduced)[a] °C	$\Delta t_{0.5}$ (disulfide reduced)[b] °C	$\Delta t_{0.5}$ (disulfide oxidized)[b,c] °C	Disease Duration (years)[d]	Predicted Aggregation Propensity[e]	Predicted Aggregation Propensity + Instability[f]	Observed Aggregation Propensity[g]
H46R	52.8 ± 0.4	4.3	3.0	17.6	0.28	0.00	0.00
V148I	50.0 ± 0.1	1.5	1.4	1.7	0.45	0.20	0.11
pWT	48.5 ± 0.3	n/a	n/a	n/a	0.56	0.32	0.06
G85R	41.2 ± 0.3	-7.3	-3.8	6.0	0.25	0.34	0.13
A4V	36.3 ± 0.2	-12.2	-8.9	1.2	1.00	1.00	0.96
H43R	35.4 ± 0.4	-13.1	-10.7	1.8	0.00	0.35	1.00
G93R	35.4 ± 1.8	-13.1	-10.1	5.3	0.16	0.46	0.70
E100G	35.3 ± 0.7	-13.2	-7.7	4.7	0.93	0.98	0.56
G93A	34.6[h]	-14.9	-10.3	3.1	0.54	0.77	0.42
G37R	33.5 ± 1.2	-15.0	-9.7	17.0	0.25	0.58	0.88
G93S	33.4 ± 1.2	-15.1	-8.6	8.0	0.50	0.75	0.53
A4S	32.5[h]	-16.0	-13.0	n/a	0.39	0.70	0.45
A4V	30.9 ± 0.3	-17.6	-14.9	1.5	0.56	0.87	0.82

n/a, not applicable

[a]Values are the apparent melting temperature where the observed C_p in the DSC scan is a maximum. The values listed are the average of at least two independent measurements unless otherwise noted. All experiments were performed by Kenrick A. Vassall, except V148I, which was performed by Helen R. Broom.

[b]Calculated as $t_{0.5,app\ mutant} - t_{0.5,app\ pWT}$, negative values indicate destabilization.

[c]$\Delta t_{0.5,app}$ data for A4V, G85R, E100G, G93S, G93A G93R were obtained from (128, 134). The $\Delta t_{0.5,app}$ data for H46R, V148I, H43R, G37R, A4S and A4T was obtained by Kenrick A. Vassall, except V148I which was obtained by Helen R. Broom.

[d]Average disease durations are from (229).

[e]Predicted aggregation propensities were calculated relative to pWT using the Chiti-Dobson method (282), and normalized using the methodology of Wang *et al*. (229), where 0 indicates low aggregation tendency and 1 indicates high aggregation tendency. Calculations were performed by Heather A. Primmer.

[f]$\Delta t_{0.5,app}$ incorporated into the predicted aggregation propensity as described by (229), and aggregation scores were normalized over a scale from 0 to 1. Calculations were performed by Heather A. Primmer.

[g]Observed aggregation propensity is based on intensity statistics from DLS measurements as shown in Figure S4.5.

[h]$t_{0.5,app}$ based on one measurement.

Table S4.3 Single species model fitting of analytical ultracentrifugation sedimentation equilibrium data.

Sample and Concentrations		Best fit molecular weight (kDa) ± standard error at different rotor speeds			
ApoSH SOD1	[SOD1] mg mL^{-1}	20 000 rpm	25 000 rpm	30 000 rpm	35 000 rpm
pWT	1.0	15.2 ± 0.4	15.0 ± 0.2	14.3 ± 0.2	13.5 ± 0.2
pWT	1.0	14.3 ± 0.3	15.1 ± 0.3	15.2 ± 0.2	14.1 ± 0.1
pWT	1.5	14.4 ± 0.3	15.6 ± 0.2	14.4 ± 0.1	12.4 ± 0.1
E100G	0.8	22.5 ± 0.4	21.3 ± 0.2	19.3 ± 0.2	17.5 ± 0.1
E100G	1.0	20.3 ± 0.4	19.3 ± 0.2	17.4 ± 0.2	16.6 ± 0.2
E100G	1.5	20.2 ± 0.3	19.3 ± 0.2	17.8 ± 0.2	16.4 ± 0.1
A4V	0.8	24.2 ± 0.6	21.1 ± 0.3	18.2 ± 0.2	16.5 ± 0.1
H43R	1.0	36.6 ± 0.6	31.6 ± 0.6	23.2 ± 0.3	19.8 ± 0.2
H43R	1.0	33.6 ± 0.4	28.4 ± 0.3	23.2 ± 0.2	20.5 ± 0.1

Experiments were performed and data analyzed by Lee-Ann K. Briere and Stanley D. Dunn.

Chapter 5

Further Aggregation Studies of Reduced Apo SOD1: Increases in protein concentration or the addition of salt both promote aggregation

Acknowledgements

Atomic force microscopy (AFM) experiments were performed in collaboration with Brenda Yasie Lee and Dr. Zoya Leonenko (Department of Physics & Astronomy and Department of Biology Waterloo Institute of Nanotechnology, University of Waterloo). I am very grateful for their expertise and for all the time they have spent helping me with this project. I would also like to thank Aron Broom for his invaluable help with the statistical analysis and interpretation of the AFM data. The Nuclear Magnetic Resonance (NMR) experiments discussed in this chapter were performed in collaboration with Dr. Ashok Sekhar and Dr. Lewis E. Kay (Departments of Molecular Genetics, Biochemistry and Chemistry, University of Toronto), and were part of a manuscript published in *eLife* in 2015 with the following authors: Sekhar, A., Rumfeldt, J.A.O., Broom, H. R.; Doyle, C.M., Bouvignies, G., Meiering, E. M., and Kay, L.E. (301).

Overview

In previous work (Chapter 4), we have characterized the stability of the most immature form of SOD1 (apoSH SOD1), which lacks both disulfide bonds and metals. This form of the protein is mainly monomeric, with marginal stability that is greatly affected by ALS-associated mutations. Surprisingly however, we found that apoSH SOD1 is remarkably resistant to aggregation under physiological-like conditions. Static and dynamic light scattering (SLS and DLS, respectively) as well as analytical ultracentrifugation (AUC) reveal higher-order interactions occur between apoSH monomers, but of the 12 mutants invested, only one showed some evidence of aggregate formation. In this chapter we demonstrate that apo aggregation is generally enhanced at higher protein concentration or in the presence of salt, and the mechanism(s) of aggregation have been characterized using a number of biophysical techniques including light scattering, atomic force microscopy (AFM), and Thioflavin-T (ThT) binding. Under conditions that promote aggregation, DLS and AFM experiments reveal that some mutants form small fibrils ranging from ~20-100 nm in length. Other mutants aggregate less, but the aggregates that do form are longer (greater than 1000 nm). Furthermore, ThT binding experiments suggest that the aggregates contain different degrees of internal β-structure. Thus, mutations appear to promote aggregation in different ways and these findings may agree with nuclear magnetic resonance (NMR) experiments, which show that mutations have complex effects on the energy landscape of apoSH SOD1, and alter the mechanisms of association.

5.1 Introduction

A characteristic feature of ALS is the presence of protein aggregates that accumulate in motor neurons (21) and SOD1 has been identified as a component of these aggregates in SOD1-linked familial ALS and some sporadic ALS patients (26, 29, 231). A major hypothesis in the field of ALS research is that mutations promote aggregation of SOD1, leading to a cascade of toxic events that culminate in motor neuron death (3). However, attempts to identify relationships between the effects of the mutations and ALS characteristics have shown that these effects are highly complex and not correlated with disease characteristics in a simple way (98, 229).

Immature SOD1 (apoSH) is a marginally stable monomer (98), subsequent metal binding and disulfide bond formation result in dimerization and marked increase in stability (151) (Section 1.3.1). The fully mature form of SOD1 (holoSS) has a melting temperature of ~92 °C (128), and can maintain enzymatic activity in strongly denaturing conditions (129). Yet, while mature SOD1 is highly stable against denaturation, ALS-associated mutants have increased tendency to be metal deficient (99), which increases the dynamics of the protein (135). Each SOD1 chain adopts an 8-stranded Greek key β-barrel structure with loops of differing length; the longest loops are referred to as the zinc-binding (Loop IV) and electrostatic loops (Loop VII). The zinc-binding loop contains the zinc-binding site, one of the cysteines in the intrasubunit disulfide bond, and residues involved in dimer interface formation (Fig. 1.5) (126, 130). Thus, zinc binding, disulfide bond formation, and dimerization limit the flexibility of the zinc binding loop and significantly increase protein stability (131). The electrostatic loop is important for SOD1 activity (133), and also for stabilizing the zinc-binding site (137). Both zinc-binding and electrostatic loops contain many hydrogen bonding interactions, which are believed to stabilize

the protein by providing a network of connections between the loops and the metal binding sites (130). Local unfolding of these loops and/or exposure of the edges of the β-barrel can participate in aberrant intermolecular interactions when metal binding is compromised (Section 1.3.6) (90, 148). In the absence of metal and disulfide bonds, vital interactions are lost causing the large loops to unravel and/or the dimer interface to be exposed, both of which could lead to aberrant intermolecular interactions (138).

In recent years, there has been extensive research on the aggregation of apoSH SOD1, as this unstable and dynamic form of the protein has been proposed to be particularly likely to aggregate in disease (1, 76, 131, 174, 180, 195). ApoSH SOD1 stability is relatively low compared to other globular proteins (1), far lower than more mature forms of SOD1 (Fig. 1.5) (128, 134), and is the form of SOD1 most destabilized by mutations (98). The thermal unfolding transition of apoSH starts to occur at only slightly above physiological temperature of 37 °C; and, mutations can greatly increase the fraction of unfolded monomers (98). Global destabilization by mutations is often accompanied by increases in local conformational dynamics and the energy landscape of apoSH appears to be complex (301). Potentially owing to this complex energy landscape, *in vitro*, the extent and type of aggregation for apoSH varies greatly with experimental conditions (Fig. 1.7) and some conditions strongly enhance aggregation of even wild type (WT) apoSH (Section 1.3.6) (2). In particular, denaturation and/or agitation of both WT and mutant apoSH can cause formation of various amyloid-like fibres (76, 179, 184). Recent studies have also shown that various forms of metal-free SOD1 can make amyloid-like fibres with smooth, unbranched morphologies under agitation conditions, and this occurs from the globally unfolded rather than the folded state (179). In contrast, we have shown that under quiescent solution conditions, both WT and pWT apoSH show little tendency to aggregate, and

mutants exhibit increased but still low levels of aggregation (Chapter 4) (174). These varying results suggest that the mode(s) of apoSH aggregation are particularly diverse and sensitive to varying conditions, due to the marginal stability of the protein and hence easily altered conformational properties. The challenge in studying physiologically relevant apoSH aggregation is to find proper experimental conditions such that aggregation is observed, but not inappropriately promoted so as to favour amyloid formation given that ALS is not considered an amyloid disease (22).

Here we show that by increasing the protein concentration and/or by adding 150 mM Na_2SO_4 or 150 mM NaCl, we observe differences in the aggregation propensity of diverse ALS-associated apoSH SOD1 mutants. By light scattering we see that some mutations promote rapid aggregation with little lag time, suggestive of aggregation from either the unfolded or native-like states, while others have more subtle effects on aggregation. Atomic force microscopy (AFM) reveals that mutations leading to high levels of aggregation tend to promote aggregation pathway(s) that result in abundant levels of small aggregates. AFM, in combination with Thioflavin-T (ThT) binding experiments, show that those apoSH mutants that exhibit lower aggregation propensity tend to form longer fibrils with more extensive β-structure. Intriguingly, such structural polymorphisms exhibited by apoSH aggregates may be analogous to different "strains" observed in prion aggregation (23). These results highlight how point mutations can have dramatic effects on the energy landscape of proteins, in particular marginally stable and highly dynamic proteins, and can modulate which aggregation pathways are either favoured or disfavoured.

5.2 Materials and Methods

5.2.1 Preparation of apoSH SOD1

ApoSH SOD1 was prepared from apo oxidized (apoSS) SOD1 as described previously (Chapter 4, Section 4.2.1) (174). Reduction of the disulfide bond was verified by SDS-PAGE as described (Chapter 4, Fig S4.1) (174). After reduction, 1 mg mL^{-1} apoSH samples were filtered using Anotop 10 filters with a 0.02 μm cut-off (GE Healthcare Life Sciences) to remove aggregates formed during the reduction procedure. 5 mg mL^{-1} samples could not be filtered using these filters, due to extensive sample loss; instead, samples were centrifuged at 16 300 rpm for 10 minutes to remove any large aggregates or dust particles. Salt samples were prepared according to the normal protocol and then salt buffered in 20mM HEPES, 1mM TCEP was added to the apoSH samples after reduction. During incubation, all samples were stored in a desiccator to avoid reoxidation. Aggregation was monitored using a variety of techniques (*vide infra*), and all these experiments were performed on 45 μL aliquots removed from the apoSH sample starting immediately after filtration (t_0) and approximately every 24 hours after t_0. To ensure that apoSH samples stayed reduced and that the samples' aggregation state was preserved, each 45 μL aliquot was flash frozen in liquid nitrogen and stored at -80 °C for future analysis.

5.2.2 Verifying the absence of metal for apoSH SOD1 samples

Preparation of apoSS SOD1 involves extensive dialysis of the protein against high concentrations of EDTA, which is later removed by further dialysis against EDTA-free buffer, as described (128, 134). Some EDTA remains bound to apoSS (302), which can protect the protein from re-binding zinc or copper; zinc, in particular, is found in trace amounts on glassware and in chemical reagents used for reducing SOD1. It is important to note that EDTA binding has been

found to have no effect on the stability of different forms of SOD1 determined by DSC (Broom, H.R., Doyle, C.M., and Meiering E.M., unpublished data). Preparation of apoSH involves unfolding the protein in GdmCl to expose the intramolecular disulfide bond to reducing agent, TCEP, which effectively removes all bound EDTA from the protein. As a result, apoSH is highly susceptible to re-metallation. To avoid this problem, initially all glassware was soaked in nitric acid. However, a high percentage of attempts to prepare metal free apoSH were nevertheless unsuccessful due to the presence of trace metals originating from reagents (Table S5.1). Even trace levels of metal can accumulate in apoSH samples due to the protein's very high affinity for metal (~6.8 x 10^{-18} M^{-1} and ~4.2 x 10^{-14} M^{-1} for copper and zinc, respectively) (303). To avoid metal accumulation, all buffers were treated with Chelex® 100 (Bio-Rad Laboratories Ltd.) metal-binding resin. Both approaches combined have proven to be effective at preventing metal contamination (Fig. 5.2, Table S5.1).

To verify that the protein did not become partially remetalled during reduction, a spectrophotometric metal-chelation assay using the chelator 4-(2-pyridylazo)rescorcinol (PAR) (Fig. 5.1) was performed. The PAR assay was originally developed by Crow *et al*. (304) and Mulligan *et al*. (258), and later refined by Heather Primmer and Colleen Doyle to measure the metal content of SOD1, as described by Doyle, C.M., 2009, unpublished MSc. thesis (305). While the PAR assay was used to assess the metal content of samples used for experiments discussed in Chapter 4 (174), metal analysis was not described and so will be described here.

PAR is a dye that binds transition metals with high affinity, resulting in a red shift in the absorbance spectrum of PAR from 415 nm to approximately 500 nm, depending on the metal (258, 304, 306). The molar absorbance coefficient of copper and zinc-bound PAR is very high,

36 300 and 69 200 M^{-1} cm^{-1}, respectively; thus, PAR is a sensitive indicator of metal ion concentration (304).

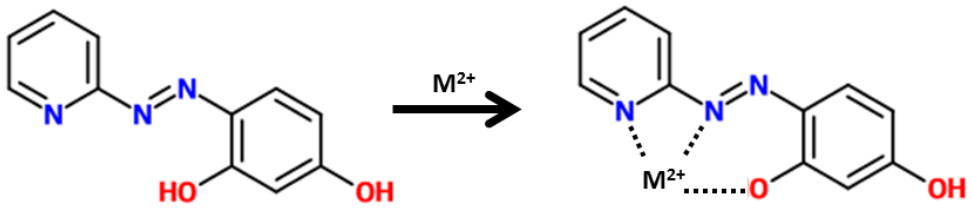

Figure 5.1 The molecular structure of apo and metal bound PAR. Copper and zinc binding to PAR is facilitated by the pyridyl nitrogen, one of the nitrogens within the azo moiety, and the oxygen of the 2-phenolate group within the resorcinol moiety. PAR binds copper in a 1:1 ratio and zinc in a 2:1 ratio when there is at least a 2.5-fold excess of PAR with respect to metal. The affinity of PAR for both metals is high, 7.7 x 10^{-11} and 2.6 x 10^{-15} M^{-1} for the $[PAR]_2$-zinc and [PAR]-copper complexes, respectively (304).

PAR_2-zinc and PAR-copper complexes exhibit different absorbance spectra (258, 304, 305). Either copper or zinc binding causes the absorbance at 490 and 520 nm to increase linearly with metal concentration relative to apo PAR. When copper binds to PAR, the increase in absorbance at both wavelengths is the same; however, when zinc binds the increase in absorbance at 490 is greater than at 520 nm (258). These differences in the absorbance spectra can be exploited to simultaneously quantify the amount of copper and zinc bound to SOD1 (Fig. 5.2). To do so, 45 µL of apoSH SOD1 was added to a mixture of PAR, GdmCl, and HEPES, pH 7.4 (final concentrations 100 µM PAR, 6 M GdmCl, and 20 mM HEPES) as described (305), and the absorbance spectrum was measured. Spectral deconvolution software, SpectraLab (http://cyp3a4.ucsd.edu/spectralab.html), developed by Dmitri Davydov, was used to deconvolute the [PAR], $[PAR]_2$-zinc and [PAR]-copper components of the experimental spectrum (307). This was done by fitting the experimental absorbance spectrum with a set of absorbance spectra standards for [PAR], $[PAR]_2$-zinc and [PAR]-copper, which returns multiplication factors for each standard that relate to the weighting of each component in the

experimental spectrum. These multiplication factors can be used to calculate the levels of copper and zinc in the sample.

The metal content in apoSH samples prepared for NMR experiments was determined by Inductively Coupled Plasma Atomic Emission Spectroscopy (ICP-AES) at the Analytical Laboratory for Environmental Science Research and Training, University of Toronto. The PAR and ICP-AES experiments confirm that the combined approach of soaking all glassware in nitric acid and treating buffers with Chelex® 100 resin prevents metal contamination.

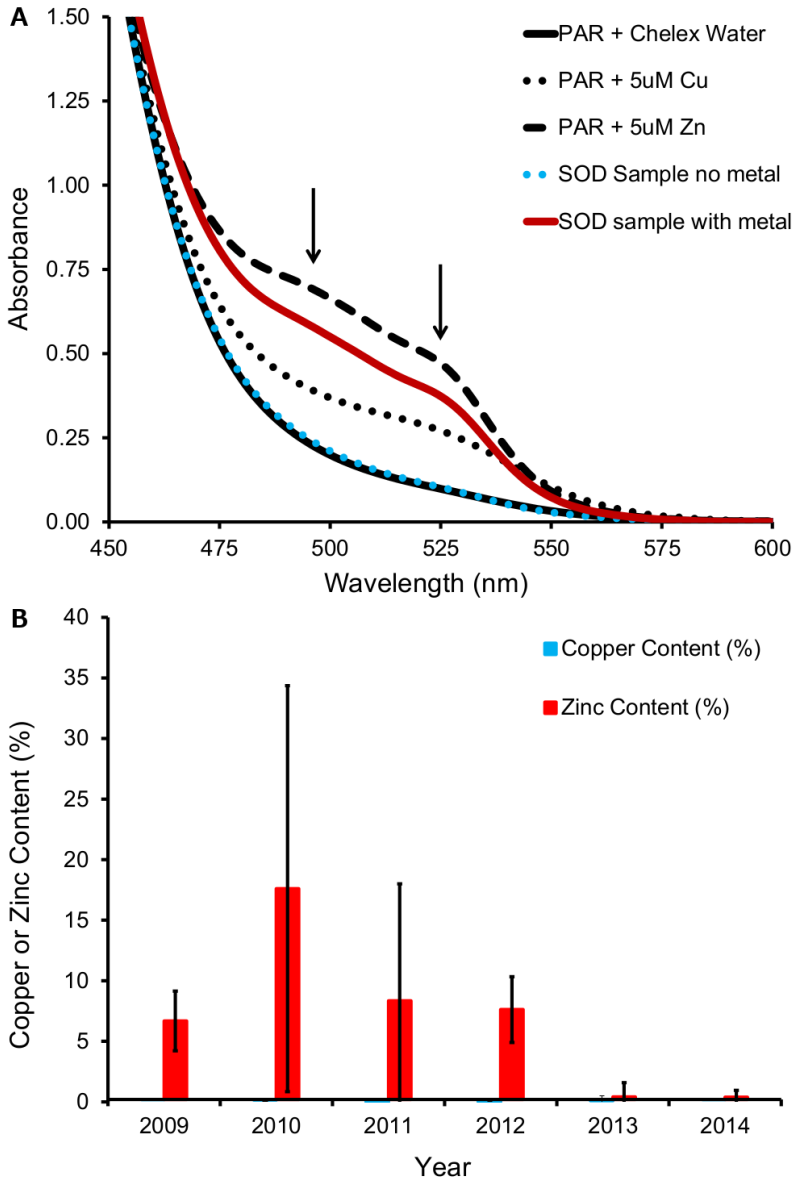

Figure 5.2 The PAR assay provides a sensitive method for determining metal content of apoSH samples. **(A)** The absorbance spectra of free PAR (solid black line), [PAR]-copper (dotted black line), and $[PAR]_2$-zinc (dashed black line) are shown. The changes observed in the [PAR]-copper and $[PAR]_2$-zinc spectra are due to the presence of 5 μM metal. Addition of a metal-free apoSH results in an absorbance spectrum that resembles free PAR (dotted blue line). An increase in absorbance at 490 and 520 nm indicates that the sample contains metal (solid red line). As illustrated in **(B)**, metal contamination was a large issue between 2009 and 2012, with numerous apoSH samples becoming highly metallated with zinc. Red bars reflect the average percentage of metal found in apoSH samples, and error bars are the standard deviation. After subsequently switching to the combined approach of soaking all glassware in nitric acid and treating all buffers with Chelex® 100 resin, very few samples were found to contain metal.

5.2.3 Light scattering experiments

Light scattering measurements were made according to the protocol described previously (Chapter 4, Section 4.2.4) (174). The intensity of light scattered (I) depends on the size and concentration of particles in solution. Fluctuations in light scattering intensity as a function of time ($I(t)$) depend on the translational diffusion coefficient (D_c) of the particles in solution (276, 308). According to the laws of Brownian motion, large particles diffuse at a slower rate than small particles. D_c relates to the hydrodynamic diameter (D_h), the diameter of a sphere that diffuses at the same rate as the particle being measured, according to the Stokes-Einstein equation (Eq. 5.1),

$$D_c = \frac{KT}{3\pi\eta D_h} \quad \text{(Eq. 5.1)}$$

where, K is the Boltzmann constant, T is the temperature, and η is the viscosity of the sample. D_c is determined from an autocorrelation function, which measures the correlation of $I(t)$ with itself after a series of delay times (τ) (276, 308). For a monodisperse sample, the decay in autocorrelation is related the translational diffusion of particles within the sample according to Eq. 5.2,

$$|g(\tau)| = \exp(-qD_c\tau) \quad \text{(Eq. 5.2)}$$

where g(τ) represents the exponential decay in autocorrelation and q is the light scattering vector, defined according to Eq. 5.3,

$$q = \frac{4\pi\eta\sin(\frac{\theta}{2})}{\lambda} \quad \text{(Eq. 5.3)}$$

where Θ is the light scattering angle and λ is the wavelength of the light (309). For polydisperse samples, the decay in autocorrelation of the signal will be polyexponential.

The PDI is related to the width (σ), or standard deviation, of the particle size distribution (Eq. 5.4) (310, 311).

$$PDI = \frac{\sigma^2}{Z_d^2} \quad \text{(Eq. 5.4)}$$

This parameter is obtained from fitting the autocorrelation function using the Cumulants method (311–313), which assumes the sample is monodisperse and the decay in autocorrelation is single exponential (311). The size obtained from this approach is referred to as the *Z*-average (Z_d), and represents the average D_h of all particles in solution. Therefore, the Z_d is only an accurate quantity when the sample is monodisperse (311, 314). In principal, monodisperse samples show PDI values less than 0.1 (308, 310, 315). For polydisperse samples, the Cumulants method of fitting is not valid and a multi-exponential fitting approach is required. This method is referred to as the CONTIN method (276, 311, 313). It is worth nothing that because many different distributions of species can lead to the same decay in autocorrelation when the sample is polydisperse, it is not possible to get precise distributions of similarly sized species that are not resolved by DLS. Therefore, PDI values provide an assessment of polydispersity, but not composition of the sample (316).

5.2.4 Seeding experiments

To test for seeding-induced aggregation of apoSH pWT and H43R, 45 μL aliquots of A4V and H43R samples left to incubate at 1 mg mL^{-1}, pH 7.4, 37 °C for ~300 hours and found to form aggregates by light scattering measurements, were added to 1 mL of freshly reduced and filtered apoSH samples. In the first experiment, A4V and evaporation-induced H43R amyloid aggregates were added to non-aggregated pWT; in the second experiment evaporation-induced H43R amyloid aggregates and as an additional control, H43R previously incubated at 1 mg mL^{-1}, pH 7.4, 37 °C for ~300 hours, that did not undergo evaporation-induced aggregation (herein referred to as non-amyloid aggregates), were also added to non-aggregated H43R. H43R does

not readily aggregate in the absence of evaporation-induced effects on the sample; therefore, this control provided a way to assess the effects of adding previously incubated and frozen apoSH samples on aggregation that are unrelated to the presence of aggregates in the sample.

5.2.5 AFM experiments

To prepare the AFM samples, 45 μL of apoSH solution was deposited on freshly cleaved mica, with a 0.15 mm thickness and 22 mm diameter (SPI Supplies, Structure Probe Ltd.). The sample was incubated on the bench at room temperature for 5 minutes to let the protein adhere to the mica surface. The excess solution was drawn off the surface of the mica by capillary action using a Kimwipe and then washed four times with 45 μL of milli-Q water using a micropipette. Between each rinse, the excess water was drawn off with a Kimwipe. Samples were then dried under a stream of air and then stored in a plastic Petri dish inside a desiccator to prevent dust or moisture accumulation.

Images were obtained using a JPK Nanowizard II atomic force microscope (JPK Instruments) in intermittent contact mode, where vertical deflection of the cantilever was recorded and used to reconstruct an image of the sample. For all experiments, monolithic silicon AFM tips with a radius of curvature less than 8 nm, force constant of 42 Nm^{-1}, and resonance frequency of 320 kHz were used (NCH type, Nanoworld Innovative Technologies). Multiple lower resolution 10 x 10 μm images were taken first (512 x 512 or 1024 x 1024 pixels) followed by multiple higher resolution 3 x 3 or 5 x 5 μm images (1024 x 1024 or 2048 x 2048 pixels). AFM images were analyzed using Scanning Probe Image Processor (SPIP) software , Particle and Pore Analysis (Image Metrology), to determine the length, breadth, height, volume, and aspect ratio of the particles detected as well as sample properties such as percent surface

coverage, which can be used to compare the extents of aggregate formation in different samples, and sample roughness, which assess how evenly distributed the protein is on the mica. Average coverage estimates obtained by SPIP were also used to gage the extent of aggregation of the different samples. Coverage is calculated by dividing the sample area (monomers and aggregates) by the total image area. Samples containing many aggregates will generally exhibit higher coverage on the mica.

SPIP software returns a number of different measures of particle size, which have differing accuracies depending on the aggregate morphology. Fiber length is defined as the longest segment within the aggregate skeleton and is found by reducing the particle to a width of one pixel and measuring the longest distance from end to end. The skeleton length, on the other hand, includes also all branches of the fibril (Fig. 5.3). Fiber width is calculated by dividing the total aggregate area by the fiber length. For particles that are highly spherical, the fiber and skeleton length will be an underestimate of the true length as there will be a significant loss in size at the ends of the aggregate when it is shrunk to one pixel in width (Fig. 5.3). In such cases, fiber width is then overestimated. This was found to be the case for apoSH particles; therefore, a different measure of length was used. Length estimates are determined simply by the end to end distance of the particle and breadth is defined as half the distance in the perpendicular direction. To obtain an estimate of the number of monomers within each particle, the volume obtained by SPIP software was divided by the volume of the apo monomer, ~18.8 nm^3, calculated from the crystal structure of the apoSS dimer (1HL4) using the Volume, Area, Dihedral Angle Reporter (VADAR) (317). There is currently no crystal structure of the apoSH monomer.

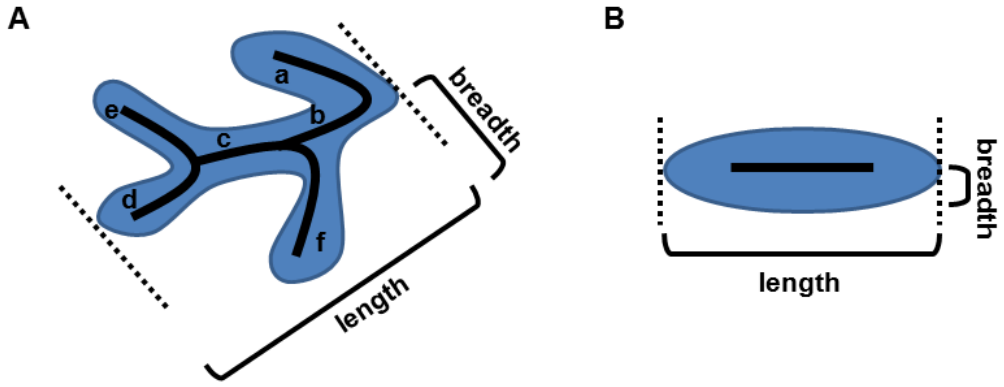

Figure 5.3 Aggregate morphology influences the accuracy of different size measurements. The measured area of the aggregates (blue) is calculated using SPIP, Particle and Pore Analysis software and is based on the number of pixels within the aggregate image (refer to SPIP manual at http://www.imagemet.com/). Fiber length is the longest segment of the aggregate reduced to a width of 1 pixel, shown as a solid black line in **(A)** and **(B)**. **(A)** For the branched fibril, fiber length is the sum of segments a, b, c, and d. Skeleton length is the sum of all segments, a, b, c, d, e, and f. **(B)** For small, more spherical aggregates, reducing the aggregate width to 1 pixel causes a significant loss in aggregate length and an underestimate of the aggregate length. Since the majority of SOD1 particles resembled the type shown in **(B)**, length as opposed to fiber length was used.

5.2.6 ThT binding experiments

Aggregated apoSH samples (45 µL aliquots) were diluted into ThT buffer, final concentration 25 µM ThT, 50 mM glycine, pH 9.0, as described (144). The final concentration of total protein was 32 µM and 160 µM for samples incubated at 1 mg mL^{-1} and 5 mg mL^{-1}, respectively. Fluorescence spectra from 455-575 nm were obtained immediately after dilution of the apoSH samples using first a Photon Technology International QuantaMaster 4 (Horiba-Jobin-Yvon Spex Inc.) (Fig. 5.6), and then a Fluorolog3-22 spectrofluorometer (Horiba-Jobin-Yvon Spex Inc.) (all other experiments), with an excitation wavelength of 440 nm. Excitation and emission slit widths of 1 and 5 nm, respectively were used. The spectra are the accumulated average of 5 scans.

5.3 Results

5.3.1 DLS experiments suggest higher order interactions between apoSH monomers at 1 mg mL^{-1}, pH 7.4, 37 ℃

Under quiescent, physiologically relevant conditions (1 mg mL^{-1}, pH 7.4, 37 °C), we have reported previously that reduced apo SOD1 (apoSH) shows increased tendency to form soluble aggregates, but that for most variants prolonged incubation does not result in high levels of aggregation (Chapter 4) (174). Light scattering offers a powerful method for detecting very small amounts of aggregated species, as the light scattering intensity is proportional to the D_h^6, where D_h is the hydrodynamic diameter (Eq. 5.1) (276). Intensity distributions, such as those reported in Figs. 4.3 and S4.4, weight particles according to the amount of light they scatter, hence will always emphasize larger particles, and such distributions can be misleading when trying to assess how much protein has aggregated. Number distributions however, weight particles according to their concentration in solution, and thus provide a more intuitive estimate of aggregation propensity.

Empirical calculations based on the polypeptide chain length show that the D_h of folded and unfolded apoSH SOD1 is ~4.2 and 7.8 nm, respectively (277). At 37 °C pWT, WT, H46R, and V148I, are predominantly folded (174); therefore, DLS measurements of a monodisperse sample should result in intensity and number distributions centred at ~4 nm, corresponding to the folded monomer. The DLS measurements obtained at t_0 for these variants show $D_{h,I}$ and $D_{h,N}$ values are consistent with the empirical calculations (average ~5.5 nm and ~3.1 nm, respectively) (Table 5.1). For destabilized mutants, especially those with $t_{0.5}$ values close to or lower than 37 °C (Fig. 4.1C, Table S4.2), the $D_{h,I}$ and $D_{h,N}$ of a monodisperse sample should be larger, between 4 and 8 nm. As expected for these mutants, the $D_{h,I}$ values at t_0 were found to be

larger (average ~7.2 nm) (Fig. 5.4, Table 5.1). While the $D_{h,N}$ values are generally smaller than 4 nm, destabilized mutants exhibit higher $D_{h,N}$ values than pWT and stabilized mutants, consistent with the trend observed for $D_{h,I}$ values (Table 5.1). Differences in $D_{h,I}$ and $D_{h,N}$ can arise when samples are not monodisperse. For instance, when both folded and unfolded monomers are populated and/or when particles larger than the apoSH monomer begin to form in solution. A single dimer, assuming it has double the volume of the monomer, will scatter ~5 times more light. Following similar logic, a trimer ~15 times more light compared to the monomer (318, 319). Thus, even low levels of higher order species will make larger contributions to the intensity distribution compared to the number distribution. Unfolded protein and/or higher order oligomers present at t_0 are unresolved by DLS measurements, and the result is a broad peak that emphasizes larger particles in the intensity distribution and smaller, more abundant particles in the number distribution. Interestingly, differences in $D_{h,I}$ and $D_{h,N}$ at t_0 are largest for A4V (~5 nm), and E100G, which is less stable and more unfolded 37 °C shows a smaller difference $D_{h,I}$ and $D_{h,N}$ values at t_0 (~3 nm). This finding suggests that the larger difference in these values observed for A4V may be due to the formation of higher order species, consistent with the higher aggregation propensity of this mutant (*vide infra*).

The PDI values, which exceed the value expected for a monodisperse sample (>0.1) also provide further confirmation that apoSH samples are not monodisperse at t_0. The PDI is also generally increased relative to pWT at t_0 for the destabilizing mutants, consistent with increases in the amount of globally unfolded protein, although we cannot rule out that destabilizing mutations may promote formation of higher order species such as dimers and trimers.

Under physiological-like conditions, light scattering intensity (Fig. S5.1), as well as intensity distributions plotted with number distributions as a function of time (Figs. 5.4 and S5.2)

reveal that, most apoSH variants aggregate very little when incubated for ~300 hours. The notable exception is A4V, where light scattering intensity and both $D_{h,I}$ and $D_{h,N}$ values increase with time. However, the average $D_{h,N}$ after ~300 hours of incubation (t_{300}) shows a high level of uncertainty (Table 5.1), demonstrating that not enough aggregates have formed in solution to give reliable estimates of their size by number distribution (Table S5.2). pWT, WT, and stabilizing mutations H46R and V148I show very little change in $D_{h,I}$ and $D_{h,N}$ over time (Fig. 5.1, Table 5.1). Yet, for destabilizing mutants (A4S, A4T, A4V, E100G, G37R, G93A, G93R, G92S, and V148G), the difference in $D_{h,I}$ and $D_{h,N}$ increases after prolonged incubation at 37 °C, due to increases in $D_{h,I}$. The exceptions are G85R, H43R which behave similar to pWT, WT, H46R, and V148I. Furthermore, aside from A4V, the $D_{h,N}$ values are very similar after incubation to values obtained at t_0, which suggests that the concentration of various species does not change much over the course of the incubation period. Although, for all variants, including pWT and WT, prolonged incubation results in an increase in the PDI, indicating that apoSH samples become more polydisperse over time, which could be due to the presence of very small amounts of aggregated protein.

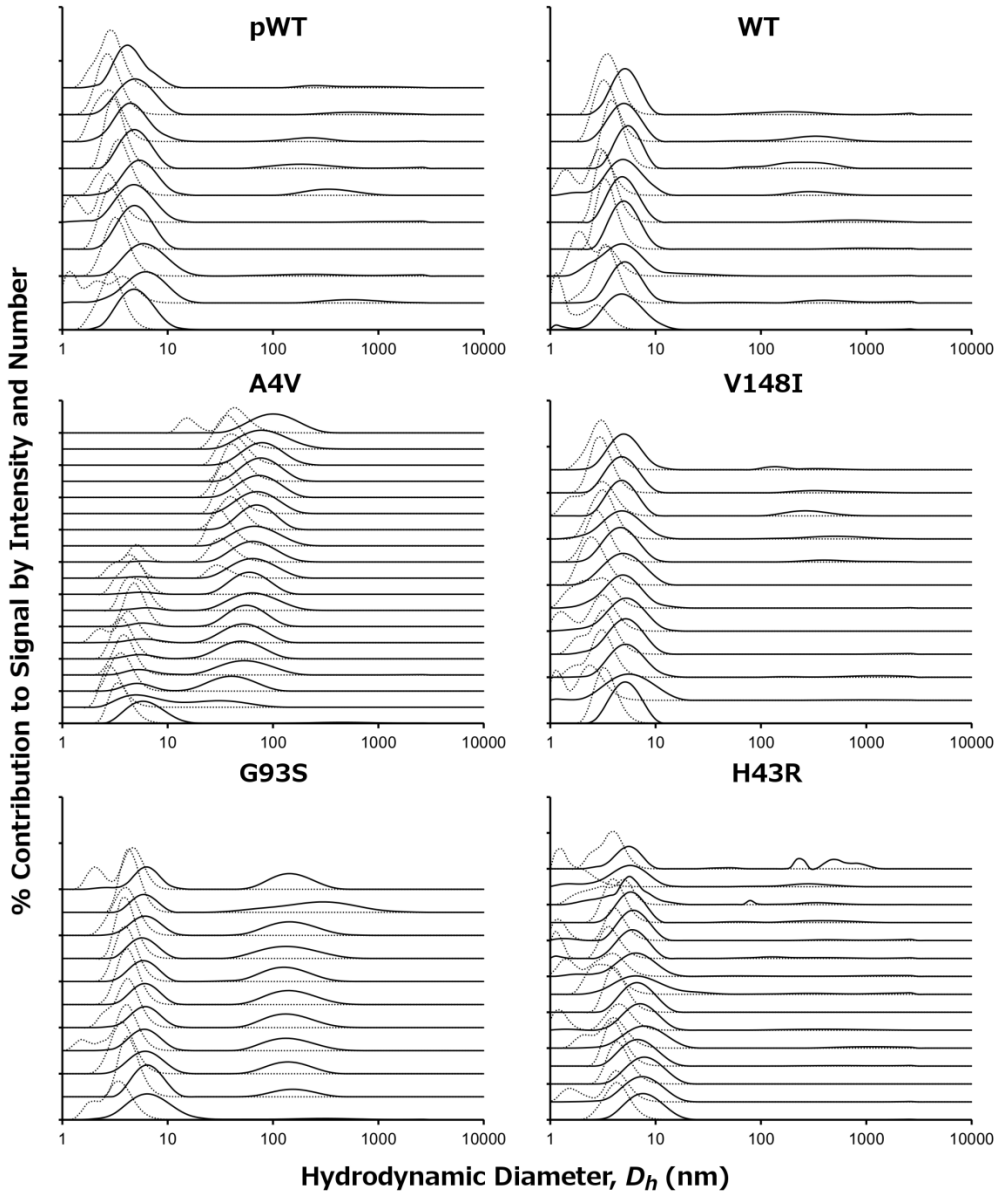

Figure 5.4 DLS shows that apoSH variants aggregate little at 1 mg mL^{-1}, pH 7.4, 37 °C. All samples were incubated in 1 mM TCEP, 20 mM HEPES. Intensity distributions are indicated by the solid lines and number distributions by the dotted lines. DLS measurements were taken approximately every 24 hours, with t_0 at the bottom of each panel and the last time point, greater than 300 hours, at the top. Intensity distributions emphasize larger particles in solution; therefore, the centre of the peak is shifted to the right compared to the number distribution. The number distributions, which are proportional to the concentration of different species in solution, indicate that only for A4V does the concentration of these larger species become abundant after incubation for more than ~300 hours.

Table 5.1 DLS data summary for apoSH SOD1 variants at 1 mg mL^{-1}, pH 7.4, 37 °C.

	t = 0				t > 300			
ApoSH SOD1 variant	PDI[a]	PDI width[b] (nm)	Intensity Distribution Hydrodynamic Diameter[c] (nm)	Number Distribution Hydrodynamic Diameter[c] (nm)	PDI[a]	PDI width[b] (nm)	Intensity Distribution Hydrodynamic Diameter[c] (nm)	Number Distribution Hydrodynamic Diameter[c] (nm)
pWT	**0.205**	**2.146**	**5.383**	**3.131**	**0.267**	**5.231**	**5.228**	**3.449**
	0.025	*0.250*	*0.332*	*0.387*	*0.083*	*5.657*	*0.253*	*0.398*
WT	**0.245**	**2.672**	**5.848**	**3.061**	**0.348**	**85.11**	**5.462**	**3.397**
	0.038	*0.874*	*1.059*	*0.959*	*0.160*	*251.6*	*0.853*	*0.694*
A4S	**0.251**	**3.532**	**8.103**	**3.302**	**0.750**	**24.35**	**80.46**	**3.449**
	0.014	*0.134*	*1.622*	*1.744*	*0.041*	*2.141*	*4.640*	*0.626*
A4T	**0.250**	**3.991**	**7.190**	**4.419**	**1.0**	**45.24**	**241.8**	**4.544**
	0.020	*0.327*	*0.202*	*0.686*	*0.0*	*5.109*	*6.424*	*0.334*
A4V	**0.224**	**5.566**	**8.593**	**3.807**	**0.312**	**29.55**	**63.46**	**15.40**
	0.043	*9.779*	*1.452*	*1.376*	*0.119*	*10.88*	*15.38*	*14.70*
E100G	**0.230**	**2.595**	**6.432**	**3.548**	**0.461**	**86.19**	**123.5**	**4.003**
	0.014	*0.151*	*0.739*	*0.706*	*0.163*	*52.04*	*353.4*	*0.357*
G37R	**0.300**	**48.10**	**5.058**	**3.499**	**0.909**	**149.0**	**596.6**	**3.467**
	0.078	*109.5*	*0.711*	*0.442*	*0.141*	*34.49*	*134.2*	*0.864*
G85R	**0.179**	**2.516**	**5.812**	**3.644**	**0.271**	**43.79**	**5.584**	**4.095**
	0.045	*0.373*	*0.259*	*0.673*	*0.060*	*67.39*	*0.715*	*0.206*
G93A	**0.224**	**3.315**	**7.683**	**3.841**	**0.621**	**122.9**	**171.8**	**4.190**
	0.049	*0.851*	*1.300*	*1.286*	*0.245*	*142.5*	*248.9*	*0.766*
G93R	**0.240**	**3.732**	**7.563**	**3.971**	**0.598**	**26.87**	**151.1**	**11.60**
	0.056	*1.155*	*0.806*	*1.053*	*0.334*	*9.509*	*104.2*	*11.58*
G93S	**0.239**	**3.226**	**7.136**	**3.899**	**0.502**	**30.34**	**84.11**	**3.880**
	0.024	*0.548*	*0.708*	*0.930*	*0.143*	*46.08*	*85.18*	*1.598*
H43R	**0.215**	**3.547**	**8.603**	**4.046**	**0.344**	**51.18**	**6.640**	**3.735**
	0.049	*0.650*	*0.457*	*0.885*	*0.110*	*150.6*	*0.651*	*1.503*
H46R	**0.186**	**2.149**	**5.671**	**3.086**	**0.192**	**5.428**	**6.113**	**3.525**
	0.019	*0.433*	*0.863*	*0.498*	*0.035*	*8.757*	*0.461*	*0.558*
H46R^{wt}	**0.227**	**20.13**	**5.109**	**2.825**	**0.496**	**1063**	**95.32**	**3.371**
	0.089	*37.77*	*0.501*	*0.905*	*0.307*	*2061*	*273.3*	*0.403*
V148G	**0.291**	**10.37**	**6.646**	**3.928**	**0.567**	**191.1**	**291.5**	**3.955**
	0.117	*13.20*	*0.522*	*1.343*	*0.138*	*197.1*	*316.3*	*1.083*
V148I	**0.178**	**1.868**	**5.262**	**3.380**	**0.471**	**94.69**	**5.179**	**3.681**
	0.029	*0.130*	*0.472*	*0.348*	*0.210*	*110.2*	*0.333*	*0.471*

Bold and italicized values are the averages and standard deviations, respectively, resulting from multiple experiments (shown in Table S5.2).

[a]PDI is obtained using the Cumulants method of fitting the autocorrelation function (Eq. 5.4). Values larger than 0.1 are indicative of polydispersity (i.e., the sample contains more than one species in solution). High PDI values result in larger peak widths, and thus greater distribution of sizes reported.

[b]Peak width reflects the range of sizes obtained from the intensity distribution and is related to the PDI according to Eq. 5.4.

[c]The sizes reported correspond to the main peak in the distributions.

5.3.2 Sample evaporation may promote aggregation

The initial aggregation experiments (Chapter 4) performed on apoSH variants involved incubating the samples in glass vials that were difficult to seal effectively. As a result, prolonged incubation at 37 °C resulted in partial sample evaporation in some cases, the extent of which differed (Figs. 5.5, 5.6). Evaporation-induced aggregation of H43R may account for the discrepancy between the aggregation propensity previously published (Chapter 4) and in Chapter 5 for this mutant. Subsequent aggregation experiments with H43R in vials that sealed more effectively failed to reproduce the initial finding that H43R has a high aggregation propensity and forms aggregates larger than those formed by A4V (98). In an attempt to explain these different results, subsequent analysis of other samples, which appeared to aggregate after a long lag time when the sample volume was low, were performed (Fig. 5.5). While, the samples stayed mainly reduced throughout the incubation period, we cannot rule out the possibility that other effects, such as partial sample degradation, are also a factor accounting for the differences in aggregation behaviour observed for these samples.

Amyloid formation occurs through a nucleation-dependent mechanism characterized by a lag time, during which the critical nucleus forms, followed by rapid fibril growth (320). Surfaces can play a large role in facilitating the formation of the initial nucleus (321–327). For example, proteins that are amyloidogenic also tend to be amphiphilic and concentrate at hydrophobic-hydrophilic interfaces such as the air-water interface and lower the surface tension of water (322, 324–326, 328). This phenomenon can catalyze the formation of amyloid because it increases the effective concentration of protein at the interface, as well as force the protein into a β-conformation where hydrophobic segments within the protein align with the hydrophobic surface (322, 328). Proteins that are only marginally stable, such as apoSH SOD1, may be more likely

to undergo surface-induced structural changes that result in the protein becoming trapped in an amyloidogenic state. Sample evaporation causes the concentration and surface-area to volume ratio to increase, both of which can elevate the levels of protein in the amyloidogenic state. Above a critical concentration amyloid fibril formation will dominate over other association pathways.

AFM experiments confirm that under certain conditions apoSH mutants can form fibrillar aggregates with smooth and twisted fibril morphology typical of amyloid fibrils (Figs. 5.6, S5.3-S5.6) (89). ThT binding experiments on these fibrillar H43R aggregates indicate that they contain extensive β-structure resembling amyloid (Fig. 5.6). It could be that the marginal stability and conformational flexibility of apoSH SOD1 may allow it to adopt different conformations that can access different aggregation pathways. Given the limited number of samples that exhibited this type of aggregation, it is unclear whether or not these samples represent different points within the same amyloid aggregation mechanism or differing mechanisms altogether. While amyloid formation by SOD1 is generally not believed to be relevant to disease (22), these findings highlight the importance of understanding factors that can influence *in vitro* aggregation experiments.

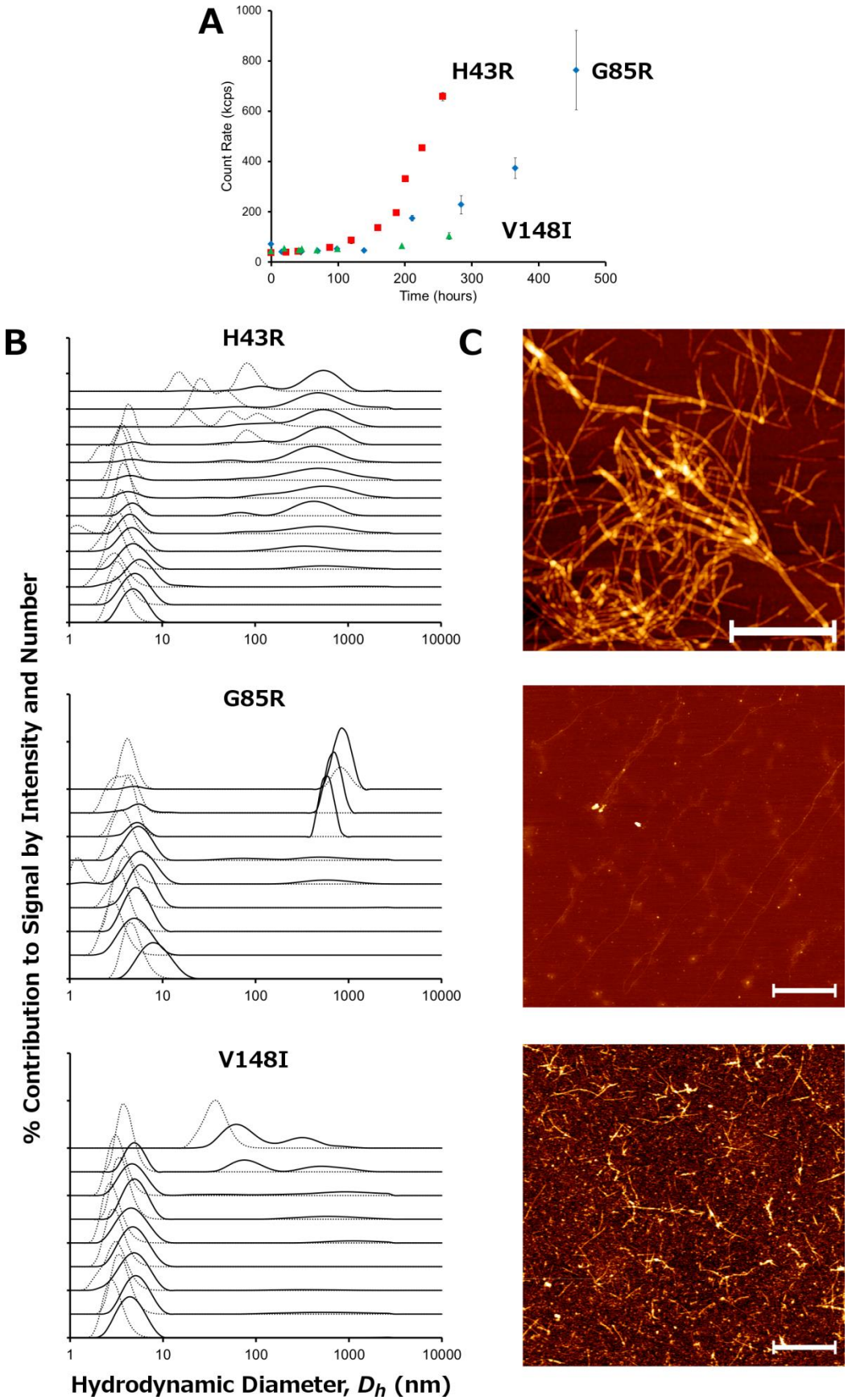
A
1000
800
600
400
200
0
Count Rate (kcps)
H43R
G85R
V148I
0
100
200
300
400
500
Time (hours)
B
H43R
G85R
V148I
1
10
100
1000
10000
% Contribution to Signal by Intensity and Number
Hydrodynamic Diameter, D_h (nm)
C

Figure 5.5 DLS and AFM reveal that sample evaporation can promote fibril formation at pH 7.4, 37 °C and initial concentration of 1 mg mL^{-1}. All samples were incubated in 1 mM TCEP, 20 mM HEPES**. (A)** SLS experiments show that evaporation-induced aggregation occurs after a lag time of ~100 hours. **(B)** DLS experiments show that sample evaporation promoted protein aggregation. As in Fig. 5.4, DLS measurements were taken approximately every 24 hours, with t_0 at the bottom of the panels and the last time point, >300 hours, at the top. Intensity distributions (solid lines) emphasize larger particles in solution; the number distributions (dotted lines) emphasize smaller particles in solution. At later time points, both intensity and number distributions shift to larger species, as aggregates become abundant in solution after a considerable lag time (~100, 150, and 300 hours for H43R, G85R, and V148I, respectively). (**C**) AFM images partially evaporated apoSH H43R, G85R, and V148I confirm that sample evaporation can lead to fibril formation. In all panels, the white bars correspond to 1 μm. The extent of this process was most pronounced for H43R, which formed thick fibrils with a twisted morphology. Fibril formation was less extensive in the other samples. G85R formed fibrils of similar lengths to H43R, but that were much thinner while V148I formed fibrils that were both thinner and shorter than those formed by H43R. These differences appear consistent with DLS data, which indicates that aggregation started earlier in the H43R sample compared to G85R and V148I. These mutants may also exhibit intrinsically different amyloid-forming propensities, although based on the Chiti *et al.*, prediction algorithm (282), the amyloid-forming propensities for H43R, G85R, and V148I are low (Fig. 4.4). For all images of these samples refer to Figs. S5.3-S5.5.

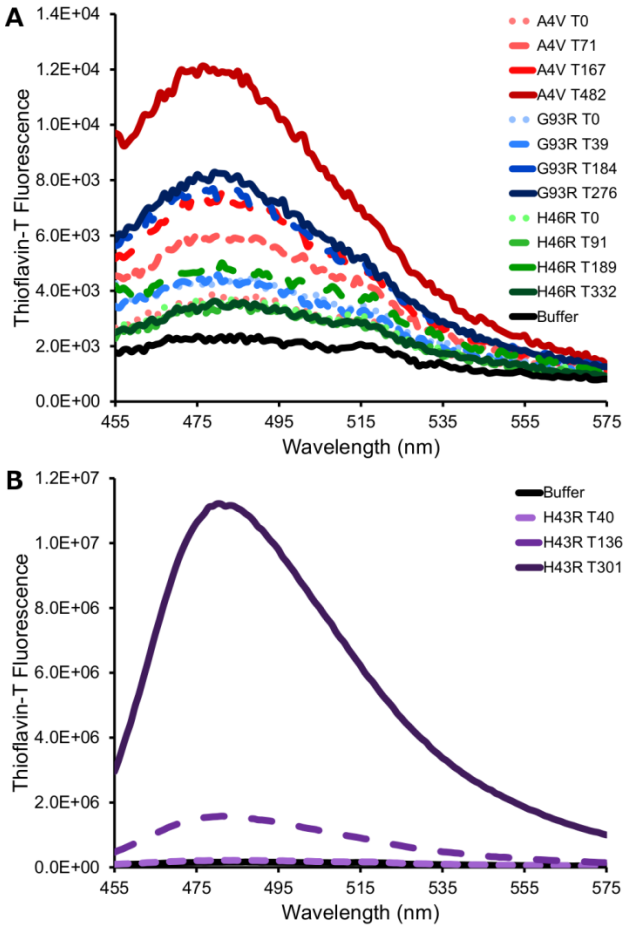

Figure 5.6 ThT binding experiments reveal that evaporation-induced H43R aggregates resemble amyloid. (A) ThT fluorescence experiments on non-evaporated apoSH samples are shown. ThT rapidly associates with fibrils composed of cross β-sheets common to amyloid, resulting in an increase in its fluorescence intensity at 482 nm (329–332). Three mutants that displayed differing aggregation behaviour when incubated at 1 mg mL^{-1}, pH 7.4, and 37 °C were selected. For all samples, four time points were measured. The initial time points (t_0) are shown by the dotted line and lightest colours and the later time points are shown by progressively darker colours and lines with increasing dash length. The final time points are indicated by the darkest colours and solid lines. A4V (red), which aggregates the most showed the largest increase in ThT fluorescence over time; G93R (blue) showed a slight tendency to aggregate and a small change in ThT fluorescence; and H46R (green) a very little tendency to aggregate and very little change in ThT fluorescence. These changes in fluorescence intensity at 482 nm are however very small, even for A4V, compared to the changes expected upon ThT binding to amyloid fibrils (329–332). **(B)** ThT fluorescence for partially evaporated H43R samples at different time points are shown. The initial time points (t_0) are indicated by the dotted line and lightest colours and the later time points are shown by progressively darker colours and lines with increasing dash length. The final time point is indicated by the darkest colour and solid line. In both panels the solid black line represents the fluorescence intensity of free ThT in sample buffer (1 mM TCEP, 20 mM HEPES) (Materials and Methods, Section 5.2.6).

5.3.3 Seeding and Cross-seeding do not promote aggregation of apoSH pWT and H43R

Light scattering data shows that, while most apoSH variants undergo very little aggregation at 1 mg mL^{-1}, pH 7.4, and 37 °C, low levels of aggregation occur. These results suggest that either these intermolecular interactions are not highly stabilizing and/or not enough collisions between proteins occur at 1 mg mL^{-1} to facilitate particle growth. Often conformational changes in the native state are required to initiate aggregation and the rate at which proteins aggregate depends on the concentration of protein in an aggregation-prone state (53). Once aggregation-promoting nuclei (seeds) are formed, they can recruit protein resulting in aggregate growth. The addition of seeds, therefore, can increase the rate of aggregation by providing a surface that supports addition of aggregation-prone monomers. There is some controversy regarding the degree of specificity of aggregation, and different specificity requirements have been demonstrated for different proteins and modes of aggregation. One study found that sequences with more than 70 percent identity were capable of co-aggregating (333); on the other hand, there is strong evidence that even single point mutations in the prion protein (PrP) can create transmission barriers that limit propagation of the misfolded protein (334, 335). Protein inclusions formed *in vivo* also tend to be highly homogenous (336). In contrast, other studies have shown that different proteins with low sequence similarity are capable of co-aggregating (337–339).

In an attempt to accelerate aggregation of apoSH, two seeding experiments were performed. In the first experiments, A4V aggregates and H43R amyloid aggregates were added to freshly prepared pWT samples, to assess potential differences in cross-seeding efficiency (Fig. 5.7A, C, E, G). It was hypothesized that the different morphologies of the aggregates may lead to very different abilities to induce aggregation of pWT. Given the presence of aggregates in

these samples and the high sequence identity between the different SOD1 variants, the hope was that increasing the concentration of aggregation nuclei would promote aggregation. As ALS-linked SOD1 mutations are autosomal dominant, the effects of mutant protein on the aggregation properties of the wild-type protein are pertinent to the understanding of disease mechanisms (3).

As shown in Fig. 5.7A, C, E, G, the addition of A4V seeds and H43R amyloid seeds resulted in little aggregation. These results suggest that either the concentration of aggregation nuclei was too low to induce aggregation in these samples, or that the efficiency of co-aggregation between these samples was low due to high sequence and/or conformational specificity requirements. A second experiment was performed in which H43R amyloid seeds were added to non-aggregated H43R. An aliquot of an H43R sample that did not undergo evaporation-induced aggregation was also added to a sample of non-aggregated H43R as a control (Materials and Methods, Section 5.2.4), herein referred to as non-amyloid seeds even though this sample contained very few aggregates (Fig. 5.7B, D, F, H). Like the first experiment, neither the addition of amyloid or non-amyloid seeds led to any dramatic change in aggregation behaviour. The sample containing amyloid aggregates did exhibit an increase in light scattering intensity with time, although the standard deviation in the measurements were high, and by DLS it is evident that the concentration of aggregates was low (Fig. 5.7B, F). It is possible that these seeding experiments were not successful because the concentration of aggregates added was too low to initiate aggregation. Or it could be that the end stage amyloid aggregates are less effective at inducing aggregation of apoSH compared to smaller oligomers. Now that we have established better experimental conditions for measuring apoSH aggregation (*vide infra*), it will be valuable to return to these experiments to assess the cross-seeding ability

of different apoSH mutants as well as the different seeding properties of early versus late stage aggregates.

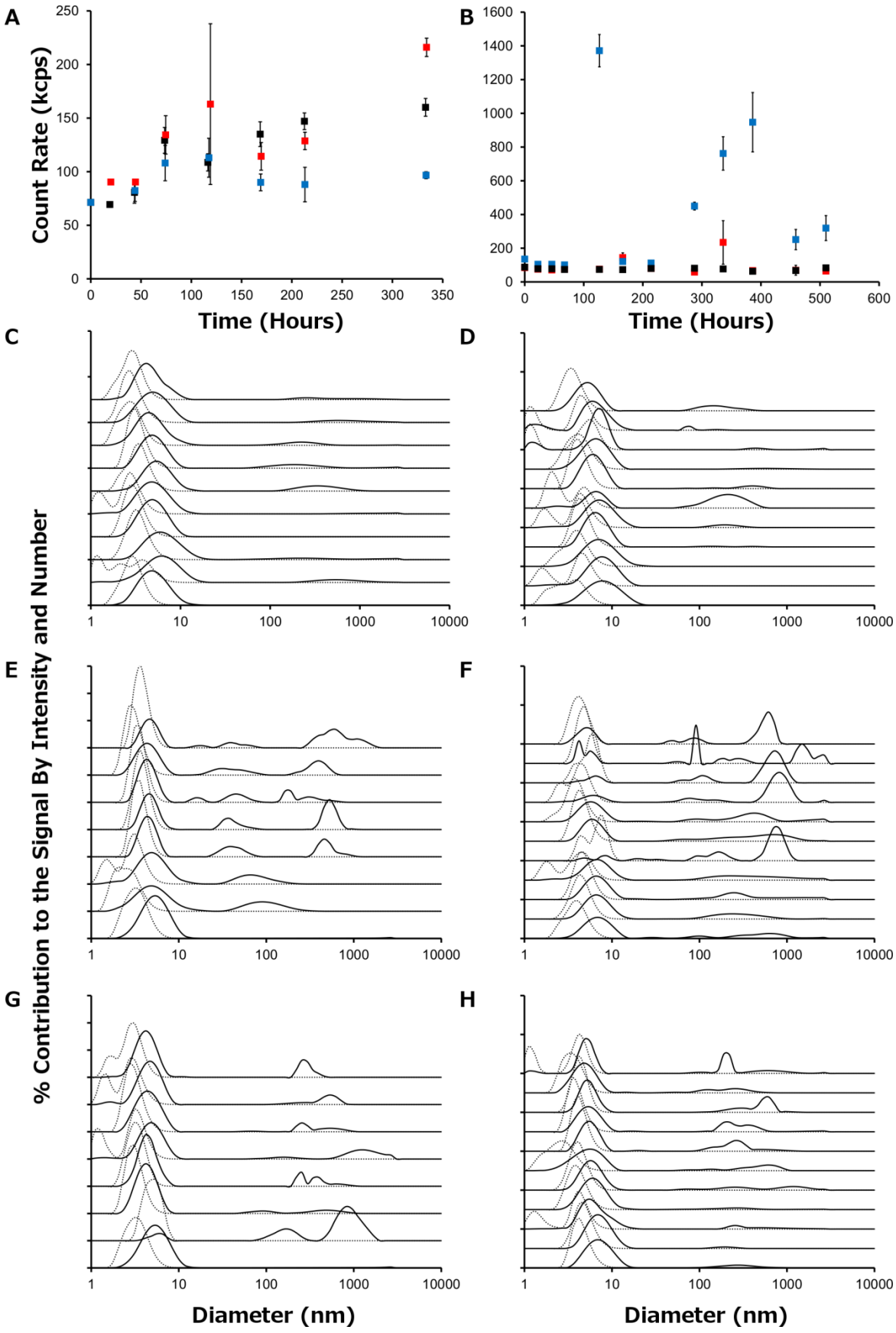
A
Count Rate (kcps)
Time (Hours)
B
Time (Hours)
C
D
E
F
G
H
% Contribution to the Signal By Intensity and Number
Diameter (nm)
Diameter (nm)

Figure 5.7 Light scattering measurements show that addition of aggregates as seeds does not induce further aggregation at 1 mg mL^{-1}, pH 7.4, 37 °C. All samples were incubated in 1 mM TCEP, 20 mM HEPES. Seeding and cross-seeding experiments with pWT (panels **A, C, E, G**) and H43R (panels **B, D, F, H**) were carried out in an attempt to induce aggregation. In all of these experiments, 45 μL aliquots of samples left to incubate at 1 mg mL^{-1}, pH 7.4, 37 °C for ~300 hours were added to non-aggregated samples (Materials and Methods, Section 5.2.4). **(A)** SLS shows that neither the addition of A4V aggregates (red squares) or H43R amyloid aggregates (blue squares), to pWT, incubating at 1 mg mL^{-1}, pH 7.4, 37 °C, results in much change in light scattering intensity over time compared to the sample with no aggregates added (black squares). Error bars reflect the standard deviation of three measurements at each time point. **(C**, **E**, and **G)** DLS data for pWT containing no added aggregates, pWT containing A4V aggregates, and pWT containing H43R amyloid aggregates are shown, respectively. In these experiments, aggregates were added after the initial measurement, which is why only one peak was observed in the intensity distribution (solid lines) at t_0. After aggregates were added, their presence was evident in the intensity distribution, but their concentration in the sample was too low to get reliable size estimates. **(B)** SLS shows that the addition of H43R amyloid aggregates (blue squares) to non-aggregated H43R, incubating at 1 mg mL^{-1}, pH 7.4, 37 °C, results in a marginal change in light scattering intensity compared to the sample with no aggregates added (black squares). As an additional control, H43R previously incubated at 1 mg mL^{-1}, pH 7.4, 37 °C for ~300 hours, that did not undergo evaporation-induced aggregation (herein referred to as non-amyloid aggregates), was also added to non-aggregated H43R (red squares). H43R does not readily aggregate in the absence of evaporation-induced effects on the sample; therefore as expected, the changes in light scattering intensity of this sample compared to H43R with no aggregates added (black squares) are similar. Error bars reflect the standard deviation of three measurements at each time point. **(D**, **F**, and **H)** DLS data for H43R with no added aggregates, H43R containing H43R amyloid aggregates, and H43R containing non-amyloid aggregates are shown, respectively. In all seeding and cross-seeding experiments, DLS data indicates that very little additional aggregation takes place after the addition of aggregates to the sample. While the intensity distributions (solid lines) show that there are aggregates in solution, the number distributions (dotted lines) indicate that concentrations of these species remain very small. DLS measurements were taken approximately every 24 hours, with t_0 at the bottom of the panels and the last time point, >300 hours, at the top.

5.3.4 Light scattering shows that apoSH variants exhibit increased aggregation at higher concentration

Aggregation experiments were performed under the same conditions as described in Section 5.3.1, but at higher protein concentration to further promote intermolecular interactions and so observe more measureable levels of aggregation. To this end, only destabilized mutants A4V, G37R, G93A, G93R, and G93S were selected, as they were expected to have higher aggregation propensities at higher protein concentration. For apoSH mutants more stable than pWT, it was thought that increasing the concentration of the sample alone would not be enough to promote aggregation; therefore, 150 mM Na_2SO_4, known to enhance aggregation (Section 5.3.7), was also added to V148I to assess if this mutant would aggregate via a similar mechanism when provided with an extra push.

SLS measurements show that for pWT, G93A, and G93S at increased protein concentration the light scattering intensity does not change significantly with time, suggesting low levels of aggregation even at higher protein concentration (Fig. 5.8). For V148I in 150 mM Na_2SO_4, the average light scattering intensity does not change greatly with time; however, the uncertainty in later measurements is very high, pointing to the presence of small amounts of large particles in solution. On the other hand, A4V, G37R and G93R exhibit notably increased level of aggregation at higher protein concentration (Fig. 5.9). These mutants aggregate with no discernible lag time, suggesting that the energetic barrier between the unfolded or native state(s) and aggregation-prone state(s) is low. Consistent with experiments at 1 mg mL^{-1}, A4V aggregates more than all other variants when incubated at 5 mg mL^{-1}, rapidly forming aggregates that over time become too large to be analyzed quantitatively by light scattering, as shown by the decrease in light scattering intensity after ~50 hours of incubation. SLS is an excellent method

for determining differences in aggregation; yet, it is less suited for assessing subtle changes in intermolecular association for samples that undergo much less aggregation, for which DLS is a more powerful tool.

At higher protein concentration, $D_{h,I}$ and $D_{h,N}$ values at t_0 for pWT and V148I are consistent with the empirical estimate of ~4 nm for folded monomer (Fig. 5.9, Table 5.2) (277). For A4V, G37R and G93R, $D_{h,I}$ was measured to be 20.1, 9.3, and 9.0 nm, respectively at t_0, ~1.5-12 nm larger compared to measurements obtained for 1 mg mL^{-1} samples, corresponding to sizes larger than expected for monomeric apoSH SOD1. Although, the $D_{h,N}$ values for these mutants are lower, 4.6, 5.3, and 5.4 nm, respectively, they are still increased for 5 mg mL^{-1} compared to 1 mg mL^{-1} samples. The other destabilizing mutants, G93A and G93S, exhibit less change in $D_{h,I}$ and $D_{h,N}$ values with protein concentration, and they are more consistent with the expected D_h values of ~4-8 nm for a mixture of unfolded and folded monomers stated above (277), 7.0 and 5.0 nm, respectively, for G93A and 6.9 and 4.0 nm, respectively, for G93S. The $D_{h,N}$ values at t_0 are less influenced by small increases in associated species, although for pWT and all mutants they increased slightly at high protein concentration. The PDI at t_0 is also higher for pWT and all mutants at 5 mg mL^{-1}, compared to 1 mg mL^{-1}, providing further evidence of increased oligomerization at higher concentration. Taken together, t_0 DLS measurements reveal that some mutants, A4V, G93R, and G37R, show increased aggregation, while other mutants, G93A, G93S, and V148I in 150 mM Na_2SO_4, display similar aggregation compared to pWT. On the whole, however, higher order interactions are more apparent at higher protein concentration for all apoSH variants studied.

After ~300 hours of incubation, all the 5 mg mL^{-1} samples, except for V148I, show an increased discrepancy in $D_{h,I}$ and $D_{h,N}$ relative to measurements at t_0. $D_{h,I}$ and $D_{h,N}$ differ the

most for pWT, G93A, and G93S with differences ranging from ~400-1200 nm, due to increases in $D_{h,I}$ but not $D_{h,N}$ (Table 5.2). For V148I in 150 mM Na_2SO_4, the $D_{h,I}$ and $D_{h,N}$ values are fairly similar, and relatively unchanged with time. A4V displayed the most aggregation at 5 mg mL^{-1}; light scattering was only measureable up to 120 hours after which based on visual inspection the protein had formed large aggregates beyond the DLS detection limit (>1000 nm) (Fig 5.9). Furthermore, pWT, A4V, G93A, G93S, and V148I in 150 mM Na_2SO_4 samples similarly exhibit a large increase in PDI with incubation time leading to large uncertainty in $D_{h,I}$ values after ~300 hours (Table 5.2). Taken together, these results suggest that large aggregates form in these samples, which scatter a large amount of light but, except for A4V, remain low in concentration. Thus, size estimates by DLS are difficult.

On the other hand, G37R and G93R exhibit smaller discrepancies in $D_{h,I}$ and $D_{h,N}$ at ~t_{300}, although still larger relative to t_0 measurements. Both values increase with time, pointing to a clear increase in the concentration of aggregates. A4V, G37R and G93R also show large increases in the $D_{h,N}$ values measured after t_{300} for 5 mg mL^{-1} compared to 1 mg mL^{-1} samples, indicating more aggregation higher concentrations. Furthermore, the PDI values for G37R and G93R samples decrease with incubation time, indicating that the samples become more monodisperse, which may be due to an increase in aggregate concentration and a decrease in the monomer and oligomer concentration. The other apoSH variants showed little change in $D_{h,N}$ at t_{300} compared to t_0 as well as t_{300} measurements at lower protein concentration, but the PDI increased with protein concentration.

SLS and DLS data together indicate that different apoSH variants demonstrate different aggregation behaviour. Changes in total light scattering intensity, D_h, and PDI measurements indicate that at increased protein concentration, intermolecular interactions are enhanced leading

to clearly increased levels of aggregation in A4V, G93R and G37R samples. Alternatively, while at higher concentration intermolecular interactions are also enhanced in pWT, G93A, G93S and V148I in Na_2SO_4 samples, they do not lead to extensive aggregation. Rather, some aggregates may form but they remain low in concentration.

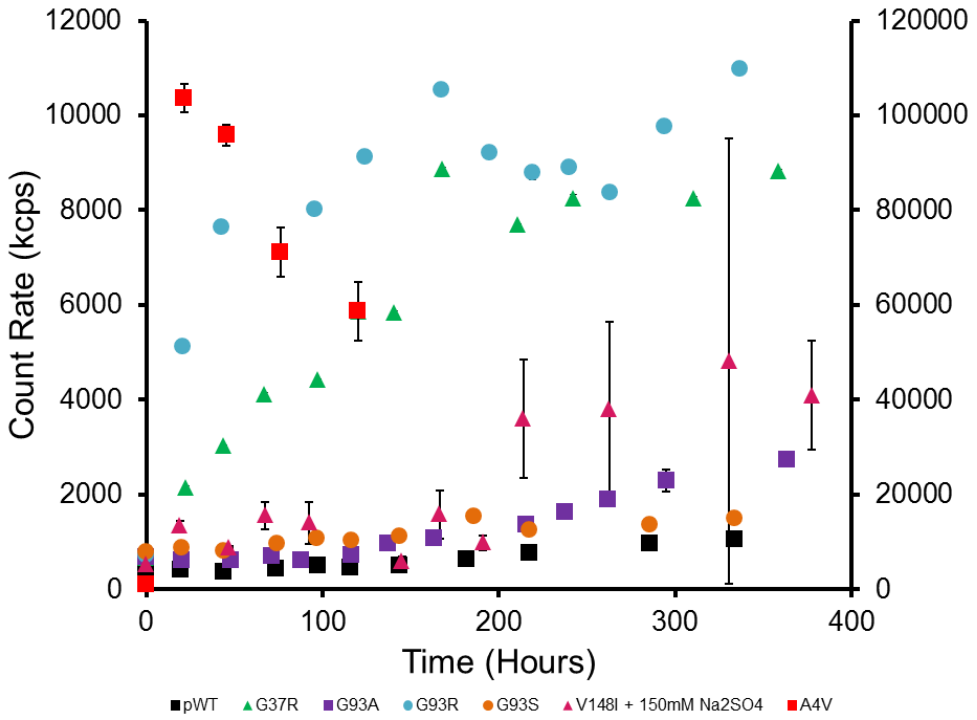

Figure 5.8 SLS reveals different levels of aggregation for apoSH variants incubated at higher concentration (5 mg mL^{-1}, pH 7.4, 37 °C). All samples were incubated in 1 mM TCEP, 20 mM HEPES. At higher protein concentration, aggregation becomes more favourable for some mutants. A4V, the only mutant plotted on the right hand axis (red squares), aggregated the most and was only measurable by light scattering for ~120 hours. After this point the aggregates were too large to be detected. G37R (green triangles) and G93R (blue circles) also aggregated with very little detectible lag time. Incubation at higher protein concentration however, does not lead to much change in light scatter intensity over time for pWT, G93A, and G93S (black squares, purple squares and orange circles, respectively). V148I (pink triangles), a mutant more stable than pWT, was incubated at higher concentration with the addition of 150 mM Na_2SO_4, which promotes aggregation (Section 5.3.7). In this case, the light scattering intensity fluctuated greatly between the measurements giving rise to large standard deviations in the measurements. This finding indicates that large particles are present in solution, yet these species are not abundant. Error bars represent the standard deviation of three measurements at each time point.

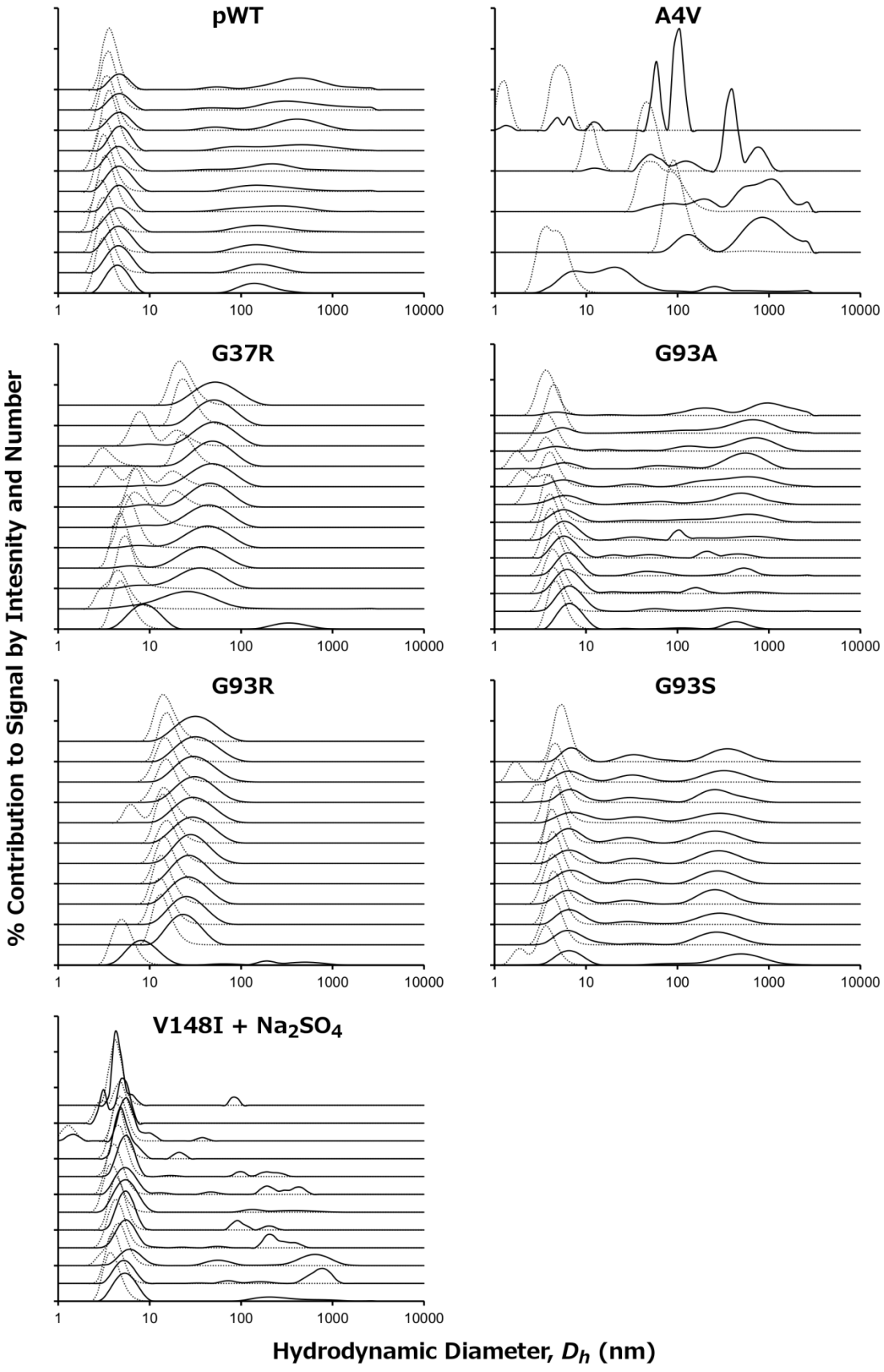
pWT
A4V
G37R
G93A
G93R
G93S
V148I + Na2SO4
1
10
100
1000
10000
% Contribution to Signal by Intesnity and Number
Hydrodynamic Diameter, Dh (nm)

Figure 5.9 DLS also reveals different levels of aggregation for apoSH variants incubated at higher concentration (5 mg mL^{-1}, pH 7.4, 37 °C). All samples were incubated in 1 mM TCEP, 20 mM HEPES. At increased protein concentration A4V shows the highest aggregation propensity. At t_0 there is a large discrepancy in the size reported by intensity and number distribution, suggesting that aggregates form immediately. After ~24 hours most of the sample formed aggregates of similar size to those observed at 1 mg mL^{-1}; however, larger aggregates are also apparent. Subsequent measurements revealed that a significant amount of protein had formed aggregates too large to be detected by DLS, resulting in poor estimates of particle size. After ~120 hours the sample was not measureable by DLS. G37R and G93R showed much higher levels of aggregation at higher concentration, forming aggregates similar in size to those formed by A4V and 1 mg mL^{-1} as indicated by the shift in intensity and number distributions to larger values. DLS measurements of G93A, G93S, and V148I incubated with 150 mM Na_2SO_4 over time reveal that the majority of particles in solution exhibit little change in size.

Table 5.2 DLS data summary for apoSH SOD1 variants at 5 mg mL^{-1}, pH 7.4, 37 °C.

	t = 0				t > 300			
ApoSH SOD1 variant	PDI[a]	PDI width (nm)[b]	Intensity Distribution Hydrodynamic Radius (nm)[c]	Number Distribution Hydrodynamic Radius (nm)[c]	PDI[a]	PDI width (nm)[b]	Intensity Distribution Hydrodynamic Radius (nm)[c]	Number Distribution Hydrodynamic Radius (nm)[c]
pWT	**0.363**	**7.785**	**4.620**	**3.340**	**0.926**	**65.05**	**707.1**	**3.845**
	0.053	*2.993*	*0.041*	*0.115*	*0.104*	*11.39*	*404.5*	*0.080*
A4V[d]	**0.374**	**27.00**	**20.15**	**4.616**	**1.0**	**1679**	**514.9**	**36.00**
	0.150	*25.92*	*11.08*	*1.288*	*0.0*	*322.4*	*221.7*	*22.36*
G37R	**0.404**	**7.876**	**9.252**	**5.317**	**0.242**	**22.26**	**60.06**	**24.23**
	0.017	*0.453*	*0.072*	*0.365*	*0.014*	*0.676*	*1.920*	*2.190*
G93A	**0.321**	**62.11**	**7.030**	**4.961**	**0.931**	**285.1**	**1256**	**3.910**
	0.036	*54.47*	*0.050*	*0.178*	*0.120*	*49.43*	*445.1*	*0.529*
G93R	**0.327**	**37.70**	**9.025**	**5.352**	**0.215**	**14.33**	**35.81**	**15.98**
	0.078	*48.06*	*0.684*	*0.716*	*0.014*	*0.435*	*0.655*	*0.917*
G93S	**0.806**	**38.76**	**6.852**	**3.977**	**0.833**	**32.16**	**398.6**	**5.664**
	0.045	*11.59*	*0.199*	*1.184*	*0.068*	*5.263*	*72.75*	*0.431*
V148I	**0.330**	**10.29**	**5.568**	**4.066**	**1.0**	**5551**	**4.774**	**4.378**
Na_2SO_4	*0.026*	*4.689*	*0.258*	*0.221*	*0.0*	*3028*	*0.728*	*0.344*

Bold and italicized values are the averages and standard deviations respectively resulting from three measurements of a single sample (shown in Table S5.3).

[a]PDI is obtained from the Cumulants method of fitting the autocorrelation function (Eq. 5.4). Values larger than 0.1 are indicative of polydispersity (i.e., the sample contains more than one species in solution). High PDI values result in larger peak widths and greater uncertainty in the sizes reported.

[b]Peak width reflects the uncertainty in the hydrodynamic diameter obtained from the intensity distribution and is related to the PDI according to Eq. 5.4.

[c]The sizes reported correspond to the main peak in the distributions.

[d]A4V aggregated readily at higher protein concentration, leading to the formation of aggregates visible by the eye. Such aggregates diffuse too slowly to be measureable by DLS, thus the sample could only be measured for ~120 hours.

5.3.5 AFM images of aggregated apoSH variants point to different modes of aggregation

DLS experiments reveal that apoSH variants exhibit increased aggregation at increased protein concentration, but the extent to which aggregation is promoted differs. For simplicity the apoSH variants were categorized into two groups, the first containing variants that undergo little change in light scattering intensity and average particle size with time, pWT, G93A, G93S, and V148I in 150 mM Na_2SO_4, and the second containing the variants with more pronounced aggregation, A4V, G93R and G37R (Figs. 5.8 and 5.9, Table 5.2). To account for these differences between the two groups, the properties of the aggregates formed were investigated by AFM imaging.

As shown in Figs. 5.10 and 5.11, the size and morphology of the aggregates differs between the two groups of apoSH variants. Consistent with the light scattering data, the pWT sample contained the fewest aggregates, yet there is evidence indicating low levels of fibril formation (Figs. 5.11, 5.12, S5.6). SPIP software was used to estimate aggregate length, breadth, height, aspect ratio and volume (Section 5.2.5); and estimates of particle volume were compared to the crystal structure volume of the apoSS SOD1 dimer to ascertain how many monomers associate to form the aggregates, assuming no significant volume changes in the monomer upon association (Fig. 5.13). These values are summarized in Table 5.3.

Given the asymmetry of the data, median rather than average values were used to compare the data obtained for different apoSH variants (340). The median length and breadth estimates (Fig. 5.13, Table 5.3) of the pWT particles deposited on mica were ~20 nm and ~12 nm, respectively, larger than the size of the size of the dominant species, the apoSH monomer, reported by DLS (Table 5.2). By AFM the majority of measured particle heights range from 0.2-0.5 nm, smaller than the approximate diameter of the apo monomer (~3.3 nm), determined from

estimates of the apoSS volume (37.5 nm^3) (317). This apparent flattening may be due to the protein unfolding at the mica surface (341). Furthermore, apoSH monomers, oligomers, and aggregates may bind to the mica surface in different ways, and certain species may be more easily washed away during sample preparation. This process may also vary between different samples. It is also worth noting that the distributions of length, breadth, and monomers per particle can convey misleading information regarding the number of aggregates in solution, particularly for samples containing large aggregates, such as A4V. Formation of these large assemblies will decrease the levels of smaller fibrils, generating regions of low aggregate density. Because it is not possible to exhaustively image the entire mica surface, it can be challenging to interpret differences in the absolute number of particles detected between two samples, but comparing the shapes of the distributions is meaningful. Given these caveats, there is good agreement between DLS and AFM results.

For pWT, the majority of particles detected are composed of ~1 to 4 monomers. This finding is consistent with DLS results that suggest pWT may form low levels of small oligomers that are not distinguishable from the monomer but broaden the D_h distributions. As indicated by the median aspect ratio of 1.4 (Table 5.3), the pWT particles in general resemble flattened spheres. For the few particles larger than 200 nm, the average aspect ratio is larger consistent with fibril formation. The low average coverage estimates also indicate that very little aggregation has occurred, as was evident by light scattering.

By AFM, aggregation is more apparent for all mutants analyzed (Figs. 5.10 and 5.11). Even those mutants categorized into group one that showed less aggregation by light scattering, G93A, G93S, and V148I, exhibited larger median length and breadth estimates, and more particles larger than 200 nm compared to pWT (Fig. 5.13, Table 5.3). The median length and

breadth estimates, ranged from 22-39 nm and 15-25 nm, respectively, indicating higher levels of larger particles relative to pWT. Likewise, volume estimates indicate that more particles containing ~10 monomers are observed for these mutants compared to pWT. Thus, the long fibrils observed in the AFM images, most notably for G93A (Figs. 5.10, 5.11, and S5.10) and V148I (Figs. 5.10, 5.11, and S5.13), are considered outliers given their low concentration, and have little impact on the shapes of the size distributions (Fig. 5.13). Yet, the presence of these fibrils is reflected in the larger median aspect ratios of particles greater than 200 nm in length (~2-5) (Table 5.3). It is noteworthy that the lengths of fibrils that are not linearly displayed on the mica will be underestimated and the breadths overestimated; therefore, the aspect ratios (length divided by breadth) will similarly be underestimated.

Given the large size of these long fibrils (>1000 nm), they would scatter a great deal of light and thus be evident in the $D_{h,I}$, but not $D_{h,N}$, distributions; although, given the low concentration of these long fibrils they may not be observed in all measurements and give rise to large standard deviation in SLS measurements. Both of these observations are evident in the light scattering data for group one apoSH variants. Taken together, the larger average length and breadth estimates for G93A, G93S, and V148I, together with the higher average coverage, point to enhanced aggregation propensity relative to pWT, consistent with light scattering data.

AFM imaging confirms that the second group of apoSH variants aggregate considerably more than the first (Figs. 5.10, 5.11, 5.13, S5.7, S5.9, S5.11). For these mutants, median length and breadth estimates ranged from 24-48 nm and 14-30 nm, respectively (Table 5.3), and were highest for A4V and G93R. Also, aggregates composed of up to 100 monomers were detected relatively frequently, most notably for A4V and G93R (Fig. 5.13). Particles with lengths greater than 200 nm tend to be numerous in group two compared to group one samples (Table 5.3).

Interestingly, while these mutants aggregate more than those in the first group by both DLS and AFM, there does not appear to be evidence for the formation of long fibrils observed in G93A and V148I samples. The aspect ratios of aggregates formed by A4V, G37R and G93R are only slightly higher for the particles greater than 200 nm, which suggests that long fibril formation is rare. Group two mutants also show higher values for average coverage of the aggregates (Table 5.3), which also points to higher levels of aggregation for these samples.

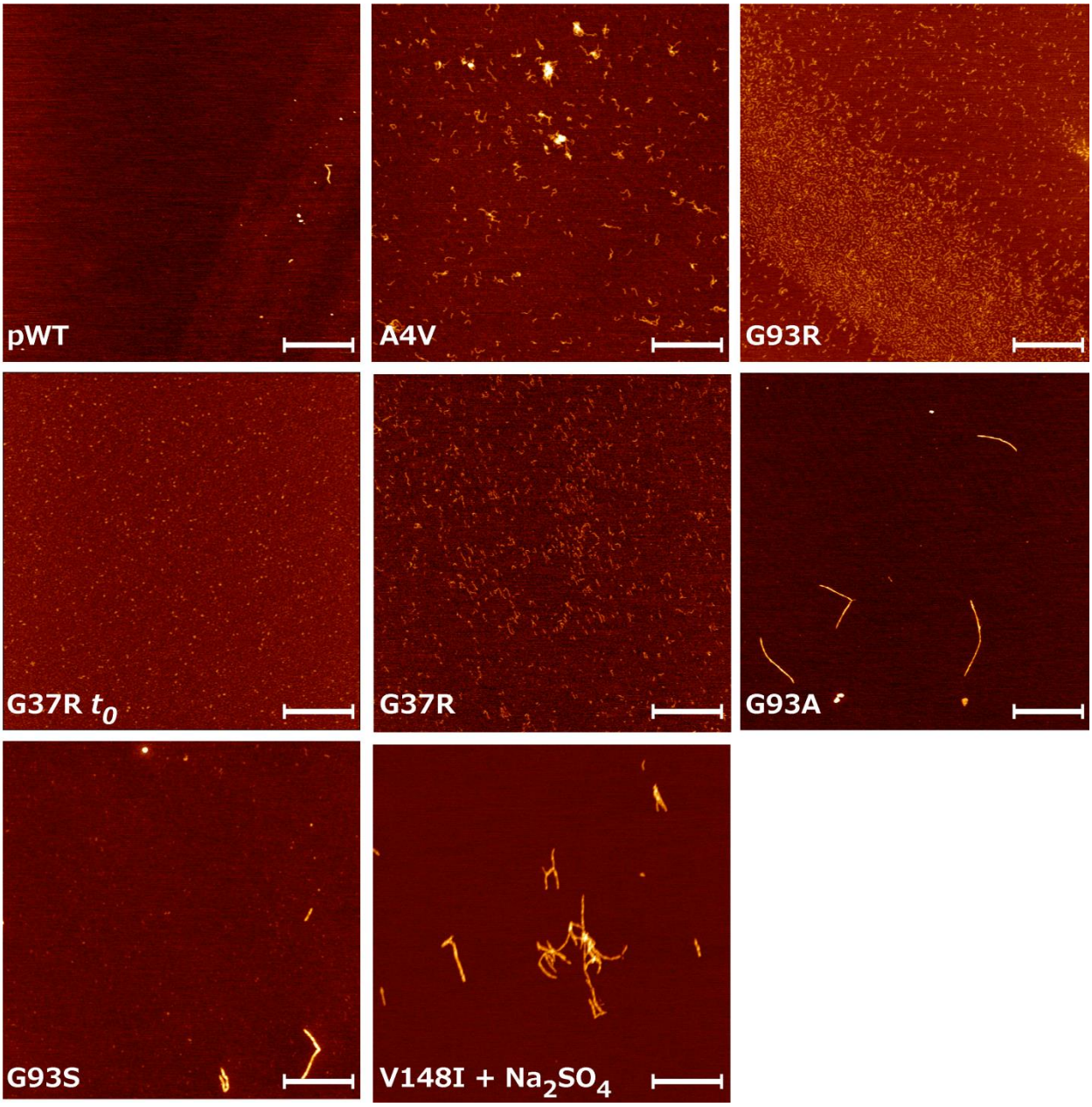

Figure 5.10 AFM reveals that different apoSH variants form aggregates of differing sizes and morphologies when incubated at higher concentration (5 mg mL^{-1}). AFM images of apoSH variants incubated for ~300 hours, except A4V which was only incubated for ~120 hours. Images are 5 x 5 μm and white bars indicate 1 μm. Consistent with DLS results, pWT showed the lowest levels of aggregate formation, although some fibrils are apparent. Samples that exhibited the highest levels of aggregation, A4V, G37R, and G93R formed numerous particles ~25-80 nm in length. Samples that displayed lower aggregation propensity, G93A, G93S and V148I, formed a small number of long fibrils, greater than 1 μm. For all images, the aggregates are so large that they mask the presence of small particles resembling monomers and oligomers.

To better illustrate the morphological differences in the aggregates and the presence of these small oligomers refer to refer to Figs. 5.11 and Fig. 5.12. For all images of these samples refer to Figs. S5.6-S5.13.

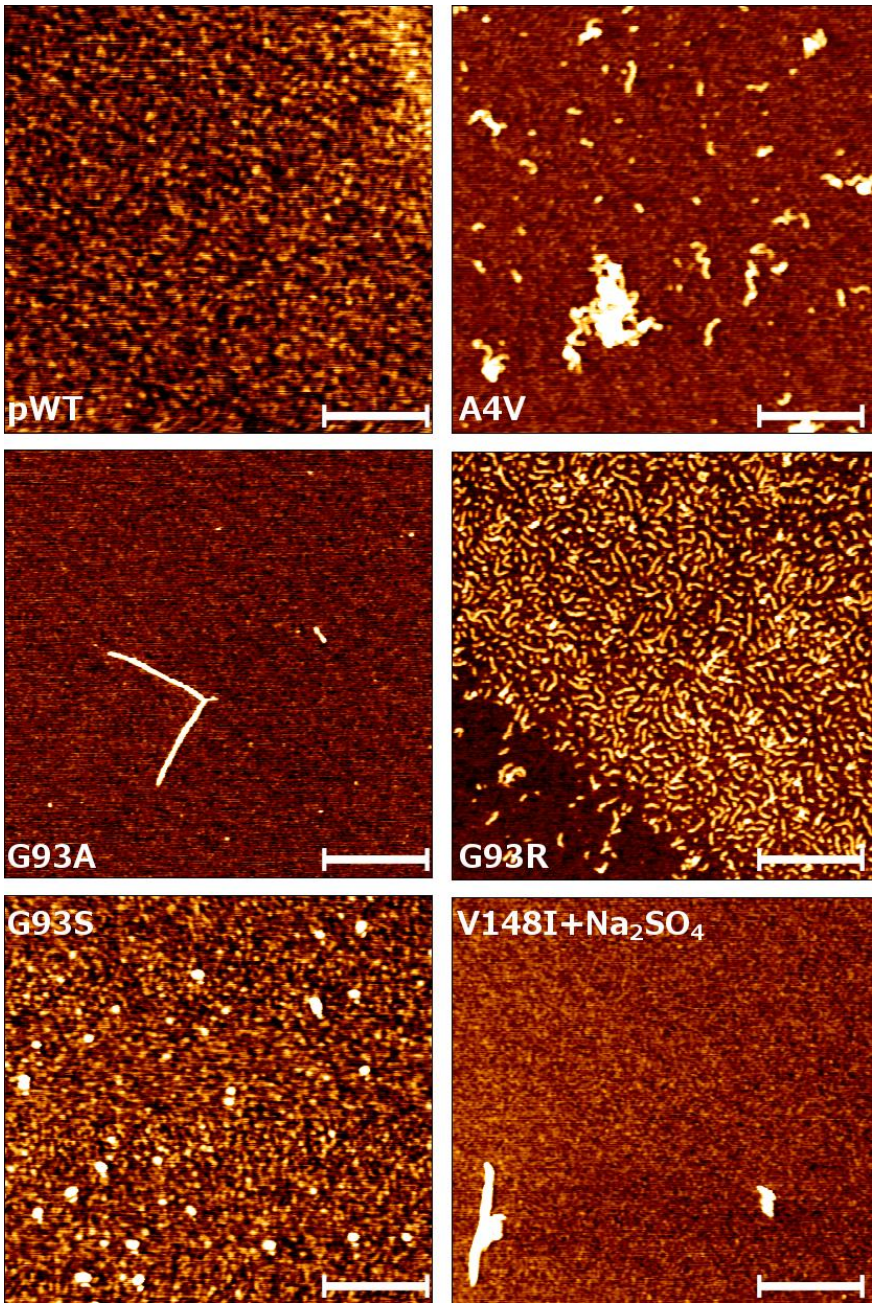

Figure 5.11 Close-up AFM images of different apoSH variants incubated at higher concentration (5 mg mL^{-1}) reveal the abundance of monomers and small oligomers. Here 2 x 2 µm images of apoSH samples incubated at 5 mg mL^{-1} are shown. White bars indicate 500 nm. For images of aggregated G37R, refer to Fig. 5.14.

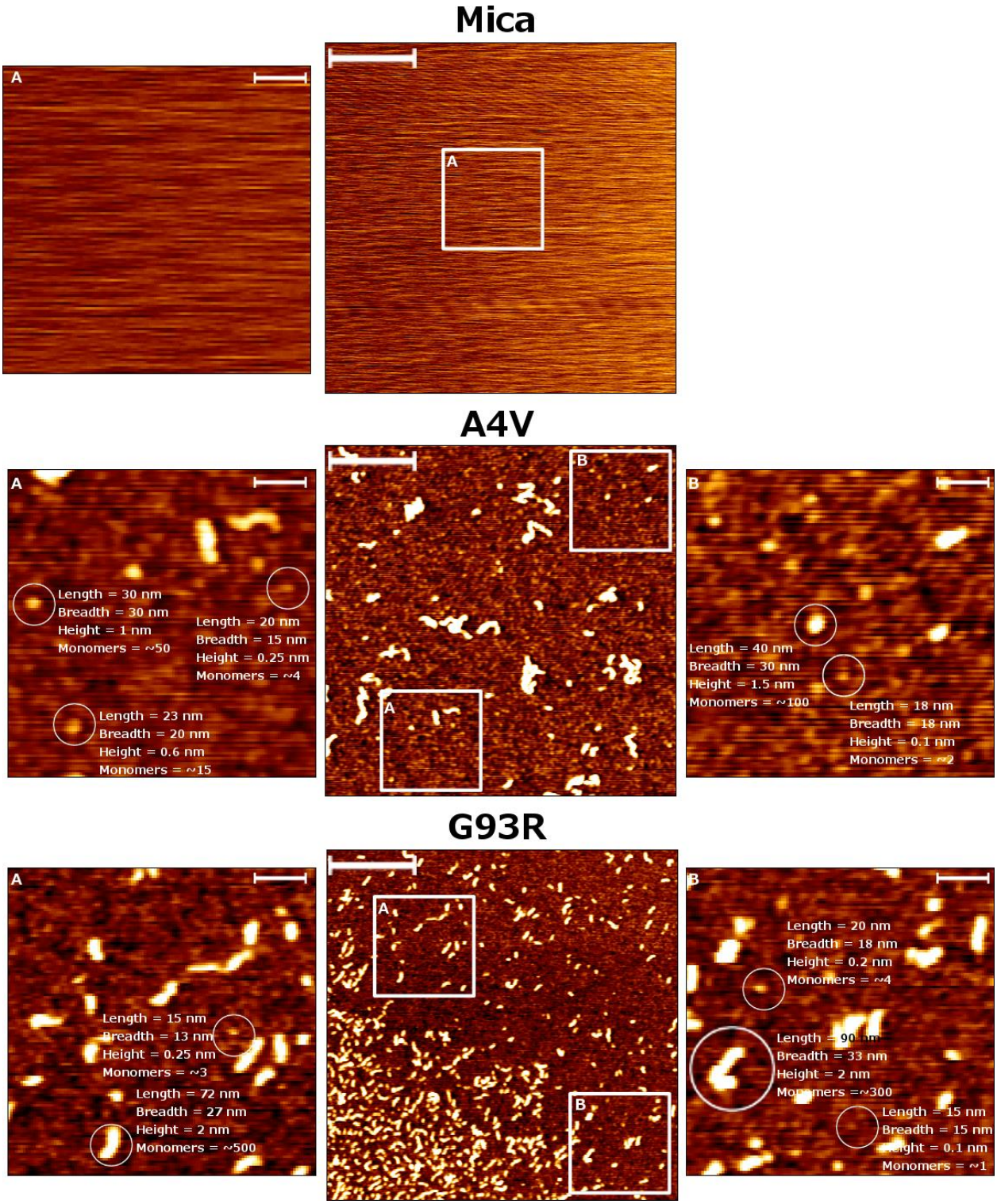

Figure 5.12 Size estimates of small oligomers that are abundant in the AFM images of apoSH variants incubated at high concentration (5 mg mL^{-1}). Numerous small particles representing monomers and small oligomers 10-20 nm in length are evident in the background of the 5 x 5 µm images shown in Fig. 5.11. The presence of these particles is clear when

comparing the images to those obtained for cleaved mica (top images). In this figure, centre images are 2 x 2 µm and white bars represent 500 nm. White boxes represent the regions that are shown close-up (~580 x 580 nm) in the right and left panels, and in these images white bars represent 100 nm. Size estimates were calculated by hand using JPK Data Processing Software (JPK Instruments AG).

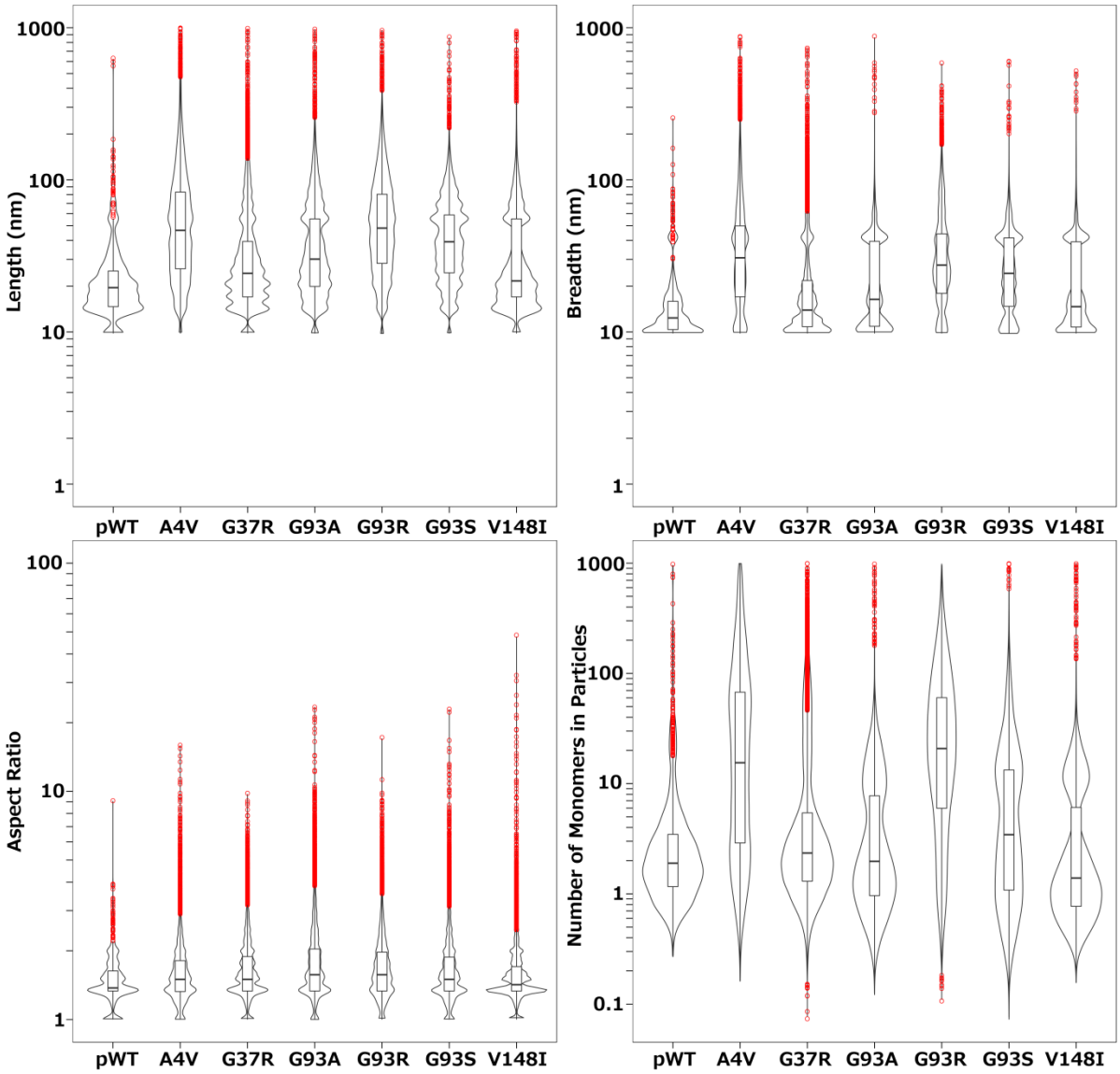

Figure 5.13 AFM measurements of aggregated apoSH SOD1 variants represented as box and whisker superimposed on violin plots. In each panel, the median of the data is shown by a horizontal line in the middle of the box and the box represents the first to third quartile of the data (i.e., the middle 50% of the data). The whiskers extend 1.5 times the interquartile range from the edges of the box and all points outside this range, which are considered outliers, are shown individually as red circles. Violin plots were superimposed on the box and whisker plots to illustrate the density of the data. Length, breadth, and aspect ratio distributions (top right, top left, and bottom left panels, respectively) show that the median of the data is shifted to higher values for all mutants compared to pWT. Furthermore, the mutant distributions are broader and there are more large particles considered outliers. Distributions showing the number of monomers within the particles (lower right panel) are also broader for all mutants. Although the resolution of these distributions is lower than the others due to the higher uncertainty in the data, they reveal large populations of particles ~1-2 monomers for all samples and for pWT, G93A, and V148I, these particles are the most abundant particles detected. For G37R and G93S, the

median is shifted to slightly higher values, although the majority of particles observed are very small (>10 monomers). Only for A4V and G93R are particles containing more than 10 monomers the most abundant.

5.3.6 AFM images of apoSH G37R at t_0 and t_{300} reveal that the distribution of particles shifts to higher order oligomers with time

To assess the progression of aggregate growth, G37R at t_0 was also imaged (Figs. 5.14, S5.8, S5.9). The median length and breadth estimates at t_0 were ~20 and 13 nm, respectively. Volume estimates indicate that the majority of particles observed are monomers, dimers and small amounts of oligomers containing ~10 monomers. At ~t_{300}, the median length and breadth estimates were 24 and 14 nm, respectively; thus, aggregates grew more in length than breadth (Figs. 5.14, 5.15, and Table 5.3). Although image analysis reveals that the aspect ratio of the particles changes little with incubation time (Table 5.3), the images clearly show that G37R particles are more fibrillar at t_{300}. It is likely that image processing results in an over-estimation of particle breadth, as these small fibrils adopt different, non-linear conformations on the mica surface. At t_{300}, the monomers per particle distribution shifts to dimers and higher order oligomers. However, the small fibrils evident at t_{300} appeared to coalesce on the mica, resulting in their detection as very large particles, reducing the apparent proportion of small fibrils which resemble those formed by A4V and G93R. Due to the coalescence of these small fibrils, differences in the length, breadth, monomer per particle, and aspect ratio distributions at t_0 and t_{300} are smaller than would be if these small fibrils were consistently detected as individual particles.

Taken together, AFM imaging provides further evidence that apoSH forms small oligomers even prior to prolonged incubation at 5 mg mL^{-1}, pH 7.4, 37 °C, providing a rationalization for the high PDI values observed by DLS. While image statistics reveal subtle shifts in the particle size distributions to higher values, by eye it is evident that small fibrils are abundant, as observed for A4V and G93R samples.

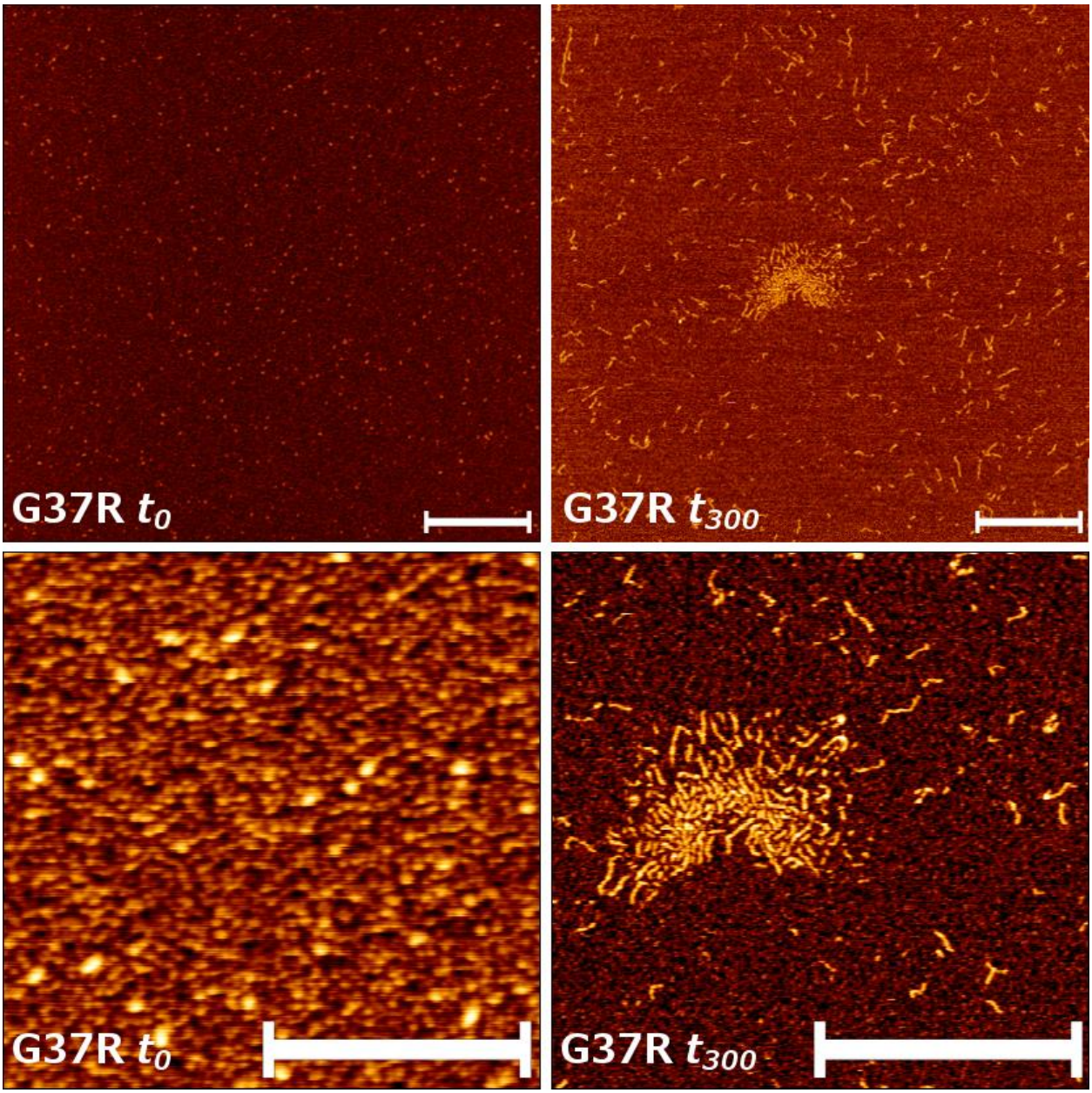

Figure 5.14 AFM reveals that apoSH G37R forms small oligomers at t_0 that appear to transition to longer fibrils abundant at t_{300}. AFM images of G37R at t_0 (prior to incubation) and at ~t_{300} (after ~300 hours of incubation at 5 mg mL^{-1}, pH 7.4, 37 °C) indicate abundant levels of small particles representing monomers and small oligomers with volumes consistent with ~10 monomers. After incubation for ~300 hours, small fibrils become evident. Top panels are 5 x 5 µm and bottom panels are close-up (2 x 2 µm) images of the top panels. White bars indicate 1 µm. For all images of these samples refer to Figs. S5.8 and S5.9.

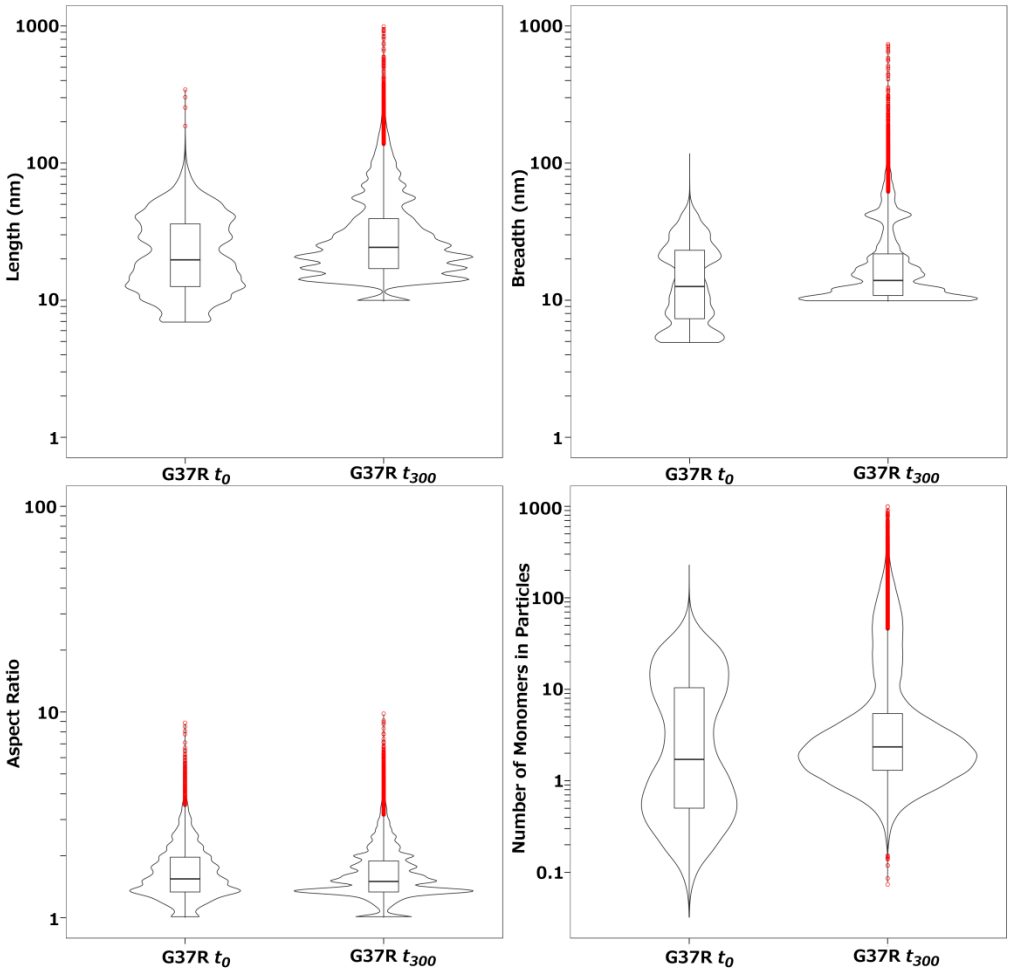

Figure 5.15 AFM measurements of apoSH G37R at t_0 and t_{300} represented as box and whisker superimposed on violin plots. In each panel, the median of the data is shown by a horizontal line in the middle of the box and the box represents the first to third quartile of the data (i.e., the middle 50% of the data). The whiskers extend 1.5 times the interquartile range from the edges of the box and all points outside this range, which are considered outliers, are shown individually as red circles. Violin plots were superimposed on the box and whisker plots to illustrate the density of the data. Length and breadth distributions (top right and top left panels, respectively) show that the median of the data shifts to higher values for t_{300} samples compared to t_0 samples. Furthermore, more outliers are present in the t_{300} distributions due to the formation of large clumps of small fibrils (Figs. 5.10, 5.11, S5.9, and S5.10). The aspect ratio distributions (lower left panel) appear fairly consistent between t_0 and t_{300} samples, possibly owing to the non-linear conformation of the fibrils present at t_{300} on the mica surface. Distributions showing the number of monomers within the particles (lower right panel) reveal that monomers and small oligomers (containing <10 monomers) are the dominant species at t_0. At t_{300}, there is an increase in the number of particles containing >100 monomers, although monomers and small oligomers remain the dominant species.

Table 5.3 AFM image statistics of apoSH variants incubated at 5 mg mL^{-1}, pH 7.4, 37 °C.

Red Apo SOD1[a]	Median Length (nm)[b]	Median Breadth (nm)[b]	Average Height (nm)[b]	Number of Large Particles (>200 nm)[c]	Median Aspect Ratio[b,d]	Median Aspect Ratio of Large Particles (>200nm)[b,d,e]	Average Coverage (%)[f]	Average Roughness (nm)[g]
pWT	19.6 (14.7-25.2)	12.4 (10.4-15.9)	0.26 (0.21-0.32)	1	1.38 (1.33-1.63)	3.91 (3.05-6.50)	0.30 ± 0.55	0.12 ± 0.03
A4V	46.9 (26.0-83.0)	30.7 (17.0-49.8)	0.44 (0.24-0.70)	58	1.50 (1.33-1.81)	1.71 (1.44-2.14)	8.85 ± 4.39	1.19 ± 0.47
G37R t_0	16.4 (12.6-28.4)	9.9 (7.3-19.4)	0.21 (0.16-0.32)	1	1.54 (1.33-1.99)	3.37 (2.97-3.77)	1.86 ± 0.91	0.26 ± 0.05
G37R	24.3 (17.0-39.3)	13.9 (10.8-21.8)	0.24 (0.18-0.31)	55	1.50 (1.33-1.89)	2.23 (1.72-2.79)	9.72 ± 2.03	0.26 ± 0.06
G93A	30.1 (19.9-55.4)	16.4 (10.9-39.4)	0.15 (0.12-0.20)	48	1.57 (1.33-2.04)	3.37 (2.38-4.90)	4.98 ± 2.65	0.22 ± 0.25
G93R	48.1 (28.2-80.4)	27.5 (17.9-44.1)	0.50 (0.32-0.67)	117	1.57 (1.33-1.97)	2.02 (1.63-2.54)	14.1 ± 7.14	0.30 ± 0.12
G93S	39.1 (24.5-58.8)	24.3 (14.7-41.5)	0.13 (0.10-0.18)	9	1.50 (1.33-1.88)	2.29 (1.71-3.30)	7.61 ± 4.55	0.20 ± 0.09
V148I+ Na_2SO_4	21.6 (17.0-55.4)	14.7 (10.8-39.1)	0.14 (0.12-017)	14	1.42 (1.33-1.71)	2.86 (2.04-3.99)	2.61 ± 1.49	0.16 ± 0.04

[a]All apoSH SOD1 samples were incubated for over 300 hours at 37 °C before being deposited on the mica and imaged. The exception is G37R labelled t_0, which was not incubated.

[b]Data represents the median and first to third quartile range in brackets of SPIP measurements obtained from all AFM images. Due to asymmetry in the values, the median rather than the average is shown.

[c]The number of large particles was calculated by summing the total number of particles over 200 nm and diving that number by the number of images obtained for that sample. Thus, values represent the average number of particles detected per image. In cases where very few large aggregates were detected and normalization according to the number of images obtained resulted in a number between 0 and 1, the value was rounded to 1.

[d]The aspect ratio equals the particle length divided by breadth.

[e]The aspect ratio of particles with lengths greater than 200 nm.

[f]The coverage is the area taken up by aggregates divided by the total area. Values represent the average and standard deviation of all images.

[g]The roughness is average vertical deviation from the mica surface. Values represent the average and standard deviation of all images. Average roughness should be comparable to particle height if the particles are deposited evenly on the mica surface.

5.3.7 Aggregates formed by different apoSH variants exhibit differences in ThT binding.

The structure of the apoSH aggregates formed at 5 mg mL^{-1} was investigated further with ThT binding experiments. Since its discovery in 1959, ThT binding has become one of the most widely used methods for detecting amyloid structures (331). Upon binding to amyloid, ThT exhibits a shift in excitation and emission maximum from 385 to 450 nm and 445 to 482 nm, respectively, and a several orders of magnitude increase in fluorescence intensity (see also Section 5.3.2) (329–332). This increase in fluorescence intensity has been attributed to the molecular properties of free versus amyloid-bound ThT. ThT is a benzothiazole that contains a combination of polar and hydrophobic regions (Fig. 5.16).

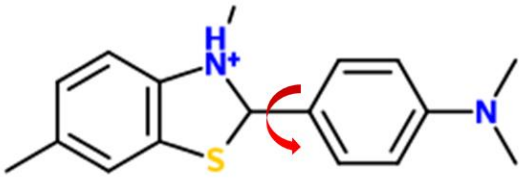

Figure 5.16 Molecular structure of ThT. Free ThT in solution can undergo rotation, as indicated by the red arrow. Immobilization of ThT occurs upon interaction with amyloid fibrils resulting in an increase in fluorescence intensity at 482 nm.

In solution the benzylamine and benzathiole rings are able to rotate, which rapidly quenches the excited state. But when ThT binds to amyloid structures, free rotation of these rings is inhibited and the excited state is preserved (331, 342). ThT appears to bind to diverse amyloid fibrils suggesting that common structural properties within the fibrils are recognized, although the exact mechanism of ThT binding is only beginning to be understood. The consensus is that ThT binds to the surface of amyloid fibrils between the grooves created by sidechains, usually aromatic and hydrophobic side chains, in an orientation that is parallel to the fibril axis (331, 343, 344). Highly charged fibrils tend to exhibit very low levels of ThT binding (331, 345). Furthermore, ThT does not generally interact strongly with misfolded protein, soluble oligomers, or

amorphous aggregates, thus it has some specificity for extended β-sheet structure (346, 347). However, there is evidence for ThT binding to the hydrophobic pockets within non-fibrillar, globular proteins; therefore, when using ThT has to investigate the structure of aggregated protein, it is necessary to demonstrate that increases in ThT fluorescence are not a consequence of binding to the native protein (331). As discussed previously, little ThT fluorescence was observed for samples containing very few aggregates (Fig. 5.6A), which demonstrates that ThT does not bind to non-aggregated apoSH SOD1.

The aggregates formed by the apoSH variants incubated at higher concentration displayed differences in ThT-binding (Fig. 5.17); interestingly, these differences cannot be explained simply by the presence of more aggregates, suggesting that there are differences in the degree and nature of extended β-sheet structure in different aggregates. ThT fluorescence was highest for V148I in 150 mM Na_2SO_4, even though light scattering and AFM indicate that low levels of long fibrils are present in this sample (Section 5.3.5). G93A, which also forms low amounts of long fibrils exhibited an increase in ThT fluorescence comparable to A4V, which aggregates more than all other mutants investigated (Figs. 5.8, 5.9). G93S exhibited very little increase in ThT fluorescence, even lower than pWT, suggesting that there are lower levels of long fibrils in this sample compared to V148I in 150 mM Na_2SO_4, G93A, and pWT.

Of the mutants that extensively aggregate, G93R caused the largest change in ThT fluorescence; A4V caused a modest change in ThT fluorescence while for G37R the change was even smaller. While AFM indicates that the lengths of A4V and G93R fibrils were comparable, differences in ThT fluorescence may be due to coalescence of the fibrils in the A4V sample, reducing the availability of ThT-binding sites, and fibrils formed by G37R were smaller than those formed by A4V and G93R (Figs. 5.10, 5.11, 5.13, S5.7, S5.9, S5.11, Table 5.3). Such a

finding would be consistent with previous work showing that ThT fluorescence is often lower for oligomers and amorphous aggregates (346, 347). Interestingly, the ThT fluorescence maximum for G93R, A4V, and G37R is blue-shifted by roughly 5 nm, which may also be an indicator of different features underlying the structure of these aggregates compared to those formed by pWT, G93A, G93S, and V148I.

Taken together, ThT fluorescence appears to depend on both the concentration of fibrils and the specific structural features within the aggregates. These experiments indicate that V148I in 150 mM Na_2SO_4, and to a lesser extent G93A, form amyloid-like aggregates with an extended β-sheet that result in large increases in ThT fluorescence, even though their concentration is low in solution. Other mutants, such as A4V and G93R, with high levels of aggregated protein cause some increase in ThT fluorescence, but the effect is far less pronounced, which suggests that the underlying structures of the aggregates are different.

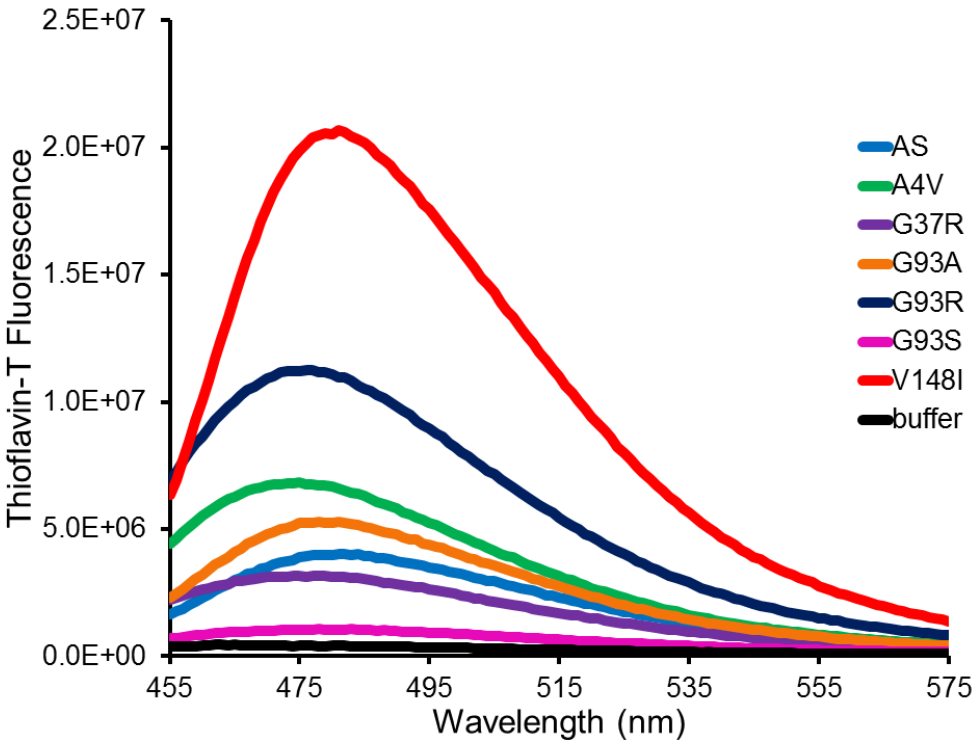

Figure 5.17 Differences in ThT fluorescence upon binding apoSH aggregates formed at high concentration (5 mg mL^{-1}) points to structural differences in the aggregates. Aggregates formed by apoSH incubated at 5 mg mL^{-1} display differences in ThT fluorescence, which suggest that the β-sheet content of these aggregates differs. Free ThT in 1 mM TCEP, 20mM HEPES buffer does not fluoresce at 482 nm (black), but upon binding to aggregates containing an extended β-sheet there is a dramatic increase in fluorescence. Thus the increase in fluorescence intensity is related to both the levels of aggregates as well as the specific structural features that lead to difference enhancements in fluorescence intensity. These experiments show that all aggregates increase the intensity of ThT fluorescence, albeit to different extents, indicating that they all contain some degree of β-sheet. Aggregates formed by V148I in 150 mM Na_2SO_4 have the highest degree of internal β-structure, resembling amyloid. The fluorescence intensity increase is lower for the other mutants, even those that extensively aggregate, G93R (blue) and A4V (green).

5.3.8 Light scattering experiments reveal that Na_2SO_4 and NaCl can increase the aggregation propensity of apoSH SOD1 variants

Another approach to generating higher levels of aggregation is to add salt to the sample buffer. The effects of different salts on protein stability can be highly complex and protein specific, but general trends have emerged from numerous years of work (69, 348–351). Protein association can be enhanced by the addition of salt through various general effects, such as screening charged regions of the protein and reducing electrostatic repulsion between proteins, reducing protein stability by decreasing the strength of salt bridges and/or by binding to the partially charged polypeptide backbone. Salts can also affect protein stability in non-specific ways according to their position in the Hofmeister series; anions have stronger effects than cations (348). The Hofmeister series for anions is as follows:

$SCN^- > ClO_4 > I^- > ClO_3^- > Br^- > NO_3^- > Cl^- > CH_3CO^{2-} > HPO_4^{2-} > SO_4^{2-}$

Chaotropic anions are on the left and destabilize the native state and solubilize proteins, whereas kosmotropic anions on the right stabilize the native state and decrease protein solubility. The Cl^- ion is considered the midpoint of the series, with neither chaotropic or kosmotropic properties (69, 348, 349, 351). The difference between chaotropes and kosmotropes arises from their interactions with native and unfolded proteins. Chaotropes, or denaturants, bind more to the unfolded state and promote unfolding. Kosmotropes on the other hand, are excluded from the solvent surrounding the protein and the degree of exclusion is in proportion to the solvent exposed surface area of the protein. Therefore, when the protein is unfolded there is a larger degree of exclusion, which increases the energy of the unfolded state relative to the folded state and favours protein folding and further assembly (69).

Since the isoelectric point of apoSH SOD1 is pH 5.7 (352, 353), it will have a net negative charge at physiological pH, which may be a factor limiting aggregation in the absence of salt. Na_2SO_4, previously shown to enhance irreversible thermal denaturation of apoSH (K.A. Vassall and E.M. Meiering, unpublished data), and NaCl were therefore added to the samples to try to promote aggregation at 1 mg mL^{-1}. This approach is not unreasonable, given that the intracellular ionic strength is ~100-200 mM (354).

For these experiments a subset of destabilized mutants were selected, as they were expected to be more likely to aggregate at 37 °C compared to more stable, and thus more folded, variants. For pWT, E100G, H43R, and V148G, neither the addition of 150 mM Na_2SO_4 nor 150 mM NaCl caused the light scattering intensity to change markedly with time, similar to samples containing no added salt. Thus, the aggregation propensity of these variants remains low in both salts (Fig. 5.18). For E100G in NaCl, H43R in Na_2SO_4, and V148G in Na_2SO_4, the average light scattering intensity did not change greatly with time; however, the uncertainty in a number of measurements is very high, pointing to the presence of small amounts of large particles in solution (Section 5.3.4). On the other hand, A4V and G93R exhibit considerably higher levels of aggregation in Na_2SO_4 and NaCl, with the former promoting aggregation more than the latter, based on the absolute light scattering intensity after ~t_{300} (Fig. 5.18). This finding is consistent with aggregation experiments in the absence of salt that show A4V and G93R aggregate more than other apoSH variants (Section 5.3.4). Similar to aggregation experiments at 5 mg mL^{-1}, in both Na_2SO_4 and NaCl A4V and G93R aggregate with little apparent lag time, suggesting aggregation from the native state or a low energetic barrier between the native and aggregation-prone state(s).

To assess whether the increased aggregation propensity observed in the presence of Na_2SO_4 was due to increased ionic strength, aggregation was also monitored for samples containing a higher NaCl concentration (450 mM) (Fig. 5.18, Table 5.4). From this one experiment, it appears that Na_2SO_4 retains the ability to promote aggregation over NaCl, even when ionic strength differences are accounted for. If aggregation was promoted primarily by charge screening, then the effects of different salts at the same ionic strength would be identical. In fact, increasing the concentration of NaCl actually decreased aggregation to levels observed for salt free samples (Fig. 5.18), which is consistent with other work that suggests protein aggregation has a bell-shaped dependence on salt (355). Although, additional experiments are required to confirm the validity of these results, it appears that the kosmotropic properties of Na_2SO_4 exert an enhancing effect on aggregation of A4V and G93R. G93S was also found to aggregate more in Na_2SO_4, yet the light scattering intensity plateaued at a lower level compared to A4V and G93R samples indicating the effect of Na_2SO_4 on G93S aggregation is less pronounced.

At t_0, the $D_{h,I}$ and $D_{h,N}$ for pWT are ~5.3 and 2.8 nm, respectively in Na_2SO_4 and ~5.8 and 3.0 nm, respectively in NaCl (Fig. 5.19A), which are fairly close to values obtained for samples with no added salt, 5.4 and 3.1, respectively (Table 5.4). Relative to pWT, mutants exhibit a 1.0-3.1 nm, 2.2-4.7 nm, and 1.0-3.6 nm increase in the $D_{h,I}$ at t_0 for salt free, Na_2SO_4, and NaCl containing samples, respectively, and this increase was most pronounced for A4V and G93R Na_2SO_4 and NaCl samples. The differences in $D_{h,N}$ between pWT and mutant samples are smaller and generally within the margin of uncertainty in the measurements, which is not surprising given that $D_{h,I}$ is more sensitive to subtle changes in the levels of oligomers, as discussed previously.

After ~300 hours of incubation, both the $D_{h,I}$ and $D_{h,N}$ increase for all A4V and G93R samples, however the increase is larger and standard deviation in the values considerably lower for samples containing Na_2SO_4 and NaCl (Fig. 5.17B, Table 5.4). For G93S and V148G Na_2SO_4 samples, only $D_{h,I}$ increases significantly with time and is much larger than $D_{h,N}$ (Fig. 5.19B, Table 5.4). Therefore, Na_2SO_4 has a marginal effect on aggregation propensity of G93S and V148G, while NaCl has little effect. For pWT, H43R, and E100G, little change was observed in $D_{h,I}$ and $D_{h,N}$ values over time in both salt free and salt containing buffers.

When incubated in Na_2SO_4 and NaCl, A4V and G93R samples show a slight decrease in average PDI with time. Alternatively, the change in PDI with time generally increases for all other samples, and for H43R, G93S, and V148G the increase is most pronounced for samples containing Na_2SO_4 and NaCl (Table 5.4). Thus, as discussed above, samples that form aggregates appear to become more monodisperse with time, while samples that aggregate little tend to become more polydisperse with time.

It is further evident from these results that different apoSH mutants display very different aggregation propensities. Aggregation is enhanced by Na_2SO_4, and to a lesser extent NaCl; however, the addition of salt does not result in clearly increased aggregation of all apoSH variants. As was observed for aggregation experiments at 5 mg mL^{-1}, A4V and G93R undergo much higher levels of aggregation in Na_2SO_4 and NaCl compared to the other mutants under all conditions.

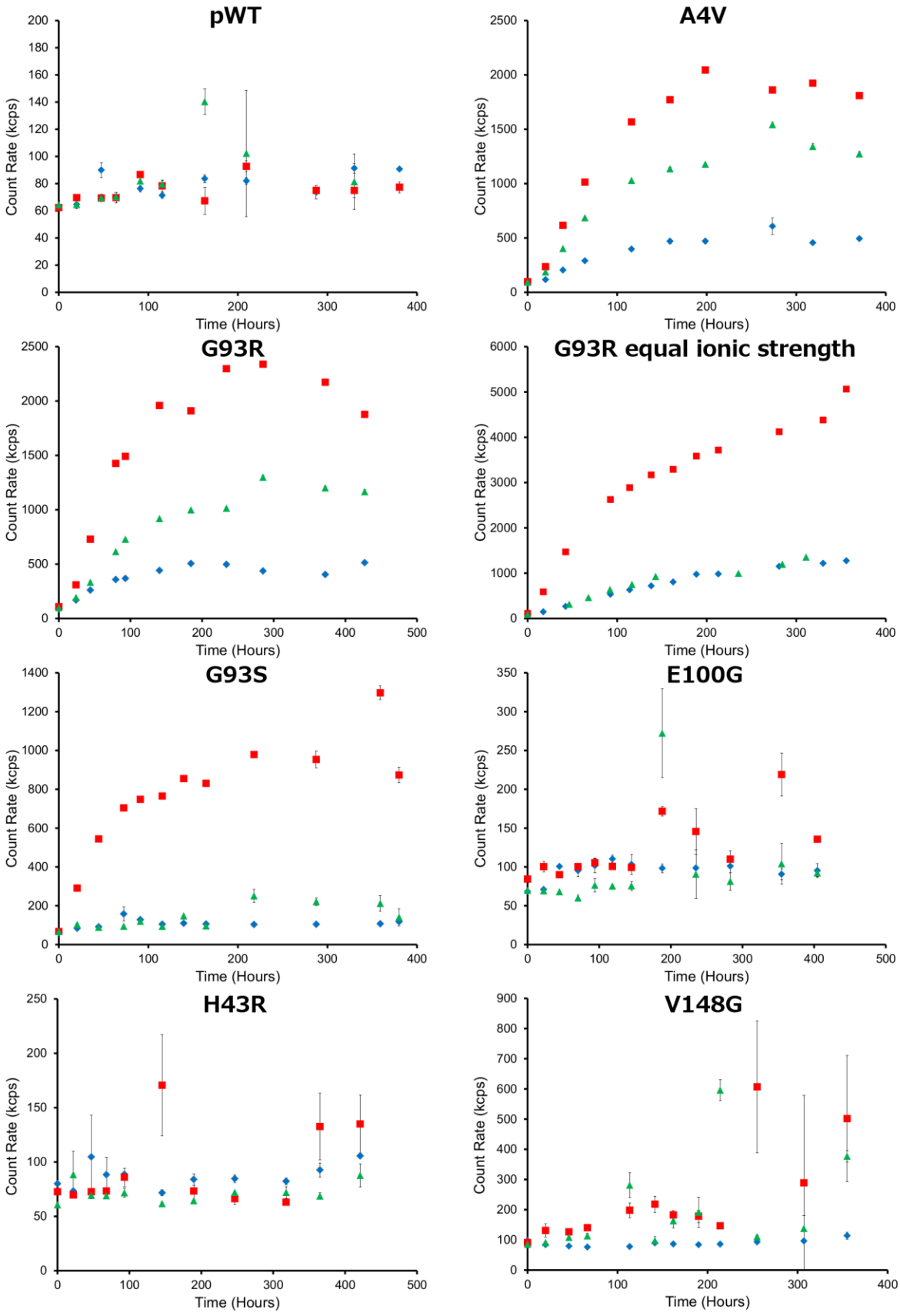
pWT
A4V
G93R
G93R equal ionic strength
G93S
E100G
H43R
V148G
Count Rate (kcps)
Time (Hours)

Figure 5.18 SLS reveals that mutants tend to exhibit increased aggregation propensity when incubated in salt. For all panels, apoSH variants were incubated in buffer, 1 mM TCEP, 20mM HEPES, pH 7.4, with either no salt (blue diamonds), 150 mM Na_2SO_4 (red squares), or 150 mM NaCl (green triangles). In the panel labelled G93R equal ionic strength, the concentration of NaCl was 450 mM. Na_2SO_4 promotes aggregation of all mutants, but the effect was most pronounced for A4V, G93R, and G93S. NaCl only appears to enhance aggregation of A4V and G93R, and the effect is lower compared to Na_2SO_4. Error bars represent the standard deviation of three measurements at each time point.

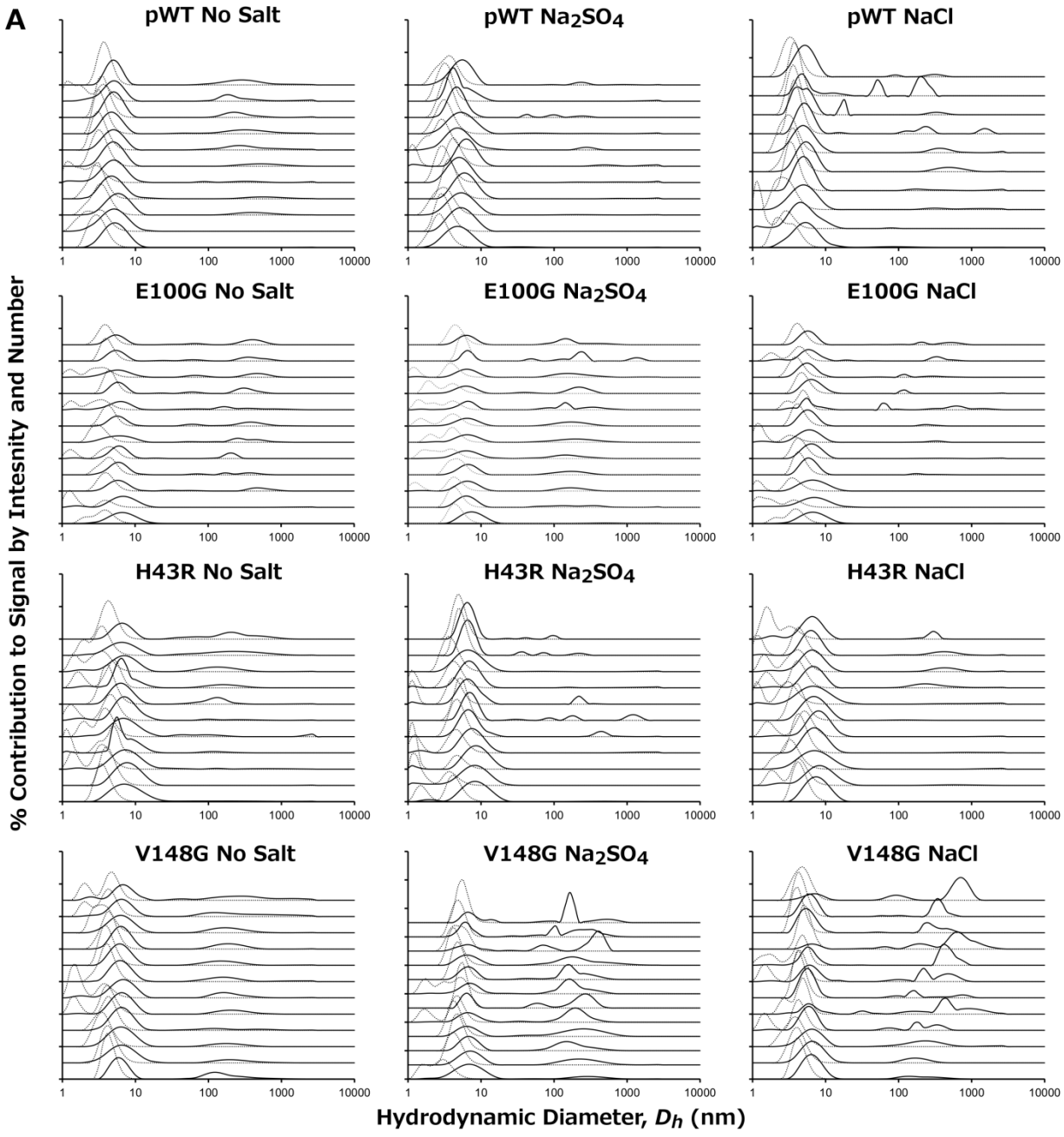
A
pWT No Salt
pWT Na2SO4
pWT NaCl
E100G No Salt
E100G Na2SO4
E100G NaCl
H43R No Salt
H43R Na2SO4
H43R NaCl
V148G No Salt
V148G Na2SO4
V148G NaCl
% Contribution to Signal by Intesnity and Number
Hydrodynamic Diameter, Dh (nm)
1
10
100
1000
10000

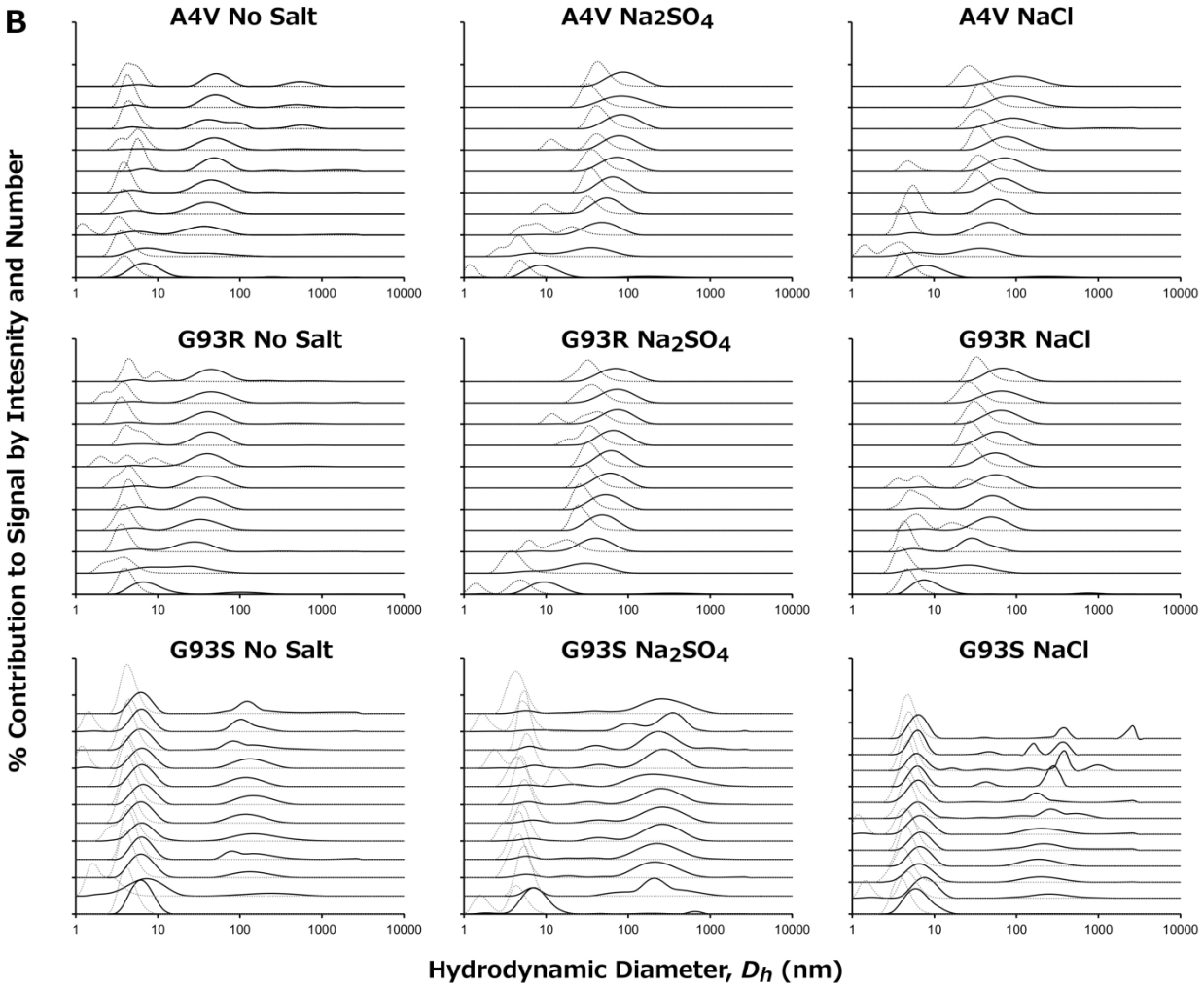

Figure 5.19 DLS experiments indicate that Na_2SO_4 and NaCl promote aggregate formation, most notably for A4V and G93R mutants. Sample conditions are the same as those described in Fig. 5.18. **(A)** The effect of salt on the size of particles in solution is shown for mutants that displayed little increase in light scattering intensity with incubation time. For these apoSH variants, DLS indicates that very low levels of aggregation are observed under all conditions. **(B)** The effect of salt on the size of particles in solution is shown for mutants that displayed an increase in light scattering intensity with incubation time (Fig. 5.18). For A4V and G93R, aggregation is enhanced in 150 mM Na_2SO_4 and NaCl as indicated by the shift in intensity (solid lines) and number distributions (dotted lines) to larger values. While G93S showed an increase in light scattering intensity with incubation time in 150 mM Na_2SO_4 (Fig. 5.18), DLS data indicates that the aggregates formed never become the most abundant species. At t_0 there is a difference in the size reported by intensity and number distribution for all samples, which suggests that the samples exhibit some degree of heterogeneity. Table 5.4 provides a summary of DLS data shown here.

Table 5.4 DLS data summary for apoSH SOD1 variants at 1 mg mL^{-1}, pH 7.4, 37 °C, 150 mM salt.

	t = 0				t > 300			
ApoSH SOD1 variant	PDI[a]	PDI width (nm)[b]	Intensity Distribution Hydrodynamic Radius (nm)[c]	Number Distribution Hydrodynamic Radius (nm)[c]	PDI[a]	PDI width (nm)[b]	Intensity Distribution Hydrodynamic Radius (nm)[c]	Number Distribution Hydrodynamic Radius (nm)[c]
pWT	**0.205**	**2.146**	**5.383**	**3.131**	**0.267**	**5.231**	**5.228**	**3.449**
No Salt	*0.025*	*0.250*	*0.332*	*0.387*	*0.083*	*5.657*	*0.253*	*0.398*
pWT	**0.240**	**2.197**	**5.262**	**2.816**	**0.236**	**61.37**	**5.551**	**3.292**
Na_2SO_4	*0.023*	*0.093*	*0.502*	*0.541*	*0.066*	*79.72*	*0.888*	*1.050*
pWT	**0.228**	**2.298**	**5.800**	**3.013**	**0.350**	**127.9**	**5.350**	**3.522**
NaCl	*0.031*	*0.273*	*0.117*	*0.980*	*0.135*	*214.9*	*0.213*	*0.619*
A4V	**0.224**	**5.566**	**8.593**	**3.807**	**0.312**	**29.55**	**63.46**	**15.40**
No Salt	*0.043*	*9.779*	*1.452*	*1.376*	*0.119*	*10.88*	*15.38*	*14.70*
A4V	**0.273**	**4.665**	**9.907**	**4.446**	**0.212**	**33.47**	**90.67**	**43.77**
Na_2SO_4	*0.024*	*0.540*	*0.804*	*2.712*	*0.022*	*4.221*	*8.127*	*6.920*
A4V	**0.269**	**4.418**	**9.239**	**3.907**	**0.211**	**31.79**	**86.95**	**43.86**
NaCl	*0.015*	*0.268*	*0.409*	*1.466*	*0.013*	*1.610*	*3.608*	*3.869*
E100G	**0.230**	**2.595**	**6.432**	**3.548**	**0.461**	**86.19**	**123.5**	**4.003**
No Salt	*0.014*	*0.151*	*0.739*	*0.706*	*0.163*	*52.04*	*353.4*	*0.357*
E100G	**0.267**	**3.937**	**8.087**	**4.756**	**0.390**	**105.8**	**6.566**	**5.821**
Na_2SO_4	*0.013*	*0.298*	*0.477*	*0.405*	*0.058*	*86.10*	*0.112*	*0.078*
E100G	**0.217**	**2.820**	**7.309**	**3.763**	**0.414**	**162.2**	**5.876**	**3.645**
NaCl	*0.033*	*0.154*	*0.354*	*1.132*	*0.049*	*174.3*	*0.214*	*1.548*
G93R	**0.240**	**3.732**	**7.563**	**3.971**	**0.598**	**26.87**	**151.1**	**11.60**
No Salt	*0.056*	*1.155*	*0.806*	*1.053*	*0.334*	*9.509*	*104.2*	*11.58*
G93R	**0.257**	**14.51**	**9.754**	**4.390**	**0.233**	**36.20**	**96.74**	**40.40**
Na_2SO_4	*0.035*	*29.85*	*0.920*	*1.633*	*0.030*	*6.532*	*16.03*	*6.737*
G93R	**0.254**	**4.889**	**9.355**	**4.297**	**0.245**	**30.78**	**83.08**	**35.06**
NaCl	*0.037*	*1.813*	*1.326*	*1.378*	*0.018*	*3.004*	*9.362*	*7.290*
G93R[d]	**0.285**	**71.70**	**8.259**	**4.968**	**0.337**	**56.19**	**142.2**	**34.19**
NaCl	*0.038*	*116.6*	*1.266*	*0.676*	*0.044*	*5.427*	*10.12*	*22.31*
G93S	**0.239**	**3.226**	**7.136**	**3.899**	**0.502**	**30.34**	**84.11**	**3.880**
No Salt	*0.024*	*0.548*	*0.708*	*0.930*	*0.143*	*46.08*	*85.18*	*1.598*
G93S	**0.239**	**4.570**	**8.312**	**3.944**	**0.629**	**214.8**	**331.8**	**4.354**
Na_2SO_4	*0.023*	*1.851*	*0.346*	*1.660*	*0.264*	*19.22*	*17.33*	*2.296*
G93S	**0.236**	**61.46**	**6.788**	**4.136**	**0.704**	**837.6**	**6.287**	**5.099**
NaCl	*0.050*	*101.5*	*1.105*	*0.503*	*0.143*	*353.3*	*0.186*	*0.558*
H43R	**0.215**	**3.547**	**8.603**	**4.046**	**0.344**	**51.18**	**6.640**	**3.735**
No Salt	*0.049*	*0.650*	*0.457*	*0.885*	*0.110*	*150.6*	*0.651*	*1.503*
H43R	**0.255**	**3.745**	**9.258**	**3.595**	**0.763**	**908.9**	**6.760**	**5.359**
Na_2SO_4	*0.014*	*0.183*	*1.138*	*1.754*	*0.286*	*995.7*	*0.416*	*0.162*
H43R	**0.233**	**2.984**	**8.104**	**4.658**	**0.255**	**12.72**	**6.604**	**3.460**
NaCl	*0.003*	*0.202*	*0.551*	*0.371*	*0.007*	*13.23*	*0.177*	*1.941*
V148G	**0.291**	**10.37**	**6.646**	**3.928**	**0.567**	**191.1**	**291.5**	**3.955**
No Salt	*0.117*	*13.20*	*0.522*	*1.343*	*0.138*	*197.1*	*316.3*	*1.083*
V148G	**0.319**	**4.906**	**7.458**	**2.761**	**0.877**	**1247**	**280.1**	**5.759**
Na_2SO_4	*0.012*	*0.296*	*0.490*	*1.014*	*0.145*	*904.4*	*197.9*	*0.274*
V148G	**0.238**	**11.13**	**6.803**	**4.533**	**0.741**	**414.1**	**725.3**	**4.879**
NaCl	*0.105*	*11.56*	*0.673*	*0.389*	*0.081*	*161.5*	*53.00*	*0.991*

Bold and italicized values are the averages and standard deviations, respectively resulting from multiple experiments (shown in Table S5.4).

[a]PDI is obtained from the Cumulants method of fitting the autocorrelation function (Eq. 5.4). Values larger than 0.1 are indicative of polydispersity (i.e., the sample contains than one species in solution). High PDI values result in larger peak widths, and thus greater uncertainty in the sizes reported.

[b]Peak width reflects the uncertainty in the hydrodynamic diameter obtained from the intensity distribution and is related to the PDI according to Eq. 5.4.

[c]The sizes reported correspond to the main peak in the distributions

[d]Ionic strength of this sample was identical to Na_2SO_4 samples.

5.3.9 AFM imaging shows that Na_2SO_4 and NaCl promote fibrillization of A4V, G93R and G93S

To account for the increase in light scattering intensity observed for A4V, G93R, and G93S in Na_2SO_4 and to a lesser extent NaCl, AFM was again used to assess the size and morphology of the aggregates formed. The absolute light scattering intensity will increase if the size and/or number of aggregates increase. As shown in Fig. 5.19, DLS experiments suggest that the size of the aggregates does increase, shown by the increase in $D_{h,N}$, and the magnitude is similar for both A4V and G93R samples in Na_2SO_4 and NaCl. The same increase in $D_{h,N}$ was not observed for G93S in Na_2SO_4 and NaCl sample, but an increase in $D_{h,I}$ as well as an increase in light scattering intensity was evident, which together point to lower levels of aggregate formation. The $D_{h,I}$ and $D_{h,N}$ distributions are, however, quite broad and may not reflect subtle differences in the size of the particles formed under the different conditions. AFM, on the other hand, provides a more powerful technique for assessing these differences.

AFM imaging confirms that Na_2SO_4 and NaCl generally promote fibrillization of A4V, G93R, and G93S (Figs. 5.20-5.22, S5.14-S5.23). For both A4V and G93R, median length and breadth estimates indicate that longer and thicker fibrils form in Na_2SO_4 and NaCl, and size estimates are fairly consistent with DLS data given the caveats mentioned previously (Figs. 5.20-5.22, S5.14-S5.21, Tables 5.4, 5.5). For both A4V and G93R, particles larger than 200 nm are more numerous in samples containing salt (Figs. 5.20, 5.21), and the average coverage estimates for these samples are also generally higher (Table 5.5).

At 1 mg mL^{-1}, the average aspect ratio of these larger aggregates appear similar in salt free and salt containing buffers; yet, far fewer of these larger aggregates are detected in salt free buffer which leads to less accurate size statistics. Comparing the average aspect ratios of the

larger aggregates formed in Na_2SO_4 and NaCl with those formed at higher protein concentration (5 mg mL^{-1}) in salt free buffer, it is evident that A4V and G93R aggregates formed in salt have higher aspect ratios than those formed at 5 mg mL^{-1} in the absence of salt (Section 5.3.5). Thus, salt appears to promote aggregation and more specifically growth in the length of fibrils (Figs. 5.20-5.22, Table 5.5).

G93S appears to form formed fewer, but much longer fibrils in Na_2SO_4 and to a lesser extent in NaCl (Figs. 5.20, 5.21, S5.22, S5.23), compared to A4V and G93R. Given that salt free and NaCl containing samples exhibited similar levels of aggregation by light scattering, only Na_2SO_4 and NaCl samples were imaged. Although the median length and breadth estimates suggest that most particles in solution are quite small (12-30 nm in length), there are a fair number of aggregates larger than 200 nm detected in both samples. The large aggregates formed in Na_2SO_4 tend to have the highest aspect ratios (Fig. 5.19, Table 5.5), even larger than aggregates formed at 5 mg mL^{-1} in salt free buffer. These long fibrils also tend to form branches that are suggestive of either secondary nucleation sites, or bundling of fibrils together. G93S fibrils formed in NaCl also showed evidence of branching and/or bundling, although to a lesser extent (Figs. 5.20, 5.21, S5.23).

Thus, it can be concluded that aggregates formed in salt are more fibrillar compared to those formed in the absence of salt. The morphology of A4V and G93R aggregates formed in Na_2SO_4 and NaCl were similar, although the aspect ratios of G93R aggregates longer than 200 nm were found to be higher. For G93S, Na_2SO_4 and to a lesser extent NaCl induced formation of fibrils much longer with several branches, although overall much lower levels of aggregation were observed compared to A4V and G93R. This trend is familiar; at 5 mg mL^{-1}, apoSH mutants that displayed lower aggregation propensity formed longer aggregates (Section 5.3.5). It

could be that such mutants form more stable interactions that lead to the formation of longer fibrils.

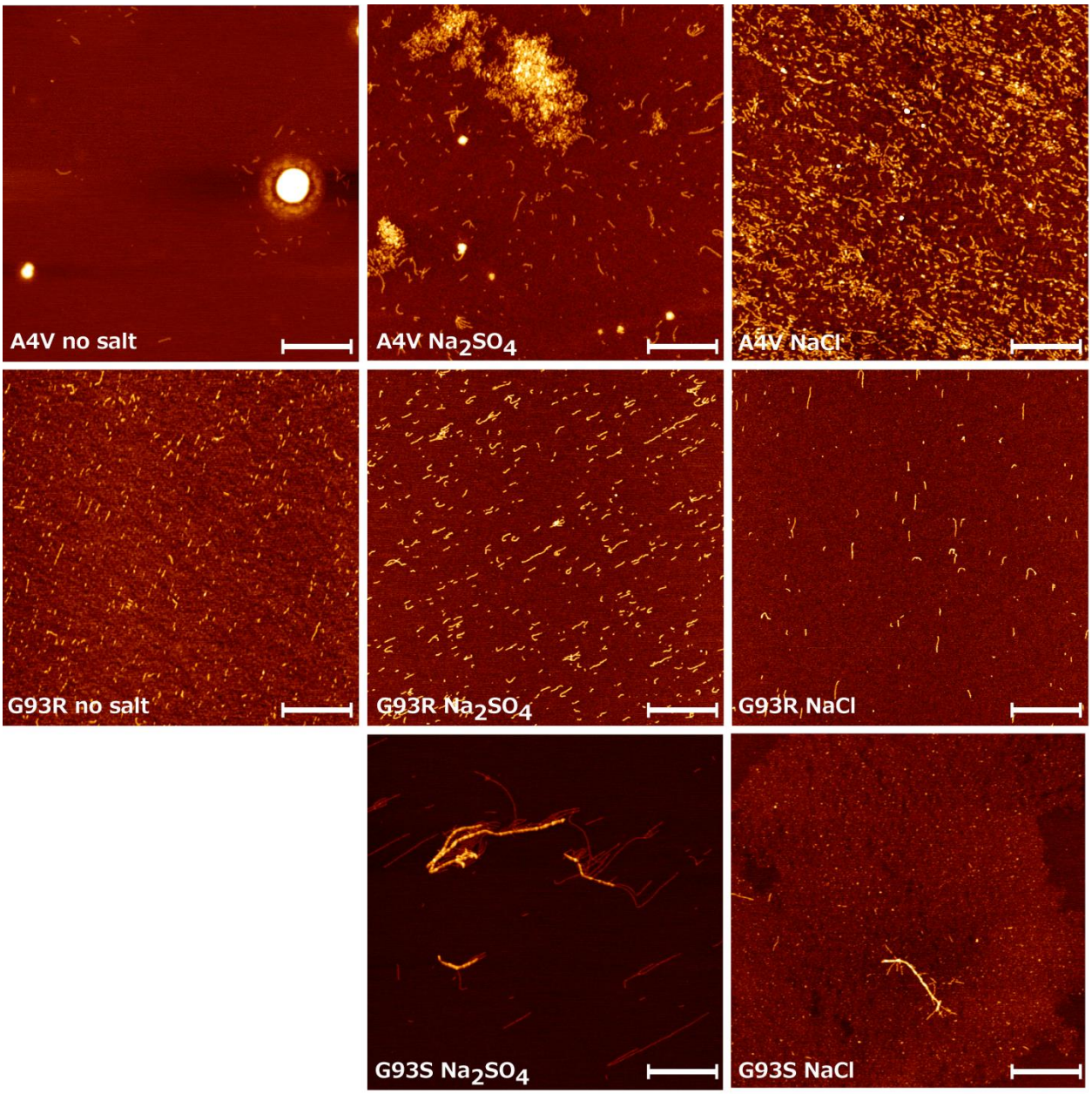

Figure 5.20 AFM reveals that A4V, G93R, and G93S form aggregates of differing sizes and morphologies in Na_2SO_4 and NaCl. AFM images of apoSH variants incubated in salt free, Na_2SO_4, and NaCl for ~300 hours. All images are 5 x 5 μm and white bars indicate 1 μm. Only samples exhibiting high levels of aggregation by light scattering were imaged. Since salt free and NaCl G93S samples showed similar levels of aggregation by light scattering, only the later was imaged. Consistent with DLS results, less aggregation was observed for salt free samples. SPIP software indicates that fibrils formed in salt tend to be longer than those formed in salt free buffer (Fig. 5.25). For all images of these samples refer to Figs. S5.14-S5.23.

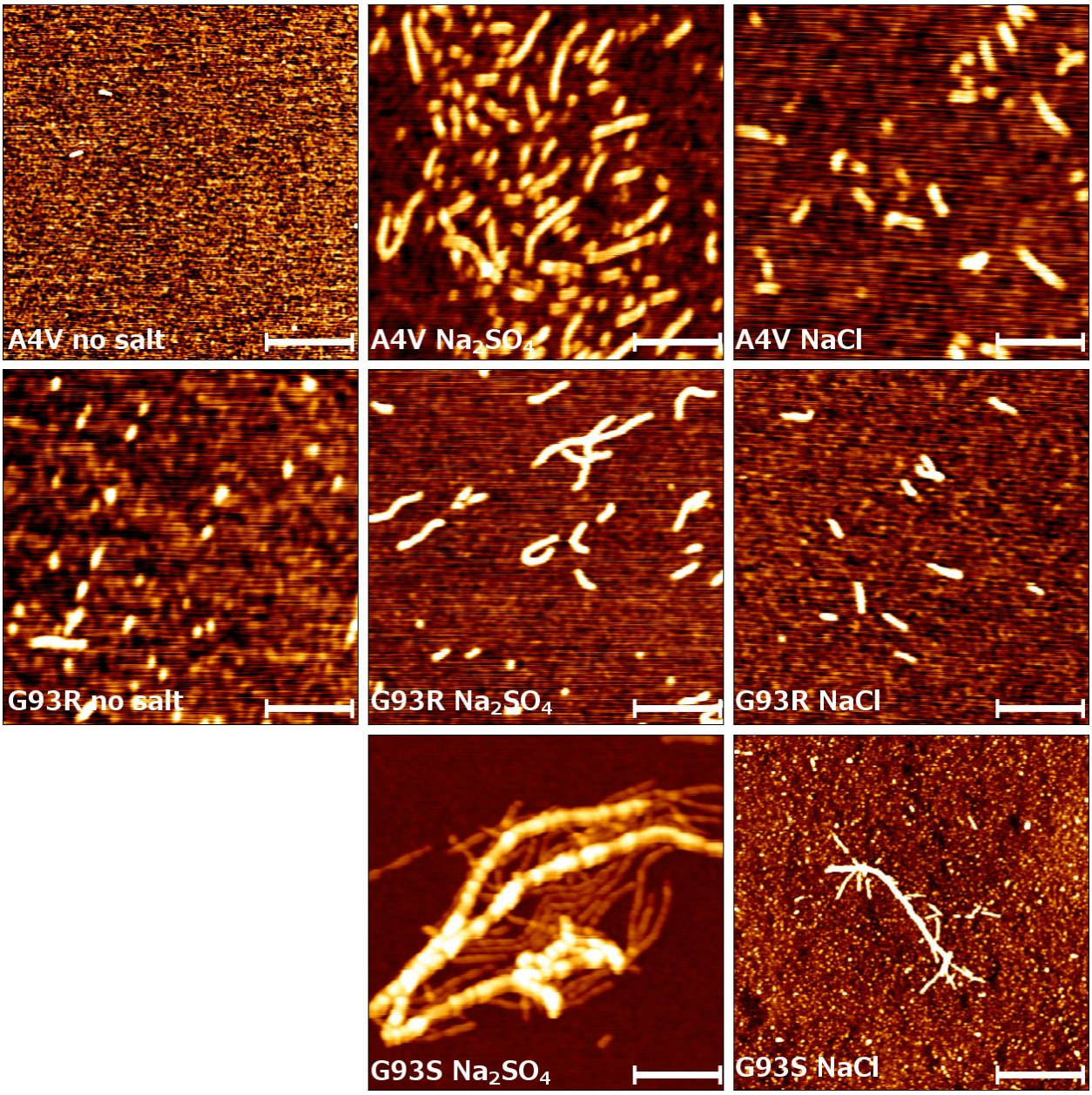

Figure 5.21 Close-up AFM images of different apoSH variants incubated in salt free, Na_2SO_4, and NaCl buffer reveal the abundance of monomers, small oligomers, and larger aggregates with diverse morphologies. Close-up images of those shown in Fig. 5.20 reveal small particles resembling monomers and small oligomers are abundant. Aggregates formed in salt tend to be more fibrillar, with the longest fibrils formed by G93S in Na_2SO_4. These images are 2 x 2 µm and white bars indicate 500 nm.

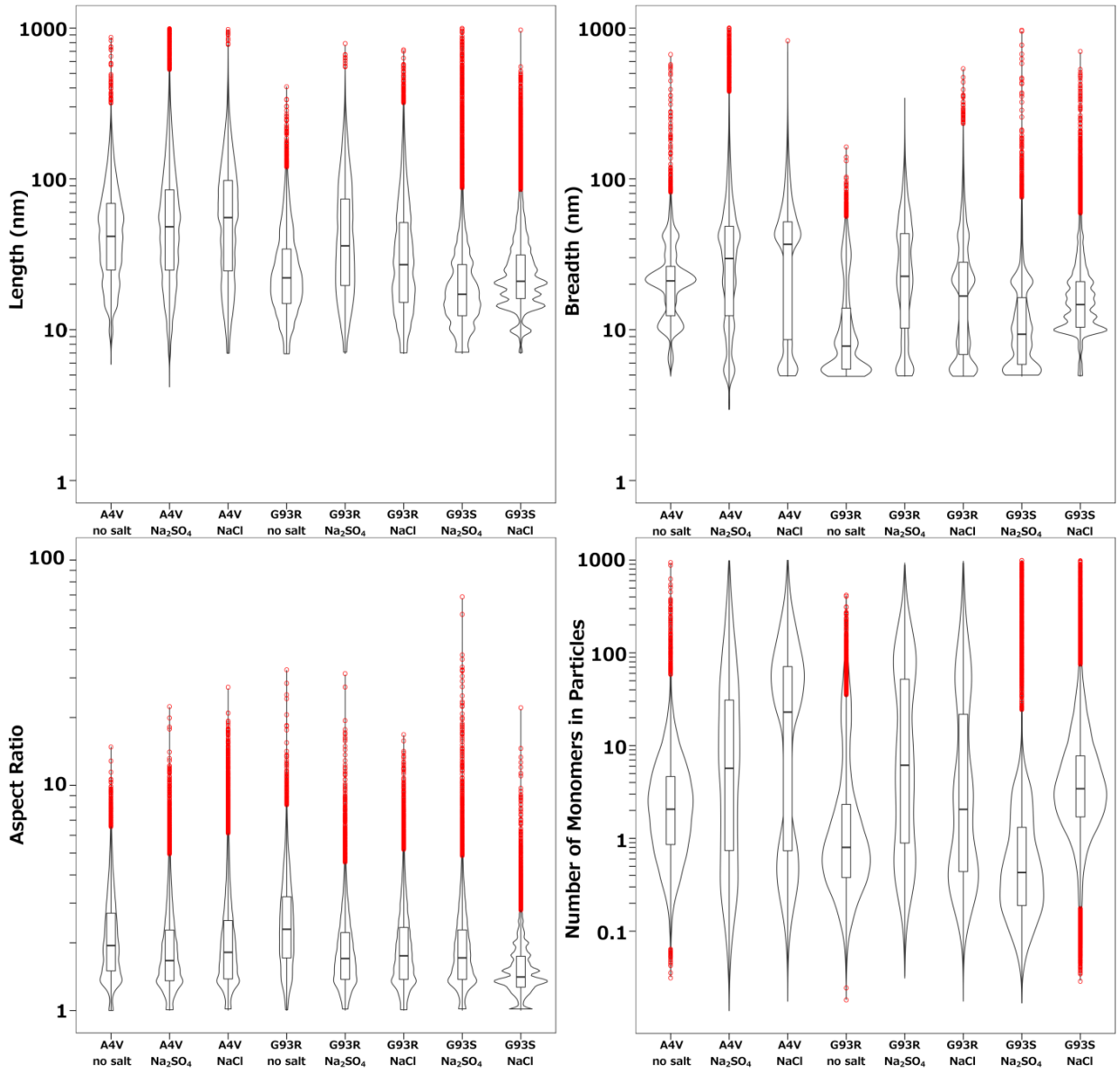

Figure 5.22 AFM measurements of aggregated apoSH variants in salt free, Na_2SO_4, and NaCl represented as box and whisker superimposed on violin plots. In each panel, the median of the data is shown by a horizontal line in the middle of the box and the box represents the first to third quartile of the data (i.e., the middle 50% of the data). The whiskers extend 1.5 times the interquartile range from the edges of the box and all points outside this range, which are considered outliers, are shown individually as red circles. Violin plots were superimposed on the box and whisker plots to illustrate the density of the data. Length, breadth, and aspect ratio distributions (top right, top left, and bottom left panels, respectively) show that the median of the data is shifted to higher values for samples containing Na_2SO_4 and NaCl. Furthermore, particle length and breadth estimates were larger for A4V and G93R compared to G93S, which is consistent with light scattering results that point to higher aggregation propensity of A4V and G93R Furthermore, the A4V and G93R distributions are broader than G93S distributions. For G93S, in all distributions there are more large particles considered outliers (red dots), which can

be accounted for by the presence of long fibrils in the images. Distributions showing the number of monomer per particle indicate that the majority of particles detected have volumes consistent with ~1-5 monomers for salt free A4V and G93R samples, as well as G93S Na_2SO_4 and NaCl samples. For A4V and G93R Na_2SO_4 and NaCl samples, these distributions become broader as more particles contain 10-100 monomers are detected.

Table 5.5. AFM image statistics of aggregated apoSH variants at 1 mg mL^{-1}, pH 7.4, 37 °C, 150 mM salt.

Red Apo SOD1[a]	Median Length (nm)[b]	Median Breadth (nm)[b]	Median Height (nm)[b]	Number of Large Particles (>200 nm)[c]	Median Aspect Ratio[b,d]	Median Aspect Ratio of Large Particles (>200nm)[b,d,e]	Average Coverage (%)[f]	Average Roughness (nm)[g]
A4V no salt	21.9 (14.9-55.0)	12.4 (9.8-33.9)	0.12 (0.10-0.39)	5	1.56 (1.33-2.22)	2.01 (2.47-3.07)	1.32 ± 1.96	0.19 ± 0.18
A4V Na_2SO_4	48.2 (24.9-85.7)	29.7 (12.4-48.6)	0.12 (0.10-0.28)	109	1.67 (1.35-2.28)	2.03 (1.57-2.76)	16.4 ± 7.48	0.55 ± 0.33
A4V NaCl	55.4 (24.5-97.6)	36.8 (8.6-51.9)	0.33 (0.12-0.45)	167	1.81 (1.38-2.51)	2.11 (1.63-2.80)	13.4 ± 3.50	0.30 ± 0.08
G93R no salt	22.0 (14.9-34.2)	7.8 (5.5-13.9)	0.16 (0.11-0.54)	7	2.29 (1.71-3.20)	3.69 (2.74-4.97)	4.39 ± 1.04	0.17 ± 0.00
G93R Na_2SO_4 t_{22}	15.3 (9.8-36.0)	9.0 (5.4-22.1)	0.31 (0.20-0.50)	0	1.57 (1.33-2.00)	1.93 (1.75-3.71)	0.35 ± 0.06	0.13 ± 0.05
G93R Na_2SO_4 t_{143}	68.4 (34.5-119.2)	33.2 (21.0-41.3)	0.64 (0.41-0.50)	61	2.23 (1.61-3.18)	4.73 (3.38-5.64)	3.02 ± 0.29	0.19 ± 0.00
G93R Na_2SO_4	35.9 (19.6-73.5)	22.6 (10.2-43.3)	0.25 (0.16-0.53)	78	1.70 (1.38-2.22)	2.87 (2.12-3.75)	8.31 ± 6.06	0.27 ± 0.11
G93R NaCl	27.0 (15.2-51.3)	16.7 (6.8-28.0)	0.16 (0.11-0.54)	52	1.75 (1.38-2.34)	2.25 (1.70-3.32)	6.11 ± 6.62	0.30 ± 0.29
G93S Na_2SO_4	17.2 (12.4-27.1)	9.3 (5.9-16.3)	0.10 (0.07-0.12)	30	1.71 (1.38-2.28)	5.09 (3.32-8.19)	2.68 ± 0.80	0.15 ± 0.05
G93S NaCl	20.9 (16.1-31.3)	14.7 (10.4-20.8)	0.32 (0.21-0.46)	17	1.41 (1.27-1.74)	2.19 (1.62-2.79)	6.51 ± 2.34	0.30 ± 0.11

[a]All apoSH SOD1 samples were incubated for over 300 hours at 37 °C before being deposited on the mica and imaged. The exception is G93R in 150 mM Na_2SO_4 labelled t_{22} and t_{143}, where samples were incubated for 22 and 143 hours respectively.

[b]Data represents the median and first to third quartile range in brackets of SPIP measurements obtained from all AFM images. Due to asymmetry in the values, the median rather than the average is shown.

[c]The number of large particles was calculated by summing the total number of particles over 200 nm and diving that number by the number of images obtained for that sample. Thus, values represent the average number of particles detected per image. In cases where very few large aggregates were detected and normalization according to the number of images obtained resulted in a number between 0 and 1, the value was rounded to 1.

[d]The aspect ratio equals the particle length divided by breadth.

[e]The aspect ratio of particles with lengths greater than 200 nm.

[f]The percent coverage is the area taken up by aggregates divided by the total area. Values represent the average and standard deviation of all images.
[g]The roughness is average vertical deviation from the mica surface. Values represent the average and standard deviation of all images. Average roughness should be comparable to particle height if the particles are deposited evenly on the mica surface.

5.3.10 ApoSH G93R in Na_2SO_4 initially forms small fibrils that lengthen over time

Samples from the early, middle, and end stages of apoSH G93R aggregation in Na_2SO_4 were imaged by AFM to assess changes in aggregate structure that coincide with increases in light scattering intensity (Figs. 5.20, S5.18-S5.20). As shown in Fig. 5.20, small fibrils have already begun to form in the first 22 hours of incubation. The median length and breadth estimates of the particles are ~15 nm and 9 nm, respectively, and volume estimates suggest that the majority of particles in solution are monomers with some oligomers present as well (Fig. 5.21). This result indicates that oligomerization begins rapidly in Na_2SO_4, consistent with SLS data that shows little detectible lag time before light scattering intensity increases (Fig. 5.16). As mentioned previously, detection of more than one species in solution after only 22 hours of incubation may account for the high PDI values obtained by DLS before aggregates become abundant (Section 5.3.7).

After 143 hours of incubation, the median length and breadth of particles increases to ~68 nm and 33 nm, respectively. The distributions of the length, breadth, and number of monomers per particle broaden, pointing to an increase in the proportion of larger particles. Furthermore, the aggregates become more elongated, as indicated by the increase in aspect ratio, which is even more pronounced for particles longer than 200 nm (Table 5.5). Interestingly, at 143 hours of incubation the fibrils appear to have reached their maximum size. At 234 hours, aggregate sizes and aspect ratios are comparable to estimates at 143 hours (Fig. 5.17). Nevertheless, the average coverage of the sample on the mica surface increases with time; therefore, the increase in light scatter intensity between 143 to 234 hours of incubation appears not to be due to further aggregate growth, but rather an increase in abundance of these fibrils.

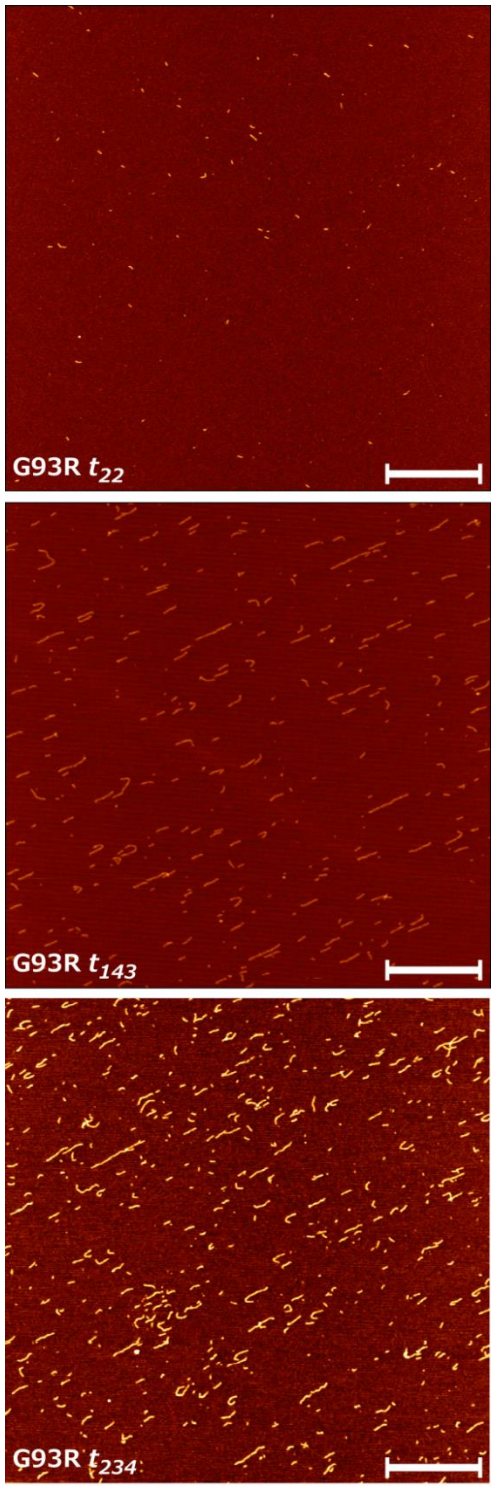

Figure 5.23 AFM images of apoSH G93R in 150 mM Na_2SO_4 as a function of time. ApoSH G93R was imaged at different time points over the course of the incubation period. The top, middle, and bottom panels correspond to 22, 143, and 234 hours of incubation, respectively. These times correspond to initial nucleation, exponential, and plateau phases of the aggregation mechanism (Fig. 5.18). All images are 5 x 5 μm and white bars indicate 1 μm. For all images of these samples refer to Figs. S5.17-S5.20.

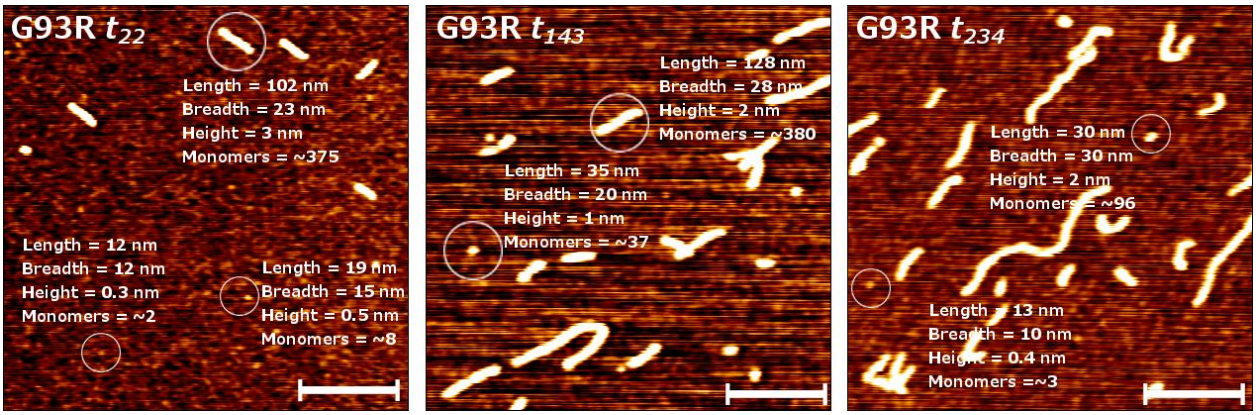

Figure 5.24 Close-up AFM images of apoSH G93R in Na_2SO_4 as a function of time. Close-up images of those shown in Fig. 5.23 reveal small particles resembling monomers and small oligomers as well as longer fibrils are abundant. The left, middle, and right panels correspond to 22, 143, and 234 hours of incubation, respectively, corresponding to the initial nucleation, exponential, and plateau phases of the aggregation mechanism (Fig. 5.18). Size estimates were calculated by hand using JPK Data Processing Software (JPK Instruments AG). All images are 2 x 2 μm and white bars indicate 500 nm. For all images of these samples refer to Figs. S5.18-S5.20.

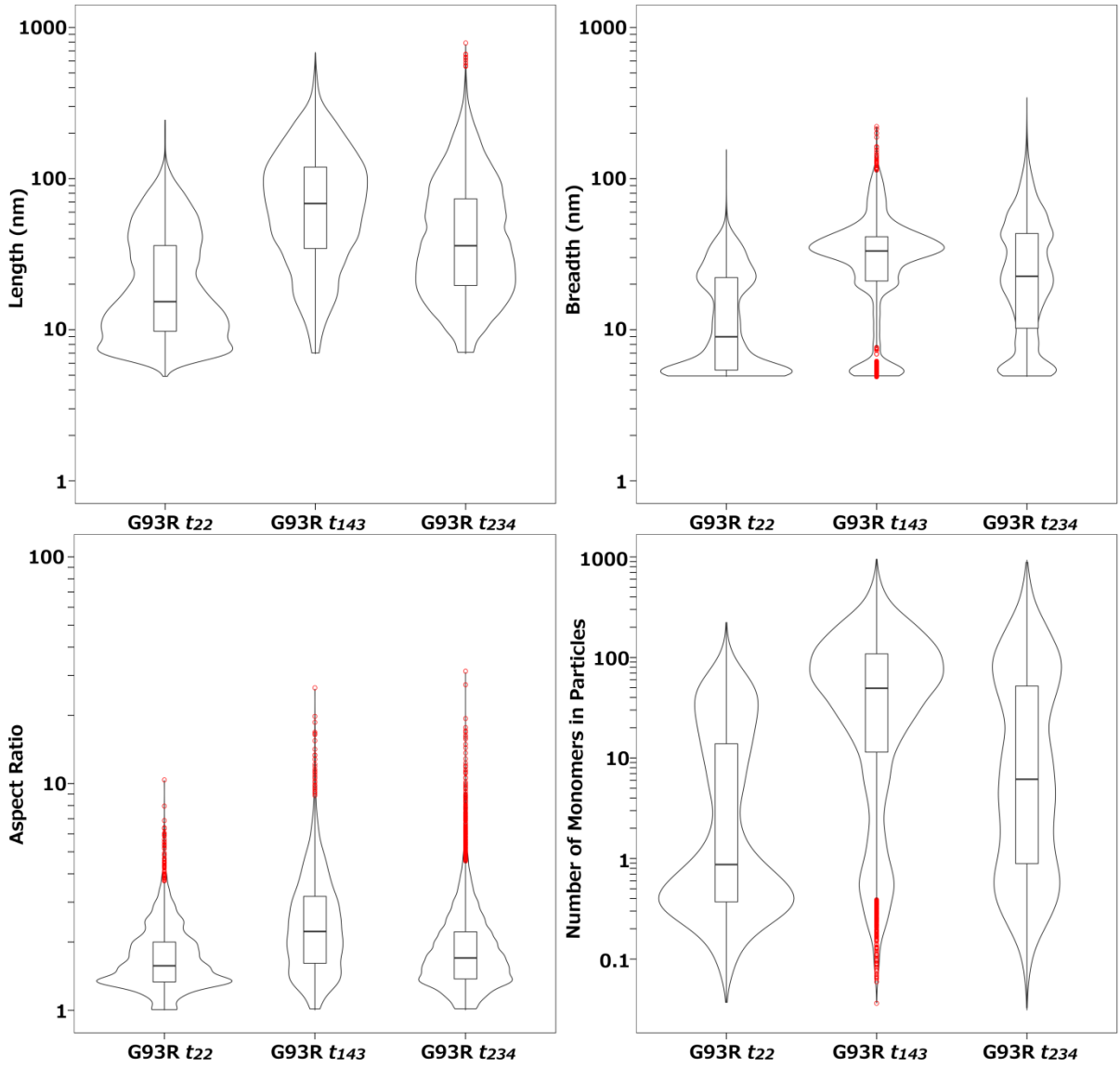

Figure 5.25 AFM measurements of apoSH G93R incubated in Na_2SO_4 for 22 143, and 234 hours represented as box and whisker superimposed on violin plots. In each panel, the median of the data is shown by a horizontal line in the middle of the box and the box represents the first to third quartile of the data (i.e., the middle 50% of the data). The whiskers extend 1.5 times the interquartile range from the edges of the box and all points outside this range, which are considered outliers, are shown individually as red circles. Violin plots were superimposed on the box and whisker plots to illustrate the density of the data. Length, breadth, and aspect ratio distributions (top right, top left, and bottom left panels, respectively) show that the median of the data is shifted to higher values for samples for t_{143} compared to t_0 samples. After t_{143} aggregate growth is less apparent. Distributions showing the number of monomer per particle (lower right panel) indicate that the majority of particles detected at t_{22} range from ~1-10 monomers and over time the proportion of particles containing 10-100 monomers increases.

5.3.11 Fibrils formed in salt compared to salt free samples display increases in ThT binding

ThT binding experiments were performed on a subset of mutants that exhibited different aggregation propensities in salt to further investigate structural differences in the aggregates formed. The mutants selected were A4V and G93R, which both exhibit high levels of aggregation in salt; G93S which aggregates slightly in Na_2SO_4, but much less in NaCl; and E100G which aggregates very little under all conditions. As discussed in Section 5.3.6, upon binding to aggregates that contain an extended β-sheet, ThT exhibits a shift in excitation and emission maximum from 385 to 450 nm and 445 to 482 nm, respectively, and a several orders of magnitude increase in fluorescence intensity (329–332). Thus, differences in ThT binding properties can point to differences in the underlying structure within the aggregates.

In general, samples containing Na_2SO_4 displayed the highest levels of ThT fluorescence. Fluorescence was lower in NaCl samples and even lower in the salt free samples (Fig. 5.26), consistent with the level of aggregation observed by light scattering and AFM. G93R samples were the exception to this trend; all displayed similar levels of ThT fluorescence. As shown in section 5.3.6, apoSH variants that form long fibrils at 5 mg mL^{-1}, in the absence of salt, display high levels of ThT fluorescence, even though the concentration of these aggregates is low. Thus, ThT fluorescence is highly sensitive to aggregates with amyloid-like properties.

Although the distribution of sizes is large, AFM experiments suggest that A4V fibrils formed in Na_2SO_4 and NaCl are longer than those formed in the absence of salt. G93S in Na_2SO_4 formed fibrils much longer than those observed in A4V and G93R samples (Fig. 5.22). Given that G93S aggregates formed in Na_2SO_4 display the highest levels of ThT fluorescence, even though these fibrils are not highly abundant suggests that the longer fibrils may contain more extensive β-sheet structure. All E100G samples, as well as salt free and containing G93S

samples, which displayed little change in light scattering intensity over time, showed the smallest increases in ThT fluorescence consistent with low levels of aggregation. These results highlight the advantages of combining light scattering and ThT-binding experiments. Fibrils longer than 1000 nm are difficult to detect by light scattering, especially if present at low concentrations. On the other hand, ThT-binding appears to be highly sensitive to detecting low levels of these fibrils. When both changes in light scattering intensity are small and ThT fluorescence is low, it can be concluded that little aggregation takes place.

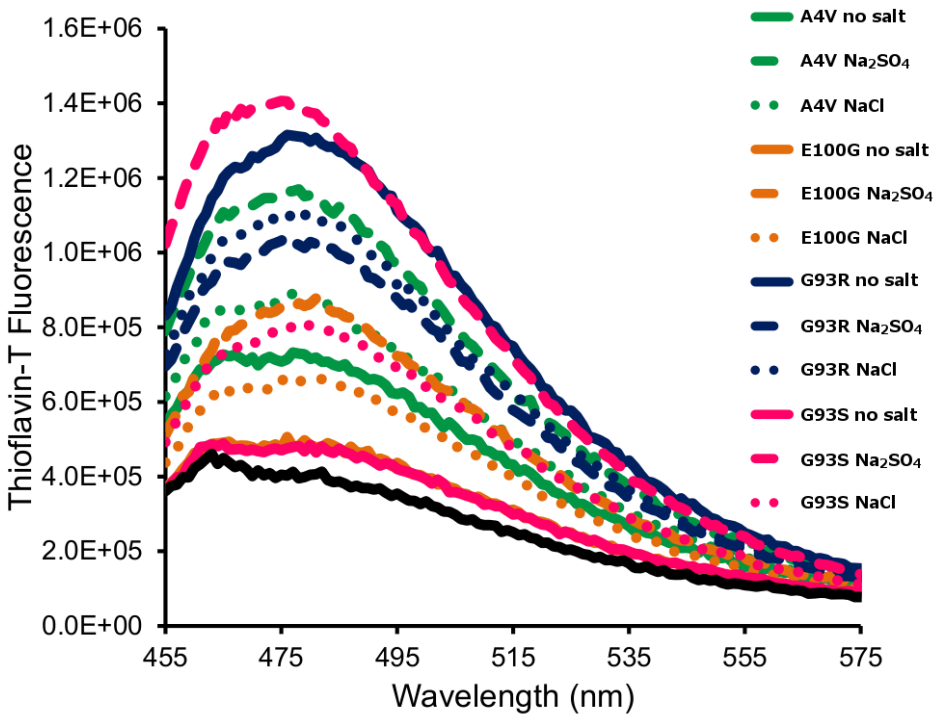

Figure 5.26 ThT fluorescence is generally enhanced for aggregates formed in salt compared to salt free samples. ThT binding experiments were performed on aggregates formed in salt free, 150 mM Na_2SO_4, and 150 mM NaCl buffer (1 mM TCEP, 20 mM HEPES, pH 7.4). The black line indicates the fluorescence of free ThT in 1 mM TCEP, 20 mM HEPES, pH 7.4, and neither Na_2SO_4 nor NaCl changed the ThT fluorescence spectrum (data not shown). Free ThT in pH 7.4 buffer shows very little fluorescence at 482 nm, but upon binding to aggregates containing an extended β-sheet there is a dramatic increase in fluorescence. These experiments show that all aggregates increase the intensity of ThT fluorescence, albeit to different extents, indicating that they all contain some degree of β-sheet. The mutants selected ranged from those that aggregate extensively, A4V (green) and G93R (blue), as well as mutants that undergo much less aggregation, G93S (pink) and E100G (orange). Salt free, Na_2SO_4, and NaCl samples are indicated by solid, dashed, and dotted lines, respectively.

5.4 Discussion

A number of different groups have undertaken a range of strategies to study aggregation of immature forms of SOD1, as discussed in Section 1.3.6. Our group has found apoSH is generally fairly resistant to aggregation under physiological-like solution conditions (174). To speed up the process, other groups have used agitation, or other means to destabilize the protein and generate higher levels of aggregation on an experimentally tractable time scale. Given that the initial conformation of a protein often dictates the types of aggregation pathways accessible (94, 356), and in particular that unfolded SOD1 will form amyloid fibrils under destabilizing conditions (Section 5.3.2) (179), we have attempted here to measure aggregation under conditions that are physiologically relevant. Initial attempts to induce aggregation by adding aggregate seeds were unsuccessful, suggesting that either higher levels of seeds are required to initiate aggregation and/or that apoSH mutants tend to exhibit specificity in the intermolecular interactions that lead to aggregate formation. Differences in aggregation behaviour of different apoSH mutants became observable when the concentration of the sample was increased and/or salt was added to the buffer. We hypothesized that both of these changes would encourage protein association without dramatically altering the stability, and thus initial conformation of apoSH.

5.4.1 ApoSH variants form intermolecular interactions that can support aggregation at higher than physiological concentration

Light scattering, and AFM experiments indicate that interactions between apoSH variants are generally enhanced at increasing protein concentrations or in the presence of salt. Here only salt free experiments will be discussed and in the following sections the effects of salt will be

elaborated on. As reported previously (Chapter 4) (174), apoSH pWT and stabilized mutants, H46R and V148I, unfold at temperatures well above 37 °C (48-53 °C) and so will be mainly folded at physiological (and incubation) temperature. Destabilizing mutations A4V, T, S, E100G, G93A, R, S, and V148G unfold at temperatures in the range of 31-40 °C; therefore, a considerably higher level of unfolded protein will be present at 37 °C (174). DLS measurements reveal that apoSH variants incubated at 1 mg mL^{-1} exhibit $D_{h,I}$ and $D_{h,N}$ values that are consistent with mixtures of folded and unfold apoSH (Tables 5.1, S5.2) (277). The difference in $D_{h,I}$ and $D_{h,N}$ values at t_0 was larger for the destabilized mutants, which could indicate oligomerization. The PDI values obtained at t_0 are also high for all variants and even higher for destabilized mutants, which is consistent with increases in the population of unfolded protein although could also be due to enhanced oligomerization (Tables 5.1, S5.2).

Incubation for ~300 hours (t_{300}) at 1 mg mL^{-1}, pH 7.4, 37 °C leads to little change in light scattering intensity for most apoSH variants (Fig. S5.1); A4V, the most common North American fALS mutation with particularly short disease duration (7, 8), showed the greatest change in light scattering intensity with time and consistently aggregates more than other variants under all conditions explored (*vide infra*), but interestingly is not the most destabilized mutant (174). The $D_{h,I}$ and $D_{h,N}$ values for pWT, stabilizing mutants H46R and V148I, and destabilized mutants G85R and H43R, did not change significantly with time. The other destabilized mutants (A4T, S, E100G, G37R, G85R, G93A, S, and V148G) exhibited an increase in $D_{h,I}$ but not $D_{h,N}$; only for A4V and G93R were changes in $D_{h,N}$ observed (Figs. 5.4, S5.2, Tables 5.1, S5.2). All variants exhibit an increase in PDI with incubation time; thus, some aggregates do form at 1 mg mL^{-1}, but their concentrations remain very low (Tables 5.1, S5.2). These results were very surprising given the marginal stability of apoSH and the numerous

studies suggesting that this form of the protein is the form that exhibits the greatest manifestation of mutation effects and is most highly, and very, prone to aggregate (76, 131, 147, 180, 184, 195).

The differences in aggregation propensity between SOD1 variants became more pronounced at higher protein concentration (5 mg mL^{-1}) (Figs. 5.8, 5.9). For some (pWT, G93A, G93S, and V148I) the light scattering intensity did not change significantly over the incubation period, while for others (A4V, G37R, and G93R) the light scattering intensity increased rapidly. For convenience the mutants were categorized as group one, lower aggregation propensity, and group two, higher aggregation propensity. Interestingly, these differences in aggregation propensity could not be accounted for based merely on protein stability differences; G93A and G93S unfold at lower temperatures, with apparent melting temperatures of ~34.6 and 33.4 °C, respectively, than A4V and G93R, 36.3 and 35.4 °C, respectively. G37R is even less stable, unfolding at 33.4 °C (Table S4.2) (174). SLS revealed that mutants categorized in group two appear to aggregate with little lag time, signifying aggregation either from the unfolded or native-like state (Fig. 5.8). However, DLS measurements, which are able to detect subtle changes in intermolecular interactions, reveal that all variants exhibit an increase in intermolecular interactions at higher protein concentration. First, $D_{h,N}$ values at t_0 are between 0.1 and 1.8 nm larger at 5 mg mL^{-1} compared to 1 mg mL^{-1}, which points to an increase in concentration of small oligomers (Tables 5.1, 5.2, S5.2, S5.3). It is noteworthy that for mutants with higher aggregation propensity, group two, there is a 1.5-12 nm increase in the $D_{h,I}$ at t_0. Secondly, the PDI values at t_0 are larger for 5 mg mL^{-1} samples compared to 1 mg mL^{-1} samples. Thus, t_0 measurements suggest that intermolecular interactions are promoted at increased protein concentration. This hypothesis was further supported by AFM imaging of freshly prepared (i.e.,

non-incubated) G37R. The majority of particles detected were monomers, and oligomers containing up to 10 monomers (Figs. 5.14, 5.15). In general, the behaviour exhibited by apoSH variants resembles the type of reversible aggregation described below (Section 5.4.5) whereby proteins in their native or native-like states interact weakly and these interactions are promoted at higher protein concentration.

5.4.2 Native and non-native dimerization of apoSH

Recent advances in NMR spectroscopy have made it possible to detect alternative, potentially misfolded, conformations of a protein that are populated by as little as ~0.5% (357). Our collaborators, Dr. Ashok Sekhar and Dr. Lewis Kay at the University of Toronto, have performed a combination of Chemical Exchange Saturation Energy Transfer (CEST) and Carr-Purcell-Meiboom-Gill (CPMG) NMR relaxation experiments (357–359), to assess the energy landscape of apoSH SOD1, in particular any misfolded conformations that may account for the higher aggregation propensity of apoSH compared to more mature forms of SOD1 that display an extremely low tendency to aggregate (301). The results of these experiments indicate that the energy landscape of apoSH is rugged; multiple conformations and oligomerization states form transiently, which likely have important consequences for the mechanism(s) of aggregation (*vide infra*, Fig. 5.28). NMR analyses of apoSH pWT reveals that the β-barrel is largely intact, but the absence of defined structure in zinc-binding and electrostatic loops (IV and VII, respectively) enables promiscuous interactions that may underlie the first steps in the aggregation pathway.

Combined CEST and CPMG experiments revealed four apoSH conformers in equilibrium with the native state (Fig. 5.28). Two of the conformers locally fold into states that resemble more mature forms of SOD1, the first forming the native dimer (Process I) and the

second forming the α-helix in the electrostatic loop that is important for zinc binding (Process II). The other two conformers are non-native dimers that form through interactions between residues in the native dimer interface and the electrostatic loop. The first non-native dimer (Process III) resembles the native dimer and is similar in stability with one of the monomers rotated by 180 °. Thus, the residues buried in this non-native interface are very similar to those buried in the native interface. The second non-native dimer (Process IV) forms through interactions between residues that form the native dimer interface of one monomer (β1, β8, the zinc-binding loop (loop IV), and loop VI) and the zinc-binding and electrostatic loops of another. Unlike the other dimers described, the second non-native dimer is asymmetric; one of the monomers is rotated 90° relative to the other. Such interactions between the β-barrel and the long loops are not unlike the type of interactions observed in crystallographic studies of oxidized apo and part-metallated SOD1 fibrils (90, 136, 138). The K_d's of the apoSH native and non-native dimer formation are ~100 ± 50 mM at 37 °C, which confirms that at 5 mg mL^{-1}, ~0.5-1.8% of the protein exists as a dimer. While these levels are very low, light scattering is particularly sensitive to detecting larger particles (i.e. apoSH dimers will scatter 5 times more light) and under these conditions dimeric apoSH will scatter ~2.5-8.5% of the incident light beam.

These results indicate that apoSH can interconvert between a number of states with little change in monomer conformation, which may account for the heterogeneity of apoSH samples that give rise to differences in $D_{h,I}$ and $D_{h,N}$ as well as the high PDI values at t_0 (Figs. 5.27, 5.28). Furthermore, we observe that aggregation of apoSH proceeds with very little detectable lag time (*vide infra*) (Figs. 5.8, 5.18), which also suggests that little conformational change in apoSH is required to initiate aggregation (53). Interestingly, the native dimer interface is involved in the

formation of all 3 types of dimers, and in only one case is it exposed after dimer formation. We speculate that formation of symmetric dimers could be protective due to the burial of hydrophobic residues exposed in the apoSH monomer (see Chapter 2) (173). On the other hand, formation of the assymmetic non-native dimer may facilitate further assembly because the native dimer interface residues remain exposed (Fig. 5.27). While it is too early to assess how native and non-native dimer formation relate to aggregate formation, the observation that apoSH can rapidly convert to different oligomeric forms, may account for the complex aggregation behaviour observed. If particular types of association are more favoured by certain mutations compared to others, this in turn may lead to differences in aggregation propensity and aggregate morphology (Fig 5.28) (52, 356, 360).

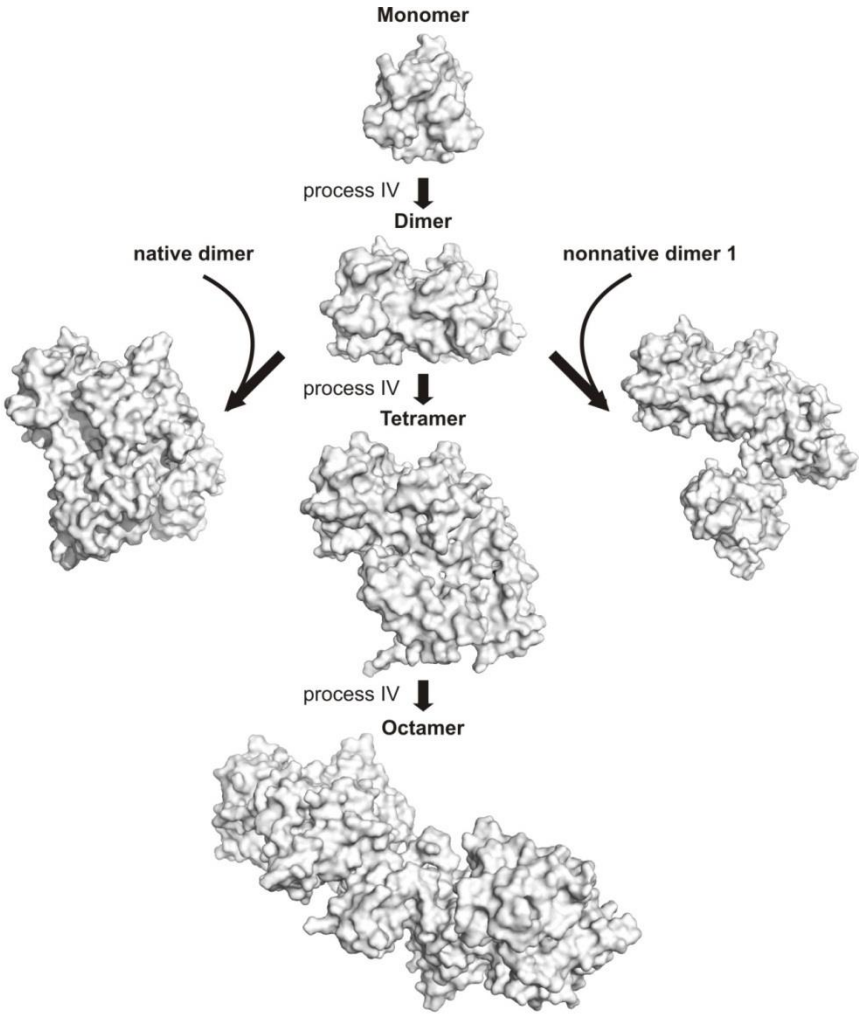

Figure 5.27 Asymmetric dimer formation can serve as template for further aggregate growth. The asymmetric dimer (Process IV) can serve as a template for addition of monomers and other dimers to form oligomers. The pathway shown in the middle involves the apoSH monomer forming the asymmetric non-native dimer (Process IV), which then associates with another non-native asymmetric dimer to form a tetramer. The process is then repeated to form an octamer. Alternatively, the asymmetric dimer can recruit other dimers, such as the native dimer (left) or the symmetric non-native dimer (right) to form different tetramers (301). Oligomers were built using HADDOCK docking software (361).

5.4.3 At increased protein concentration apoSH variants exhibit differences in aggregation behaviour

After ~t_{300}, the differences in $D_{h,I}$ and $D_{h,N}$ values are generally more pronounced for 5 mg mL^{-1} samples compared to 1 mg mL^{-1} samples. This discrepancy is most notable for group one mutants, which form low levels of large aggregates leading to pronounced increases in $D_{h,I}$ but not $D_{h,N}$. At higher protein concentration, large differences in $D_{h,I}$ and $D_{h,N}$ were also evident for A4V, which first forms a mixture of small fibrils resembling those observed in G37R and G93R samples as well as much larger aggregates, described further below. Similar to experiments at 1 mg mL^{-1}, for all group one mutants and A4V, there is a large increase in PDI with time, which further points to an increase in sample heterogeneity, and for group one variants, indicates low levels of aggregate formation given that monomers remain the most abundant species at the end of the incubation period. Group two mutants show smaller differences in $D_{h,I}$ and $D_{h,N}$ values at t_{300}, consistent with aggregates being more abundant in these samples. As well, for this group the PDI decreases with incubation time. Together these results indicate that group two samples become more uniform with time as the levels of monomers and oligomers present at t_0 may decrease, while the concentration of aggregates increases with time.

AFM experiments on aggregated apoSH variants, incubated at 5 mg mL^{-1}, were performed to assess aggregate morphologies. As only very low levels of aggregation occur for most variants when incubated at 1 mg mL^{-1}, only 5 mg mL^{-1} samples were imaged. For apoSH pWT, the majority of particles detected were small, consistent with volume estimates of the monomer, dimer, and oligomers containing up to ~4 monomers (Fig. 5.13, Table 5.3). Aggregates larger than 200 nm in length were rarely observed; yet, the very few that were

resembled the long fibrils formed by group one mutants, G93A, G93S, and V148I (in 150 mM Na_2SO_4) (Figs. 5.10, 5.11). For these mutants, the detected particles exhibited slightly larger length and breadth estimates (Fig. 5.12, Table 5.3). Additionally, more particles larger than 200 nm in length were detected, and these particles showed larger aspect ratios. Nevertheless, most particles in these samples were small (i.e., 1-10 monomers), indicating that the long fibrils detected are very low in concentration. Taken together, AFM results confirm that large uncertainties in SLS data, discrepancies in $D_{h,I}$ and $D_{h,N}$, as well as high PDI values observed in group one samples, are likely due to the presence of low levels of long fibrils.

Mutants that showed the highest levels of aggregation at 5 mg mL^{-1} by light scattering, A4V, G37R, and G93R (group two), similarly were found to contain far more aggregates by AFM (Fig. 5.11). In the most extreme case, small A4V aggregates, like those formed by G37R and G93R, appear to coalesce into large amorphous-like aggregates (Figs. 5.10, 5.11, S5.7). The presence of these large aggregates may explain the large decrease in light scattering intensity between 50 and 120 hours of incubation, as large aggregates form from the soluble monomers and/or small aggregates and are invisible to this technique. Average length and breadth estimates, as well as the relative proportion of particles containing more than 10 dimers were larger compared to group one variants. Interestingly, while group two mutants aggregate far more than group one, there is no evidence of long fibrils, which suggests that there may be structural differences in the aggregates formed by the different groups that affect the maximum length of the aggregates. Group one aggregates appeared to resemble flexible, worm-like fibrils that have been observed in aggregation studies of β-lactoglobulin, hen-egg-white lysozyme, and mouse PrP (362–364). ThT binding experiments also suggest there may be differences in the underlying secondary structure of the aggregates (Fig. 5.17). Since ThT fluorescence depends

both on aggregate concentration and β-sheet content, the results can be difficult to interpret. In general though, differences in fluorescence intensity appear to relate to aggregate length, with those mutants forming the longest fibrils (i.e., V148I) exhibiting the largest increase in ThT fluorescence (Fig. 5.17).

5.4.4 Salt has diverse effects on the aggregation propensity of apoSH

It is clear from the aggregation experiments described above that increasing the protein concentration alone does not noticeably increase aggregation of all apoSH SOD1 mutants. One factor limiting aggregation may be the net negative charge of apoSH at neutral pH (352, 353). If this negative charge inhibits aggregation, the addition of salt should screen the repulsive charge between apoSH monomers and promote aggregation. Salts tend to have complex effects on protein aggregation that depend on how they affect the balance of hydrophobic and electrostatic interactions between proteins (348, 349, 355, 365). In addition to screening charges, they can also change the hydration of proteins, affecting the ensemble of conformations a protein is able to access (348–351). The effects of salt on the aggregation of other marginally stable proteins, α-synuclein (366), yeast prion protein (sup35) (367), mammalian prion protein (PrP) (355), and amyloid-β (365), as well as globular proteins β2-microglobulin (368), and human immunoglobulin G1 (369), has been an area of active research. We hypothesized that both Na_2SO_4, which encourages protein folding and association through the Hofmeister effect (348), and NaCl, which has less impact on protein hydration but can screen electrostatic interactions, would promote aggregation through a combination of these complex effects. Light scattering measurements, however, showed that pWT, E100G, H43R, and V148G remain fairly resistant to aggregation in Na_2SO_4 and NaCl. In contrast, A4V, G93R, and G93S aggregate more in the

presence of salt, and in all three cases, the effects were most pronounced for samples containing Na_2SO_4. A4V and G93R in both Na_2SO_4 and NaCl and G93S in Na_2SO_4 aggregated with little detectable lag time suggesting a low energy barrier to aggregation, as described above. Given that Na_2SO_4 has been shown to increase the stability of the apoSS monomer (134), the population of unfolded apoSH would be reduced in Na_2SO_4 at 37 °C. Thus, aggregation for these mutants is likely occurring from native-like, folded, rather than unfolded states (53). For pWT, DLS data reveal that the addition of salt has little effect on the $D_{h,I}$ and $D_{h,N}$ at t_0. Interesting though, the $D_{h,I}$ values reported for all mutants were increased relative to pWT ranging by 1-3 nm, 2-5 nm, and 1-4 nm for salt free, Na_2SO_4, and NaCl samples, respectively, and the increases were most pronounced for A4V and G93R samples containing salt (Table 5.4). Salt concentration-dependent increases in the $D_{h,I}$ have also been observed for mammalian PrP, and were proposed to be due to anion-specific binding that causes conformational changes that in turn promote oligomer formation (355).

Over time, relatively large increases in both $D_{h,I}$ and $D_{h,N}$ values were evident for A4V and G93R samples containing salt, but not for salt free samples. For G93S and V148G Na_2SO_4 samples, only $D_{h,I}$ increased significantly with time and was much larger than $D_{h,N}$. In contrast, there was little change in $D_{h,I}$ and $D_{h,N}$ values for G93S and V148G salt free and NaCl samples, as well as all pWT, E100G, and H43R samples. A slight decrease in PDI values with time for A4V and G93R samples containing salt is also consistent with higher levels of aggregation, compared to all other samples, including A4V and G93R in the absence of salt, that exhibit an increase in PDI with incubation time. Again we see that conditions suitable for promoting aggregation of some mutants, notably A4V, G93R, and to a lesser extent G93S, did not obviously increase the observed aggregation of other mutants. The effects of Na_2SO_4 and NaCl

on the aggregation propensity of apoSH reported here are consistent with the numerous studies of the Hofmeister effect on protein aggregation (348–351, 367, 369, 370). Strong kosmotropes, such as Na_2SO_4, tend to promote aggregation by encouraging association (367, 369, 370).

By AFM we see that Na_2SO_4 and NaCl promote fibrillization of A4V, G93R, and G93S samples (Figs. 5.20, 5.21, Table 5.5). For all three mutants, the largest aggregates (those with lengths longer than 200 nm) formed in salt exhibit larger aspect ratios compared to those formed at higher protein concentration in salt free buffer (Tables 5.4, 5.5). It is noteworthy that images of G93R in Na_2SO_4 taken over the course of the aggregation experiment reveal that fibril elongation occurs up to the midpoint of the exponential growth phase at which point fibrils appear to stop growing (Figs. 5.23, 5.24, S5.18-S5.20). Alternatively, G93S, which exhibited lower levels of aggregation in salt compared to A4V and G93R, formed the longest fibrils and some of these fibrils also appear to either bundle together and/or form branches indicative of secondary nucleation sites (Figs. 5.20, 5.21, S5.22, S5.23). The fibrils formed by G93S in Na_2SO_4, and to a lesser extent NaCl, resembled those formed by G93A at 5 mg mL^{-1} in salt free buffer and V148I at 5 mg mL^{-1} in 150 mM Na_2SO_4, but interestingly were not observed for G93S at 5 mg mL^{-1} in salt free buffer, although further experiments are required to assess whether the internal structure of these aggregates are similar.

Aggregation experiments in salt exhibit similar trends to those reported for experiments at high protein concentration in the absence of salt; mutants that exhibit low levels of aggregation as indicated by slight changes in light scattering intensity with time, large uncertainties in the measurements, and increases in $D_{h,I}$ but not $D_{h,N}$ tend to form low levels of long fibrils. On the other hand, mutants with higher aggregation propensity form smaller fibrils that are more abundant. Without exhaustively imaging all regions of the mica surface, it is

difficult to relate the quantity of fibrils in the image (sample coverage) to the levels in solution, yet it is clear that the coverage is higher for samples that exhibit higher aggregation by light scattering. Thus, the combination of longer, as well as more numerous, fibrils in samples containing salt may be the cause of the higher light scattering intensity observed for these samples (Fig. 5.18). Similar trends were observed for Sup35, where kosmotropic salts induced rapid aggregation, but the aggregates formed were less robust and found to fragment (370). Lower overall aggregation of Sup35 was evident in chaotropic salts, these conditions promoted the formation of stronger aggregates that were more rigid and longer. Though we have not yet explored the effects of chaotropic salts on apoSH aggregation, the results are analogous to the effects of mutations on the type of aggregation behaviour observed. Mutants that rapidly aggregate tend to form small fibrils. On the other hand, mutants that exhibit lower levels of aggregation form long fibrils that may form branches or bundle but tend not to fragment.

ThT binding experiments were performed on A4V, G93R, G93S, and E100G samples incubated for ~300 hours in salt free, Na_2SO_4, and NaCl buffers to probe the differences in structure that may account for the differences in aggregation behaviour exhibited (Fig. 5.26). In general, samples containing Na_2SO_4 showed the largest increase in ThT fluorescence, which was most pronounced for G93S aggregates formed in Na_2SO_4. Thus, again we see that mutants that form long fibrils (i.e., with the highest aspect ratios) even at low levels, display the highest levels of ThT fluorescence (Section 5.3.6, Fig. 5.17).

Light scattering, AFM, and ThT binding experiments reveal that Na_2SO_4 and NaCl promote aggregation of some, but not all, apoSH mutants. The effects of salt on the levels of apoSH aggregation correlate with the abilities of the different anions to stabilize and encourage protein association, according to the Hofmeister series (i.e., SO_4^{2-} promotes aggregation more

than Cl^{-1}). Our findings are also consistent with other studies of other marginally stable proteins have shown that different salts and even the same salt at different concentrations can cause the same protein to form aggregates with very different morphologies (355, 364, 370).

5.4.5 ApoSH exhibits different modes of aggregation that vary with mutation and solution conditions

Many proteins can undergo multiple types of aggregation, characterized both by different rates of aggregate formation as well as diverse arrays of aggregate morphologies (371–374). In many cases, the more malleable the protein, the higher the number of aggregation-prone conformations that can be generated and in turn the higher the diversity of aggregate structures formed (94, 356).

Proteins can reversibly aggregate from native or native-like states that form weak interactions that in turn lead to formation of dimers and small oligomers, often observed only at increased protein concentration (371, 375). The dynamic equilibrium established between monomers and oligomers is governed by the thermodynamic stability of each state (53); higher order species will only become abundant at protein concentrations above the equilibrium dissociation constant (K_d) (375). For apoSH pWT, a rough estimate of the K_d for native and non-native dimer formation has been obtained by NMR (Section 5.4.2) (301); more experiments are in progress to assess how mutations modulate the energetics of native and non-native dimerization. Preliminary studies reveal that the A4V mutation, located in the dimer interface, abolishes both native and non-native dimerization (301); therefore, mutations may play pivotal roles in modulating the accessibility of different oligomerization pathways. Given evidence that a number of different oligomers form reversibly from the native state (Section 5.4.2), it is

possible that they could initiate different interactions that may become irreversible, as has been observed for amyloid-forming proteins (94, 360). Irreversible aggregation generally involves more substantial conformational changes and the formation of aggregates that do not readily dissociate unless exposed to high levels of chemical denaturant (371, 375). In such cases, partial protein unfolding leads to the exposure of segments capable of forming new, and often very strong, hydrogen-bonding or hydrophobic interactions. Partial unfolding can occur preceding or, often at higher protein concentrations, after association (375). The complex mechanism(s) underlying irreversible aggregation tend to be governed more by the rates of association and are therefore, under kinetic rather than thermodynamic control (92). The rates of unfolding and association are highly dependent on protein conformation and solution conditions. Changing the interactions between proteins has a large impact on the rate of each step in the aggregation process. Furthermore, structural changes often only need to involve a small proportion of monomer in order to facilitate irreversible aggregation and often these conformational changes involve an increase in β-structure (371). Irreversible species often can grow via different mechanisms, for example, through monomer addition to existing aggregates and/or through coalescence of aggregates. It is important to note that reversible and irreversible aggregation pathways are not necessarily mutually exclusive; reversible aggregates can convert to irreversible species upon conformational changes in the protein (375).

For apoSH, low levels of oligomers may be present at t_0, but in most cases these oligomers do not transition into larger aggregates at 1 mg mL^{-1}. Increasing the concentration of the sample to 5 mg mL^{-1} and/or adding Na_2SO_4 and NaCl leads to higher levels of oligomer formation and substantial changes in the rates of aggregation for some but not all mutants, which is consistent with our current understanding of how both primary sequence and

environmental conditions can alter the aggregation of proteins. Conformational heterogeneity leading to polymorphism in aggregate structure has been commonly observed for other aggregation-prone proteins and has been proposed to underlie the species barrier in prion diseases and the severity of different amyloid strains (sections 1.2.1, 1.2.2) (83, 89, 97, 356). Mutations modulate the structural features of the fibres, resulting in distinct, or common, protease-resistant cores under different conditions (Section 1.3.6) (181, 185). NMR also reveals that A4V and G85R have very different effects on the energy landscape of apoSH (301). In some cases, mutations appear to promote rapid formation of small aggregates that are unable to grow very long, potentially due to their low stability and high frangibility, while in other cases mutations, under the same conditions, disfavour rapid aggregation and instead promote the formation of long fibrils with extensive β-sheet content (Fig. 5.24). Given the low levels of these long fibrils, we speculate that more extensive conformational changes are required to facilitate growth. By experimenting with a number of different solution conditions, but without promoting aggregation too aggressively (e.g., sonication, agitation) (75, 76, 180, 192), we have been able to see different effects of ALS-mutations on the aggregation propensity of apoSH, and gain valuable insights mechanisms of SOD1 aggregation that may be involved in disease.

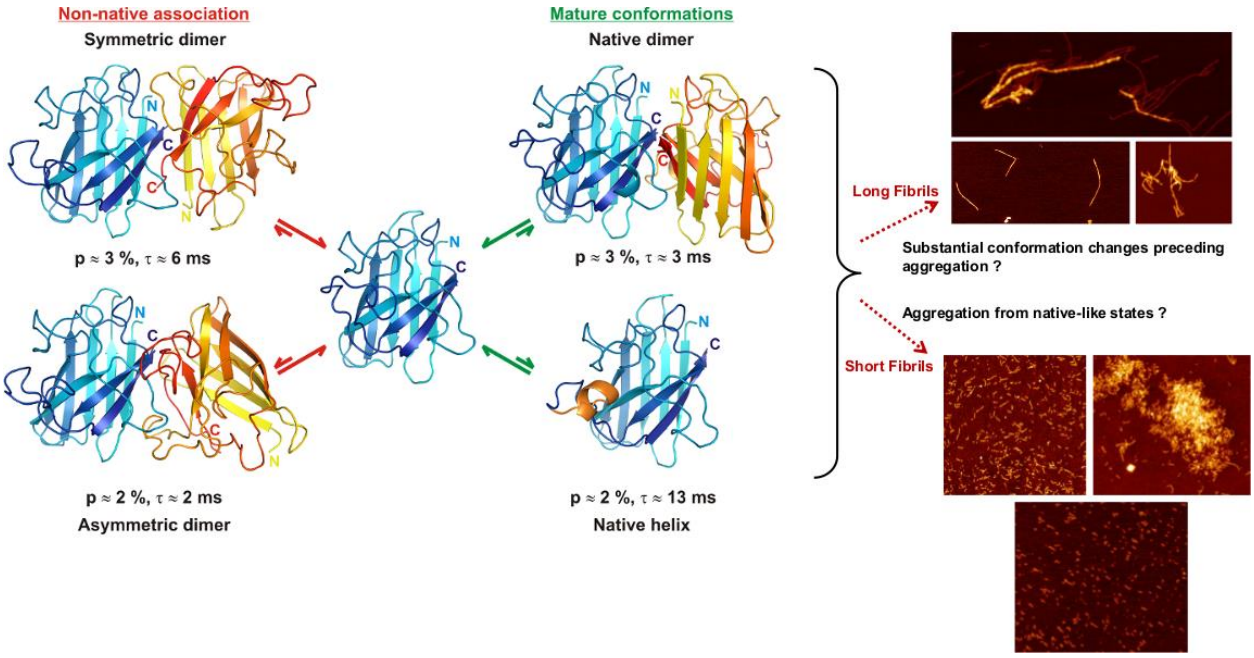

Figure 5.28 Monomeric apoSH is in equilibrium with native and non-native conformations that can represent templates for different aggregation pathways. On the left are the conformations of native apoSH (blue) shown by NMR to be transiently populated. Some states exhibit features similar to the native state of holoSS SOD1, referred to as mature conformations, and include native dimerization (top right) and electrostatic loop helix formation (bottom right). The other dimers formed do not resemble holoSS and arise from "non-native association" (top left and bottom left structures) (301). The heterogeneity of conformations formed by apoSH may account for the different types of aggregates formed (shown on the left). Mutations may modulate the energy landscape of apoSH, such that certain local folding and/or association pathways are favoured over others and this in turn may dictate the type of aggregates formed. DLS, AFM, and ThT binding experiments reveal that some mutations lead to low levels of aggregation, where aggregates formed exhibit substantial increases in β-content and undergo little fragmentation (top right AFM images). Other mutations promote rapid aggregation that leads to abundant small aggregates that in some cases coalesce but rarely form long fibrils (bottom right AFM images).

5.5 Supplementary Data

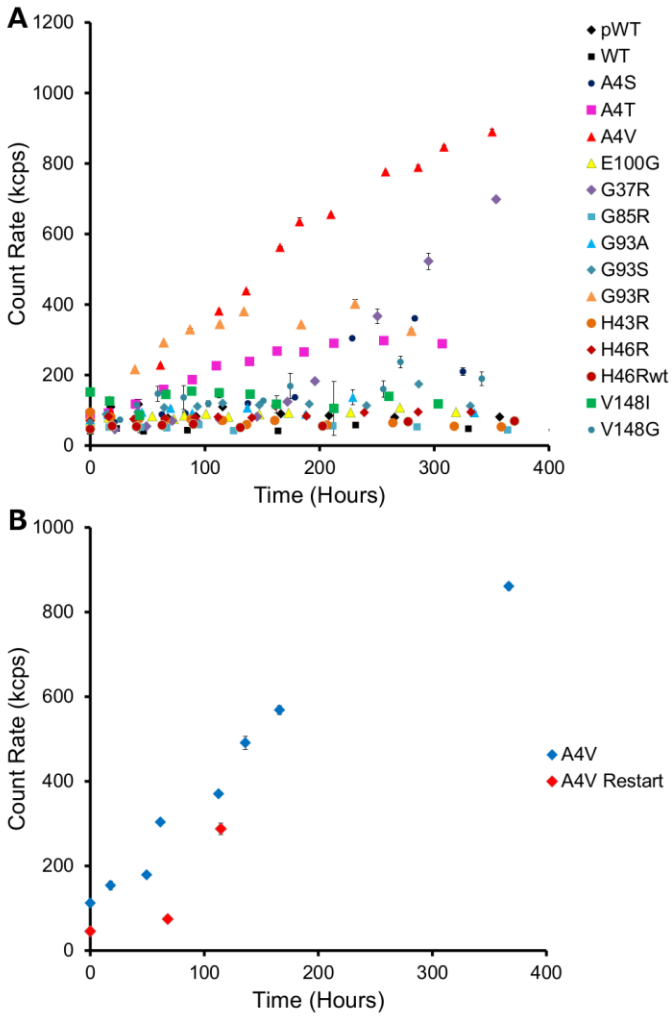

Figure S5.1 SLS reveals that most apoSH variants undergo very little aggregation at 1 mg mL^{-1}, pH 7.4, 37 °C. All samples were incubated in 1 mM TCEP, 20 mM HEPES**. (A)** Most apoSH variants aggregate little when incubated at 1 mg mL^{-1}, pH 7.4, 37 °C, as indicated by little change in light scattering intensity (discussed in Chapter 4). A4V (red triangles) and to a lesser extent A4T (purple squares), G37R (purple diamonds), and G93R (peach triangles) samples exhibit an increase in light scattering intensity over the incubation period; however, DLS reveals that the aggregates formed remain low in concentration with the exception of A4V. **(B)** A4V was left to aggregate for approximately 400 hours (blue diamonds) at which point the aggregates formed were filtered from the sample and the experiment was restarted (red diamonds). Filtration and removal of aggregated protein decreases the concentration of the sample, as suggested by the decrease in initial counts between the first and restart experiments; however, aggregation proceeds in the restarted experiment at the same rate as the first. Experiments shown in both panels are single representative aggregation experiments. Error bars reflect the standard deviation in light scattering intensity measurements made in triplicate every ~24 hours.

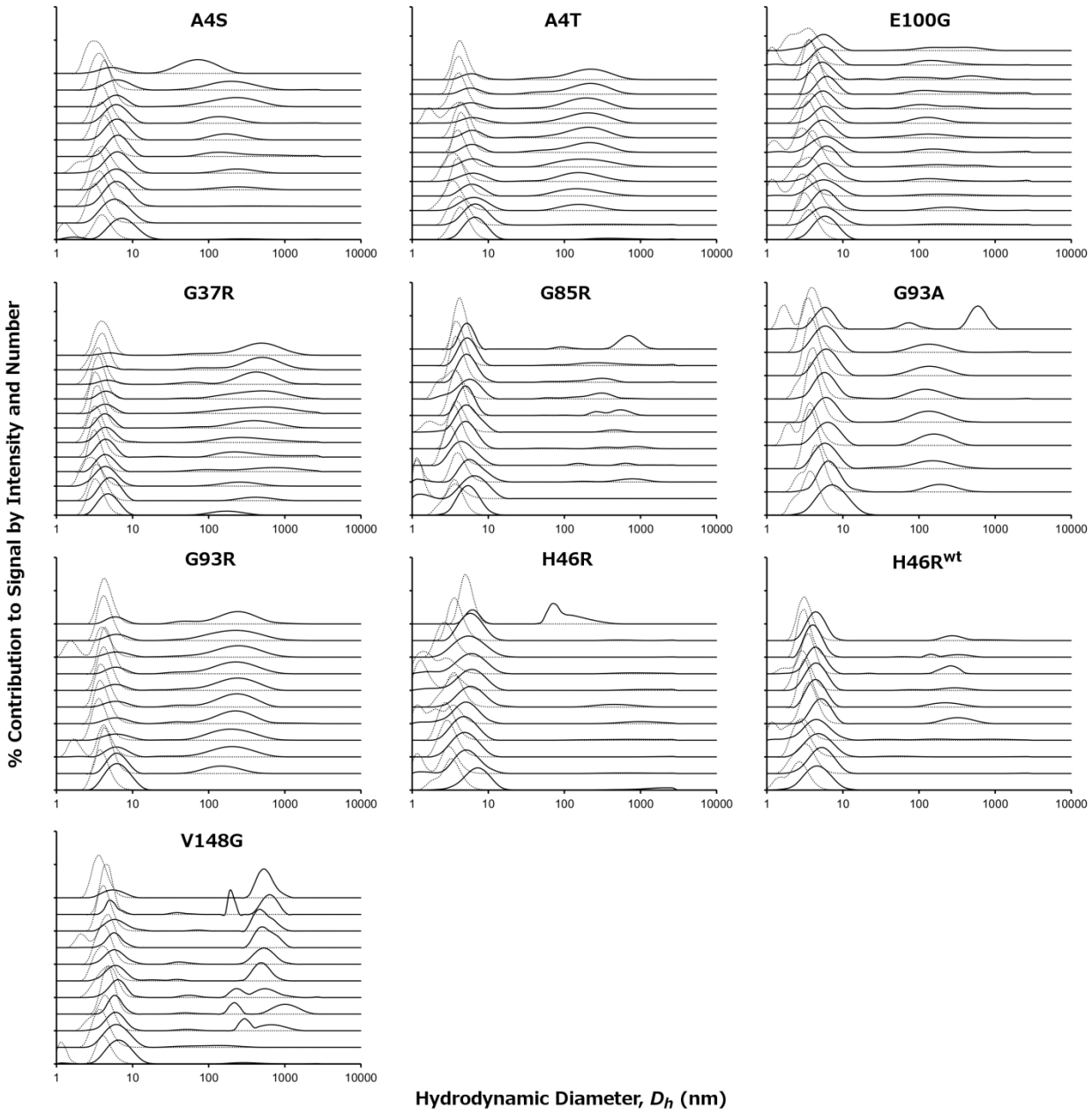

Figure S5.2 DLS reveals that most apoSH variants, incubated at 1 mg mL^{-1}, pH 7.4, 37 °C, show very little increase in size. All samples were incubated in 1 mM TCEP, 20 mM HEPES. Intensity distributions are indicated by the solid line and number distributions by the dotted line. DLS measurements were taken approximately every 24 hours, with t_0 at the bottom of the page and the last time point, greater than 300 hours, at the top. Intensity distributions emphasize larger particles in solution; therefore, the centre of the peak is shifted slightly to larger values. The number distributions, which reflect the concentration of different species in solution, indicate small particles corresponding to monomers and possibly small oligomers are the most abundant species after incubation for greater than 300 hours. Data obtained from the DLS experiments shown in Figures 5.4 and S5.2 are summarized in Table S5.2.

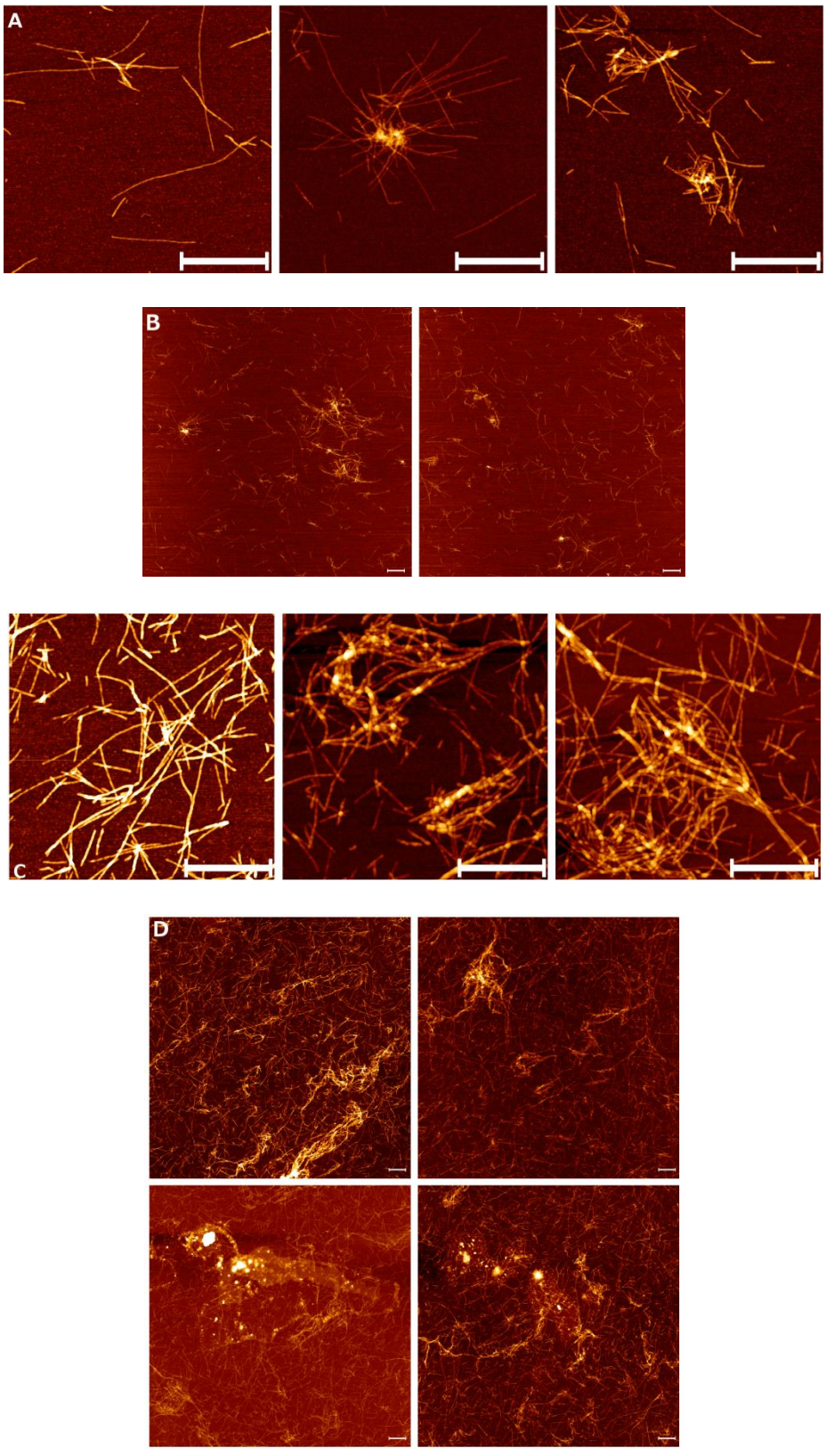
A
B
C
D

Figure S5.3 AFM images of partially evaporated apoSH H43R after ~130 and 300 hours of incubation at, pH 7.4, 37 °C. AFM images confirm that sample evaporation can lead to fibril formation. In all panels, the white bars correspond to 1 µm. **(A)** and **(B)** are 3 x 3 and 15 x15 µm images of samples incubated for ~130 hours, respectively. **(C)** and **(D)** are 3 x 3 and 15 x 15 images µm of samples incubated for ~300 hours, respectively. Fibrils are present at 130 hours of incubation, even before the peak representing small particles is no longer detected by DLS (Fig. 5.5), but become more numerous and coiled together after 300 hours of incubation.

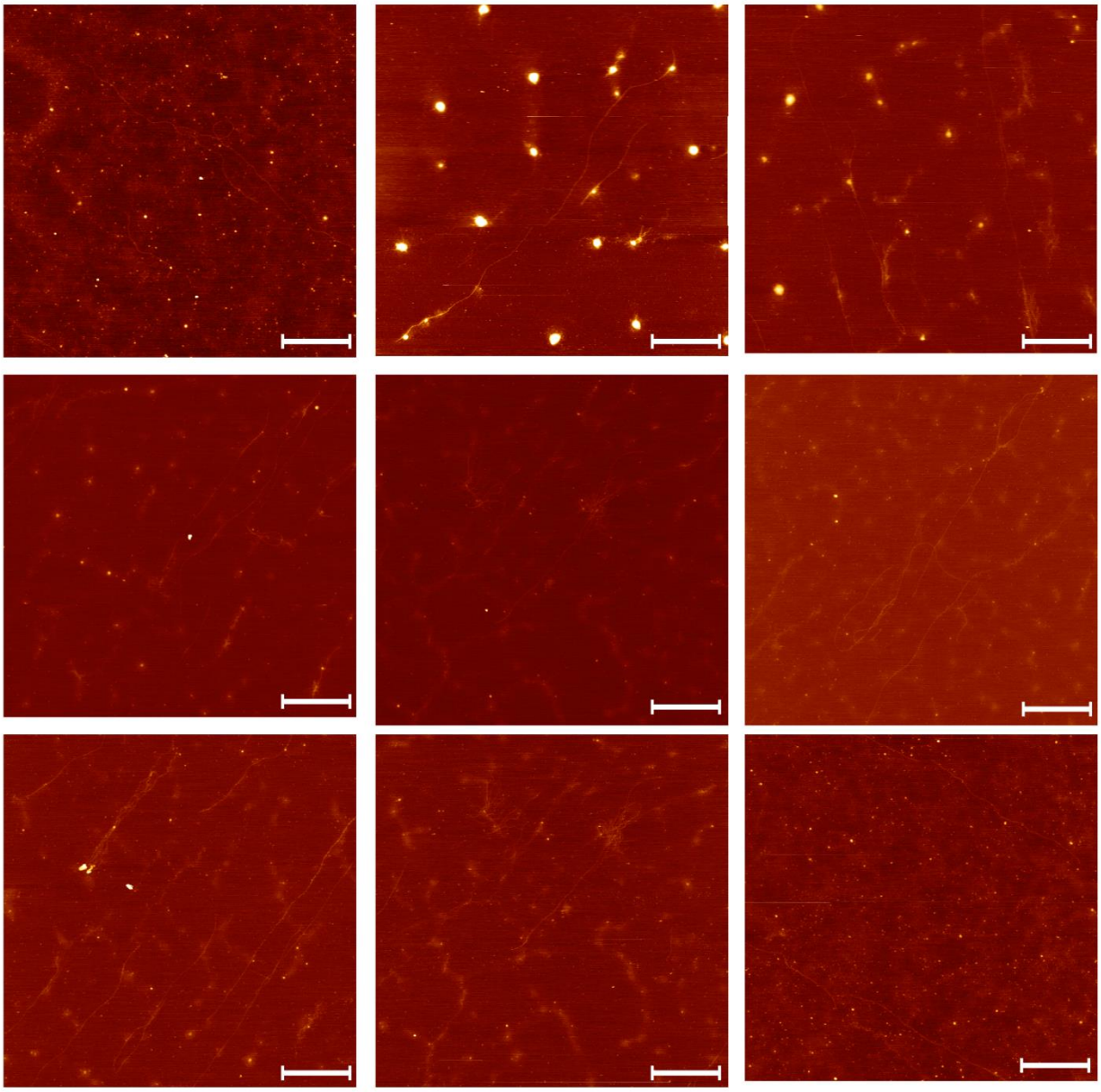

Figure S5.4 AFM images of partially evaporated apoSH G85R after ~300 hours of incubation at pH 7.4, 37 °C. AFM images confirm that sample evaporation can lead to fibril formation. All panels are 5 x 5 μm images and the white bars correspond to 1 μm. Evaporation can induce formation of long, thin fibrils that appear coiled together in regions. There is also evidence of spherical, amorphous-like aggregates that may be fibrils clumped together as they often appear to have fibrillar components emerging from them.

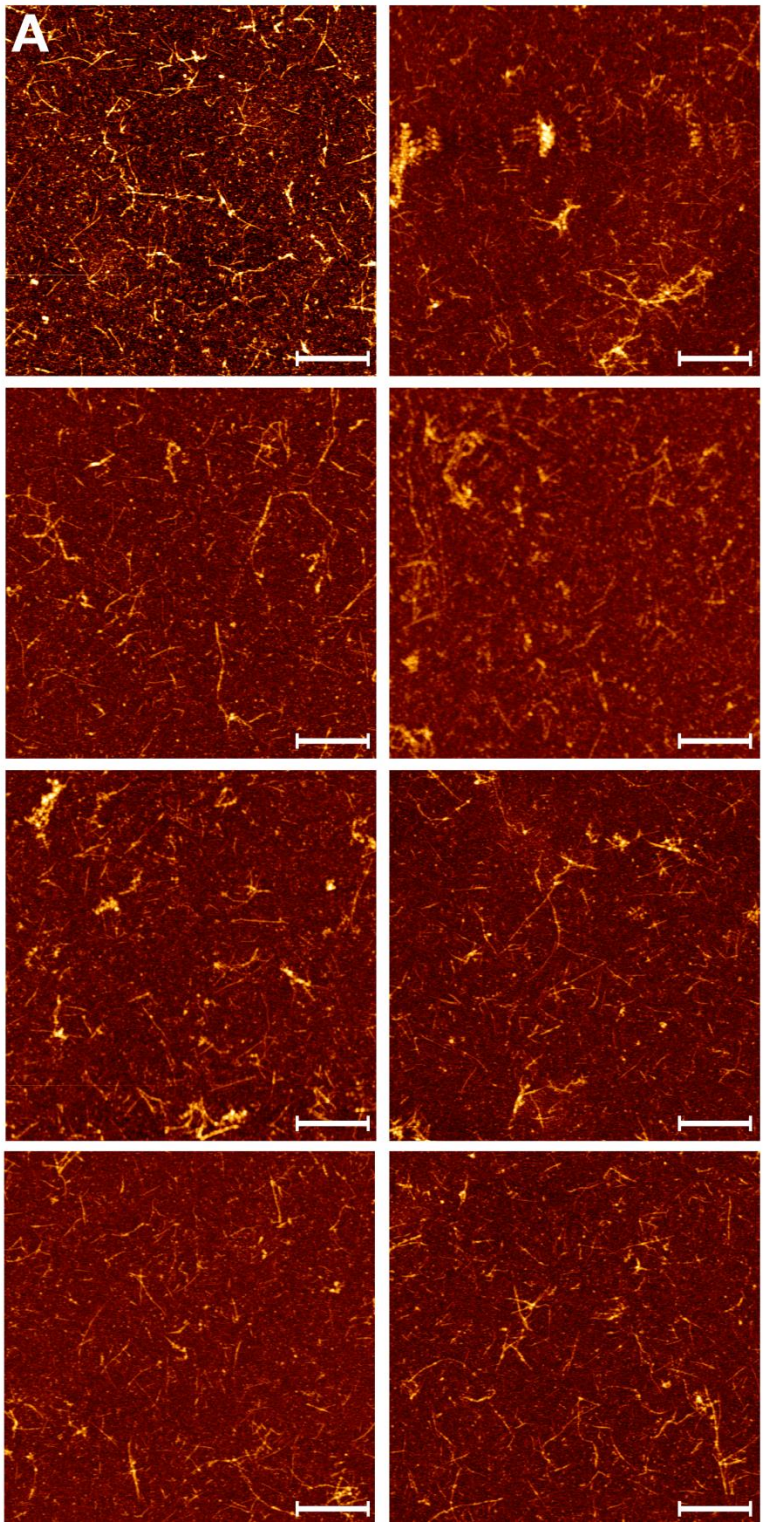
A

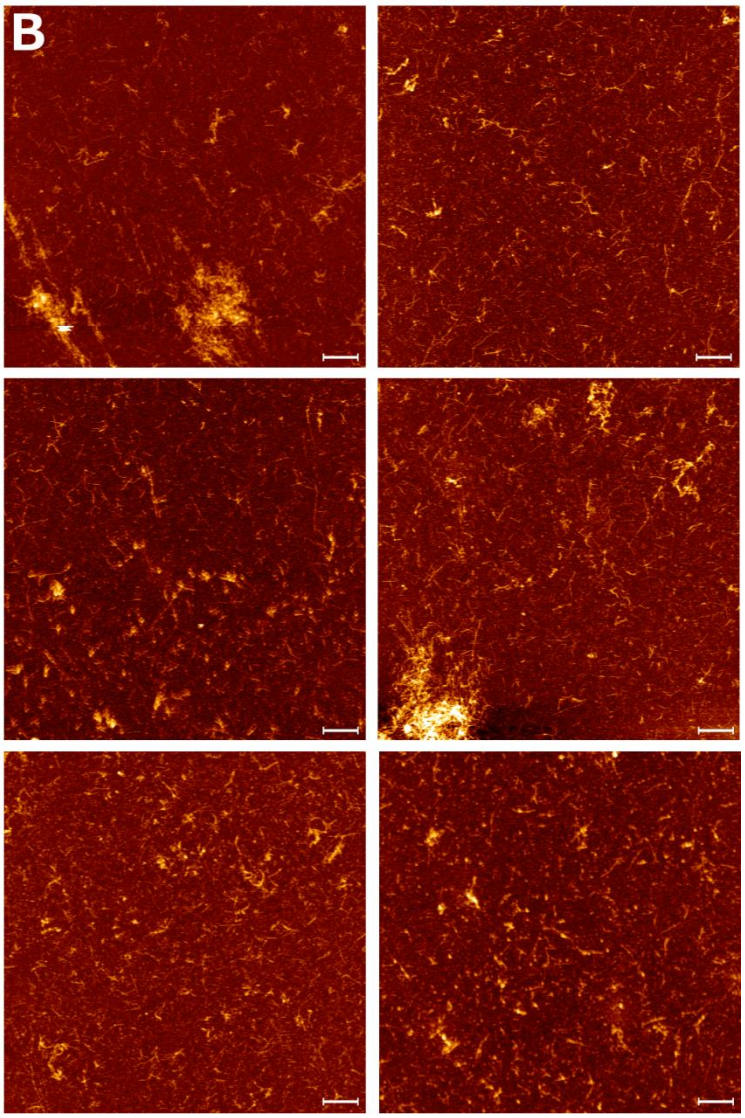

Figure S5.5 AFM images of partially evaporated apoSH V148I after ~300 hours of incubation at pH 7.4, 37 °C. AFM images confirm that sample evaporation can lead to fibril formation. **(A)** and **(B)** show 5 x 5 and 10 x 10 μm images, respectively, and the white bars correspond to 1 μm. Fibrils formed in the partially evaporated V148I sample are shorter than those formed by H43R and G85R, which is consistent with DLS data indicating that aggregation did not begin as early in this sample.

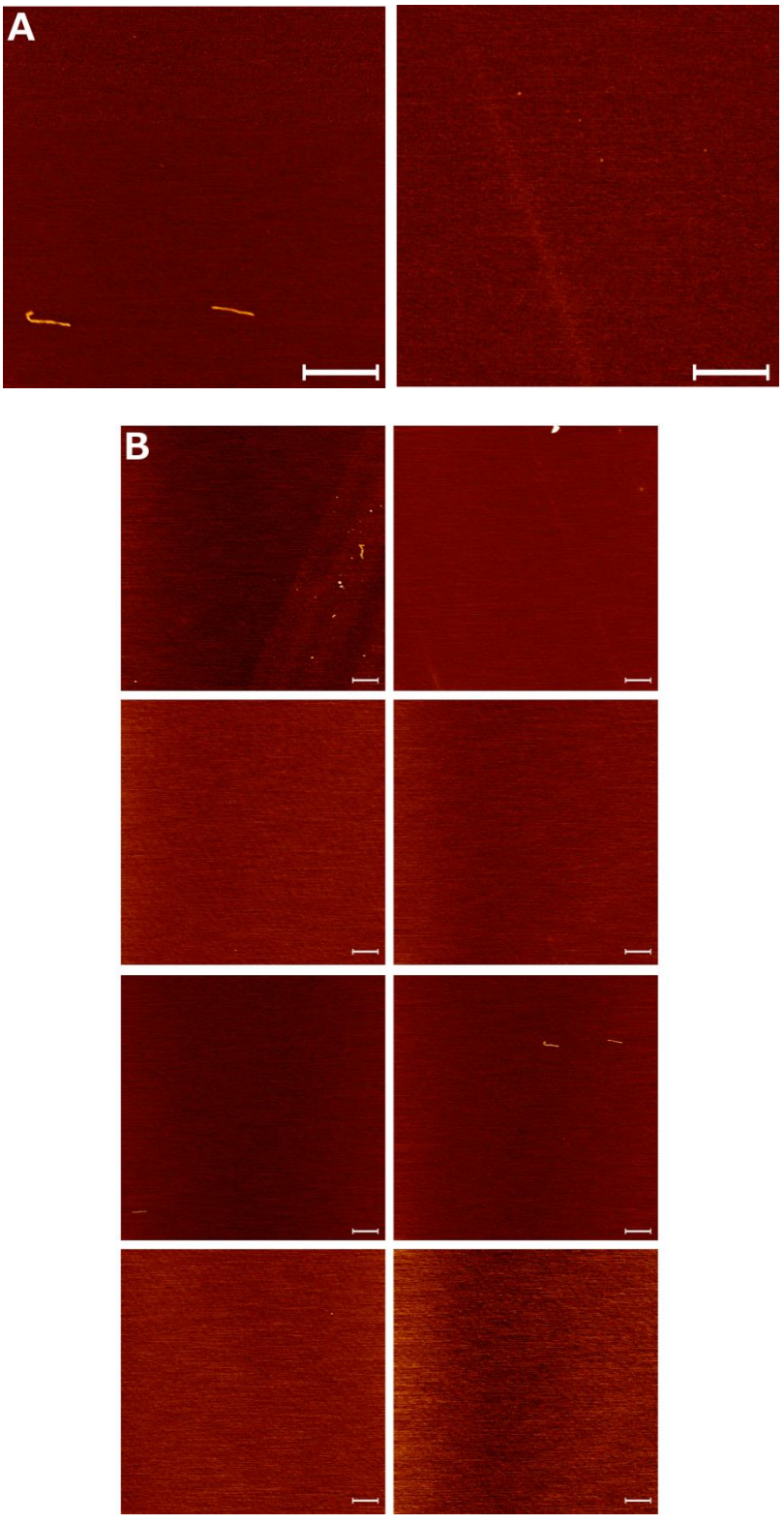

Figure S5.6 Images of apoSH pWT incubated for ~300 hours at 5 mg mL^{-1}, pH 7.4, 37 °C. **(A)** and **(B)** show 5 x 5 and 10 x 10 μm images, respectively, and the white bars correspond to 1 μm.

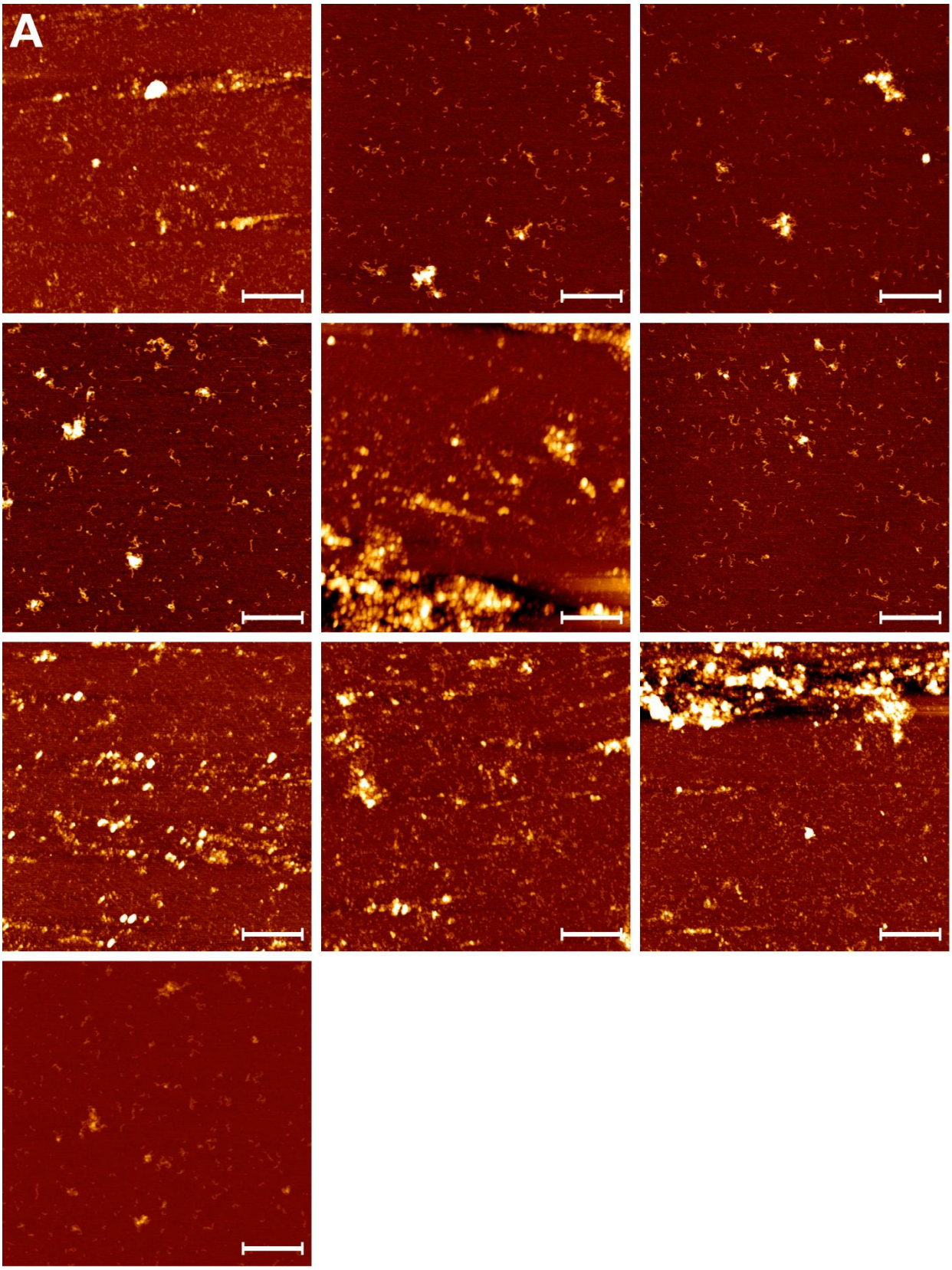
A

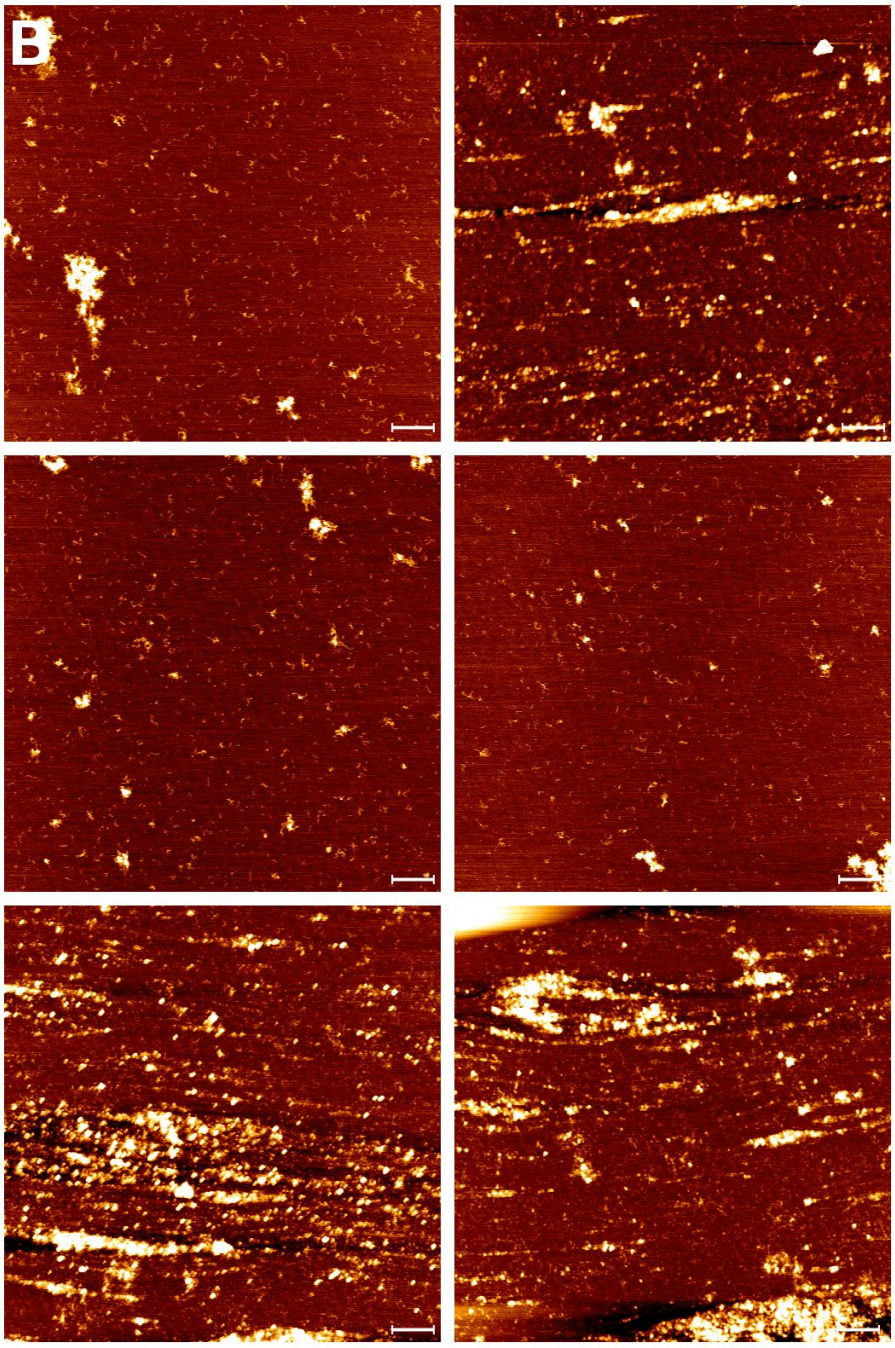

Figure S5.7 Images of apoSH A4V incubated for ~120 hours at 5 mg mL^{-1}, pH 7.4, 37 °C. **(A)** and **(B)** show 5 x 5 and 10 x 10 μm images, respectively, and the white bars correspond to 1 μm.

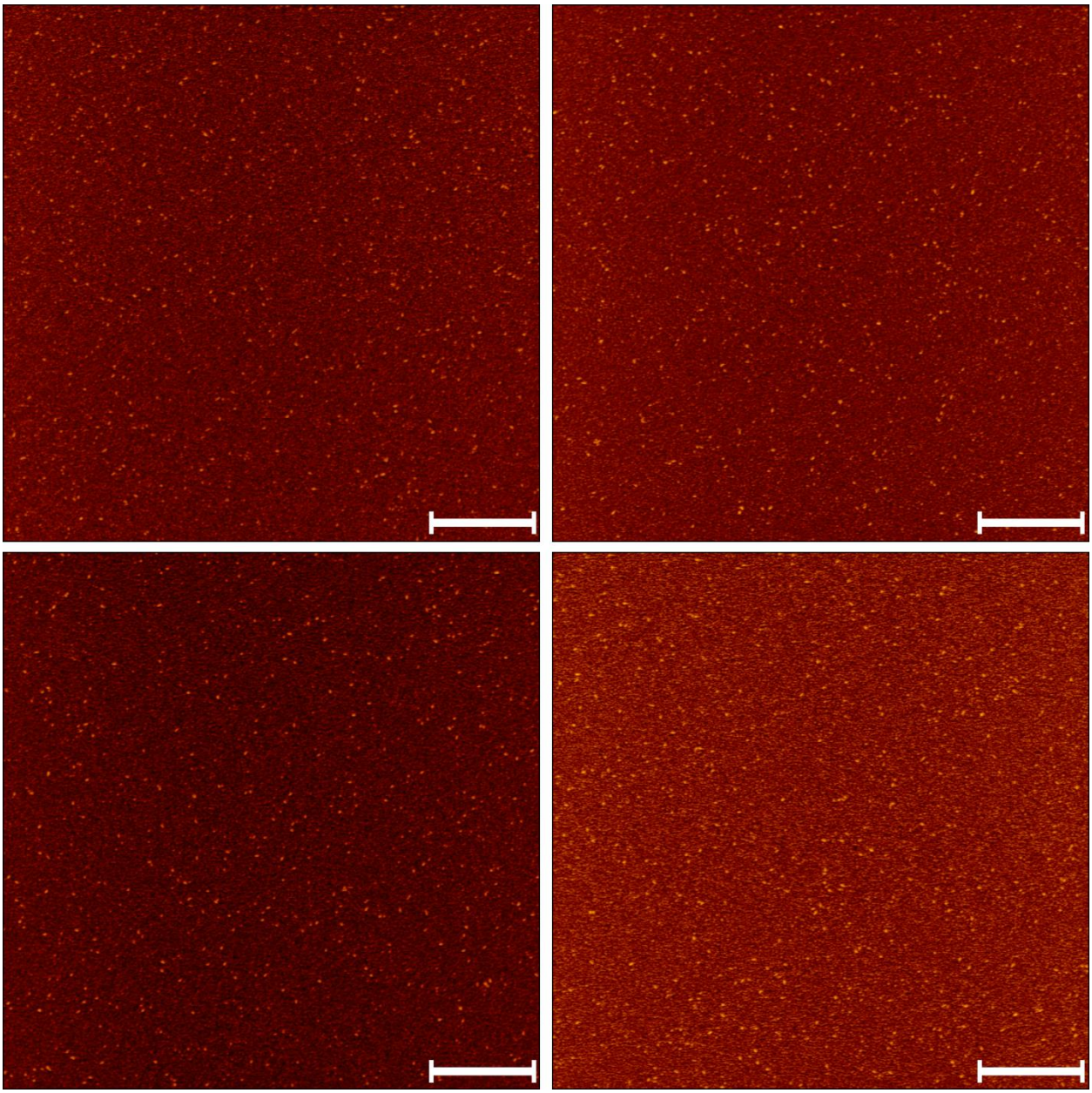

Figure S5.8 Images of apoSH G37R at t_0 (5 mg mL^{-1}, pH 7.4, 37 °C). All images are 5 x 5 μm and the white bars correspond to 1 μm.

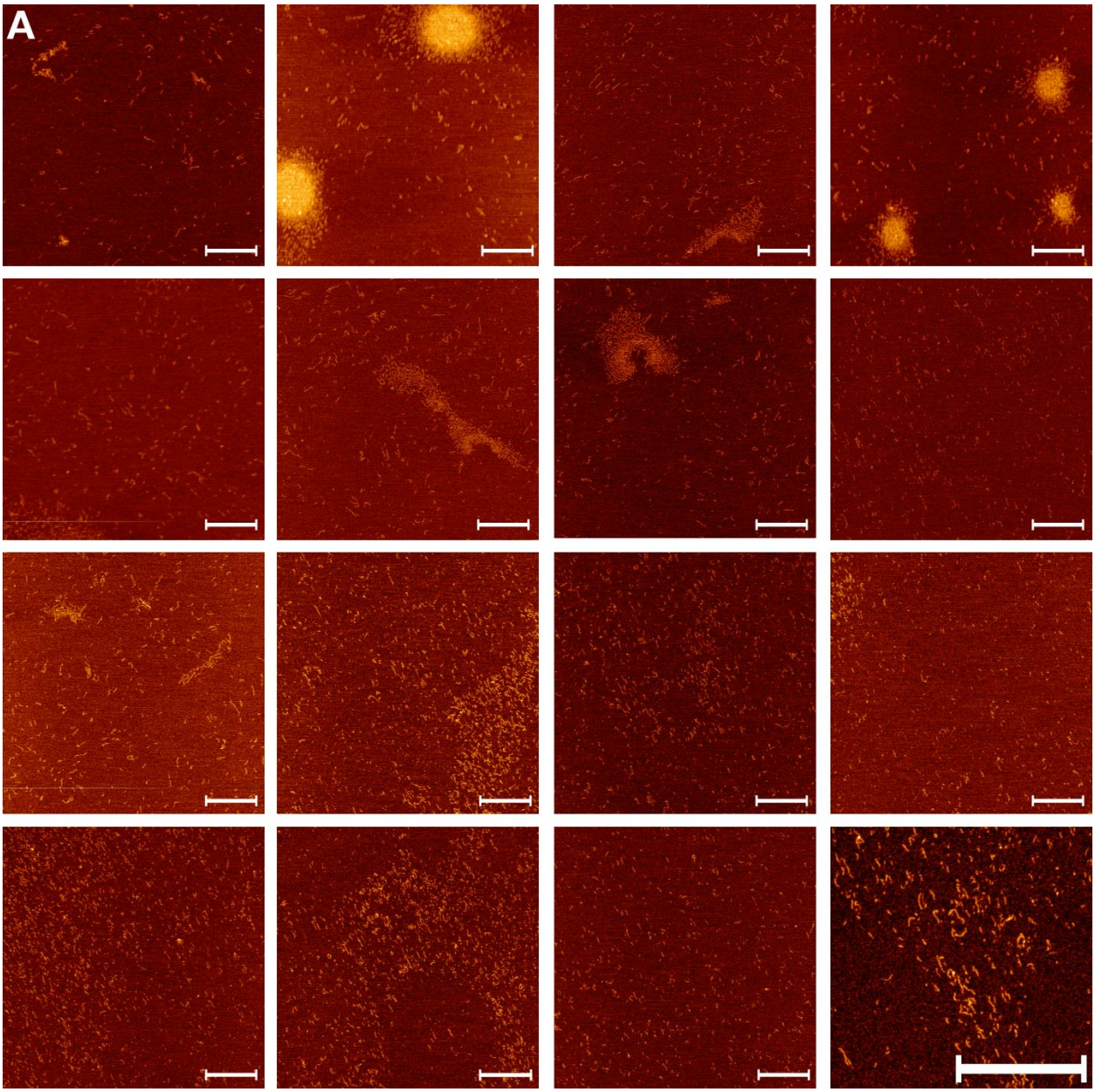
A

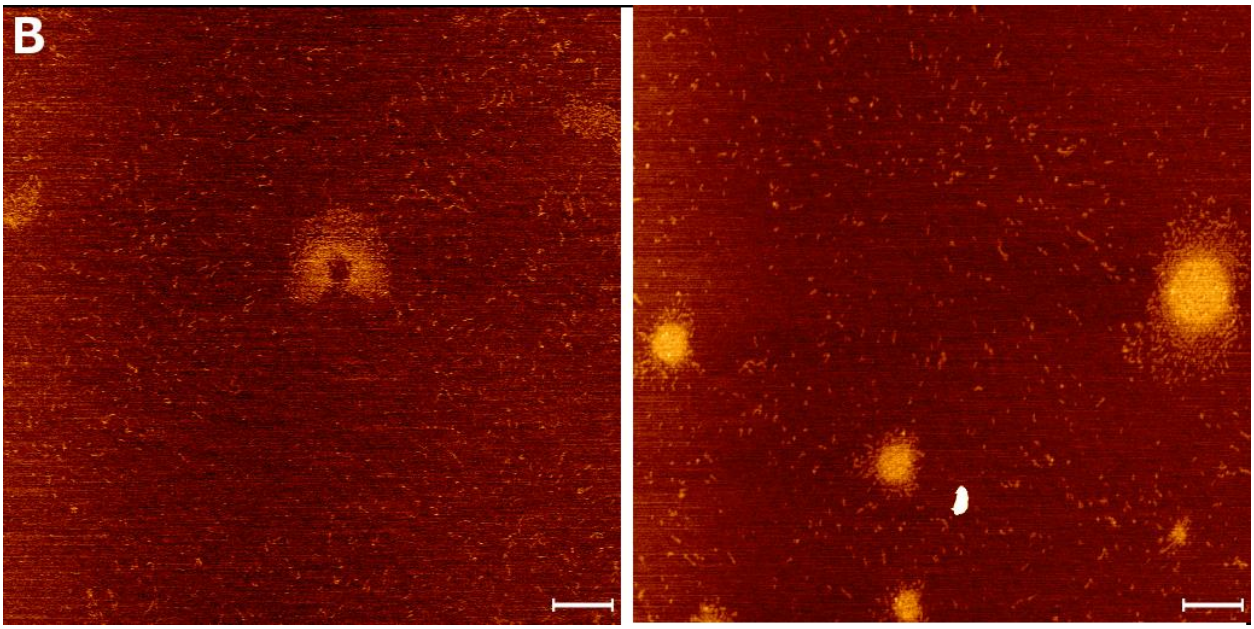

Figure S5.9 Images of apoSH G37R at ~t_{300} (5 mg mL^{-1}, pH 7.4, 37 °C). **(A)** and **(B)** show 5 x 5 and 10 x 10 μm images, respectively, and the white bars correspond to 1 μm.

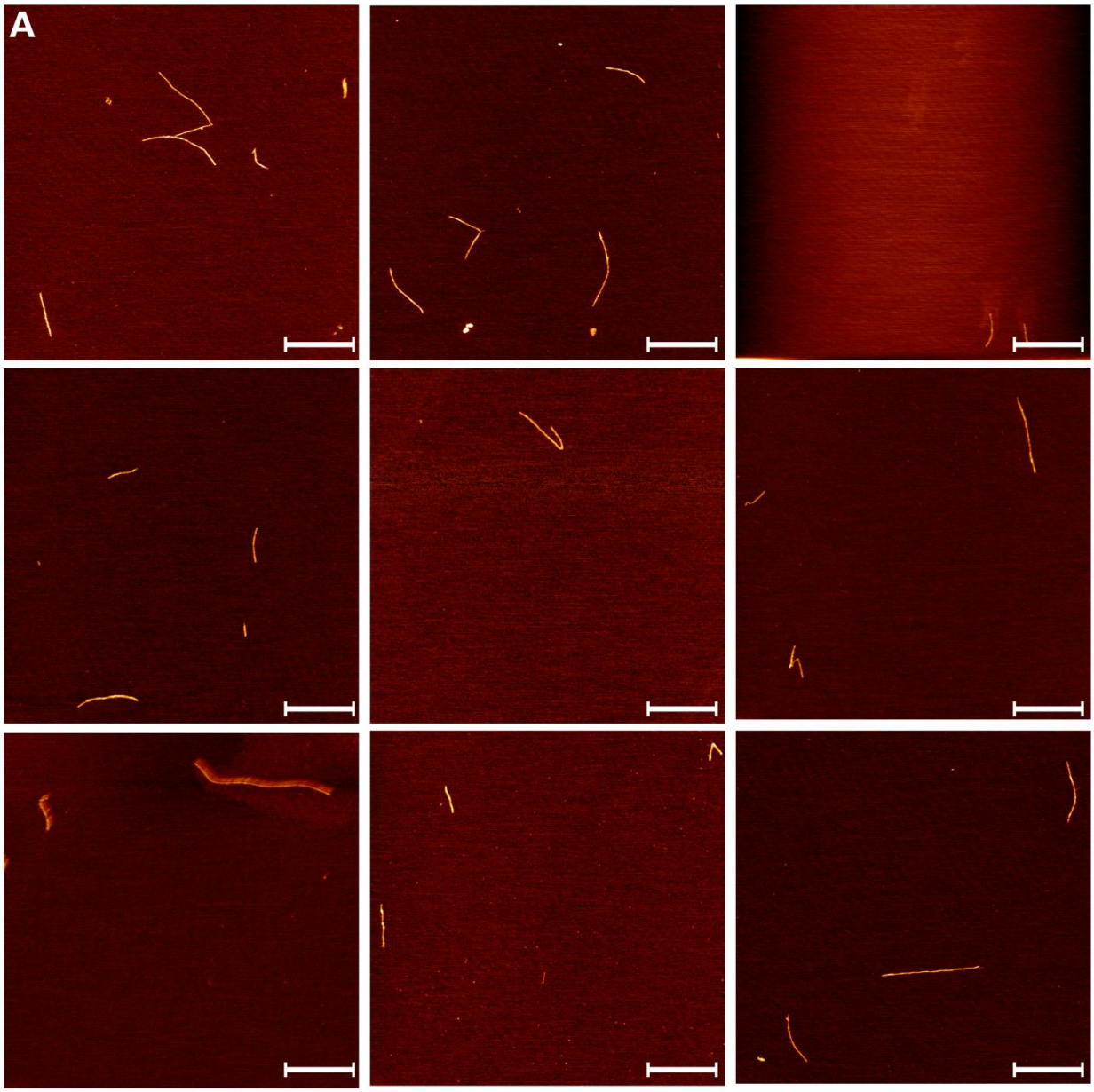
A

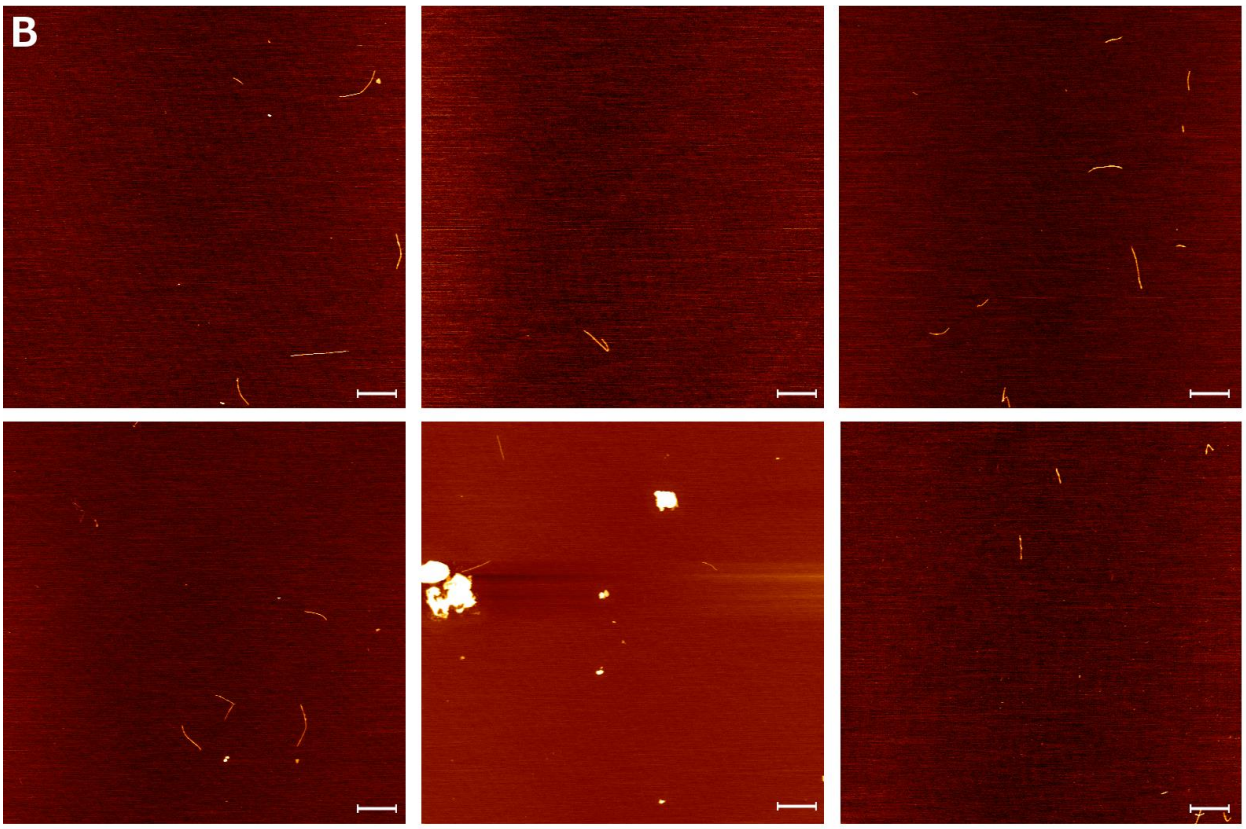

Figure S5.10 Images of apoSH G93A at ~t_{300} (5 mg mL^{-1}, pH 7.4, 37 °C). (A) and **(B)** show 5 x 5 and 10 x 10 μm images, respectively, and the white bars correspond to 1 μm.

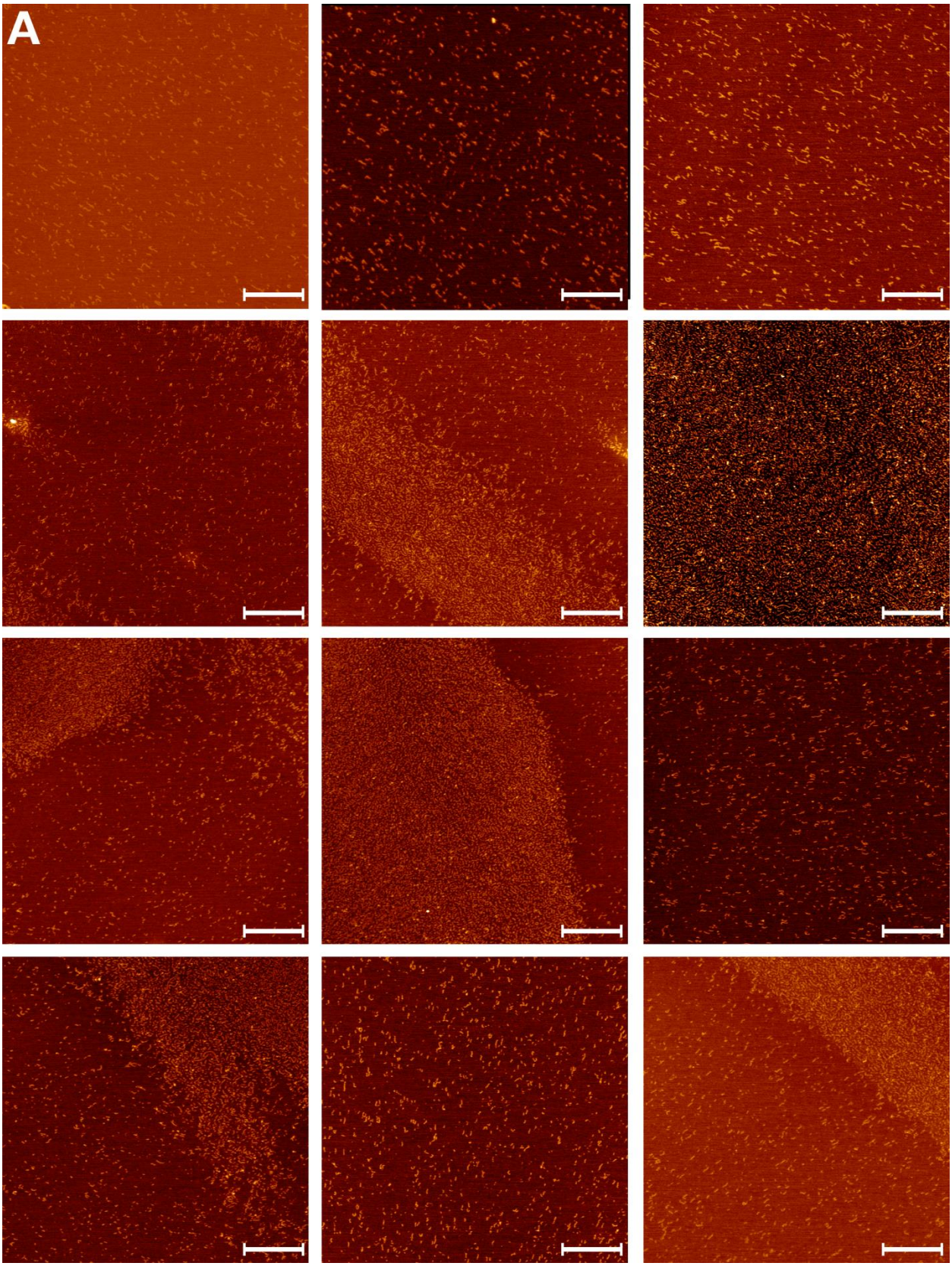
A

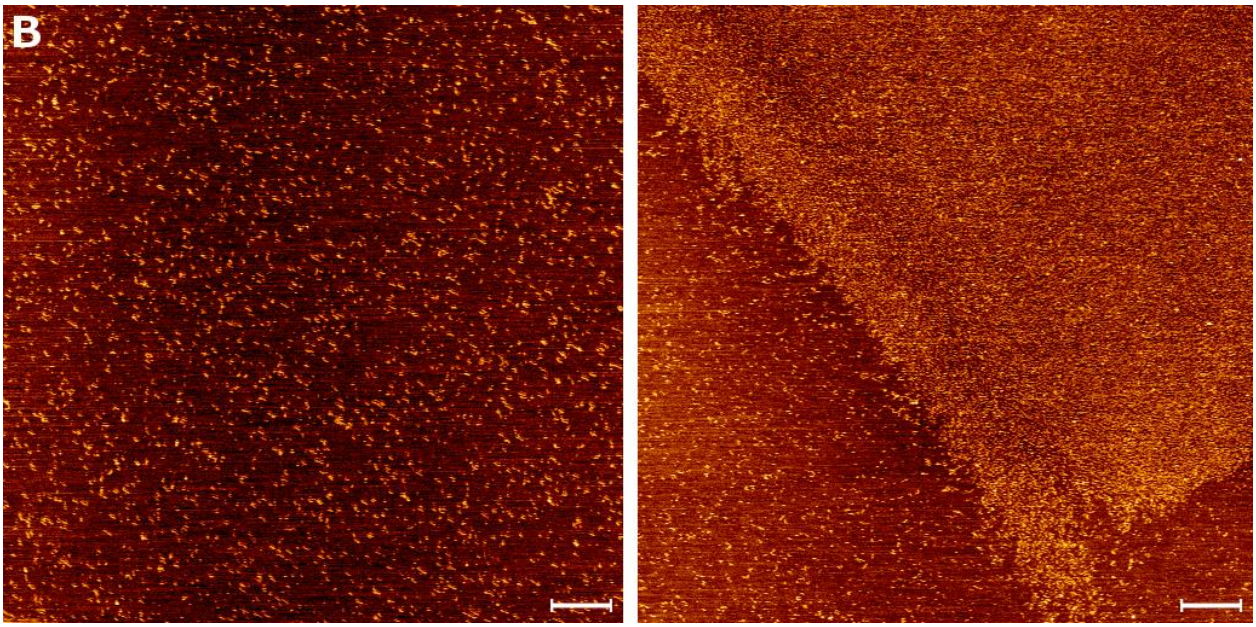

Figure S5.11 Images of apoSH G93R at ~t_{300} (5 mg mL^{-1}, pH 7.4, 37 °C). (A) and **(B)** show 5 x 5 and 10 x 10 μm images, respectively, and the white bars correspond to 1 μm.

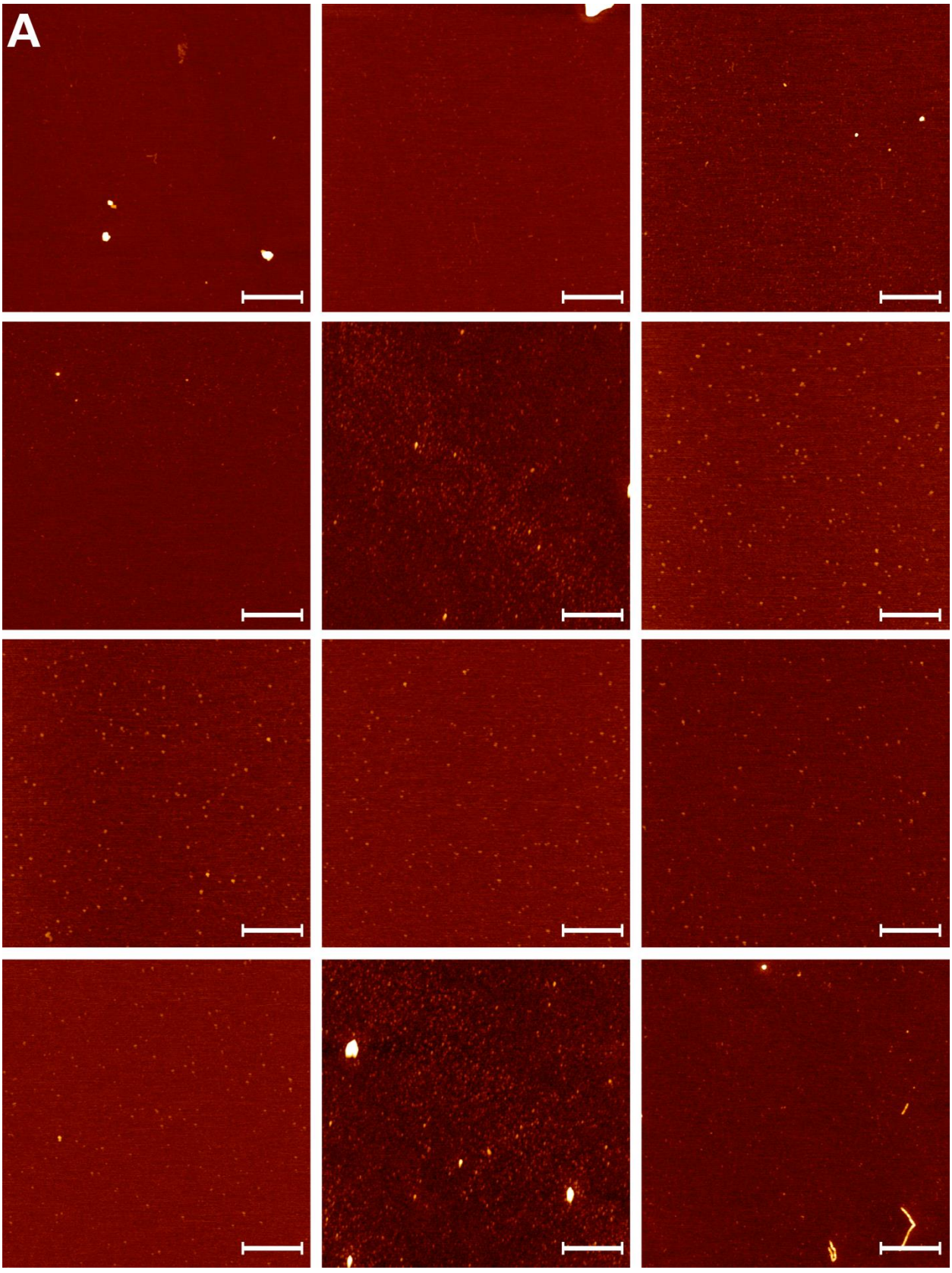
A

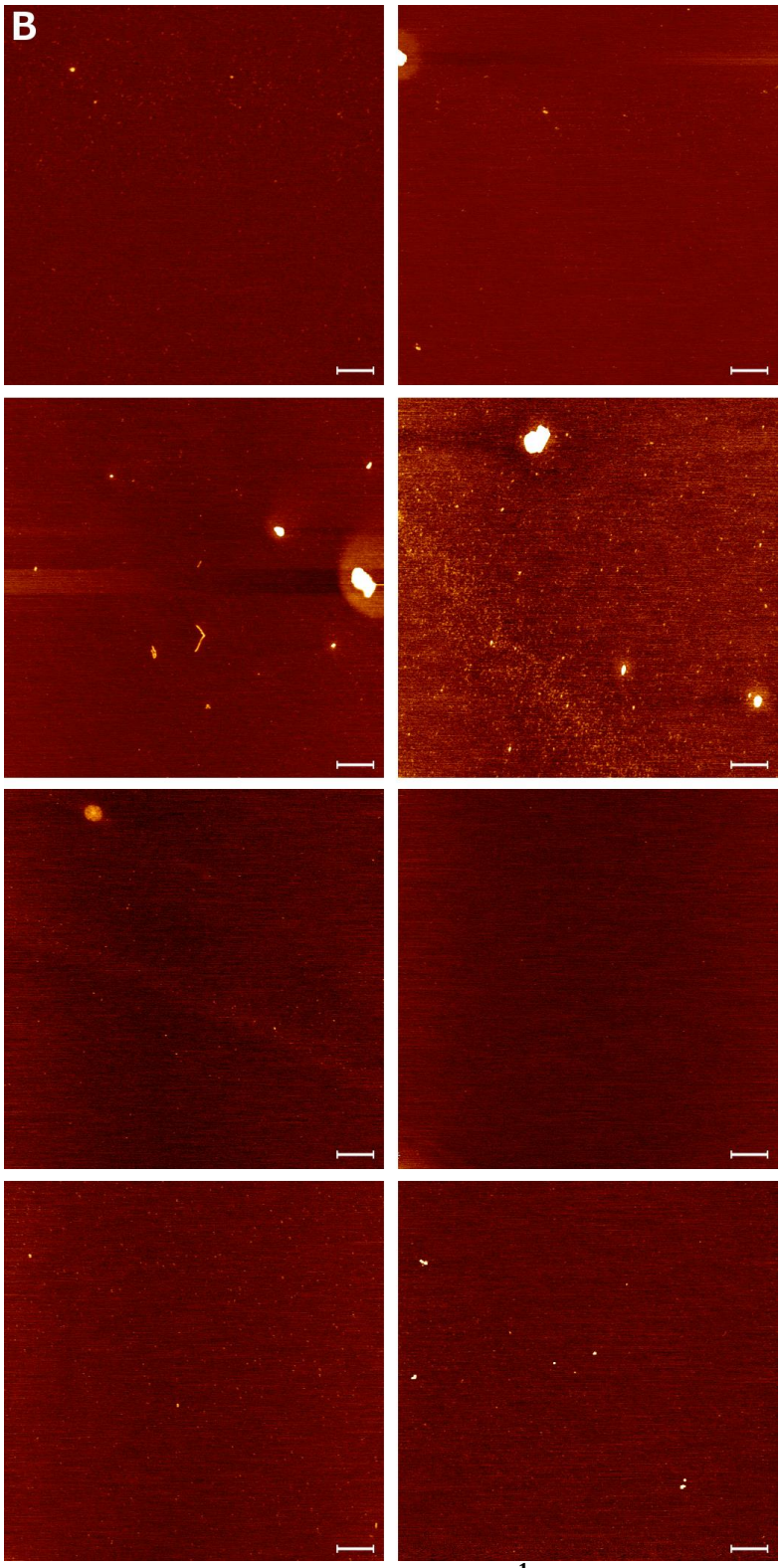

Figure S5.12 Images of apoSH G93S at ~t_{300} (5 mg mL^{-1}, pH 7.4, 37 °C). (A) and **(B)** show 5 x 5 and 10 x 10 μm images, respectively, and the white bars correspond to 1 μm.

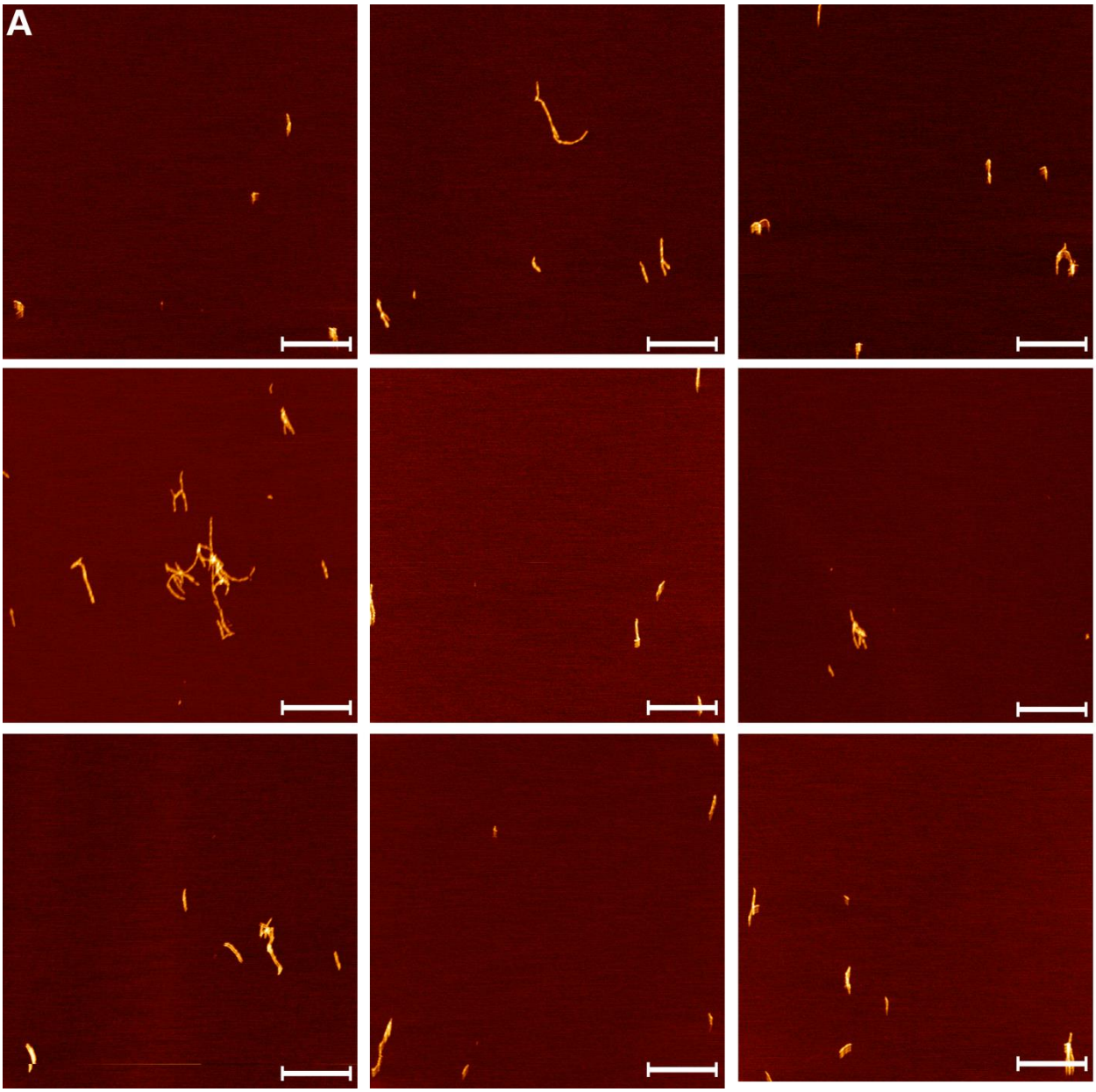
A

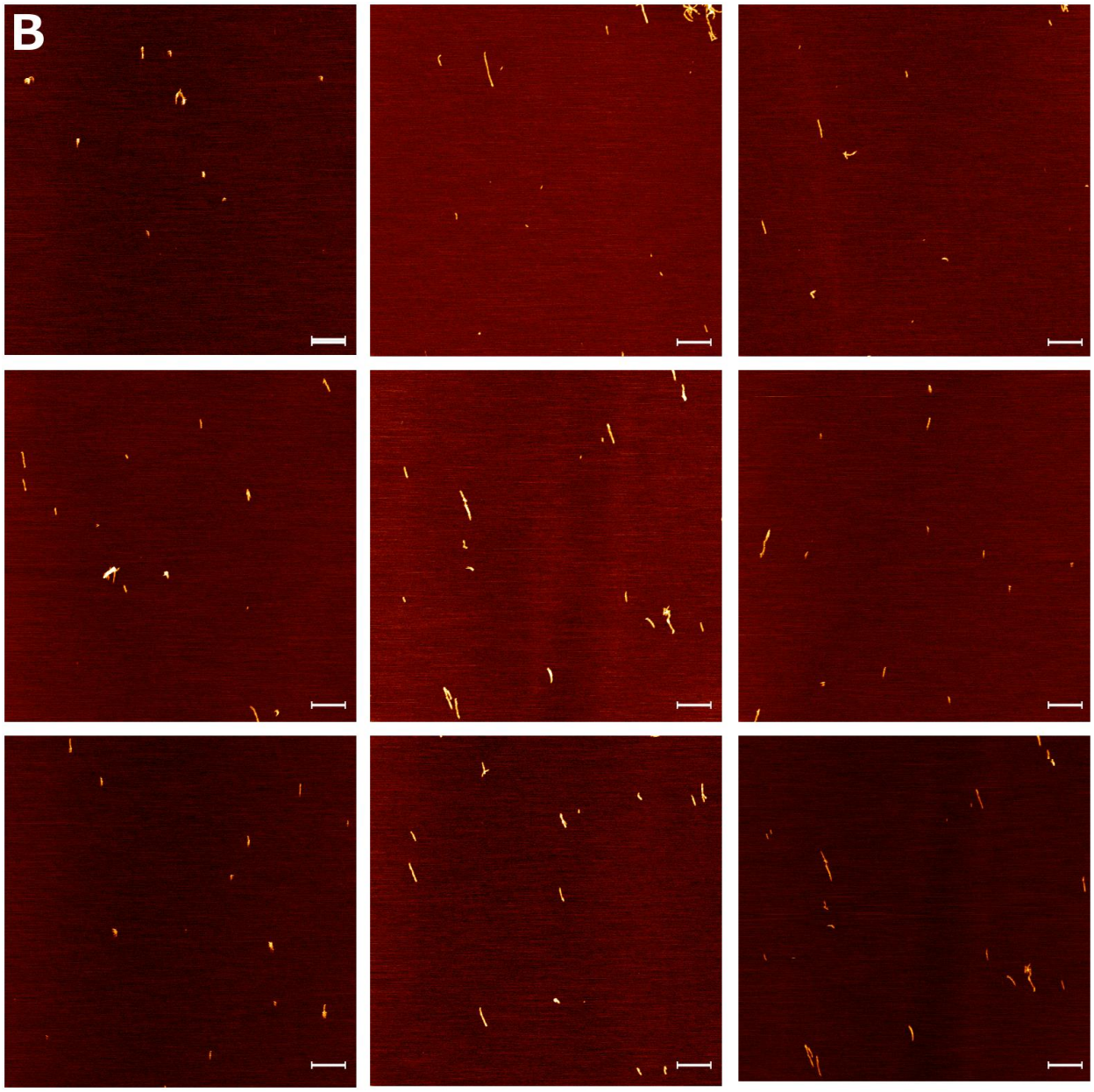

Figure S5.13 Images of apoSH V148I at ~t_{300} (5 mg mL^{-1}, pH 7.4, 37 °C, 150 mM Na_2SO_4). **(A)** and **(B)** show 5 x 5 and 10 x 10 μm images, respectively, and the white bars correspond to 1 μm.

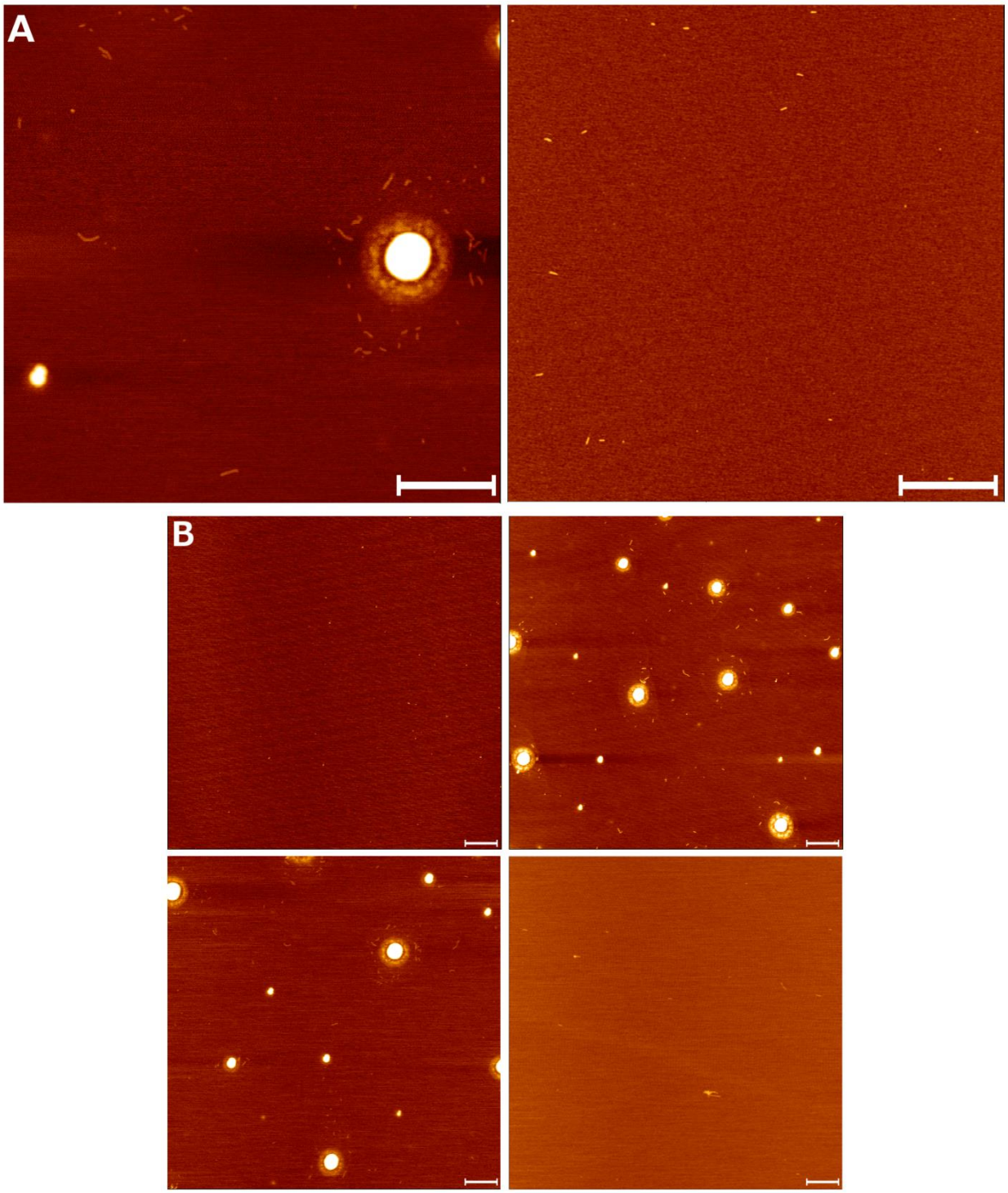

Figure S5.14 Images of apoSH A4V at ~t_{300} (1 mg mL^{-1}, pH 7.4, 37 °C). (A) and **(B)** show 5 x 5 and 10 x 10 μm images, respectively, and the white bars correspond to 1 μm.

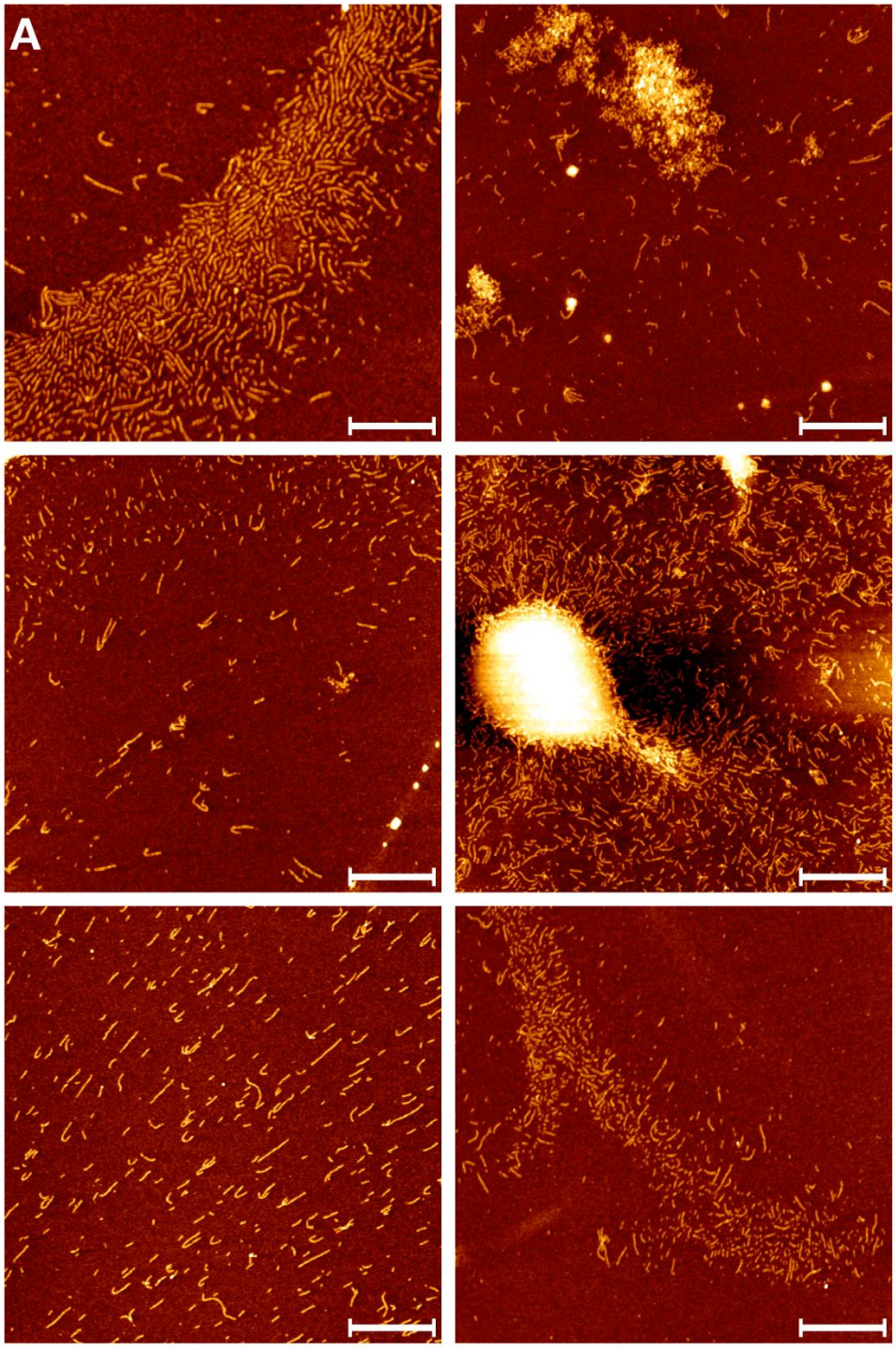
A

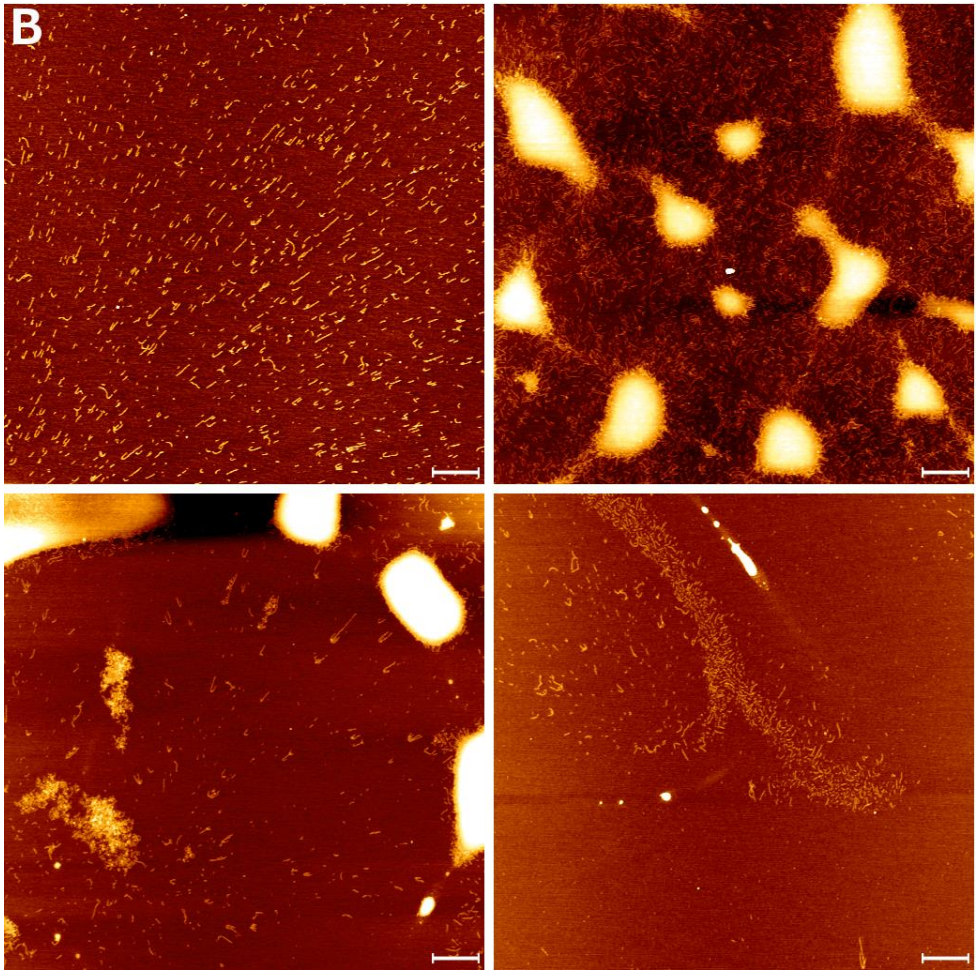

Figure S5.15 Images of apoSH A4V at ~t_{300} (1 mg mL^{-1}, pH 7.4, 37 °C, 150 mM Na_2SO_4). **(A)** and **(B)** show 5 x 5 and 10 x 10 μm images, respectively, and the white bars correspond to 1 μm.

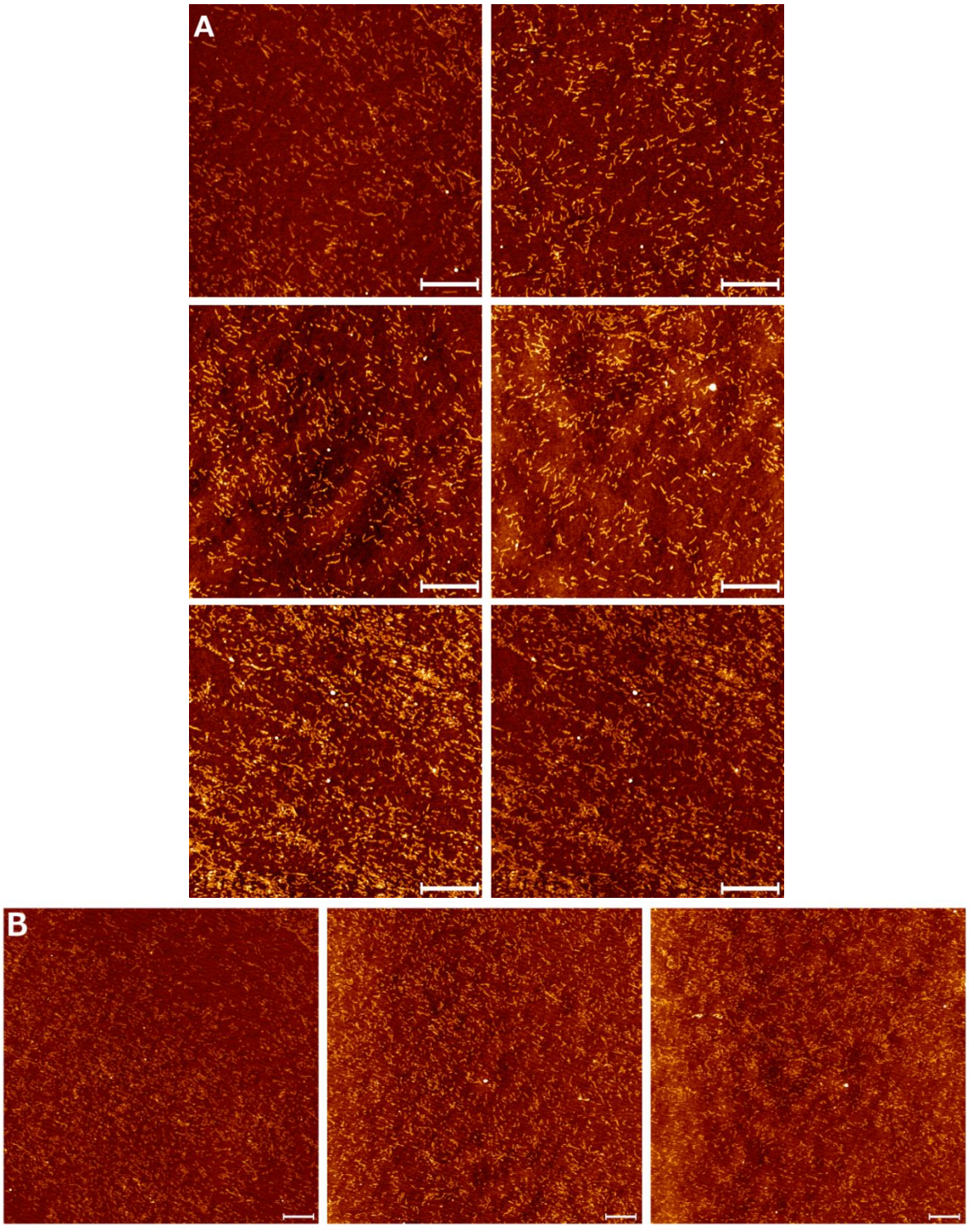

Figure S5.16 Images of apoSH A4V at ~t_{300} (1 mg mL^{-1}, pH 7.4, 37 °C, 150 mM NaCl). (A) and **(B)** show 5 x 5 and 10 x 10 μm images, respectively, and the white bars correspond to 1 μm.

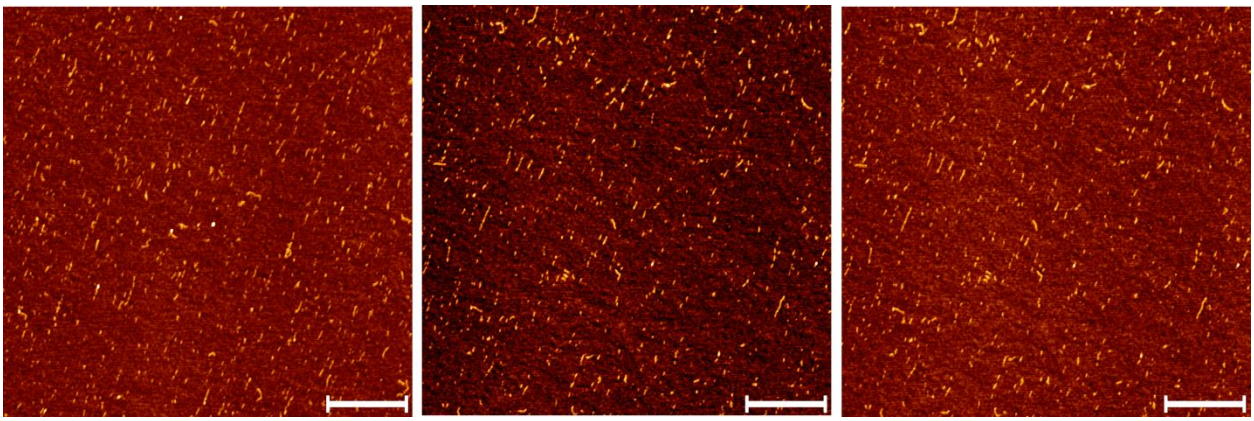

Figure S5.17 Images of apoSH G93R at ~t_{300} (1 mg mL^{-1}, pH 7.4, 37 °C). All images are 5 x 5 μm and the white bars correspond to 1 μm.

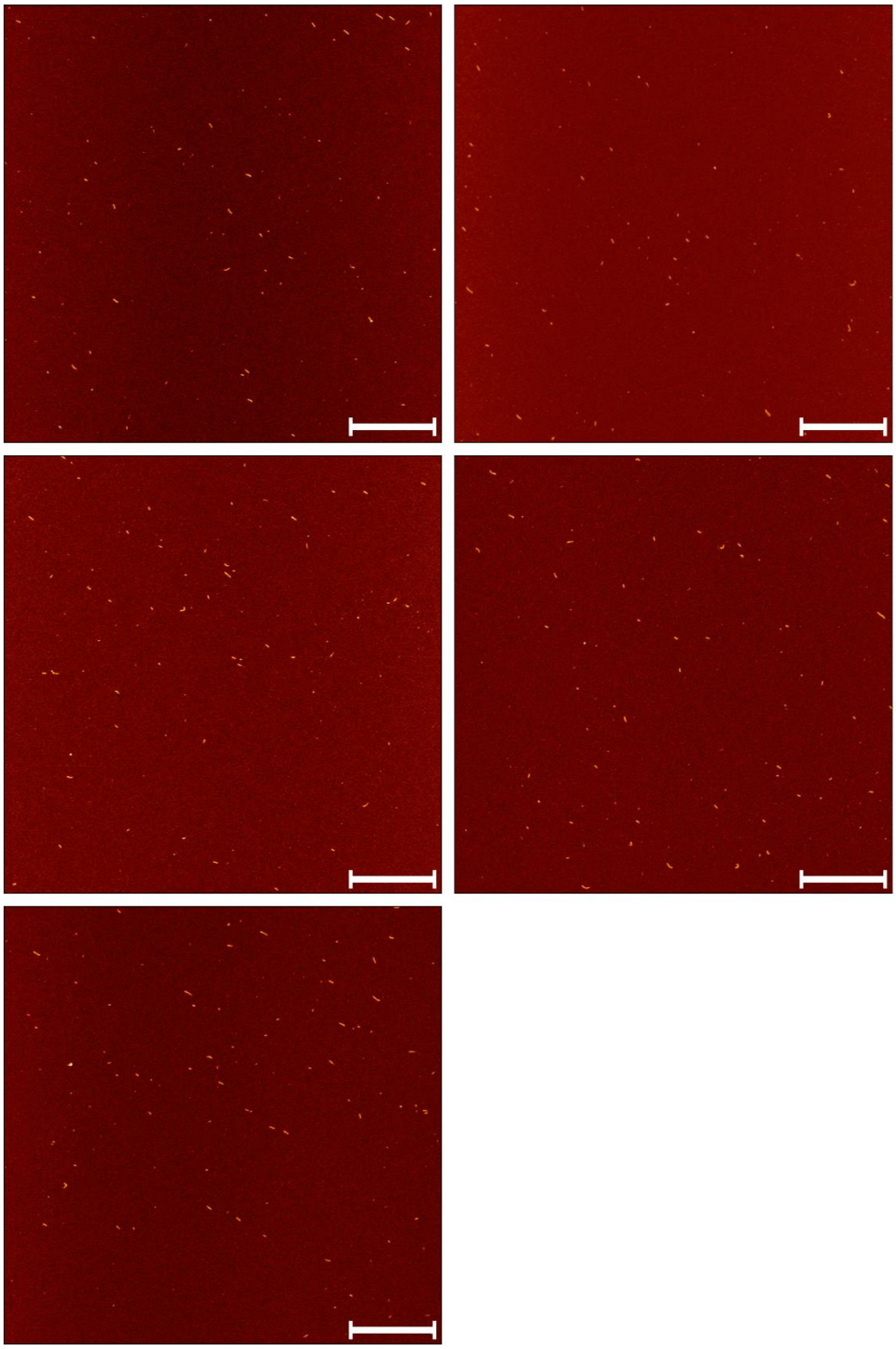

Figure S5.18 Images of apoSH G93R at ~t_{22} (1 mg mL^{-1}, pH 7.4, 37 °C, 150 mM Na_2SO_4). All images are 5 x 5 μm and the white bars correspond to 1 μm.

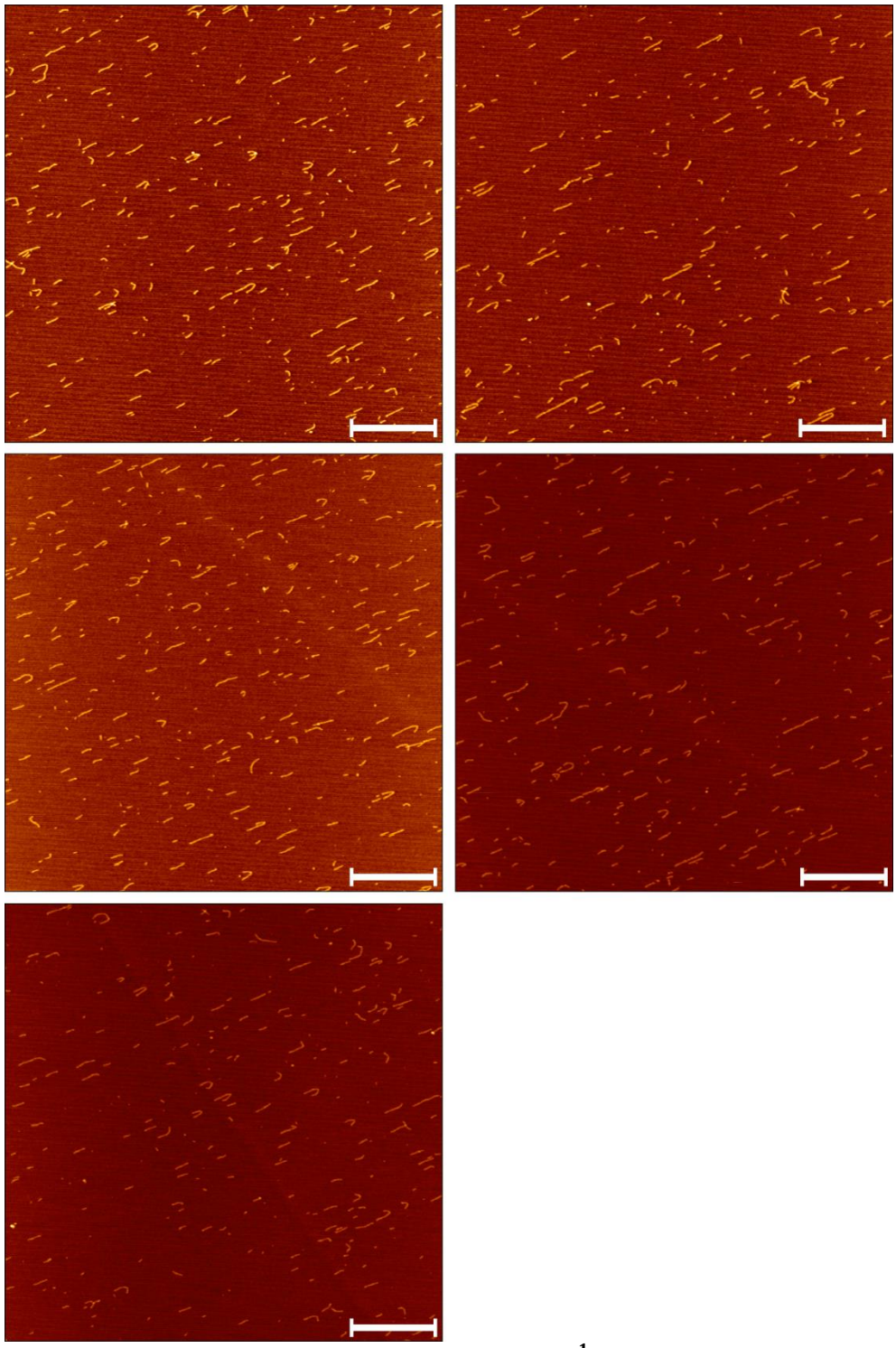

Figure S5.19 Images of apoSH G93R at ~t_{143} (1 mg mL^{-1}, pH 7.4, 37 °C, 150 mM Na_2SO_4). All images are 5 x 5 μm and the white bars correspond to 1 μm.

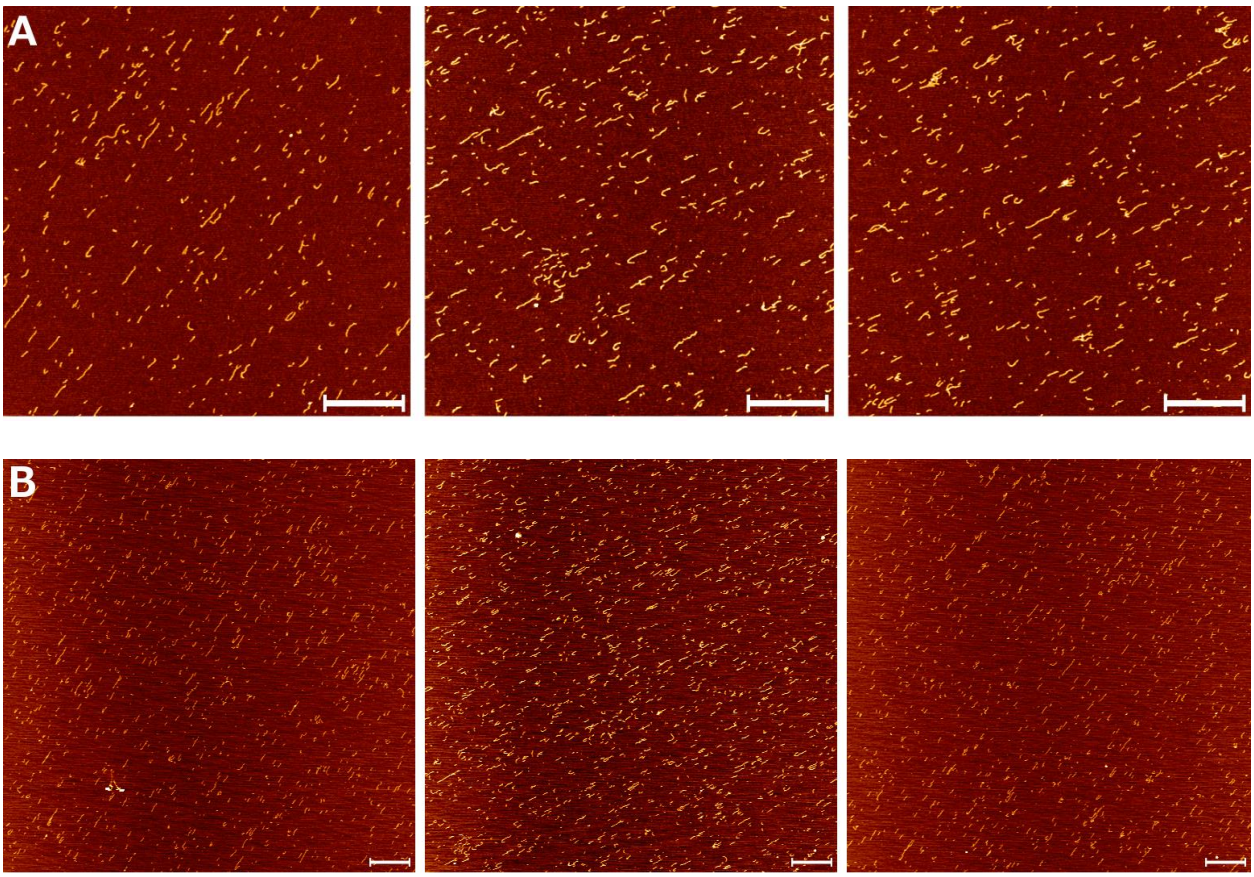

Figure S5.20 Images of apoSH G93R at ~t_{300} (1 mg mL^{-1}, pH 7.4, 37 °C, 150 mM Na_2SO_4). **(A)** and **(B)** show 5 x 5 and 10 x 10 µm images, respectively, and the white bars correspond to 1 µm.

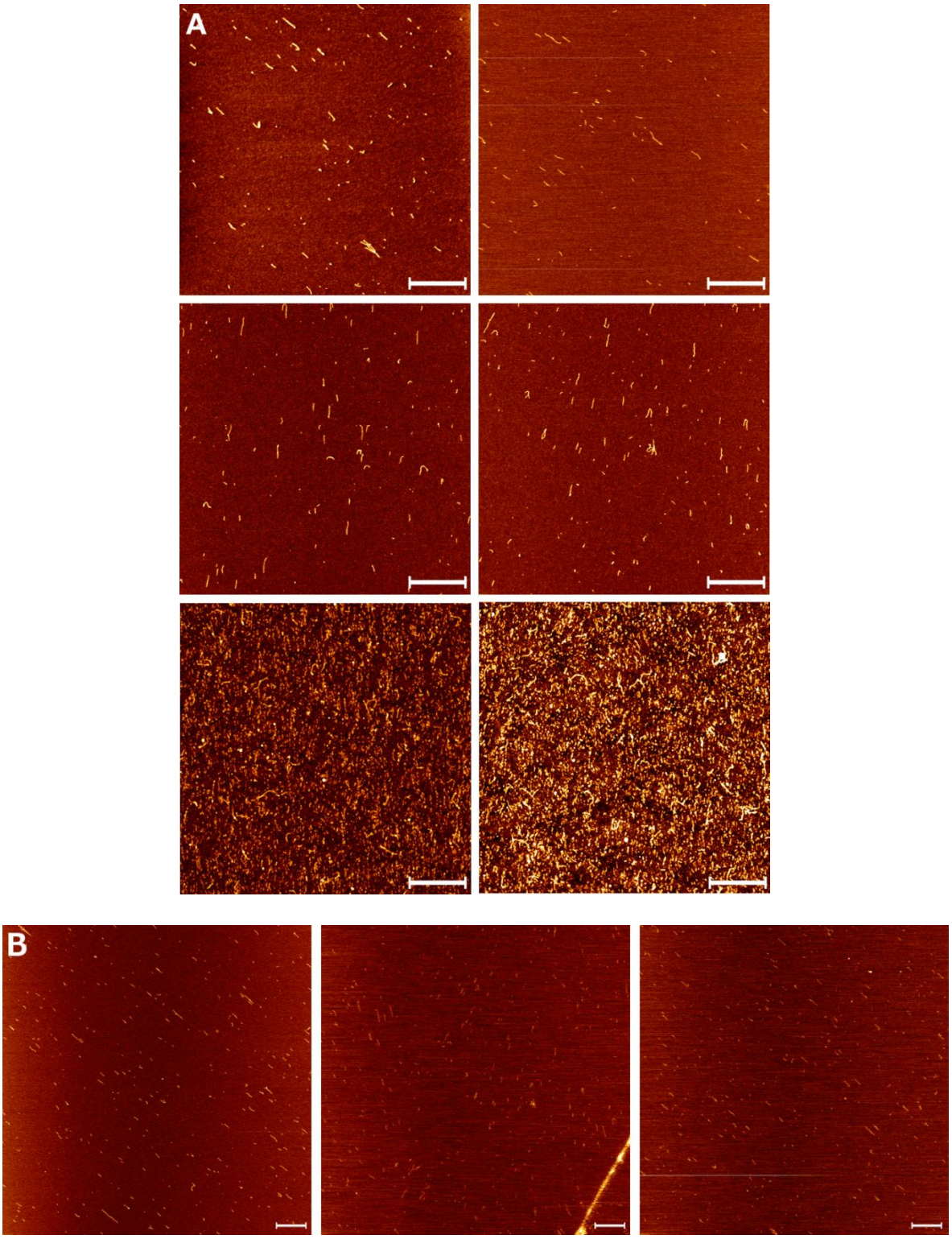

Figure S5.21 Images of apoSH G93R at ~t_{300} (1 mg mL^{-1}, pH 7.4, 37 °C, 150 mM NaCl). (A) and **(B)** show 5 x 5 and 10 x 10 μm images, respectively, and the white bars correspond to 1 μm.

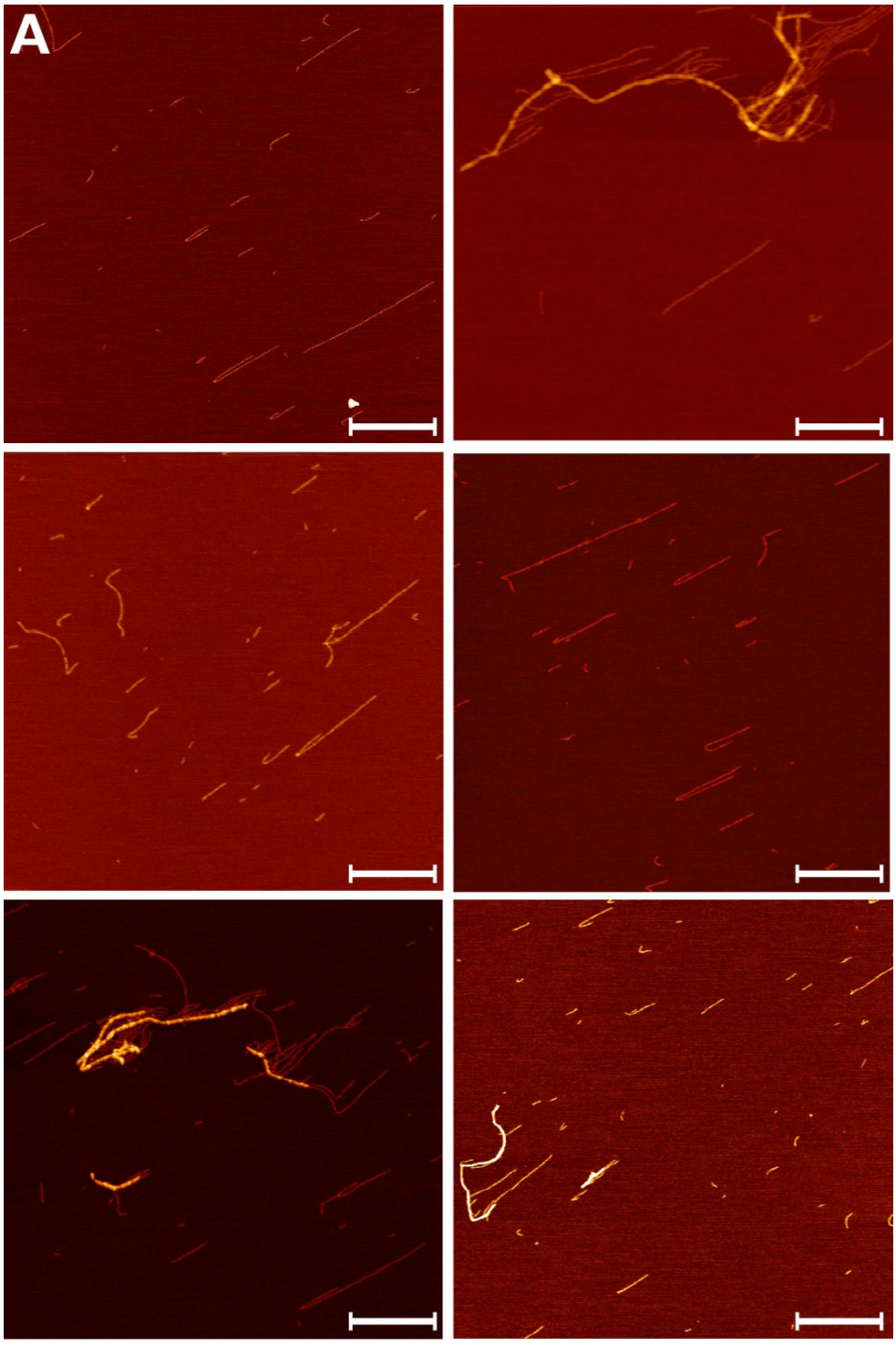
A

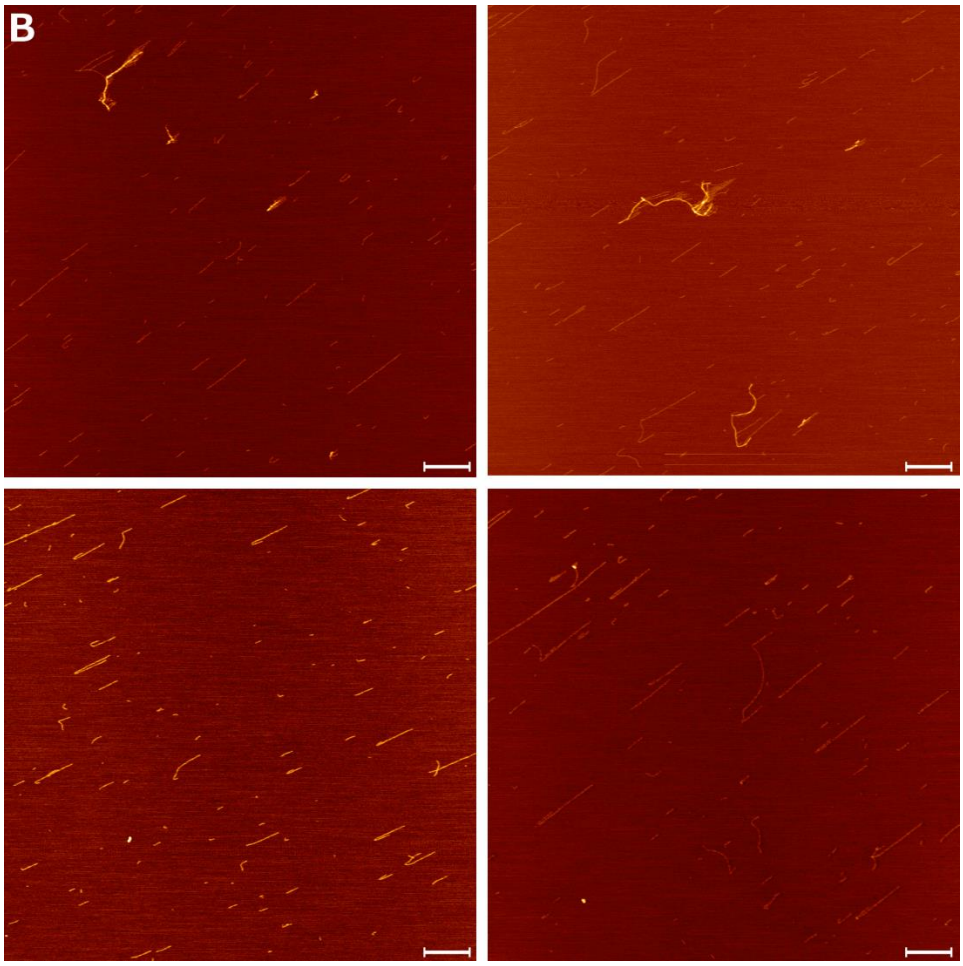

Figure S5.22 Images of apoSH G93S at ~t_{300} (1 mg mL^{-1}, pH 7.4, 37 °C, 150 mM Na_2SO_4). **(A)** and **(B)** show 5 x 5 and 10 x 10 μm images, respectively, and the white bars correspond to 1 μm.

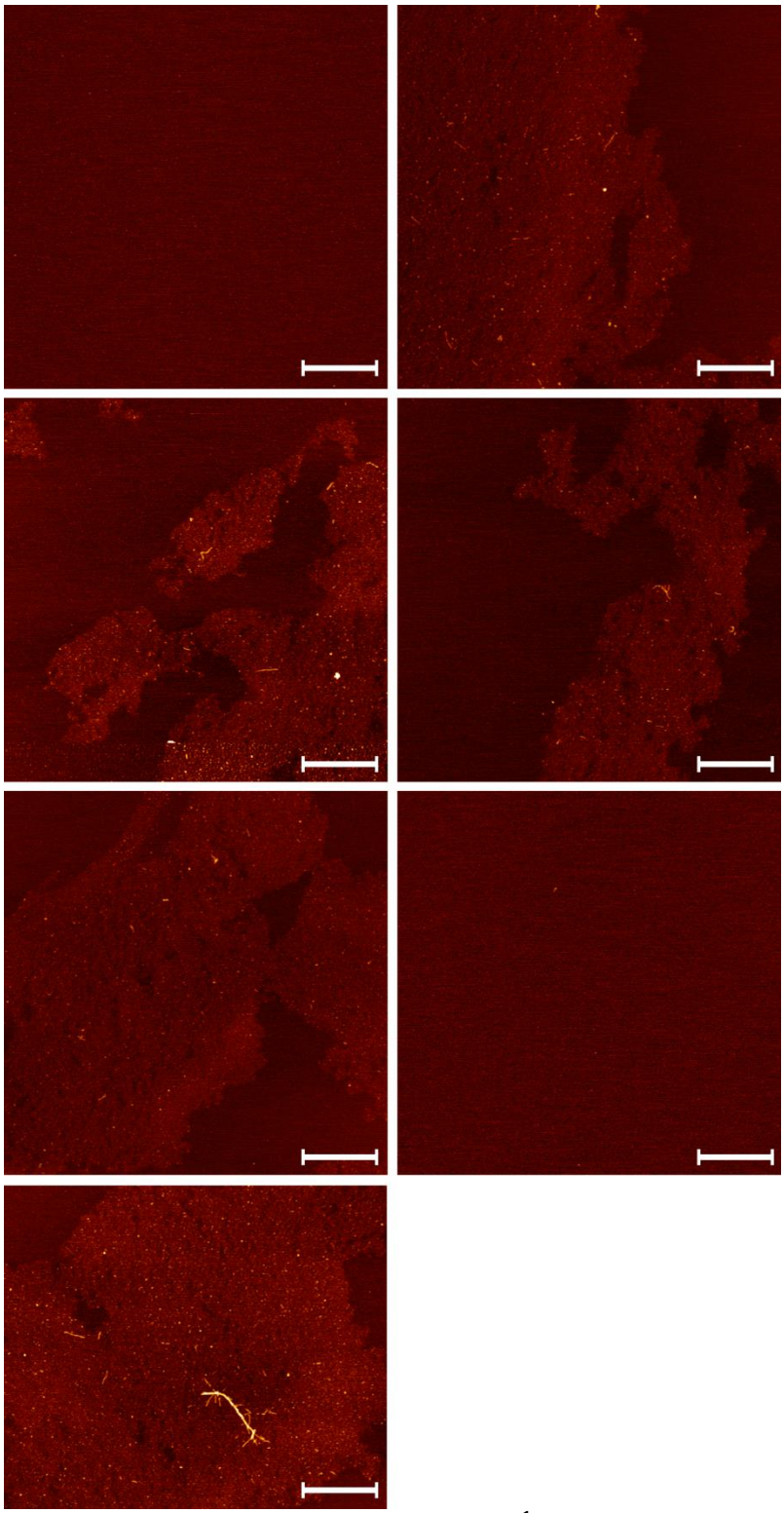

Figure S5.23 Images of apoSH G93S at ~t_{300} (1 mg mL^{-1}, pH 7.4, 37 °C, 150 mM NaCl). All images are 5 x 5 μm and the white bars correspond to 1 μm.

Table S5.1 Metal content of apoSH samples.

ApoSH sample[a]	Date Prepared[b]	Copper content %[c]	Zinc Content %[c]
pWT	03/07/09	-0.01	7.28
pWT	03/07/09	0.00	7.59
pWT	03/07/09	0.00	5.99
A4V	16/07/09	-0.01	4.88
E100G	31/07/09	0.00	2.98
pWT	**09/08/09**	**0.01**	**10.14**
G85R	02/02/10	0.00	7.50
G85R	02/02/10	0.00	7.15
G93A	**22/04/10**	**0.04**	**10.11**
G93A	22/04/10	0.01	7.09
A4S	**20/05/10**	**0.00**	**16.81**
V148I	25/05/10	0.02	9.96
G37R	27/05/10	0.01	9.64
A4S	21/06/10	0.00	8.08
A4S	**24/06/10**	**0.00**	**31.91**
A4T	**24/06/10**	**0.02**	**40.86**
A4T	**24/06/10**	**0.04**	**87.31**
V148I	09/09/10	-0.20	8.30
V148I	09/09/10	-0.20	7.65
H46R	**15/09/10**	**-0.21**	**24.69**
A4S	**12/10/10**	**0.03**	**21.43**
G85R	**18/10/10**	**0.01**	**18.25**
A4T	25/10/10	0.01	8.10
H46R	28/10/10	0.00	10.10
A4S	**07/11/10**	**0.05**	**19.70**
G93R	08/11/10	0.02	9.96
G93S	**11/11/10**	**0.01**	**14.52**
E100G	**15/11/10**	**-0.20**	**18.20**
G93S	**15/11/10**	**-0.20**	**11.67**
G93S	**15/11/10**	**-0.21**	**12.21**
G93R	**18/11/10**	**-0.21**	**13.74**
pWT	**10/05/11**	**-0.23**	**8.23**
AS	20/07/11	-0.20	2.72
pWT + A4V seeds	20/07/11	-0.20	2.58
pWT + H43R seeds	20/07/11	-0.21	2.36
H43R	**08/11/11**	**-0.20**	**24.85**
A4V	**22/05/12**	**-0.14**	**12.22**
H43R	29/05/12	-0.21	6.87
H43R	01/08/12	-0.19	5.97
H43R	01/08/12	-0.19	6.19

H43R	01/08/12	-0.21	5.84
H43R	07/01/13	-0.18	2.74
H43R	07/01/13	-1.75	3.27
A4V no salt	04/06/13	0.00	0.31
A4V Na_2SO_4	04/06/13	0.00	-0.09
A4V NaCl	04/06/13	0.00	0.09
G93R no salt	20/06/13	0.00	0.91
G93R Na_2SO_4	20/06/13	0.00	0.67
G93R NaCl	20/06/13	0.00	0.71
E100G no salt	07/07/13	0.00	-0.64
E100G Na_2SO_4	07/07/13	0.00	-0.80
E100G NaCl	07/07/13	0.00	-0.04
AS no salt	22/10/13	0.00	-0.79
AS Na_2SO_4	22/10/13	0.00	0.17
AS NaCl	22/10/13	0.00	-0.75
H43R no salt	29/10/13	0.00	-0.01
H43R Na_2SO_4	29/10/13	0.01	-1.64
H43R NaCl	29/10/13	0.00	-0.63
A4V Na_2SO_4	26/11/13	0.00	0.30
A4V NaCl	26/11/13	0.00	0.12
G93R no salt	08/01/14	0.00	0.56
G93R Na_2SO_4	08/01/14	0.00	-0.67
G93R NaCl	08/01/14	0.00	0.63
G93S no salt	22/01/14	0.00	0.32
G93S Na_2SO_4	22/01/14	0.00	-0.36
G93S NaCl	22/01/14	0.00	0.64

[a]Samples analyzed for metal content. Samples highlighted in red contain too much metal for results to be interpreted. Samples containing less than 10 % metal were used.
[b]The date the sample was prepared listed as day, month, year. Samples prepared in 2013-2014 had much less metal contamination than samples prepared before.
[c]Metal concentration divided by apoSH concentration.

Table S5.2 All DLS data for apoSH SOD1 variants at 1 mg mL^{-1}, pH 7.4, 37 °C.

	t = 0				t > 300			
ApoSH SOD1 variant	PDI[a]	PDI width (nm)[b]	Intensity Distribution Hydrodynamic Radius (nm)[c]	Number Distribution Hydrodynamic Radius (nm)[c]	PDI[a]	PDI width (nm)[b]	Intensity Distribution Hydrodynamic Radius (nm)[c]	Number Distribution Hydrodynamic Radius (nm)[c]
pWT	0.154	1.761	5.094	3.314	0.215	2.768	5.084	3.256
	0.187	1.986	5.473	2.436	0.252	2.644	5.384	3.216
	0.206	2.117	5.445	3.345	0.176	1.911	4.875	3.182
	0.224	2.552	5.757	3.104	0.243	2.520	5.337	3.028
	0.223	2.310	5.517	3.503	0.237	2.452	5.566	3.478
	0.235	2.468	5.560	3.582	0.224	2.349	5.045	3.336
	0.170	1.777	5.144	3.082	0.315	7.762	4.875	3.122
	0.203	1.914	4.627	2.687	0.204	2.241	5.404	3.095
	0.219	2.148	5.169	3.045	0.219	2.458	5.626	3.930
	0.233	2.284	5.392	2.741	0.450	7.483	5.252	4.320
	0.203	2.210	5.565	3.737	0.404	6.354	5.290	3.583
	0.198	2.226	5.849	3.000	0.264	21.83	4.994	3.839
Avg.	**0.205**	**2.146**	**5.383**	**3.131**	**0.267**	**5.231**	**5.228**	**3.449**
Stdev.	***0.025***	***0.250***	***0.332***	***0.387***	***0.083***	***5.657***	***0.253***	***0.398***
WT	0.211	2.570	6.724	4.617	0.754	631.5	4.393	3.574
	0.243	2.719	6.104	3.209	0.442	52.54	5.140	4.053
	0.257	2.861	5.333	3.049	0.826	1008	4.661	4.049
	0.219	2.609	6.427	4.330	0.279	4.229	5.085	3.232
	0.220	2.662	6.402	4.568	0.347	14.40	5.040	3.863
	0.219	2.583	5.138	3.450	0.336	4.768	5.201	3.706
	0.246	2.188	5.539	3.074	0.239	11.93	4.726	3.059
	0.222	2.211	6.015	1.189	0.290	3.787	5.756	4.062
	0.201	2.367	5.926	1.970	0.300	4.096	5.350	3.418
	0.264	2.076	5.937	2.549	0.223	2.643	5.521	4.247
	0.245	2.070	4.458	2.797	0.248	3.034	4.873	3.232
	0.213	2.078	4.822	3.344	0.308	5.045	5.606	3.603
	0.226	2.233	6.614	2.067	0.344	4.946	5.219	2.705
	0.212	2.085	5.181	2.429	0.236	2.776	5.823	3.323
	0.221	2.173	4.769	2.666	0.198	2.368	6.978	4.439
	0.239	2.245	5.276	3.196	0.256	3.126	8.325	1.903
	0.267	2.143	9.593	1.431	0.230	5.783	5.271	2.269
	0.240	2.193	5.131	2.770	0.321	4.461	5.042	3.492
	0.324	4.658	5.801	3.239	0.383	6.073	5.090	3.604
	0.322	4.584	5.752	4.147	0.382	6.096	5.739	2.012
	0.330	4.803	5.870	4.194	0.362	5.639	5.869	3.484
Avg.	**0.245**	**2.672**	**5.848**	**3.061**	**0.348**	**85.11**	**5.462**	**3.397**
Stdev.	***0.038***	***0.874***	***1.059***	***0.959***	***0.160***	***251.6***	***0.853***	***0.694***
A4S	0.236	3.378	7.546	4.752	0.704	21.93	83.96	3.047
	0.255	3.626	6.834	3.787	0.781	26.00	82.23	3.130
	0.263	3.592	9.930	1.366	0.765	25.12	75.20	4.171
Avg.	**0.251**	**3.532**	**8.103**	**3.302**	**0.750**	**24.35**	**80.463**	**3.449**
Stdev.	***0.014***	***0.134***	***1.622***	***1.744***	***0.041***	***2.141***	***4.640***	***0.626***
A4T	0.242	4.399	6.911	4.810	1.0	40.06	235.9	4.280
	0.214	4.386	7.014	3.710	1.0	41.25	247.1	4.561
	0.265	3.964	7.419	4.982	1.0	40.49	233.4	4.729
	0.255	3.659	7.370	4.212	1.0	49.61	249.9	4.442
	0.262	3.736	7.284	5.215	1.0	50.60	244.1	5.090
	0.263	3.802	7.142	3.582	1.0	49.41	240.4	4.163
Avg.	**0.250**	**3.991**	**7.190**	**4.419**	**1.0**	**45.24**	**241.8**	**4.544**

Stdev.	***0.020***	***0.327***	***0.202***	***0.686***	***0.0***	***5.109***	***6.424***	***0.334***
A4V	0.264	3.399	7.243	3.660	0.248	38.17	102.4	42.02
	0.240	3.017	6.044	3.961	0.261	39.26	94.19	45.83
	0.212	2.730	6.639	3.609	0.261	38.76	108.0	35.61
	0.258	4.434	10.43	1.292	0.269	24.40	65.40	7.532
	0.264	4.300	11.08	1.351	0.259	23.58	61.19	29.59
	0.271	4.489	10.58	3.084	0.261	23.48	62.64	6.666
	0.245	3.519	7.430	4.566	0.244	22.53	60.54	30.47
	0.187	2.939	7.601	3.953	0.243	22.73	61.09	31.40
	0.147	2.784	8.562	4.845	0.234	22.38	60.24	33.35
	0.277	4.807	11.25	1.667	0.268	22.20	58.60	4.422
	0.263	4.273	10.29	3.925	0.262	21.73	56.88	5.631
	0.258	4.204	10.28	1.676	0.263	21.75	57.87	5.102
	0.102	3.227	7.885	3.954	0.279	22.26	57.00	4.859
	0.236	3.443	7.987	4.704	0.272	22.36	59.08	5.266
	0.216	3.351	7.185	4.585	0.294	22.92	61.80	5.065
	0.208	3.435	9.099	5.966	0.251	23.11	60.24	33.65
	0.152	2.963	8.497	5.745	0.256	23.05	60.73	5.231
	0.203	3.263	9.623	1.637	0.240	22.12	59.80	6.988
	0.212	3.462	8.300	4.866	0.212	40.00	46.91	4.915
	0.223	3.561	8.698	4.868	0.384	25.70	54.33	6.238
	0.222	3.584	8.396	5.063	0.457	29.63	50.18	4.807
	0.234	3.554	7.700	4.856	0.570	59.04	54.46	4.556
	0.239	3.450	8.439	3.370	0.662	50.77	54.61	6.255
	0.248	51.40	6.992	4.164	0.528	47.26	54.93	4.240
Avg.	**0.224**	**5.566**	**8.593**	**3.807**	**0.312**	**29.55**	**63.46**	**15.40**
Stdev.	***0.043***	***9.779***	***1.452***	***1.376***	***0.119***	***10.88***	***15.38***	***14.70***
E100G	0.226	2.451	6.325	4.355	0.275	88.37	5.716	3.956
	0.232	2.536	6.406	3.829	0.379	97.29	5.127	3.857
	0.230	2.330	5.947	3.026	0.441	8.945	6.064	4.100
	0.243	2.715	5.622	3.495	0.765	101.7	5.730	3.192
	0.245	2.675	5.699	3.138	0.692	176.3	1066	3.951
	0.234	2.530	5.851	3.106	0.479	116.8	5.444	4.160
	0.240	2.825	7.392	2.429	0.405	114.5	5.576	4.047
	0.223	2.700	7.533	3.893	0.340	21.61	5.740	4.292
	0.200	2.595	7.111	4.664	0.376	50.16	5.884	4.469
Avg.	**0.230**	**2.595**	**6.432**	**3.548**	**0.461**	**86.19**	**123.5**	**4.003**
Stdev.	***0.014***	***0.151***	***0.739***	***0.706***	***0.163***	***52.04***	***353.4***	***0.357***
G37R	0.288	3.880	5.272	3.892	0.720	181.4	831.6	4.405
	0.282	3.638	5.088	3.153	0.736	189.1	488.0	3.173
	0.285	3.510	4.698	3.380	1.0	169.2	600.2	4.174
	0.454	271.7	4.019	3.068	1.0	118.2	497.9	3.895
	0.243	2.946	5.086	3.318	1.0	115.2	501.0	2.076
	0.250	2.980	6.184	4.185	1.0	120.9	660.6	3.080
Avg.	**0.300**	**48.10**	**5.058**	**3.499**	**0.909**	**149.0**	**596.6**	**3.467**
Stdev.	***0.078***	***109.5***	***0.711***	***0.442***	***0.141***	***34.49***	***134.2***	***0.864***
G85R	0.162	2.106	5.954	2.876	0.319	121.6	5.130	4.151
	0.230	2.835	5.970	3.926	0.204	5.954	6.408	4.267
	0.144	2.606	5.513	4.129	0.291	3.824	5.213	3.866
Avg.	**0.179**	**2.516**	**5.812**	**3.644**	**0.271**	**43.79**	**5.584**	**4.095**
Stdev.	***0.045***	***0.373***	***0.259***	***0.673***	***0.060***	***67.39***	***0.715***	***0.206***
G93A	0.215	2.893	8.418	2.800	0.467	187.2	6.049	1.775
	0.245	3.033	7.849	4.265	0.516	277.2	5.917	4.133
	0.226	3.087	7.834	4.390	0.469	391.0	678.3	4.367
	0.220	3.188	7.520	5.850	0.378	204.6	5.947	3.581

	0.240	3.309	6.950	4.722	0.479	306.8	5.968	3.390
	0.253	3.505	6.848	4.176	0.374	99.95	5.906	3.592
	0.305	4.794	7.864	4.804	0.581	11.95	5.938	4.369
	0.256	3.984	8.658	4.645	0.559	11.28	6.215	4.570
	0.265	3.974	7.131	3.527	0.558	11.21	6.145	4.604
	0.241	3.567	7.208	3.781	0.206	48.47	5.925	3.755
	0.237	3.730	7.766	4.592	0.555	504.4	6.052	4.411
	0.254	3.518	9.433	1.170	0.372	6.035	6.813	4.165
	0.252	4.388	8.604	4.976	0.600	13.02	155.2	4.063
	0.177	2.991	8.522	4.805	0.563	11.87	174.3	4.390
	0.177	2.993	8.394	4.279	0.545	11.40	6.536	4.402
	0.238	3.771	8.996	2.139	0.933	29.15	218.9	5.331
	0.265	3.995	7.965	3.792	0.943	29.80	235.3	5.508
	0.244	3.952	9.847	1.515	0.950	29.86	195.3	4.984
	0.155	1.782	5.180	4.865	1.0	135.0	502.1	4.035
	0.126	1.607	5.085	1.517	1.0	141.4	732.0	4.513
	0.107	1.561	5.270	4.054	1.0	119.8	643.6	4.062
Avg.	**0.224**	**3.315**	**7.683**	**3.841**	**0.621**	**122.9**	**171.8**	**4.190**
Stdev.	***0.049***	***0.851***	***1.300***	***1.286***	***0.245***	***142.5***	***248.9***	***0.766***
G93R	0.160	2.349	6.847	3.726	1.0	49.44	322.6	4.392
	0.159	2.379	6.415	4.068	1.0	43.14	256.6	4.643
	0.155	2.380	7.108	4.528	1.0	43.91	261.7	4.640
	0.210	2.730	6.581	3.309	0.783	20.32	181.5	5.224
	0.211	2.730	7.196	3.900	0.710	17.32	256.7	4.602
	0.195	2.621	7.500	1.774	0.610	20.47	170.5	4.730
	0.184	2.720	7.123	4.131	0.952	28.38	260.9	4.582
	0.235	3.044	6.314	4.302	0.978	29.8	257.9	4.619
	0.217	2.781	7.005	2.811	0.983	29.92	260.1	4.510
	0.311	5.046	7.158	4.683	0.579	27.62	50.63	2.548
	0.287	4.563	8.698	4.423	0.491	27.71	47.91	4.358
	0.304	4.922	8.430	3.920	0.419	23.43	50.59	3.735
	0.303	5.060	8.315	4.699	0.174	21.23	61.72	34.43
	0.275	4.607	8.628	5.552	0.194	22.23	63.47	31.05
	0.274	4.595	8.161	4.723	0.173	21.1	61.68	33.95
	0.239	5.241	7.820	3.719	0.240	20.18	51.52	22.48
	0.317	4.998	8.247	1.722	0.244	19.14	53.81	23.16
	0.287	4.410	8.589	5.484	0.238	18.32	50.13	11.12
Avg.	**0.240**	**3.732**	**7.563**	**3.971**	**0.598**	**26.87**	**151.1**	**11.60**
Stdev.	***0.056***	***1.155***	***0.806***	***1.053***	***0.334***	***9.509***	***104.2***	***11.58***
G93S	0.223	3.075	7.135	4.276	0.597	12.98	169.5	5.275
	0.266	3.939	8.133	3.513	0.597	13.00	164.8	2.251
	0.267	3.820	7.767	2.220	0.617	13.57	150.7	4.588
	0.234	3.148	6.376	4.711	0.239	124.3	6.439	5.130
	0.236	2.797	6.421	4.044	0.461	8.520	6.603	1.498
	0.207	2.574	6.981	4.630	0.500	9.658	6.643	4.536
Avg.	**0.239**	**3.226**	**7.136**	**3.899**	**0.502**	**30.34**	**84.11**	**3.880**
Stdev.	***0.024***	***0.548***	***0.708***	***0.930***	***0.143***	***46.08***	***85.18***	***1.598***
H43R	0.218	3.527	8.509	3.780	0.208	4.024	6.858	1.250
	0.210	3.452	8.629	4.568	0.246	3.031	6.388	4.354
	0.236	3.727	7.961	5.190	0.238	3.135	6.321	4.428
	0.263	4.582	8.303	4.564	0.508	529.2	5.259	3.509
	0.178	3.171	9.463	3.433	0.314	4.489	6.208	4.508
	0.201	3.354	9.280	5.306	0.284	12.80	5.948	4.544
	0.140	2.703	8.262	4.735	0.247	21.10	7.519	1.209
	0.158	2.754	8.513	3.259	0.325	4.869	7.336	6.267
	0.155	2.808	8.606	2.215	0.335	4.684	7.008	4.838

	0.272	4.257	8.542	4.146	0.516	10.13	6.655	3.699
	0.260	3.722	8.104	3.725	0.445	8.075	6.900	4.032
	0.284	4.510	9.064	3.627	0.461	8.592	7.280	2.187
Avg.	**0.215**	**3.547**	**8.603**	**4.046**	**0.344**	**51.18**	**6.640**	**3.735**
Stdev.	***0.049***	***0.650***	***0.457***	***0.885***	***0.110***	***150.6***	***0.651***	***1.503***
H46R	0.208	2.844	7.065	3.994	0.218	2.713	5.999	4.026
	0.208	2.667	6.463	3.600	0.227	3.244	6.010	3.998
	0.202	2.593	6.855	2.424	0.216	2.503	6.926	3.723
	0.158	1.712	5.053	3.171	0.206	2.478	5.636	3.524
	0.176	1.970	5.088	3.124	0.125	1.900	6.229	3.246
	0.179	2.088	5.363	3.131	0.184	2.195	6.517	2.219
	0.191	1.848	5.096	2.500	0.146	28.76	5.392	3.921
	0.161	1.791	4.968	3.069	0.213	2.647	6.368	3.395
	0.188	1.825	5.084	2.760	0.190	2.415	5.944	3.673
Avg.	**0.186**	**2.149**	**5.671**	**3.086**	**0.192**	**5.428**	**6.113**	**3.525**
Stdev.	***0.019***	***0.433***	***0.863***	***0.498***	***0.035***	***8.757***	***0.461***	***0.558***
H46R^{wt}	0.133	1.598	4.991	3.245	0.511	427.8	4.104	3.116
	0.175	1.766	5.269	1.722	0.299	90.06	3.965	3.246
	0.109	1.386	4.650	2.750	0.170	3.494	4.700	3.344
	0.218	2.459	5.154	3.428	0.438	130.0	4.504	3.121
	0.222	2.378	5.801	3.604	1.0	6197	4.150	4.113
	0.217	2.331	5.947	2.315	1.0	2345	824.0	3.932
	0.263	43.94	5.005	1.189	0.490	122.9	4.372	3.301
	0.299	11.38	4.541	3.361	0.230	90.15	4.173	3.321
	0.405	113.9	4.619	3.808	0.327	162.9	3.905	2.842
Avg.	**0.227**	**20.13**	**5.109**	**2.825**	**0.496**	**1063**	**95.32**	**3.371**
Stdev.	***0.089***	***37.77***	***0.501***	***0.905***	***0.307***	***2061***	***273.3***	***0.403***
V148G	0.272	3.780	6.998	4.654	0.484	366.2	504.6	3.655
	0.250	3.337	7.294	1.205	0.637	366.1	542.7	4.017
	0.237	3.138	6.969	4.215	0.814	380.6	678.7	4.008
	0.130	36.99	5.947	4.516	0.498	9.429	9.704	2.113
	0.434	7.644	6.459	4.583	0.443	11.79	6.209	4.565
	0.422	7.301	6.210	4.393	0.525	12.33	6.758	5.372
Avg.	**0.291**	**10.37**	**6.646**	**3.928**	**0.567**	**191.1**	**291.5**	**3.955**
Stdev.	***0.117***	***13.20***	***0.522***	***1.343***	***0.138***	***197.1***	***316.3***	***1.083***
V148I	0.221	2.050	4.493	2.734	0.656	14.31	4.876	3.840
	0.175	1.778	4.909	3.288	0.496	14.07	4.961	3.907
	0.210	1.936	4.662	3.053	0.378	51.49	5.269	4.331
	0.186	1.869	5.581	3.922	0.409	149.6	4.993	3.543
	0.146	1.690	5.425	3.347	0.308	29.22	5.252	3.346
	0.149	1.683	5.195	3.317	0.265	3.443	5.976	2.648
	0.136	1.856	5.667	3.661	0.443	264.5	5.017	3.881
	0.190	1.980	5.736	3.576	0.342	43.21	5.265	3.775
	0.190	1.973	5.689	3.520	0.938	282.4	5.000	3.859
Avg.	**0.178**	**1.868**	**5.262**	**3.380**	**0.471**	**94.69**	**5.179**	**3.681**
Stdev.	***0.029***	***0.130***	***0.472***	***0.348***	***0.210***	***110.2***	***0.333***	***0.471***

Bold and italicized values are the averages and standard deviations, respectively.

[a]PDI is obtained from the Cumulants method of fitting the autocorrelation function (Eq. 5.4). Values larger than 0.1 are indicative of polydispersity (i.e., the sample contains than one species in solution). High PDI values result in larger peak widths, and thus greater uncertainty in the sizes reported.

[b]Peak width reflects the uncertainty in the hydrodynamic diameter obtained from the intensity distribution and is related to the PDI according to Eq. 5.4.

[c]The sizes reported correspond to the main peak in the distributions.

Table S5.3 All DLS data for apoSH SOD1 variants at 5 mg mL^{-1}, pH 7.4, 37 °C.

	t = 0				t > 300			
ApoSH SOD1 variant	PDI[a]	PDI width (nm)[b]	Intensity Distribution Hydrodynamic Radius (nm)[c]	Number Distribution Hydrodynamic Radius (nm)[c]	PDI[a]	PDI width (nm)[b]	Intensity Distribution Hydrodynamic Radius (nm)[c]	Number Distribution Hydrodynamic Radius (nm)[c]
pWT	0.302	11.230	4.627	3.473	0.970	64.64	529.7	3.937
	0.403	6.299	4.575	3.278	1.000	53.88	1170	3.793
	0.383	5.826	4.657	3.270	0.807	76.64	421.5	3.804
Avg.	**0.363**	**7.785**	**4.620**	**3.340**	**0.926**	**65.05**	**707.1**	**3.845**
Stdev.	***0.053***	***2.993***	***0.041***	***0.115***	***0.104***	***11.39***	***404.5***	***0.080***
A4V	0.200	56.91	19.80	4.218	1.0	1314	770.3	11.38
	0.460	11.25	9.252	6.056	1.0	1924	401.6	55.03
	0.461	12.83	31.40	3.573	1.0	1800	372.8	41.60
Avg.	**0.374**	**27.00**	**20.15**	**4.616**	**1.0**	**1679**	**514.9**	**36.00**
Stdev.	***0.150***	***25.92***	***11.08***	***1.288***	***0.0***	***322.4***	***221.7***	***22.36***
G37R	0.397	7.685	9.205	5.039	0.233	22.31	62.22	26.67
	0.391	7.550	9.216	5.731	0.234	21.56	58.54	22.43
	0.423	8.394	9.335	5.181	0.258	22.91	59.43	23.58
Avg.	**0.404**	**7.876**	**9.252**	**5.317**	**0.242**	**22.26**	**60.06**	**24.23**
Stdev.	***0.017***	***0.453***	***0.072***	***0.365***	***0.014***	***0.676***	***1.920***	***2.190***
G93A	0.325	125.0	6.974	4.848	0.793	318.9	802.3	4.520
	0.355	29.75	7.069	4.869	1.000	228.4	1692	3.601
	0.283	31.59	7.046	5.166	1.000	308.1	1275	3.608
Avg.	**0.321**	**62.11**	**7.030**	**4.961**	**0.931**	**285.1**	**1256**	**3.910**
Stdev.	***0.036***	***54.47***	***0.050***	***0.178***	***0.120***	***49.43***	***445.1***	***0.529***
G93R	0.269	93.17	8.389	4.713	0.209	14.16	35.06	16.83
	0.296	11.56	8.939	6.126	0.206	14.00	36.10	16.11
	0.415	8.376	9.748	5.216	0.231	14.82	36.27	15.01
Avg.	**0.327**	**37.70**	**9.025**	**5.352**	**0.215**	**14.33**	**35.81**	**15.98**
Stdev.	***0.078***	***48.06***	***0.684***	***0.716***	***0.014***	***0.435***	***0.655***	***0.917***
G93S	0.777	34.99	507.6	4.765	0.758	37.94	337.6	5.767
	0.783	29.53	654.9	4.551	0.851	30.91	479.1	6.034
	0.857	51.77	485.7	2.615	0.891	27.64	379.0	5.191
Avg.	**0.806**	**38.76**	**549.4**	**3.977**	**0.833**	**32.16**	**398.6**	**5.664**
Stdev.	***0.045***	***11.59***	***92.02***	***1.184***	***0.068***	***5.263***	***72.75***	***0.431***
V148I	0.300	11.47	5.863	4.320	1.0	7548	4.446	4.349
Na_2SO_4	0.344	14.27	5.386	3.956	1.0	7038	4.268	4.050
	0.347	5.119	5.454	3.922	1.0	2067	5.608	4.736
Avg.	**0.330**	**10.29**	**5.568**	**4.066**	**1.0**	**5551**	**4.774**	**4.378**
Stdev.	***0.026***	***4.689***	***0.258***	***0.221***	***0.0***	***3028***	***0.728***	***0.344***

Bold and italicized values are the averages and standard deviations, respectively.

[a]PDI obtained from the Cumulants method of fitting the autocorrelation function (Eq. 5.4). Values larger than 0.1 are indicative of polydispersity (i.e., the sample contains than one species in solution). High PDI values result in larger peak widths, and thus greater uncertainty in the sizes reported.

[b]Peak width reflects the uncertainty in the hydrodynamic diameter obtained from the intensity distribution and is related to the PDI according to Eq. 5.4.

[c]The sizes reported correspond to the main peak in the distributions.

Table S5.4 All DLS data for apoSH SOD1 variants at 1 mg mL^{-1}, pH 7.4, 37 °C, 150 mM salt.

	t = 0				t > 300			
ApoSH SOD1 variant	PDI[a]	PDI width (nm)[b]	Intensity Distribution Hydrodynamic Radius (nm)[c]	Number Distribution Hydrodynamic Radius (nm)[c]	PDI[a]	PDI width (nm)[b]	Intensity Distribution Hydrodynamic Radius (nm)[c]	Number Distribution Hydrodynamic Radius (nm)[c]
pWT No Salt	0.154	1.761	5.094	3.314	0.215	2.768	5.084	3.256
	0.187	1.986	5.473	2.436	0.252	2.644	5.384	3.216
	0.206	2.117	5.445	3.345	0.176	1.911	4.875	3.182
	0.224	2.552	5.757	3.104	0.243	2.520	5.337	3.028
	0.223	2.310	5.517	3.503	0.237	2.452	5.566	3.478
	0.235	2.468	5.560	3.582	0.224	2.349	5.045	3.336
	0.170	1.777	5.144	3.082	0.315	7.762	4.875	3.122
	0.203	1.914	4.627	2.687	0.204	2.241	5.404	3.095
	0.219	2.148	5.169	3.045	0.219	2.458	5.626	3.930
	0.233	2.284	5.392	2.741	0.450	7.483	5.252	4.320
	0.203	2.210	5.565	3.737	0.404	6.354	5.290	3.583
	0.198	2.226	5.849	3.000	0.264	21.83	4.994	3.839
Avg.	**0.205**	**2.146**	**5.383**	**3.131**	**0.267**	**5.231**	**5.228**	**3.449**
Stdev.	***0.025***	***0.250***	***0.332***	***0.387***	***0.083***	***5.657***	***0.253***	***0.398***
pWT Na_2SO_4	0.224	2.099	4.773	2.196	0.270	152.8	4.615	2.678
	0.229	2.207	5.776	3.187	0.160	6.411	6.381	4.505
	0.266	2.284	5.237	3.066	0.278	24.91	5.656	2.694
Avg.	**0.240**	**2.197**	**5.262**	**2.816**	**0.236**	**61.37**	**5.551**	**3.292**
Stdev.	***0.023***	***0.093***	***0.502***	***0.541***	***0.066***	***79.72***	***0.888***	***1.050***
pWT NaCl	0.261	2.476	5.666	2.287	0.371	5.578	5.573	4.180
	0.225	2.434	5.880	2.623	0.473	376.0	5.329	2.950
	0.199	1.984	5.853	4.128	0.205	2.198	5.149	3.436
Avg.	**0.228**	**2.298**	**5.800**	**3.013**	**0.350**	**127.9**	**5.350**	**3.522**
Stdev.	***0.031***	***0.273***	***0.117***	***0.980***	***0.135***	***214.9***	***0.213***	***0.619***
A4V No Salt	0.264	3.399	7.243	3.660	0.248	38.17	102.4	42.02
	0.240	3.017	6.044	3.961	0.261	39.26	94.19	45.83
	0.212	2.730	6.639	3.609	0.261	38.76	108.0	35.61
	0.258	4.434	10.43	1.292	0.269	24.40	65.40	7.532
	0.264	4.300	11.08	1.351	0.259	23.58	61.19	29.59
	0.271	4.489	10.58	3.084	0.261	23.48	62.64	6.666
	0.245	3.519	7.430	4.566	0.244	22.53	60.54	30.47
	0.187	2.939	7.601	3.953	0.243	22.73	61.09	31.40
	0.147	2.784	8.562	4.845	0.234	22.38	60.24	33.35
	0.277	4.807	11.25	1.667	0.268	22.20	58.60	4.422
	0.263	4.273	10.29	3.925	0.262	21.73	56.88	5.631
	0.258	4.204	10.28	1.676	0.263	21.75	57.87	5.102
	0.102	3.227	7.885	3.954	0.279	22.26	57.00	4.859
	0.236	3.443	7.987	4.704	0.272	22.36	59.08	5.266
	0.216	3.351	7.185	4.585	0.294	22.92	61.80	5.065
	0.208	3.435	9.099	5.966	0.251	23.11	60.24	33.65
	0.152	2.963	8.497	5.745	0.256	23.05	60.73	5.231
	0.203	3.263	9.623	1.637	0.240	22.12	59.80	6.988
	0.212	3.462	8.300	4.866	0.212	40.00	46.91	4.915
	0.223	3.561	8.698	4.868	0.384	25.70	54.33	6.238
	0.222	3.584	8.396	5.063	0.457	29.63	50.18	4.807
	0.234	3.554	7.700	4.856	0.570	59.04	54.46	4.556
	0.239	3.450	8.439	3.370	0.662	50.77	54.61	6.255
	0.248	51.40	6.992	4.164	0.528	47.26	54.93	4.240

Avg.	**0.224**	**5.566**	**8.593**	**3.807**	**0.312**	**29.55**	**63.46**	**15.40**
Stdev.	***0.043***	***9.779***	***1.452***	***1.376***	***0.119***	***10.88***	***15.38***	***14.70***
A4V	0.277	4.878	9.349	5.038	0.224	36.96	101.6	47.79
Na_2SO_4	0.290	5.125	9.522	5.629	0.228	37.62	98.08	48.46
	0.292	5.094	10.69	1.241	0.227	36.95	92.27	49.11
	0.292	4.918	9.093	5.145	0.201	30.23	84.60	37.04
	0.238	3.855	9.677	1.346	0.219	31.28	86.95	33.01
	0.248	4.122	11.11	8.274	0.172	27.79	80.54	47.19
Avg.	**0.273**	**4.665**	**9.907**	**4.446**	**0.212**	**33.47**	**90.67**	**43.77**
Stdev.	***0.024***	***0.540***	***0.804***	***2.712***	***0.022***	***4.221***	***8.127***	***6.920***
A4V	0.264	4.480	9.663	4.254	0.198	31.51	83.28	44.61
NaCl	0.277	4.614	9.050	4.798	0.197	29.80	84.64	39.65
	0.284	4.676	8.921	4.760	0.206	30.01	83.55	39.82
	0.283	4.570	9.228	3.127	0.217	33.47	91.84	48.46
	0.256	4.105	9.795	1.298	0.221	32.72	89.83	42.56
	0.249	4.060	8.779	5.205	0.229	33.23	88.54	48.03
Avg.	**0.269**	**4.418**	**9.239**	**3.907**	**0.211**	**31.79**	**86.95**	**43.86**
Stdev.	***0.015***	***0.268***	***0.409***	***1.466***	***0.013***	***1.610***	***3.608***	***3.869***
E100G	0.226	2.451	6.325	4.355	0.275	88.37	5.716	3.956
No Salt	0.232	2.536	6.406	3.829	0.379	97.29	5.127	3.857
	0.230	2.330	5.947	3.026	0.441	8.945	6.064	4.100
	0.243	2.715	5.622	3.495	0.765	101.7	5.730	3.192
	0.245	2.675	5.699	3.138	0.692	176.3	1066	3.951
	0.234	2.530	5.851	3.106	0.479	116.8	5.444	4.160
	0.240	2.825	7.392	2.429	0.405	114.5	5.576	4.047
	0.223	2.700	7.533	3.893	0.340	21.61	5.740	4.292
	0.200	2.595	7.111	4.664	0.376	50.16	5.884	4.469
Avg.	**0.230**	**2.595**	**6.432**	**3.548**	**0.461**	**86.19**	**123.5**	**4.003**
Stdev.	***0.014***	***0.151***	***0.739***	***0.706***	***0.163***	***52.04***	***353.4***	***0.357***
E100G	0.263	3.597	7.812	5.145	0.377	203.9	6.550	5.907
Na_2SO_4	0.282	4.154	7.811	4.337	0.340	42.63	6.685	5.756
	0.257	4.060	8.637	4.787	0.454	71.00	6.463	5.801
Avg.	**0.267**	**3.937**	**8.087**	**4.756**	**0.390**	**105.8**	**6.566**	**5.821**
Stdev.	***0.013***	***0.298***	***0.477***	***0.405***	***0.058***	***86.10***	***0.112***	***0.078***
E100G	0.232	2.870	6.901	4.082	0.457	362.9	5.878	4.897
NaCl	0.240	2.943	7.529	2.505	0.424	48.71	5.661	1.914
	0.179	2.647	7.498	4.701	0.361	74.94	6.088	4.124
Avg.	**0.217**	**2.820**	**7.309**	**3.763**	**0.414**	**162.2**	**5.876**	**3.645**
Stdev.	***0.033***	***0.154***	***0.354***	***1.132***	***0.049***	***174.3***	***0.214***	***1.548***
G93R	0.160	2.349	6.847	3.726	1.0	49.44	322.6	4.392
No Salt	0.159	2.379	6.415	4.068	1.0	43.14	256.6	4.643
	0.155	2.380	7.108	4.528	1.0	43.91	261.7	4.640
	0.210	2.730	6.581	3.309	0.783	20.32	181.5	5.224
	0.211	2.730	7.196	3.900	0.710	17.32	256.7	4.602
	0.195	2.621	7.500	1.774	0.610	20.47	170.5	4.730
	0.184	2.720	7.123	4.131	0.952	28.38	260.9	4.582
	0.235	3.044	6.314	4.302	0.978	29.80	257.9	4.619
	0.217	2.781	7.005	2.811	0.983	29.92	260.1	4.510
	0.311	5.046	7.158	4.683	0.579	27.62	50.63	2.548
	0.287	4.563	8.698	4.423	0.491	27.71	47.91	4.358
	0.304	4.922	8.430	3.920	0.419	23.43	50.59	3.735
	0.303	5.060	8.315	4.699	0.174	21.23	61.72	34.43
	0.275	4.607	8.628	5.552	0.194	22.23	63.47	31.05
	0.274	4.595	8.161	4.723	0.173	21.10	61.68	33.95
	0.239	5.241	7.820	3.719	0.240	20.18	51.52	22.48

	0.317	4.998	8.247	1.722	0.244	19.14	53.81	23.16
	0.287	4.410	8.589	5.484	0.238	18.32	50.13	11.12
Avg.	**0.240**	**3.732**	**7.563**	**3.971**	**0.598**	**26.87**	**151.1**	**11.60**
Stdev.	***0.056***	***1.155***	***0.806***	***1.053***	***0.334***	***9.509***	***104.2***	***11.58***
G93R	0.265	4.592	10.36	4.525	0.185	29.25	82.94	47.32
Na_2SO_4	0.286	5.169	10.32	5.872	0.189	27.32	78.10	38.18
	0.311	5.837	11.32	1.460	0.214	28.02	79.34	29.25
	0.267	4.467	9.279	5.040	0.267	42.04	94.20	47.93
	0.248	4.026	10.09	5.363	0.245	37.15	95.44	45.46
	0.217	3.765	9.670	6.282	0.245	37.29	100.4	42.93
	0.197	94.09	8.081	3.874	0.267	45.57	127.6	33.01
	0.273	4.583	9.076	4.947	0.248	40.12	111.7	35.20
	0.247	4.033	9.594	2.150	0.236	39.01	100.9	44.35
Avg.	**0.257**	**14.51**	**9.754**	**4.390**	**0.233**	**36.20**	**96.74**	**40.40**
Stdev.	***0.035***	***29.85***	***0.920***	***1.633***	***0.030***	***6.532***	***16.03***	***6.737***
G93R	0.327	8.550	7.037	5.091	0.263	28.68	78.68	28.15
NaCl	0.240	4.128	9.990	4.400	0.256	28.10	71.46	34.31
	0.235	3.979	9.323	5.539	0.262	28.45	76.63	25.18
	0.257	4.651	11.05	1.792	0.236	35.86	97.46	41.29
	0.237	4.132	9.095	5.175	0.227	32.12	88.34	37.80
	0.227	3.893	9.637	3.786	0.225	31.49	85.88	43.63
Avg.	**0.254**	**4.889**	**9.355**	**4.297**	**0.245**	**30.78**	**83.08**	**35.06**
Stdev.	***0.037***	***1.813***	***1.326***	***1.378***	***0.018***	***3.004***	***9.362***	***7.290***
G93R[a]	0.322	206.3	6.924	4.618	0.387	62.38	132.5	58.88
NaCl	0.285	4.565	8.413	5.747	0.302	52.25	141.5	28.18
	0.247	4.245	9.441	4.539	0.322	53.94	152.7	15.50
Avg.	**0.285**	**71.70**	**8.259**	**4.968**	**0.337**	**56.19**	**142.2**	**34.19**
Stdev.	***0.038***	***116.6***	***1.266***	***0.676***	***0.044***	***5.427***	***10.12***	***22.31***
G93S	0.223	3.075	7.135	4.276	0.597	12.98	169.5	5.275
No Salt	0.266	3.939	8.133	3.513	0.597	13.00	164.8	2.251
	0.267	3.820	7.767	2.220	0.617	13.57	150.7	4.588
	0.234	3.148	6.376	4.711	0.239	124.3	6.439	5.130
	0.236	2.797	6.421	4.044	0.461	8.520	6.603	1.498
	0.207	2.574	6.981	4.630	0.500	9.658	6.643	4.536
Avg.	**0.239**	**3.226**	**7.136**	**3.899**	**0.502**	**30.34**	**84.11**	**3.880**
Stdev.	***0.024***	***0.548***	***0.708***	***0.930***	***0.143***	***46.08***	***85.18***	***1.598***
G93S	0.247	6.680	8.012	5.020	0.934	230.9	333.8	6.320
Na_2SO_4	0.213	3.217	8.234	4.780	0.468	219.9	348.1	1.830
	0.258	3.814	8.690	2.032	0.486	193.5	313.6	4.911
Avg.	**0.239**	**4.570**	**8.312**	**3.944**	**0.629**	**214.8**	**331.8**	**4.354**
Stdev.	***0.023***	***1.851***	***0.346***	***1.660***	***0.264***	***19.22***	***17.33***	***2.296***
G93S	0.292	178.6	5.553	4.096	0.823	1193	6.457	5.675
NaCl	0.222	3.088	7.129	3.654	0.745	833.2	6.314	5.063
	0.194	2.679	7.683	4.658	0.545	486.5	6.089	4.560
Avg.	**0.236**	**61.46**	**6.788**	**4.136**	**0.704**	**837.6**	**6.287**	**5.099**
Stdev.	***0.050***	***101.5***	***1.105***	***0.503***	***0.143***	***353.3***	***0.186***	***0.558***
H43R	0.218	3.527	8.509	3.780	0.208	4.024	6.858	1.250
No Salt	0.210	3.452	8.629	4.568	0.246	3.031	6.388	4.354
	0.236	3.727	7.961	5.190	0.238	3.135	6.321	4.428
	0.263	4.582	8.303	4.564	0.508	529.2	5.259	3.509
	0.178	3.171	9.463	3.433	0.314	4.489	6.208	4.508
	0.201	3.354	9.280	5.306	0.284	12.80	5.948	4.544
	0.140	2.703	8.262	4.735	0.247	21.10	7.519	1.209
	0.158	2.754	8.513	3.259	0.325	4.869	7.336	6.267
	0.155	2.808	8.606	2.215	0.335	4.684	7.008	4.838

	0.272	4.257	8.542	4.146	0.516	10.13	6.655	3.699
	0.260	3.722	8.104	3.725	0.445	8.075	6.900	4.032
	0.284	4.510	9.064	3.627	0.461	8.592	7.280	2.187
Avg.	**0.215**	**3.547**	**8.603**	**4.046**	**0.344**	**51.18**	**6.640**	**3.735**
Stdev.	***0.049***	***0.650***	***0.457***	***0.885***	***0.110***	***150.6***	***0.651***	***1.503***
H43R	0.252	3.956	8.543	4.350	1.0	2049	6.318	5.173
Na_2SO_4	0.243	3.633	10.57	1.590	0.843	467.0	6.818	5.462
	0.271	3.645	8.661	4.844	0.445	210.6	7.143	5.443
Avg.	**0.255**	**3.745**	**9.258**	**3.595**	**0.763**	**908.9**	**6.760**	**5.359**
Stdev.	***0.014***	***0.183***	***1.138***	***1.754***	***0.286***	***995.7***	***0.416***	***0.162***
H43R	0.235	3.214	8.741	4.856	0.263	27.99	6.411	4.809
NaCl	0.230	2.902	7.794	4.889	0.249	5.500	6.641	4.336
	0.234	2.837	7.778	4.230	0.253	4.668	6.760	1.235
Avg.	**0.233**	**2.984**	**8.104**	**4.658**	**0.255**	**12.72**	**6.604**	**3.460**
Stdev.	***0.003***	***0.202***	***0.551***	***0.371***	***0.007***	***13.23***	***0.177***	***1.941***
V148G	0.272	3.780	6.998	4.654	0.484	366.2	504.6	3.655
No Salt	0.250	3.337	7.294	1.205	0.637	366.1	542.7	4.017
	0.237	3.138	6.969	4.215	0.814	380.6	678.7	4.008
	0.130	36.99	5.947	4.516	0.498	9.429	9.704	2.113
	0.434	7.644	6.459	4.583	0.443	11.79	6.209	4.565
	0.422	7.301	6.210	4.393	0.525	12.33	6.758	5.372
Avg.	**0.291**	**10.37**	**6.646**	**3.928**	**0.567**	**191.1**	**291.5**	**3.955**
Stdev.	***0.117***	***13.20***	***0.522***	***1.343***	***0.138***	***197.1***	***316.3***	***1.083***
V148G	0.329	5.161	7.706	1.687	0.994	1685	169.5	6.013
Na_2SO_4	0.321	4.975	7.774	2.893	0.922	1849	162.2	5.794
	0.306	4.581	6.894	3.702	0.714	207.0	508.6	5.469
Avg.	**0.319**	**4.906**	**7.458**	**2.761**	**0.877**	**1247**	**280.1**	**5.759**
Stdev.	***0.012***	***0.296***	***0.490***	***1.014***	***0.145***	***904.4***	***197.9***	***0.274***
V148G	0.117	24.47	6.632	4.801	0.647	600.3	710.6	4.893
NaCl	0.299	4.377	6.233	4.087	0.791	329.4	784.1	3.881
	0.297	4.527	7.545	4.712	0.784	312.6	681.2	5.862
Avg.	**0.238**	**11.13**	**6.803**	**4.533**	**0.741**	**414.1**	**725.3**	**4.879**
Stdev.	***0.105***	***11.56***	***0.673***	***0.389***	***0.081***	***161.5***	***53.00***	***0.991***

Bold and italicized values are the averages and standard deviations, respectively. Salt free samples are the same as those shown in Table S5.2.

[a]PDI is obtained from the Cumulants method of fitting the autocorrelation function (Eq. 5.4). Values larger than 0.1 are indicative of polydispersity (i.e., the sample contains than one species in solution). High PDI values result in larger peak widths, and thus greater uncertainty in the sizes reported.

[b]Peak width reflects the uncertainty in the hydrodynamic diameter obtained from the intensity distribution and is related to the PDI according to Eq. 5.4.

[c]The sizes reported correspond to the main peak in the distributions.

Chapter 6

Summary and Future Work

The focus of this work has been on immature forms of SOD1, apoSS and apoSH, due to their diminished stability and ostensibly higher aggregation propensity relative to the fully mature holoSS form (99, 134, 144, 147, 174, 184, 193, 195, 198, 226, 376), and our results have uncovered important characteristics of immature SOD1 that may lead to misfolding of an otherwise extremely stable and compact protein (128).

6.1. Key findings from studies of apoSS dimer and monomer stabilities and implications of these findings for disease

A prevailing hypothesis in the field of ALS research has been that fALS-associated mutations destabilize the SOD1 dimer interface, leading to an increase in monomeric SOD1 that can nucleate aggregation (134, 143, 175, 193, 197–199). Until now however, this hypothesis was based on measurements of a few mutants made at lower than physiological temperature (176, 177, 200), as well as molecular dynamic simulations (175, 201, 202), and direct measurement of the effects of mutations at 37 °C had not been done. We have demonstrated here that ITC is a powerful, and to date underutilized, tool for characterizing the thermodynamics of protein association, and have clearly shown that the effects of numerous, structurally diverse, mutations propagate through the structure and weaken the dimer interface. Importantly, we find that apoSS dimer stability is significantly reduced, and potentially more easily perturbed, at physiological temperature (37 °C) compared to lower temperatures (134, 177, 193, 197). Furthermore, we have determined that apoSS dissociation is characterized by a high $\Delta C_{p,d}$; thus, the dissociation enthalpy is strongly temperature-dependent, and as a result, dissociation is increasingly favorable and measurable by ITC at higher temperature due to the increased heat of dissociation. This high $\Delta C_{p,d}$ points to a significant structural disruption in the monomer that

accompanies dimer dissociation, and this finding provides key information for understanding the mechanisms and energetics underlying normal maturation of SOD1, as well as toxic SOD1 misfolding pathways associated with disease. Our results indicate that dimerization may be a powerful deterrent of misfolding by structuring regions of the monomer that may otherwise form aberrant intermolecular interactions (90, 138).

A strategy for combating aggregation of SOD1 has long been sought, and attempts have been made to engineer chemical cross-links across the dimer interface or find small molecules capable of binding to and stabilizing the dimer interface (377–380). These strategies are analogous to the approach employed to combat aggregation of transthyretin (TTR), where mutations linked to familial amyloid polyneuropathy (FAP) induce conformational changes that promote dissociation of the native tetramer, leading to formation of partially folded monomers that can self-assemble into amyloid fibrils (215). Past attempts to design drugs to stabilize apoSS SOD1 have focused on stabilizing the dimer interface against dissociation by designing drugs to bind in the hydrophobic cavity within the interface created by Val 7, Gly 147, and Val 148 (380, 381), but there binding specificity for the dimer interface has been found to be low (378, 380), and their effectiveness at limiting aggregation has been controversial (378). Our results demonstrate that changes in local stability introduced by mutations have a ripple effect through apoSS, and these results may open up additional avenues for drug exploration. By the same principle, small molecules that stabilize one region of the protein may have an impact on the dimer interface and prevent dissociation. Given the high connectivity of the dimer interface and active site, small molecules able to bind to the active site with high specificity and mimic the effects of metal may result in stabilization of the entire dimeric structure.

By combining ITC measurements of dimer interface stability with DSC measurements of total stability, we have been able to distinguish the effects of mutations on the different components of total stability. With knowledge of the dimer interface and monomer stability values for different apoSS variants (Table 3.2), the fractions of N_2, M and U can be calculated as a function of temperature for a given protein concentration, which provides a powerful method for determining the state(s) likely to be populated under physiological conditions. We have found that mutations have differing effects on monomer stability, ranging from slightly stabilizing to significantly destabilizing, and this finding is important for elucidating mechanisms of mutant SOD1 aggregation and may be particularly helpful for designing strategies for stabilizing mutant SOD1.

6.2 Future studies on apoSS SOD1

Other members of the Meiering group have used NMR to gain information on the local stability and conformational flexibility of holoSS SOD1 variants. Colleen Doyle has used amide proton temperature coefficients to probe alternative conformations that are close in energy to the native state (Doyle, C. M. and Meiering E.M., unpublished data) (305). These experiments report on regions of the protein more likely to undergo conformational fluctuations, and performed at different temperatures provide a way to visualize the unfolding process. Dr. Jessica Rumfeldt has also performed amide exchange experiments to assess local dynamics of holoSS variants (Rumfeldt, J. A. O., and Meiering E.M., unpublished data) (382). These experiments on apoSS, would provide important information on the regions of the structure that may become disrupted when the protein dissociates. As reported in Chapter 2, we observe very different ΔH_d values for different apoSS variants, and this result may point to different degrees of local

unfolding that accompany dissociation in each case. Thus, probing the energy landscape using NMR techniques may provide an explanation for these differences. Given that apoSS monomers are thought to be highly prone to nucleating aggregation, such experiments would provide valuable information on the conformations of misfolded SOD1, which is highly relevant to unraveling the mechanism(s) of SOD1 aggregation (*vide infra*).

In addition, ITC could be used to gather information on the thermodynamics of metal binding to apoSS SOD1. Previous attempts to characterize metal binding using a variety of techniques were made difficult due to the presence of EDTA bound to the protein. We have now established an effective protocol for removing this bound EDTA by first unfolding the protein in GdmCl and then exchanging the protein out of GdmCl into metal and EDTA-free buffer. Data obtained from these experiments would provide important clues as to the maturation process of SOD1 in the cell and whether mutations affect this process. Banci and colleagues have established that zinc binding precedes and facilitates interaction with CCS (161); thus, mutations that disrupt zinc binding will also indirectly disrupt copper binding. While this proposal that metal binding is disrupted in mutant SOD1 is not new (283, 304), to the best of my knowledge, measurements of the thermodynamics of metal binding for a large number of SOD1 mutants have not been performed. It is possible however, that metal binding to apoSS may be too tight to be measured by ITC. If the equilibrium constant for association (K_a) is greater than 10^9, the binding curve will be too steep for accurate fitting of the data (383). For a given process to be measureable by ITC, *c*, defined according to Eq. 6.1 should be between 10 and 1000 (208, 383, 384),

$$c = K_a[P_{dimer}]n \qquad \text{(Eq. 6.1)}$$

where K_a is the association constant; P_{dimer} is the concentration of the protein in the reaction cell; and n is the stoichiometry of the reaction (385). Past kinetic folding experiments revealed that the k_d's of zinc binding to monomeric and dimeric apoSS pWT are 100 ± 122 pM and 22 ± 35 pM, respectively at 20 °C (145). ITC has been used to measure the energetics of zinc binding to apoSS WT SOD1 and found the k_d to be 100 nM at 25 °C, and the ΔC_p to be -0.67 kcal mol^{-1} °C, indicating substantial conformational changes upon metal binding (386). Given that mutations have been proposed to weaken metal binding, it may be possible to measure the thermodynamics of metal binding to mutant SOD1 by experimenting with different protein concentrations and temperatures. As mentioned in Chapter 2, large ΔC_p values lead to large changes in ΔH with temperature; given the magnitude and sign of ΔC_p, metal binding may be increasingly measureable at lower temperature for a number of mutants.

6.3 Key findings from studies of apoSH aggregation and implications of these findings for disease

Previous studies in the Meiering lab had also concentrated on characterizing the stability of various apoSH SOD1 variants (174); since 2010 the focus of further work on apoSH has been on characterizing the aggregation of apoSH *in vitro*, under experimental conditions that closely resemble physiological protein concentration, temperature, and pH (Chapter 4 and 5). We found that under these conditions (1 mg mL^{-1}, 37 °C, pH 7.4) that apoSH is remarkably resistant to aggregation, despite its marginal stability (Chapter 4). When incubated for ~300 hours at 1 mg mL^{-1}, pH 7.4, 37 °C, little change in light scattering intensity was observed for most apoSH variants with A4V, the most common North American fALS mutation with particularly short disease duration (7, 8), the exception (174). These results were very surprising given the

marginal stability of apoSH and the numerous studies suggesting that this form of the protein is the form that exhibits the greatest manifestation of mutation effects (76, 131, 147, 180, 184, 195). We therefore explored other conditions that we believed would encourage protein association, without significantly altering the levels of unfolded protein.

The differences in aggregation propensity between SOD1 variants were more pronounced at higher protein concentration (5 mg mL^{-1}). DLS measurements at t_0 suggest that intermolecular interactions are promoted for all mutants at increased protein concentration. Moreover, for the most aggregation-prone mutants $D_{h,I}$ and $D_{h,N}$ values at t_0 were higher at 5 mg mL^{-1} compared to 1 mg mL^{-1}, which may points to an increase in concentration of small oligomers**.** By AFM we were able to determine that the majority of particles detected were monomers and dimers, with low levels of oligomers also being observed. For some apoSH variants, pWT, G93A, G93S, and V148I, low levels of aggregation occur but monomers, dimers and small oligomers remained the dominant species in solution, as shown by the fairly consistent light scattering intensity, increases in the PDI, as well as increases in $D_{h,I}$ but not $D_{h,N}$, over the incubation period. AFM and ThT-binding experiments confirmed that long fibrils with increased β-structure were present in solution, but these species did not become highly abundant. For other mutants, A4V, G37R, and G93R, extensive aggregation was observed, as shown by the rapid increase in the light scattering intensity with little lag time, increases in both $D_{h,I}$ and $D_{h,N}$, as well as decreases in the PDI. Such aggregation behaviour is indicative of a low energy barrier between the unfolded, native, and aggregation-prone state(s) (53, 320). Interestingly these mutants with higher aggregation propensity appear unable to form long fibrils, which suggest that there are structural differences in the aggregates formed by the mutants that affect their abilities to grow.

Furthermore, these differences in aggregation propensity and aggregate morphology could not be accounted for based merely on protein stability differences.

We also found large differences in the aggregation propensity of apoSH mutants with the addition of Na_2SO_4 and NaCl to the samples. Light scattering measurements showed that pWT, E100G, H43R, and V148G remain fairly resistant to aggregation in Na_2SO_4 and NaCl. While the aggregation propensities of A4V, G93R, and G93S were influenced by the addition of salt, and in all three cases, the effects were most pronounced for samples containing Na_2SO_4. A4V and G93R in both Na_2SO_4 and NaCl and G93S in Na_2SO_4 aggregated with little detectable lag time suggesting a low energy barrier to aggregation, as described above. The $D_{h,I}$ values reported for all mutants were increased relative to pWT and the increases were most pronounced for A4V and G93R samples containing salt. Therefore, even prior to incubation at 37 °C, changes in $D_{h,I}$ reveal that Na_2SO_4, and to a lesser extent NaCl, promote intermolecular interactions and the effects are most obvious for A4V and G93R, which both consistently exhibit higher aggregation propensities under all conditions explored. As was observed for samples incubated at 5 mg mL^{-1}, mutants, such as A4V and G93R, that aggregated significantly in salt exhibited increases in both $D_{h,I}$ and $D_{h,N}$ and decreases in the PDI over the course of the incubation period. Again we see though that conditions suitable for promoting aggregation of some mutants, notably A4V, G93R, and to a lesser extent G93S, are not suitable for promoting aggregation of other mutants. The same increases in light scattering intensity, and both $D_{h,I}$ and $D_{h,N}$, as well as a decrease in PDI with incubation time were not observed for pWT, E100G, H43R, and V148G. By AFM as well, we see that Na_2SO_4 and NaCl promote the formation of longer and thicker fibrils in A4V, G93R, and G93S samples and for all three mutants, the largest aggregates (those with lengths longer than 200 nm) formed in salt exhibit aspect ratios greater than those formed at higher

protein concentration in salt free buffer. These results suggest that Na_2SO_4 and NaCl promote fibrillization of A4V, G93R, and G93S. It is interesting to note that G93S, which exhibited lower levels of aggregation in salt compared to A4V and G93R, formed the longest fibrils and exhibited the highest ThT fluorescence of all aggregates formed in salt, despite being less abundant. Images of G93R in Na_2SO_4 taken over the course of the aggregation experiment reveal that fibril elongation occurs up to the midpoint of the exponential growth phase at which point fibrils stop growing; thus, they never reach lengths observed for G93S suggestive of different aggregation pathways observed for the two mutants.

Taken together, light scattering, AFM, and ThT binding experiments reveal that Na_2SO_4 and NaCl promote aggregation of some, but not all, apoSH mutants. The effects of salt on the levels of apoSH aggregation correlate with the abilities of the different anions to stabilize and encourage protein association, according to the Hofmeister series (348–351). Estimates of fibril size reveal that they are longer in salt, but the distributions are too broad to distinguish differences between those formed in Na_2SO_4 and NaCl. Similar observations are evident for G93S, which formed even longer aggregates in both Na_2SO_4 and NaCl. Based on these results, and recent NMR experiments (301) it appears that point mutations have a large impact on the energy landscape of apoSH, and thus govern the type of aggregation behaviour observed, while different solution conditions may modulate the extent to which the protein proceeds down the aggregation pathway.

These findings are highly relevant to disease given that various mutant-SOD1 ALS mice models have shown that small, soluble, misfolded forms of apoSH SOD1 are enriched in the spinal cord and may be the common cytotoxic species that cause ALS (269, 270). Given that mutations have a large effect on the conformation and aggregation propensity of apoSH, these

differences may help elucidate the structural characteristics of different SOD1 variants to account for differing disease phenotypes. In ALS and a number of diseases such as Parkinson's, Alzheimer's, and Huntington's, neurodegeneration spreads through interconnected regions of the central nervous system (10, 15). Misfolded SOD1 is targeted for degradation via the ubiquitin pathway, and mutations in SOD1 may disrupt this process and in turn impair the proteasomal degradation pathway (27, 28). It has been shown that SOD1 can be excreted via a variety of distinct pathways (Chapter 1, section 1.1) and immunization targeting extracellular SOD1 has been found to increase the lifespan of transgenic mice expressing mutant SOD1 (45). Once transported to the extracellular environment, misfolded SOD1 conformers and/or SOD1 aggregates less than 0.4 μm in diameter (10, 40) can be taken up by neighbouring cells and seed aggregation of endogenous wildtype and mutant SOD1 (39). These processes have been found to be highly protein-specific and differences in the rate of cell to cell transfer of these aggregate seeds may underlie the rate of disease progression and partially account for the differences in pathology observed (40). Furthermore, labile SOD1 aggregates have been proposed to be more toxic due to their higher transmissibility (40). We have observed significant differences in both the aggregation propensity and morphological features of apoSH aggregates and these findings may be highly relevant to unraveling the complex mechanisms underlying ALS toxicity. A remaining challenge for ALS research lies in uncovering the initial event(s) that lead to disease and the toxic species, misfolded or oligomeric protein, responsible for disease onset. While it is likely that multiple forms of SOD1 are relevant to disease, the experiments presented here reveal how significantly the energy landscape of apoSH is altered by fALS-associated mutations such that particular aggregation pathways are either accessible or inaccessible depending on the mutation. Mutations may affect any number of processes including folding, proper interaction

with CCS (161), interaction with protein degradation machinery and/or components of secretory vesicles (27, 28, 44), rates of aggregation and properties of aggregates formed (Chapter 5), as well as aberrant interactions with cellular components such as the mitochondria (12, 387); thus studies aimed at uncovering the different properties of mutant SOD1 will be highly important for determining the initial events that begin the cascade of toxic events that culminate in disease.

6.4 Future studies on apoSH SOD1

Our approach thus far has been to consider a range of different experimental conditions in order to generate measurable levels of aggregation without significantly altering the conformation of apoSH, which is commonly done to accelerate the process (76, 78, 181, 188, 192). Now that suitable conditions for measuring aggregation have been established, numerous additional experiments to characterize the mechanisms of apoSH aggregation are possible. First of all, aggregation data for more apoSH mutants will be important for elucidating trends that can account for the complex aggregation behaviour observed. We have noted that apoSH stability cannot alone account for the complexity of aggregation behaviour. Likewise, the different mechanisms of apoSH aggregation cannot be explained by the structural contexts of the mutations; for example, G93A and G93R exhibit very different aggregation behaviour. As we highlighted in Chapter 2, it is important to account for both dimer and monomer stabilities to determine which states are likely formed in vivo. While apoSH is mainly monomeric, DLS, AFM, and NMR suggest very low levels of dimer formation. It is also interesting to note that A4V and G93R mutations, which render apoSH highly prone to aggregation under all conditions explored, also have large effects on the apoSS dimer interface stability (Chapter 2). Thus, these mutations may similarly reduce native apoSH dimerization, which may promote other aberrant

interactions. NMR experiments, such as those described in section 5.4.2, on additional mutants may provide important information on how mutations modulate the types of interactions between apoSH monomers and may shed light on the critical aberrant interactions that are required to support aggregation. By AFM we detect particles with volumes consistent with apoSH monomers, dimers and small oligomers during the initial, growth, and plateau phases in the aggregation mechanism, yet it is unclear whether dimerization is essential step in nucleation or protective against aggregation. Further characterization of the stability of apoSH under conditions shown to promote aggregation will also be important for determining the apoSH states important for aggregation.

Our experiments also reveal that different apoSH aggregates exhibit differences in secondary structure. Further ThT fluorescence experiments performed on early and late-stage aggregates may point to important structural changes that facilitate a particular type of aggregation versus another. Additional dyes such as 8-anilinonaphthalene-1-sulfonic acid (ANS), which exhibits an increase in fluorescence in the presence of hydrophobic residues (388), may also provide valuable information on the different structural features of apoSH aggregates. Protease digestion experiments can also be used to assess whether the cores of morphologically different aggregates are formed by different regions of the SOD1 structure, as was observed for agitation-induced aggregation of apoSH SOD1 (181).

Another important avenue to explore is how the aggregates formed *in vitro* relate to those formed *in vivo*. Many different antibodies have been developed to recognize particular specific features of misfolded SOD1 (12). These antibodies have been extremely useful for detecting misfolded SOD1 in aggregates isolated from ALS patients, but given the wide range of epitopes that are recognized by different antibodies they have also generated controversy regarding the

role of SOD1 in sALS (22, 33, 199, 389). We now have a better appreciation for the effects of mutations on the conformation of SOD1, in particular on the metal free forms of the protein. In collaboration with Dr. Christine Vande Velde, antibody binding experiments on holoSS, apoSS, non-aggregated apoSH, and aggregated apoSH will provide valuable insights into the different structural features recognized and determine why particular antibodies recognize SOD1 in sALS aggregates while others do not. Other preliminary experiments with the Vande Velde group have shown that mutant non-aggregated and aggregated apoSH bind to the mitochondria isolated from the cerebral cord and/or liver of rodents (Fig. 6.1). Mitochondria have been considered a target of misfolded and aggregated SOD1 toxicity (12). Currently, these experiments have only been performed using a polyclonal SOD1 antibody that recognizes unfolded SOD1, but such experiments with different antibodies that recognize diverse structural features will be important for assessing the form(s) of SOD1 involved in toxicity. Thus, using the knowledge gained from *in vitro* biophysical experiments on the folding and aggregation mechanism of various forms of SOD1, to design *in vivo* experiments with the specific aim of elucidating the role of different forms of SOD1 in disease will provide a powerful approach for unraveling the complex mechanisms that initiate toxicity and inevitably contribute to disease.

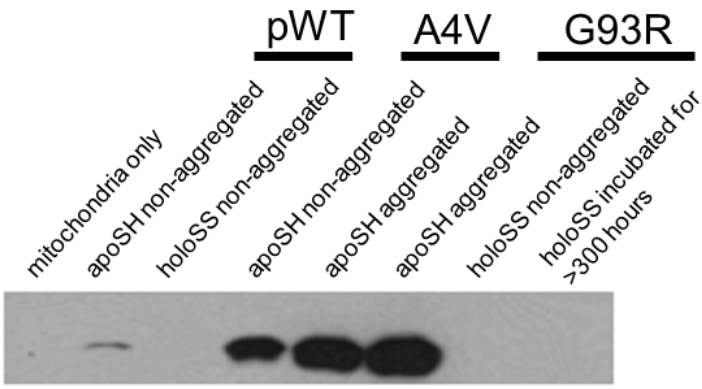

Figure 6.1 Mutant apoSH binds to rat mitochondria. The affinity of different forms of SOD1 for the mitochondria surface was assessed using western blots. In these experiments, mitochondria are isolated from the spinal cords or liver of experimental rats. Different SOD1 samples are then incubated with the mitochondria at 37 °C for 20 minutes. The samples are then centrifuged to remove the excess protein and then a west blot is run. For these experiments, SOD1 was probed using a polyclonal antibody that recognizes unfolded SOD1 (Cell Signalling Technology, New England Biolabs Ltd.). These experiments indicate that mutant apoSH binds to the mitochondria, apoSH pWT is only detected at very low levels, and metal bound SOD1 is not detected at all. It is important to note that the Cell Signalling SOD1 polyclonal antibody may not recognize more folded forms of the protein; thus, identical experiments using different antibodies capable of recognizing folded SOD1 are required to confirm that mutant apoSH SOD1 is uniquely capable of becoming localized to the mitochondria.

References

1. Broom H et al. (2011) *Amyotrophic Lateral Sclerosis.* ed Maurer MH (InTech).

2. Broom HR, Rumfeldt JAO, Meiering EM (2014) Many roads lead to Rome? Multiple modes of Cu,Zn superoxide dismutase destabilization, misfolding and aggregation in amyotrophic lateral sclerosis. *Essays Biochem* 56:149–65.

3. Robberecht W, Philips T (2013) The changing scene of amyotrophic lateral sclerosis. *Nat Rev Neurosci* 14:248–64.

4. Wijesekera LC, Leigh PN (2009) Amyotrophic lateral sclerosis. *Orphanet J Rare Dis* 4:3.

5. Mulder DW, Kurland LT, Offord KP, Beard CM (1986) Familial adult motor neuron disease: amyotrophic lateral sclerosis. *Neurology* 36:511–17.

6. Bruijn LI, Miller TM, Cleveland DW (2004) Unraveling the mechanisms involved in motor neuron degeneration in ALS. *Annu Rev Neurosci* 27:723–49.

7. Deng AH et al. (1993) Amyotrophic Lateral Defects in Cu , Zn Superoxide Dismutase. 261:1047–1051.

8. Rosen DR et al. (1993) Mutations in Cu/Zn superoxide dismutase gene are associated with familial amyotrophic lateral sclerosis. *Lett to Nat* 362:59–62.

9. Ling SC, Polymenidou M, Cleveland DW (2013) Converging mechanisms in ALS and FTD: disrupted RNA and protein homeostasis. *Neuron* 79:416–38.

10. Münch C, Bertolotti A (2012) Propagation of the prion phenomenon: beyond the seeding principle. *J Mol Biol* 421:491–8.

11. Atkin JD et al. (2014) Mutant SOD1 inhibits ER-Golgi transport in amyotrophic lateral sclerosis. *J Neurochem* 129:190–204.

12. Pickles S, Vande Velde C (2012) Misfolded SOD1 and ALS: zeroing in on mitochondria. *Amyotroph Lateral Scler* 13:333–40.

13. Régal L et al. (2014) The G93C Mutation in Superoxide Dismutase 1. *Arch Neurol* 63:1–7.

14. Polymenidou M, Cleveland DW (2011) The seeds of neurodegeneration: prion-like spreading in ALS. *Cell* 147:498–508.

15. Renner M, Melki R (2014) Protein aggregation and prionopathies. *Pathol Biol (Paris)*:1–7.

16. Manzerra P, Brown IR (1996) The neuronal stress response: nuclear translocation of heat shock proteins as an indicator of hyperthermic stress. *Exp Cell Res* 229:35–47.

17. Shinder GA, Lacourse MC, Minotti S, Durham HD (2001) Mutant Cu/Zn-superoxide dismutase proteins have altered solubility and interact with heat shock/stress proteins in models of amyotrophic lateral sclerosis. *J Biol Chem* 276:12791–6.

18. Keller BA et al. (2012) Co-aggregation of RNA binding proteins in ALS spinal motor neurons: evidence of a common pathogenic mechanism. *Acta Neuropathol* 124:733–47.

19. Bosco DA et al. (2010) Wild-type and mutant SOD1 share an aberrant conformation and a common pathogenic pathway in ALS. *Nat Neurosci* 13:1396–403.

20. Cozzolino M, Ferri A, Carrì MT (2008) Amyotrophic lateral sclerosis: from current developments in the laboratory to clinical implications. *Antioxid Redox Signal* 10:405–43.

21. Strong MJ, Kesavapany S, Pant HC (2005) The pathobiology of amyotrophic lateral sclerosis: a proteinopathy? *J Neuropathol Exp Neurol* 64:649–64.

22. Kerman A et al. (2010) Amyotrophic lateral sclerosis is a non-amyloid disease in which extensive misfolding of SOD1 is unique to the familial form. *Acta Neuropathol* 119:335–44.

23. Eisenberg D, Jucker M (2012) The amyloid state of proteins in human diseases. *Cell* 148:1188–203.

24. Aguzzi A, Rajendran L (2009) The transcellular spread of cytosolic amyloids, prions, and prionoids. *Neuron* 64:783–90.

25. Soto C (2011) Prion hypothesis: the end of the controversy? *Trends Biochem Sci* 36:151–8.

26. Kato S et al. (2000) New consensus research on neuropathological aspects of familial amyotrophic lateral sclerosis with superoxide dismutase 1 (SOD1) gene mutations: inclusions containing SOD1 in neurons and astrocytes. *Amyotroph Lateral Scler* 1:163–84.

27. Basso M et al. (2006) Insoluble mutant SOD1 is partly oligoubiquitinated in amyotrophic lateral sclerosis mice. *J Biol Chem* 281:33325–35.

28. Bendotti C et al. (2012) Dysfunction of constitutive and inducible ubiquitin-proteasome system in amyotrophic lateral sclerosis: implication for protein aggregation and immune response. *Prog Neurobiol* 97:101–26.

29. Okamoto Y et al. (2011) Colocalization of 14-3-3 proteins with SOD1 in Lewy body-like hyaline inclusions in familial amyotrophic lateral sclerosis cases and the animal model. *PLoS One* 6:e20427.

30. Murayama S et al. Immunocytochemical and ultrastructural study of Lewy body-like hyaline inclusions in familial amyotrophic lateral sclerosis.

31. Mizusawa H et al. (1989) Focal accumulation of phosphorylated neurofilaments within anterior horn cell in familial amyotrophic lateral sclerosis. *Acta Neuropathol* 79:37–43.

32. Casareno RLB, Waggoner D, Gitlin JD (1998) The Copper Chaperone CCS Directly Interacts with Copper/Zinc Superoxide Dismutase. *J Mol Biol*.

33. Rotunno MS, Bosco DA (2013) An emerging role for misfolded wild-type SOD1 in sporadic ALS pathogenesis. *Front Cell Neurosci* 7:253.

34. Beckman JS, Estévez AG, Crow JP, Barbeito L (2001) Superoxide dismutase and the death of motoneurons in ALS. *Trends Neurosci* 24:S15–20.

35. Mulligan VK et al. (2012) Early steps in oxidation-induced SOD1 misfolding: implications for non-amyloid protein aggregation in familial ALS. *J Mol Biol* 421:631–52.

36. Ogawa M, Furukawa Y (2014) A seeded propagation of Cu, Zn-superoxide dismutase aggregates in amyotrophic lateral sclerosis. *Front Cell Neurosci* 8:83.

37. Soto C (2012) Transmissible proteins: expanding the prion heresy. *Cell* 149:968–77.

38. Chia R et al. (2010) Superoxide dismutase 1 and tgSOD1 mouse spinal cord seed fibrils, suggesting a propagative cell death mechanism in amyotrophic lateral sclerosis. *PLoS One* 5:e10627.

39. Grad LI et al. (2011) Intermolecular transmission of superoxide dismutase 1 misfolding in living cells. *Proc Natl Acad Sci U S A* 108:16398–403.

40. Münch C, O'Brien J, Bertolotti A (2011) Prion-like propagation of mutant superoxide dismutase-1 misfolding in neuronal cells. *Proc Natl Acad Sci U S A* 108:3548–53.

41. Chang LY, Slot JW, Geuze HJ, Crapo JD (1988) Molecular immunocytochemistry of the CuZn superoxide dismutase in rat hepatocytes. *J Cell Biol* 107:2169–79.

42. Jacobsson J, Jonsson PA, Andersen PM, Forsgren L, Marklund SL (2001) Superoxide dismutase in CSF from amyotrophic lateral sclerosis patients with and without CuZn-superoxide dismutase mutations. *Brain* 124:1461–6.

43. Zetterström P, Andersen PM, Brännström T, Marklund SL (2011) Misfolded superoxide dismutase-1 in CSF from amyotrophic lateral sclerosis patients. *J Neurochem* 117:91–9.

44. Urushitani M et al. (2006) Chromogranin-mediated secretion of mutant superoxide dismutase proteins linked to amyotrophic lateral sclerosis. *Nat Neurosci* 9:108–18.

45. Urushitani M, Ezzi SA, Julien J-P (2007) Therapeutic effects of immunization with mutant superoxide dismutase in mice models of amyotrophic lateral sclerosis. *Proc Natl Acad Sci U S A* 104:2495–500.

46. Anfinsen CB, Haber E, Sela M, White FH (1961) The kinetics of formation of native ribonuclease during oxidation of the reduced polypeptide chain. *Proc Natl Acad Sci U S A* 47:1309–14.

47. Dobson CM (2004) Principles of protein folding, misfolding and aggregation. *Semin Cell Dev Biol* 15:3–16.

48. Dinner AR, Sali A, Smith LJ, Dobson CM, Karplus M (2000) Understanding protein folding via free-energy surfaces from theory and experiment. *Trends Biochem Sci* 25:331–9.

49. Guo Z, Thirumalai D (1995) Kinetics of Protein Folding : Nucleation Mechanism , Time. *Biopolymers* 36:83–102.

50. Matthews CR (1993) Pathways of Protein Folding. *Annu Rev Biochem* 62:653–83.

51. Karpel RL (2014) The illusive search for the lowest free energy state of globular proteins and RNAs. *DNA Repair (Amst)*.

52. Chiti F, Dobson CM (2006) Protein misfolding, functional amyloid, and human disease. *Annu Rev Biochem* 75:333–66.

53. Chiti F, Dobson CM (2009) Amyloid formation by globular proteins under native conditions. *Nat Chem Biol* 5:15–22.

54. Nick Pace C, Scholtz JM, Grimsley GR (2014) Forces stabilizing proteins. *FEBS Lett*.

55. Kauzmann W (1959) Some factors in the interpretation of protein denaturation. *Adv Protein Chem* 14:1–63.

56. Davis JG, Gierszal KP, Wang P, Ben-Amotz D (2012) Water structural transformation at molecular hydrophobic interfaces. *Nature* 491:582–5.

57. Sun T, Lin FH, Campbell RL, Allingham JS, Davies PL (2014) An antifreeze protein folds with an interior network of more than 400 semi-clathrate waters. *Science* 343:795–8.

58. Gomez J, Hilser VJ, Xie D, Freire E (1995) The Heat Capacity of Proteins. 412:404–412.

59. Bhattacharyya S, Varadarajan R (2013) Packing in molten globules and native states. *Curr Opin Struct Biol* 23:11–21.

60. Ben-Amotz D, Underwood R (2008) Unraveling water's entropic mysteries: a unified view of nonpolar, polar, and ionic hydration. *Acc Chem Res* 41:957–67.

61. Becktel WJ, Schellman JA (1987) Protein Stability Curves. *Biopolymers* 26:1859–1987.

62. Nelson R, Eisenberg D (2006) Structural models of amyloid-like fibrils. *Adv Protein Chem* 73:235–82.

63. Hwang YM (2010) Aggregation of Amyotrophic Lateral Sclerosis-Associated Cu / Zn Superoxide Dismutase.

64. Bennett MJ, Sawaya MR, Eisenberg D (2006) Deposition diseases and 3D domain swapping. *Structure* 14:811–24.

65. Proteins H et al. (2003) Relative Influence of Hydrophobicity and Net Charge in the Aggregation of Two. 15078–15083.

66. Jahn TR, Radford SE (2005) The Yin and Yang of protein folding. *FEBS J* 272:5962–70.

67. Tartaglia GG et al. (2008) Prediction of aggregation-prone regions in structured proteins. *J Mol Biol* 380:425–36.

68. Mahler H, Friess W, Grauschopf U, Kiese S (2009) Protein Aggregation : Pathways , Induction Factors and Analysis. 98:2909–2934.

69. Chi EY, Krishnan S, Randolph TW, Carpenter JF (2003) Physical stability of proteins in aqueous solution: mechanism and driving forces in nonnative protein aggregation. *Pharm Res* 20:1325–36.

70. Goers J, Permyakov SE, Permyakov EA, Uversky VN, Fink AL (2002) Conformational prerequisites for alpha-lactalbumin fibrillation. *Biochemistry* 41:12546–51.

71. Vetri V, Militello V (2005) Thermal induced conformational changes involved in the aggregation pathways of beta-lactoglobulin. *Biophys Chem* 113:83–91.

72. Necula M et al. (2007) Methylene blue inhibits amyloid Abeta oligomerization by promoting fibrillization. *Biochemistry* 46:8850–60.

73. Munishkina LA, Cooper EM, Uversky VN, Fink AL (2004) The effect of macromolecular crowding on protein aggregation and amyloid fibril formation. *J Mol Recognit* 17:456–64.

74. Sicorello A et al. (2009) Agitation and high ionic strength induce amyloidogenesis of a folded PDZ domain in native conditions. *Biophys J* 96:2289–98.

75. Stathopulos PB et al. (2004) Sonication of proteins causes formation of aggregates that resemble amyloid. *Protein Sci* 13:3017–3027.

76. Chattopadhyay M et al. (2008) Initiation and elongation in fibrillation of ALS-linked superoxide dismutase. *Proc Natl Acad Sci U S A* 105:18663–8.

77. Durazo A et al. (2009) Metal-free Superoxide Dismutase-1 and Three Different Amyotrophic Lateral Sclerosis Variants Share a Similar Partially Unfolded β-Barrel at Physiological Temperature. *J Biol Chem* 284:34382–34389.

78. Oztug Durer Z et al. (2009) Loss of metal ions, disulfide reduction and mutations related to familial ALS promote formation of amyloid-like aggregates from superoxide dismutase. *PLoS One* 4:e5004.

79. Vassall KA (2009) Folding and Stability Studies on Amyotrophic Lateral Sclerosis-Associated Cu , Zn apo Superoxide dismutases.

80. Eisenberg D et al. (2006) The structural biology of protein aggregation diseases: Fundamental questions and some answers. *Acc Chem Res* 39:568–75.

81. Sipe JD, Cohen AS (2000) Review: history of the amyloid fibril. *J Struct Biol* 130:88–98.

82. Tycko R, Wickner RB (2013) Molecular structures of amyloid and prion fibrils: consensus versus controversy. *Acc Chem Res* 46:1487–96.

83. Liu C, Sawaya MR, Eisenberg D (2011) β_2-microglobulin forms three-dimensional domain-swapped amyloid fibrils with disulfide linkages. *Nat Struct Mol Biol* 18:49–55.

84. Liu C et al. (2012) Out-of-register -sheets suggest a pathway to toxic amyloid aggregates. *Proc Natl Acad Sci*.

85. Qiang W, Kelley K, Tycko R (2013) Polymorph-specific kinetics and thermodynamics of β-amyloid fibril growth. *J Am Chem Soc* 135:6860–71.

86. Trinh CH, Smith DP, Kalverda AP, Phillips SE V, Radford SE (2002) Crystal structure of monomeric human beta-2-microglobulin reveals clues to its amyloidogenic properties. *Proc Natl Acad Sci U S A* 99:9771–6.

87. Rochet JC, Lansbury PT (2000) Amyloid fibrillogenesis: themes and variations. *Curr Opin Struct Biol* 10:60–8.

88. Sambashivan S, Liu Y, Sawaya MR, Gingery M, Eisenberg D (2005) Amyloid-like fibrils of ribonuclease A with three-dimensional domain-swapped and native-like structure. *Nature* 437:266–9.

89. Nelson R, Eisenberg D (2006) Recent atomic models of amyloid fibril structure. *Curr Opin Struct Biol* 16:260–5.

90. Elam JS et al. (2003) Amyloid-like filaments and water-filled nanotubes formed by SOD1 mutant proteins linked to familial ALS. *Nat Struct Biol* 10:461–7.

91. Kallberg Y, Gustafsson M, Persson B, Thyberg J, Johansson J (2001) Prediction of amyloid fibril-forming proteins. *J Biol Chem* 276:12945–50.

92. Morris AM, Watzky MA, Finke RG (2009) Protein aggregation kinetics, mechanism, and curve-fitting: a review of the literature. *Biochim Biophys Acta* 1794:375–97.

93. Nelson R et al. (2005) Structure of the cross-beta spine of amyloid-like fibrils. *Nature* 435:773–8.

94. Uversky VN (2010) Mysterious oligomerization of the amyloidogenic proteins. *FEBS J* 277:2940–53.

95. Eichner T, Radford SE (2011) A diversity of assembly mechanisms of a generic amyloid fold. *Mol Cell* 43:8–18.

96. Lee YJ, Savtchenko R, Ostapchenko VG, Makarava N, Baskakov I V (2011) Molecular structure of amyloid fibrils controls the relationship between fibrillar size and toxicity. *PLoS One* 6:e20244.

97. Tanaka M, Chien P, Naber N, Cooke R, Weissman JS (2004) Conformational variations in an infectious protein determine prion strain differences. *Nature* 428:323–8.

98. Vassall KA et al. (2011) Decreased stability and increased formation of soluble aggregates by immature superoxide dismutase do not account for disease severity in ALS. *Proc Natl Acad Sci U S A* 108:2210–5.

99. Hwang YM et al. (2010) Nonamyloid aggregates arising from mature copper/zinc superoxide dismutases resemble those observed in amyotrophic lateral sclerosis. *J Biol Chem* 285:41701–11.

100. Lomas DA (2013) Twenty Years of Polymers : A Personal Perspective on Alpha-1 Antitrypsin Defi ciency. 10:17–25.

101. Carrell RW, Gooptu B (1998) Conformational changes and disease--serpins, prions and Alzheimer's. *Curr Opin Struct Biol* 8:799–809.

102. Turner MS, Briehl RW, Ferrone FA, Josephs R (2003) Twisted protein aggregates and disease: the stability of sickle hemoglobin fibers. *Phys Rev Lett* 90:128103.

103. Ferrone FA (2004) Polymerization and sickle cell disease: a molecular view. *Microcirculation* 11:115–28.

104. Truscott RJW (2005) Age-related nuclear cataract-oxidation is the key. *Exp Eye Res* 80:709–25.

105. Lindner RA, Kapur A, Carver JA (1997) The interaction of the molecular chaperone, alpha-crystallin, with molten globule states of bovine alpha-lactalbumin. *J Biol Chem* 272:27722–9.

106. Truscott RJW (2003) Human cataract: the mechanisms responsible; light and butterfly eyes. *Int J Biochem Cell Biol* 35:1500–4.

107. Wang Y, Ferrone FA (2013) Dissecting the energies that stabilize sickle hemoglobin polymers. *Biophys J* 105:2149–56.

108. Uzunova V V (2010) Free Heme and the Polymerization of Sickle Cell Hemoglobin. *Biophys J* 99:1976 – 1985.

109. Ingram VM (1956) A specific chemical difference between the globins of normal human and sickle-cell anaemia haemoglobin. *Nature* 178:792–4.

110. Vekilov PG (2007) Sickle-cell haemoglobin polymerization: is it the primary pathogenic event of sickle-cell anaemia? *Br J Haematol* 139:173–84.

111. Dykes G, Crepeau RH, Edelstein SJ (1978) Three-dimensional reconstruction of the fibres of sickle cell haemoglobin. *Nature* 272:506–10.

112. Carragher B, Bluemke DA, Gabriel B, Potel MJ, Josephs R (1988) Structural analysis of polymers of sickle cell hemoglobin. I. Sickle hemoglobin fibers. *J Mol Biol* 199:315–31.

113. Knaupp AS, Bottomley SP (2009) Serpin polymerization and its role in disease--the molecular basis of alpha1-antitrypsin deficiency. *IUBMB Life* 61:1–5.

114. Whisstock JC, Bottomley SP (2006) Molecular gymnastics: serpin structure, folding and misfolding. *Curr Opin Struct Biol* 16:761–8.

115. Roussel BD et al. (2011) Unravelling the twists and turns of the serpinopathies. *FEBS J* 278:3859–67.

116. Ioachimescu OC, Stoller JK (2005) A review of alpha-1 antitrypsin deficiency. *COPD* 2:263–75.

117. Ekeowa UI et al. (2010) Defining the mechanism of polymerization in the serpinopathies. *Proc Natl Acad Sci U S A* 107:17146–51.

118. Krebs MRH, Domike KR, Donald AM (2009) Protein aggregation: more than just fibrils. *Biochem Soc Trans* 37:682–6.

119. Krebs MRH, Devlin GL, Donald AM (2007) Protein particulates: another generic form of protein aggregation? *Biophys J* 92:1336–42.

120. Langton M, Hermansson A (1992) Fine-Stranded and Particulate Gels of Beta-Lactoglobulin and Whey-Protein at Varying pH. *Food Hydrocoll* 5:523–539.

121. Moreau KL, King JA (2012) Protein misfolding and aggregation in cataract disease and prospects for prevention. *Trends Mol Med* 18:273–82.

122. Truscott RJ, Augusteyn RC (1977) The state of sulphydryl groups in normal and cataractous human lenses. *Exp Eye Res* 25:139–48.

123. Linetsky M, Hill JMW, LeGrand RD, Hu F (2004) Dehydroalanine crosslinks in human lens. *Exp Eye Res* 79:499–512.

124. Moran SD, Zhang TO, Decatur SM, Zanni MT (2013) Amyloid fiber formation in human γD-Crystallin induced by UV-B photodamage. *Biochemistry* 52:6169–81.

125. Stranks SD et al. (2009) Model for amorphous aggregation processes. *Phys Rev E Stat Nonlin Soft Matter Phys* 80:051907.

126. Valentine JS, Doucette PA, Potter SZ (2005) Copper-zinc superoxide dismutase and amyotrophic lateral sclerosis. *Annu Rev Biochem* 74:563–93.

127. Zelko IN, Mariani TJ, Folz RJ (2002) Superoxide dismutase multigene family: a comparison of the CuZn-SOD (SOD1), Mn-SOD (SOD2), and EC-SOD (SOD3) gene structures, evolution, and expression. *Free Radic Biol Med* 33:337–49.

128. Stathopulos PB et al. (2006) Calorimetric analysis of thermodynamic stability and aggregation for apo and holo amyotrophic lateral sclerosis-associated Gly-93 mutants of superoxide dismutase. *J Biol Chem* 281:6184–93.

129. Lyons TJ, Gralla EB, Valentine JS (1999) Biological chemistry of copper-zinc superoxide dismutase and its link to amyotrophic lateral sclerosis. *Met Ions Biol Syst* 36:125–77.

130. Parge HE, Hallewell RA, Tainer JA (1992) Atomic structures of wild-type and thermostable mutant recombinant human Cu,Zn superoxide dismutase. *Proc Natl Acad Sci U S A* 89:6109–13.

131. Furukawa Y, O'Halloran T V (2005) Amyotrophic lateral sclerosis mutations have the greatest destabilizing effect on the apo- and reduced form of SOD1, leading to unfolding and oxidative aggregation. *J Biol Chem* 280:17266–74.

132. Cudd A, Fridovich I (1982) Electrostatic interactions in the reaction mechanism of bovine erythrocyte superoxide dismutase. *J Biol Chem* 257:11443–7.

133. Getzoff ED et al. (1983) Electrostatic recognition between superoxide and copper, zinc superoxide dismutase. *Nature* 306:287–90.

134. Vassall KA, Stathopulos PB, Rumfeldt JAO, Lepock JR, Meiering EM (2006) Equilibrium thermodynamic analysis of amyotrophic lateral sclerosis-associated mutant apo Cu,Zn superoxide dismutases. *Biochemistry* 45:7366–79.

135. Banci L et al. (2009) Structural and dynamic aspects related to oligomerization of apo SOD1 and its mutants. *Proc Natl Acad Sci U S A* 106:6980–5.

136. Galaleldeen A et al. (2009) Structural and biophysical properties of metal-free pathogenic SOD1 mutants A4V and G93A. *Arch Biochem Biophys* 492:40–7.

137. Seetharaman S et al. (2010) Disrupted zinc-binding sites in structures of pathogenic SOD1 variants D124V and H80R. *Biochemistry* 49:5714–25.

138. Antonyuk S et al. (2005) Structural consequences of the familial amyotrophic lateral sclerosis SOD1 mutant His46Arg. *Protein Sci* 2:1201–1213.

139. Strange RW et al. (2003) The Structure of Holo and Metal-deficient Wild-type Human Cu, Zn Superoxide Dismutase and its Relevance to Familial Amyotrophic Lateral Sclerosis. *J Mol Biol* 328:877–891.

140. Kayatekin C, Zitzewitz JA, Matthews CR (2010) Disulfide-reduced ALS variants of Cu, Zn superoxide dismutase exhibit increased populations of unfolded species. *J Mol Biol* 398:320–31.

141. Lepock JR, Frey HE, Hallewell RA (1990) Contribution of conformational stability and reversibility of unfolding to the increased thermostability of human and bovine superoxide dismutase mutated at free cysteines. *J Biol Chem* 265:21612–8.

142. McRee DE et al. (1990) Changes in crystallographic structure and thermostability of a Cu,Zn superoxide dismutase mutant resulting from the removal of a buried cysteine. *J Biol Chem* 265:14234–41.

143. Rumfeldt JAO, Stathopulos PB, Chakrabarrty A, Lepock JR, Meiering EM (2006) Mechanism and thermodynamics of guanidinium chloride-induced denaturation of ALS-associated mutant Cu,Zn superoxide dismutases. *J Mol Biol* 355:106–23.

144. Stathopulos PB et al. (2003) Cu/Zn superoxide dismutase mutants associated with amyotrophic lateral sclerosis show enhanced formation of aggregates in vitro. *Proc Natl Acad Sci U S A* 100:7021–6.

145. Kayatekin C, Zitzewitz JA, Matthews CR (2008) Zinc binding modulates the entire folding free energy surface of human Cu,Zn superoxide dismutase. *J Mol Biol* 384:540–55.

146. Rumfeldt JAO, Lepock JR, Meiering EM (2009) Unfolding and folding kinetics of amyotrophic lateral sclerosis-associated mutant Cu,Zn superoxide dismutases. *J Mol Biol* 385:278–98.

147. Lindberg MJ, Normark J, Holmgren A, Oliveberg M (2004) Folding of human superoxide dismutase: disulfide reduction prevents dimerization and produces marginally stable monomers. *Proc Natl Acad Sci U S A* 101:15893–8.

148. Nordlund A et al. (2009) Functional features cause misfolding of the ALS-provoking enzyme SOD1. *Proc Natl Acad Sci U S A* 106:9667–72.

149. Nordlund A, Oliveberg M (2006) Folding of Cu/Zn superoxide dismutase suggests structural hotspots for gain of neurotoxic function in ALS: parallels to precursors in amyloid disease. *Proc Natl Acad Sci U S A* 103:10218–23.

150. Getzoff ED, Tainer JA, Stempien MM, Bell GI, Hallewell RA (1989) Evolution of CuZn superoxide dismutase and the Greek key beta-barrel structural motif. *Proteins* 5:322–36.

151. Furukawa Y, O'Halloran T V (2006) Posttranslational modifications in Cu,Zn-superoxide dismutase and mutations associated with amyotrophic lateral sclerosis. *Antioxid Redox Signal* 8:847–67.

152. Culotta VC, Yang M, O'Halloran T V (2006) Activation of superoxide dismutases: putting the metal to the pedal. *Biochim Biophys Acta* 1763:747–58.

153. Brown NM, Torres AS, Doan PE, O'Halloran T V (2004) Oxygen and the copper chaperone CCS regulate posttranslational activation of Cu,Zn superoxide dismutase. *Proc Natl Acad Sci U S A* 101:5518–23.

154. Galiazzo F et al. (1991) Activation and induction by copper of Cu/Zn superoxide dismutase in Saccharomyces cerevisiae. Presence of an inactive proenzyme in anaerobic yeast. *Eur J Biochem* 196:545–9.

155. Oh-ishi S et al. (1997) Endurance training improves the resistance of rat diaphragm to exercise-induced oxidative stress. *Am J Respir Crit Care Med* 156:1579–85.

156. Vonk WIM, Wijmenga C, Berger R, van de Sluis B, Klomp LWJ (2010) Cu,Zn superoxide dismutase maturation and activity are regulated by COMMD1. *J Biol Chem* 285:28991–9000.

157. Schmidt PJ, Kunst C, Culotta VC (2000) Copper activation of superoxide dismutase 1 (SOD1) in vivo. Role for protein-protein interactions with the copper chaperone for SOD1. *J Biol Chem* 275:33771–6.

158. Rae TD, Schmidt PJ, Pufahl RA, Culotta VC, O'Halloran T V (1999) Undetectable intracellular free copper: the requirement of a copper chaperone for superoxide dismutase. *Science* 284:805–8.

159. Kim B-E, Nevitt T, Thiele DJ (2008) Mechanisms for copper acquisition, distribution and regulation. *Nat Chem Biol* 4:176–85.

160. Banci L et al. (2010) Affinity gradients drive copper to cellular destinations. *Nature* 465:645–8.

161. Banci L et al. (2012) Human superoxide dismutase 1 (hSOD1) maturation through interaction with human copper chaperone for SOD1 (hCCS). *Proc Natl Acad Sci U S A* 109:13555–60.

162. Rae TD, Torres AS, Pufahl RA, O'Halloran T V (2001) Mechanism of Cu,Zn-superoxide dismutase activation by the human metallochaperone hCCS. *J Biol Chem* 276:5166–76.

163. Carroll MC et al. (2004) Mechanisms for activating Cu- and Zn-containing superoxide dismutase in the absence of the CCS Cu chaperone. *Proc Natl Acad Sci U S A* 101:5964–9.

164. Schmidt PJ et al. (1999) Multiple protein domains contribute to the action of the copper chaperone for superoxide dismutase. *J Biol Chem* 274:23719–25.

165. Banci L, Cantini F, Kozyreva T, Rubino JT (2013) Mechanistic aspects of hSOD1 maturation from the solution structure of Cu(I) -loaded hCCS domain 1 and analysis of disulfide-free hSOD1 mutants. *Chembiochem* 14:1839–44.

166. Bertini I, Gray HB, Stiefel EI, Valentine JS (2007) *Biological Inorganic Chemistry: Structure and Reactivity* ed Bertini I (University Science Books).

167. Lamb AL, Wernimont AK, Pufahl RA, O'Halloran T V, Rosenzweig AC (2000) Crystal structure of the second domain of the human copper chaperone for superoxide dismutase. *Biochemistry* 39:1589–95.

168. Endo T, Fujii T, Sato K, Taniguchi N, Fujii J (2000) A pivotal role of Zn-binding residues in the function of the copper chaperone for SOD1. *Biochem Biophys Res Commun* 276:999–1004.

169. Lamb AL, Torres AS, O'Halloran T V, Rosenzweig AC (2000) Heterodimer formation between superoxide dismutase and its copper chaperone. *Biochemistry* 39:14720–7.

170. Lamb AL, Torres AS, O'Halloran T V, Rosenzweig AC (2001) Heterodimeric structure of superoxide dismutase in complex with its metallochaperone. *Nat Struct Biol* 8:751–5.

171. Hejtmancik JF et al. (1997) Association properties of betaB2- and betaA3-crystallin: ability to form dimers. *Protein Eng* 10:1347–52.

172. Doyle CM et al. (2013) Energetics of oligomeric protein folding and association. *Arch Biochem Biophys* 531:44–64.

173. Rumfeldt JAO, Galvagnion C, Vassall KA, Meiering EM (2008) Conformational stability and folding mechanisms of dimeric proteins. *Prog Biophys Mol Biol* 98:61–84.

174. Vassall KA et al. (2010) Decreased stability and increased formation of soluble aggregates by immature superoxide dismutase do not account for disease severity in ALS. *PNAS*:2–7.

175. Khare SD, Caplow M, Dokholyan N V (2006) FALS mutations in Cu, Zn superoxide dismutase destabilize the dimer and increase dimer dissociation propensity: a large-scale thermodynamic analysis. *Amyloid* 13:226–35.

176. Lindberg MJ, Byström R, Boknäs N, Andersen PM, Oliveberg M (2005) Systematically perturbed folding patterns of amyotrophic lateral sclerosis (ALS)-associated SOD1 mutants. *Proc Natl Acad Sci U S A* 102:9754–9.

177. Svensson AKE et al. (2010) Metal-free ALS variants of dimeric human Cu,Zn-superoxide dismutase have enhanced populations of monomeric species. *PLoS One* 5:e10064.

178. Mulligan VK et al. (2012) Early Steps in Oxidation-Induced SOD1 Misfolding: Implications for Non-Amyloid Protein Aggregation in Familial ALS. *J Mol Biol* 421:631–52.

179. Lang L, Kurnik M, Danielsson J, Oliveberg M (2012) Fibrillation precursor of superoxide dismutase 1 revealed by gradual tuning of the protein-folding equilibrium. *Proc Natl Acad Sci U S A* 109:17868–73.

180. Oztug Durer ZA et al. (2009) Loss of metal ions, disulfide reduction and mutations related to familial ALS promote formation of amyloid-like aggregates from superoxide dismutase. *PLoS One* 4:e5004.

181. Furukawa Y, Kaneko K, Yamanaka K, Nukina N (2010) Mutation-dependent polymorphism of Cu,Zn-superoxide dismutase aggregates in the familial form of amyotrophic lateral sclerosis. *J Biol Chem* 285:22221–31.

182. Banci L et al. (2008) SOD1 and amyotrophic lateral sclerosis: mutations and oligomerization. *PLoS One* 3:e1677.

183. Banci L et al. (2007) Metal-free superoxide dismutase forms soluble oligomers under physiological conditions: a possible general mechanism for familial ALS. *Proc Natl Acad Sci U S A* 104:11263–7.

184. Furukawa Y, Kaneko K, Yamanaka K, O'Halloran T V, Nukina N (2008) Complete loss of post-translational modifications triggers fibrillar aggregation of SOD1 in the familial form of amyotrophic lateral sclerosis. *J Biol Chem* 283:24167–76.

185. Chan PK et al. (2013) Structural similarity of wild-type and ALS-mutant superoxide dismutase-1 fibrils using limited proteolysis and atomic force microscopy. *Proc Natl Acad Sci U S A* 110:10934–9.

186. Serno T, Carpenter JF, Randolph TW, Winter G (2010) Inhibition of agitation-induced aggregation of an IgG-antibody by hydroxypropyl-beta-cyclodextrin. *J Pharm Sci* 99:1193–206.

187. Carpenter JF, Kendrick BS, Chang BS, Manning MC, Randolph TW (1999) Inhibition of stress-induced aggregation of protein therapeutics. *Methods Enzymol* 309:236–55.

188. Lang L, Kurnik M, Danielsson J, Oliveberg M (2012) Fibrillation precursor of superoxide dismutase 1 revealed by gradual tuning of the protein-folding equilibrium. *Proc Natl Acad Sci U S A*:1–6.

189. Toichi K, Yamanaka K, Furukawa Y (2013) Disulfide scrambling describes the oligomer formation of superoxide dismutase (SOD1) proteins in the familial form of amyotrophic lateral sclerosis. *J Biol Chem* 288:4970–80.

190. Karch CM, Borchelt DR (2008) A limited role for disulfide cross-linking in the aggregation of mutant SOD1 linked to familial amyotrophic lateral sclerosis. *J Biol Chem* 283:13528–37.

191. Tainer JA, Getzoff ED, Beem KM, Richardson JS, Richardson DC (1982) Determination and analysis of the 2 A-structure of copper, zinc superoxide dismutase. *J Mol Biol* 160:181–217.

192. Rousseau F, Schymkowitz J, Oliveberg M (2008) ALS precursor finally shaken into fibrils. *Proc Natl Acad Sci U S A* 105:18649–50.

193. Khare SD, Caplow M, Dokholyan N V (2004) The rate and equilibrium constants for a multistep reaction sequence for the aggregation of superoxide dismutase in amyotrophic lateral sclerosis. *Proc Natl Acad Sci U S A* 101:15094–9.

194. Tiwari A, Hayward LJ (2003) Familial amyotrophic lateral sclerosis mutants of copper/zinc superoxide dismutase are susceptible to disulfide reduction. *J Biol Chem* 278:5984–92.

195. Lindberg MJ, Tibell L, Oliveberg M (2002) Common denominator of Cu/Zn superoxide dismutase mutants associated with amyotrophic lateral sclerosis: decreased stability of the apo state. *Proc Natl Acad Sci U S A* 99:16607–12.

196. Turner BJ, Talbot K (2008) Transgenics, toxicity and therapeutics in rodent models of mutant SOD1-mediated familial ALS. *Prog Neurobiol* 85:94–134.

197. Doucette PA et al. (2004) Dissociation of human copper-zinc superoxide dismutase dimers using chaotrope and reductant. Insights into the molecular basis for dimer stability. *J Biol Chem* 279:54558–66.

198. Hough MA et al. (2004) Dimer destabilization in superoxide dismutase may result in disease-causing properties: structures of motor neuron disease mutants. *Proc Natl Acad Sci U S A* 101:5976–81.

199. Rakhit R et al. (2007) An immunological epitope selective for pathological monomer-misfolded SOD1 in ALS. *Nat Med* 13:754–9.

200. Byström R, Andersen PM, Gröbner G, Oliveberg M (2010) SOD1 mutations targeting surface hydrogen bonds promote amyotrophic lateral sclerosis without reducing apo-state stability. *J Biol Chem* 285:19544–52.

201. Das A, Plotkin SS (2013) Mechanical probes of SOD1 predict systematic trends in metal and dimer affinity of ALS-associated mutants. *J Mol Biol* 425:850–74.

202. Strange RW, Yong CW, Smith W, Hasnain SS (2007) Molecular dynamics using atomic-resolution structure reveal structural fluctuations that may lead to polymerization of human Cu-Zn superoxide dismutase. *Proc Natl Acad Sci U S A* 104:10040–4.

203. Falconer RJ, Penkova A, Jelesarov I, Collins BM (2010) Survey of the year 2008: applications of isothermal titration calorimetry. *J Mol Recognit* 23:395–413.

204. Getzoff ED et al. (1992) Faster superoxide dismutase mutants designed by enhancing electrostatic guidance. *Nature* 358:347–51.

205. McCord JM, Fridovich I (1969) Superoxide dismutase. An enzymic function for erythrocuprein (hemocuprein). *J Biol Chem* 244:6049–55.

206. Lyons TJ et al. (1996) Mutations in copper-zinc superoxide dismutase that cause amyotrophic lateral sclerosis alter the zinc binding site and the redox behavior of the protein. *Proc Natl Acad Sci U S A* 93:12240–4.

207. Burrows SD et al. (1994) Determination of the monomer-dimer equilibrium of interleukin-8 reveals it is a monomer at physiological concentrations. *Biochemistry* 33:12741–5.

208. Velazquez-Campoy A, Leavitt SA, Freire E (2004) by Isothermal Titration Calorimetry. 261:35–54.

209. Manning LR et al. (1996) Subunit dissociations in natural and recombinant hemoglobins. *Protein Sci* 5:775–81.

210. Danel F, Paetzel M, Strynadka NC, Page MG (2001) Effect of divalent metal cations on the dimerization of OXA-10 and -14 class D beta-lactamases from Pseudomonas aeruginosa. *Biochemistry* 40:9412–20.

211. Erickson HP (2009) Size and shape of protein molecules at the nanometer level determined by sedimentation, gel filtration, and electron microscopy. *Biol Proced Online* 11:32–51.

212. Rakhit R et al. (2004) Monomeric Cu,Zn-superoxide dismutase is a common misfolding intermediate in the oxidation models of sporadic and familial amyotrophic lateral sclerosis. *J Biol Chem* 279:15499–504.

213. Riley PW, Cheng H, Samuel D, Roder H, Walsh PN (2007) Dimer dissociation and unfolding mechanism of coagulation factor XI apple 4 domain: spectroscopic and mutational analysis. *J Mol Biol* 367:558–73.

214. Lockless SW, Ranganathan R (1999) Evolutionarily conserved pathways of energetic connectivity in protein families. *Science* 286:295–9.

215. Johnson SM, Connelly S, Fearns C, Powers ET, Kelly JW (2012) The transthyretin amyloidoses: from delineating the molecular mechanism of aggregation linked to pathology to a regulatory-agency-approved drug. *J Mol Biol* 421:185–203.

216. Forsberg K et al. (2010) Novel antibodies reveal inclusions containing non-native SOD1 in sporadic ALS patients. *PLoS One* 5:e11552.

217. Xie D, Freire E (1994) Molecular basis of cooperativity in protein folding. V. Thermodynamic and structural conditions for the stabilization of compact denatured states. *Proteins* 19:291–301.

218. Bello M, Pérez-Hernández G, Fernández-Velasco DA, Arreguín-Espinosa R, García-Hernández E (2008) Energetics of protein homodimerization: Effects of water sequestering on the formation of b-lactoglobulin dimer. *Proteins* 70:1475–1487.

219. Prabhu N V, Sharp KA (2005) Heat capacity in proteins. *Annu Rev Phys Chem* 56:521–48.

220. Frisch C, Schreiber G, Johnson CM, Fersht AR (1997) Thermodynamics of the interaction of barnase and barstar: changes in free energy versus changes in enthalpy on mutation. *J Mol Biol* 267:696–706.

221. Khechinashvili NN, Janin J, Rodier F (1995) Thermodynamics of the temperature-induced unfolding of globular proteins. *Protein Sci* 4:1315–24.

222. Banci L, Bertini I, Cramaro F, Del Conte R, Viezzoli MS (2003) Solution structure of Apo Cu,Zn superoxide dismutase: role of metal ions in protein folding. *Biochemistry* 42:9543–53.

223. Bordo D, Djinović K, Bolognesi M (1994) Conserved patterns in the Cu,Zn superoxide dismutase family. *J Mol Biol* 238:366–86.

224. Ponstingl H, Gorse D, Thornton JM (2005) Morphological aspects of oligomeric protein structures. *Prog Biophys Mol Biol* 89:9–35.

225. Schmidlin T, Kennedy BK, Daggett V (2009) Structural changes to monomeric CuZn superoxide dismutase caused by the familial amyotrophic lateral sclerosis-associated mutation A4V. *Biophys J* 97:1709–18.

226. Khare SD, Dokholyan N V (2006) Common dynamical signatures of familial amyotrophic lateral sclerosis-associated structurally diverse Cu, Zn superoxide dismutase mutants. *Proc Natl Acad Sci U S A* 103:3147–52.

227. Chillemi G et al. (1997) The essential dynamics of Cu, Zn superoxide dismutase: suggestion of intersubunit communication. *Biophys J* 73:1007–18.

228. Janin J (2010) Protein–protein docking tested in blind predictions: the CAPRI experiment. *Mol Biosyst* 6:2351 – 2362.

229. Wang Q, Johnson JL, Agar NYR, Agar JN (2008) Protein aggregation and protein instability govern familial amyotrophic lateral sclerosis patient survival. *PLoS Biol* 6:e170.

230. Meiering EM (2008) The threat of instability: neurodegeneration predicted by protein destabilization and aggregation propensity. *PLoS Biol* 6:e193.

231. Matsumoto S et al. (1996) Sporadic amyotrophic lateral sclerosis with dementia and Cu/Zn superoxide dismutase-positive Lewy body-like inclusions. *Clin Neuropathol* 15:41–6.

232. Boillée S, Vande Velde C, Cleveland DW (2006) ALS: a disease of motor neurons and their nonneuronal neighbors. *Neuron* 52:39–59.

233. Tandan R, Bradley WG (1985) Amyotrophic lateral sclerosis: Part 1. Clinical features, pathology, and ethical issues in management. *Ann Neurol* 18:271–80.

234. Hörnberg A, Logan DT, Marklund SL, Oliveberg M (2007) The coupling between disulphide status, metallation and dimer interface strength in Cu/Zn superoxide dismutase. *J Mol Biol* 365:333–42.

235. Ray SS et al. (2004) An intersubunit disulfide bond prevents in vitro aggregation of a superoxide dismutase-1 mutant linked to familial amytrophic lateral sclerosis. *Biochemistry* 43:4899–905.

236. Pierce MM, Raman CS, Nall BT (1999) Isothermal titration calorimetry of protein-protein interactions. *Methods* 19:213–21.

237. Sturtevant JM (1987) Biochemical Applications of Differential Scanning Calorimetry. *Annu Rev Phys Chem* 38:463–488.

238. Tamura A, Sturtevant JM (1995) A thermodynamic study of mutant forms of Streptomyces subtilisin inhibitor. I. Hydrophobic replacements at the position of Met103. *J Mol Biol* 249:625–35.

239. Marky LA, Breslauer KJ (1987) Calculating thermodynamic data for transitions of any molecularity from equilibrium melting curves. *Biopolymers* 26:1601–20.

240. Robic S, Guzman-Casado M, Sanchez-Ruiz JM, Marqusee S (2003) Role of residual structure in the unfolded state of a thermophilic protein. *Proc Natl Acad Sci U S A* 100:11345–9.

241. Gribenko A V, Keiffer TR, Makhatadze GI (2006) Amino acid substitutions affecting protein dynamics in eglin C do not affect heat capacity change upon unfolding. *Proteins* 64:295–300.

242. Privalov PL, Makhatadze GI (1990) Heat capacity of proteins. II. Partial molar heat capacity of the unfolded polypeptide chain of proteins: protein unfolding effects. *J Mol Biol* 213:385–91.

243. Lemaster DM (2006) Heat capacity-independent determination of differential free energy of stability between structurally homologous proteins. *Biophys Chem* 119:94–100.

244. Privalov PL, Potekhin SA (1986) Scanning microcalorimetry in studying temperature-induced changes in proteins. *Methods Enzymol* 131:4–51.

245. Rodriguez JA et al. (2005) Destabilization of apoprotein is insufficient to explain Cu,Zn-superoxide dismutase-linked ALS pathogenesis. *Proc Natl Acad Sci U S A* 102:10516–21.

246. Cooper A, Johnson CM (1994) Differential scanning calorimetry. *Methods Mol Biol* 22:125–36.

247. Privalov GP, Privalov PL (2000) Problems and prospects in microcalorimetry of biological macromolecules. *Methods Enzymol* 323:31–62.

248. Johnson CM, Fersht AR (1995) Protein stability as a function of denaturant concentration: the thermal stability of barnase in the presence of urea. *Biochemistry* 34:6795–804.

249. Liu C et al. (2001) Thermodynamics of denaturation of hisactophilin, a beta-trefoil protein. *Biochemistry* 40:3817–27.

250. Tamura A, Kojima S, Miura K, Sturtevant JM (1994) Effect of an intersubunit disulfide bond on the stability of Streptomyces subtilisin inhibitor. *Biochemistry* 33:14512–20.

251. Kayatekin C, Cohen NR, Matthews CR (2012) Enthalpic Barriers Dominate the Folding and Unfolding of the Human Cu, Zn Superoxide Dismutase Monomer. *J Mol Biol* 424:192–202.

252. Galvagnion C et al. (2009) Folding and association of thermophilic dimeric and trimeric DsrEFH proteins: Tm0979 and Mth1491. *Biochemistry* 48:2891–906.

253. Loladze V V, Ermolenko DN, Makhatadze GI (2001) Heat capacity changes upon burial of polar and nonpolar groups in proteins. *Protein Sci* 10:1343–52.

254. Stroppolo ME, Malvezzi-Campeggi F, Mei G, Rosato N, Desideri A (2000) Role of the tertiary and quaternary structures in the stability of dimeric copper, zinc superoxide dismutases. *Arch Biochem Biophys* 377:215–8.

255. DiDonato M et al. (2003) ALS Mutants of Human Superoxide Dismutase Form Fibrous Aggregates Via Framework Destabilization. *J Mol Biol* 332:601–615.

256. Hart PJ et al. (1998) Subunit asymmetry in the three-dimensional structure of a human CuZnSOD mutant found in familial amyotrophic lateral sclerosis. *Protein Sci* 7:545–55.

257. Meiering EM, Serrano L, Fersht AR (1992) Effect of active site residues in barnase on activity and stability. *J Mol Biol* 225:585–9.

258. Mulligan VK, Kerman A, Ho S, Chakrabartty A (2008) Denaturational stress induces formation of zinc-deficient monomers of Cu,Zn superoxide dismutase: implications for pathogenesis in amyotrophic lateral sclerosis. *J Mol Biol* 383:424–36.

259. Negi SS, Kolokoltsov AA, Schein CH, Davey RA, Braun W (2006) Determining functionally important amino acid residues of the E1 protein of Venezuelan equine encephalitis virus. *J Mol Model* 12:921–9.

260. Spolar RS, Livingstone JR, Record MT (1992) Use of liquid hydrocarbon and amide transfer data to estimate contributions to thermodynamic functions of protein folding from the removal of nonpolar and polar surface from water. *Biochemistry* 31:3947–55.

261. Murphy KP, Freire E (1992) Thermodynamics of structural stability and cooperative folding behavior in proteins. *Adv Protein Chem* 43:313–61.

262. Myers JK, Pace CN, Scholtz JM (1995) Denaturant m values and heat capacity changes: relation to changes in accessible surface areas of protein unfolding. *Protein Sci* 4:2138–48.

263. Makhatadze GI, Privalov PL (1995) Energetics of protein structure. *Adv Protein Chem* 47:307–425.

264. Soto C, Estrada LD (2008) Protein misfolding and neurodegeneration. *Arch Neurol* 65:184–9.

265. Fändrich M et al. (2003) Myoglobin forms amyloid fibrils by association of unfolded polypeptide segments. *Proc Natl Acad Sci U S A* 100:15463–8.

266. Okamoto K, Hirai S, Yamazaki T, Sun XY, Nakazato Y (1991) New ubiquitin-positive intraneuronal inclusions in the extra-motor cortices in patients with amyotrophic lateral sclerosis. *Neurosci Lett* 129:233–6.

267. Cozzolino M et al. (2008) Cysteine 111 affects aggregation and cytotoxicity of mutant Cu,Zn-superoxide dismutase associated with familial amyotrophic lateral sclerosis. *J Biol Chem* 283:866–74.

268. Karch CM, Prudencio M, Winkler DD, Hart PJ, Borchelt DR (2009) Role of mutant SOD1 disulfide oxidation and aggregation in the pathogenesis of familial ALS. *Proc Natl Acad Sci U S A* 106:7774–9.

269. Wang J et al. (2009) Progressive aggregation despite chaperone associations of a mutant SOD1-YFP in transgenic mice that develop ALS. *Proc Natl Acad Sci U S A* 106:1392–7.

270. Zetterström P et al. (2007) Soluble misfolded subfractions of mutant superoxide dismutase-1s are enriched in spinal cords throughout life in murine ALS models. *Proc Natl Acad Sci U S A* 104:14157–62.

271. Lynch SM, Boswell SA, Colón W (2004) Kinetic stability of Cu/Zn superoxide dismutase is dependent on its metal ligands: implications for ALS. *Biochemistry* 43:16525–31.

272. Svensson AKE, Bilsel O, Kondrashkina E, Zitzewitz JA, Matthews CR (2006) Mapping the folding free energy surface for metal-free human Cu,Zn superoxide dismutase. *J Mol Biol* 364:1084–102.

273. Arnesano F et al. (2004) The unusually stable quaternary structure of human Cu,Zn-superoxide dismutase 1 is controlled by both metal occupancy and disulfide status. *J Biol Chem* 279:47998–8003.

274. Privalov PL (1979) Stability of proteins: small globular proteins. *Adv Protein Chem* 33:167–241.

275. Geierhaas CD, Nickson AA, Lindorff-Larsen K, Clarke J, Vendruscolo M (2007) BPPred: a Web-based computational tool for predicting biophysical parameters of proteins. *Protein Sci* 16:125–34.

276. Lomakin A, Benedek GB, Teplow DB (1999) Monitoring protein assembly using quasielastic light scattering spectroscopy. *Methods Enzymol* 309:429–59.

277. Wilkins DK et al. (1999) Hydrodynamic radii of native and denatured proteins measured by pulse field gradient NMR techniques. *Biochemistry* 38:16424–31.

278. Kiese S, Papppenberger A, Friess W, Mahler H-C (2008) Shaken, not stirred: mechanical stress testing of an IgG1 antibody. *J Pharm Sci* 97:4347–66.

279. Yamamoto K et al. (2008) Thiol compounds inhibit the formation of amyloid fibrils by beta 2-microglobulin at neutral pH. *J Mol Biol* 376:258–68.

280. Banci L et al. (2005) Fully metallated S134N Cu,Zn-superoxide dismutase displays abnormal mobility and intermolecular contacts in solution. *J Biol Chem* 280:35815–21.

281. Sandelin E, Nordlund A, Andersen PM, Marklund SSL, Oliveberg M (2007) Amyotrophic lateral sclerosis-associated copper/zinc superoxide dismutase mutations preferentially reduce the repulsive charge of the proteins. *J Biol Chem* 282:21230–6.

282. Chiti F, Stefani M, Taddei N, Ramponi G, Dobson CM (2003) Rationalization of the effects of mutations on peptide and protein aggregation rates. *Nature* 424:805–8.

283. Hayward LJ et al. (2002) Decreased metallation and activity in subsets of mutant superoxide dismutases associated with familial amyotrophic lateral sclerosis. *J Biol Chem* 277:15923–31.

284. Turner MR, Kiernan MC, Leigh PN, Talbot K (2009) Biomarkers in amyotrophic lateral sclerosis. *Lancet Neurol* 8:94–109.

285. Consalvi V et al. (2000) Thermal unfolding and conformational stability of the recombinant domain II of glutamate dehydrogenase from the hyperthermophile Thermotoga maritima. *Protein Eng* 13:501–7.

286. Jha BK et al. (2004) pH and cation-induced thermodynamic stability of human hyaluronan binding protein 1 regulates its hyaluronan affinity. *J Biol Chem* 279:23061–72.

287. McCrary BS, Bedell J, Edmondson SP, Shriver JW (1998) Linkage of protonation and anion binding to the folding of Sac7d. *J Mol Biol* 276:203–24.

288. Yang ZW et al. (2004) Dimethyl sulfoxide at 2.5% (v/v) alters the structural cooperativity and unfolding mechanism of dimeric bacterial NAD+ synthetase. *Protein Sci* 13:830–41.

289. Briere L-AK, Dunn SD (2006) The periplasmic domains of Escherichia coli HflKC oligomerize through right-handed coiled-coil interactions. *Biochemistry* 45:8607–16.

290. Pace CN (1986) Determination and analysis of urea and guanidine hydrochloride denaturation curves. *Methods Enzymol* 131:266–80.

291. Tartaglia GG, Vendruscolo M (2008) The Zyggregator method for predicting protein aggregation propensities. *Chem Soc Rev* 37:1395–401.

292. Trovato A, Chiti F, Maritan A, Seno F (2006) Insight into the structure of amyloid fibrils from the analysis of globular proteins. *PLoS Comput Biol* 2:e170.

293. Maurer-Stroh S et al. (2010) Exploring the sequence determinants of amyloid structure using position-specific scoring matrices. *Nat Methods* 7:237–42.

294. Fernandez-Escamilla A-M, Rousseau F, Schymkowitz J, Serrano L (2004) Prediction of sequence-dependent and mutational effects on the aggregation of peptides and proteins. *Nat Biotechnol* 22:1302–6.

295. Garbuzynskiy SO, Lobanov MY, Galzitskaya O V (2010) FoldAmyloid: a method of prediction of amyloidogenic regions from protein sequence. *Bioinformatics* 26:326–32.

296. Goldschmidt L, Teng PK, Riek R, Eisenberg D (2010) Identifying the amylome, proteins capable of forming amyloid-like fibrils. *Proc Natl Acad Sci U S A* 107:3487–92.

297. Cao X et al. (2008) Structures of the G85R variant of SOD1 in familial amyotrophic lateral sclerosis. *J Biol Chem* 283:16169–77.

298. Van Holde KE, Weischet WO (1978) Boundary analysis of sedimentation-velocity experiments with monodisperse and paucidisperse solutes. *Biopolymers* 17:1387–1403.

299. Schuck P (2007) *Protein Interactions: Biophysical Approaches for the Study of Complex Reversible Systems* (Springer Science & Business Media).

300. Taylor JR (1982) *An Introduction to Error Analysis* (University Science Books, Mill Valley, CA).

301. Sekhar A et al. (2015) Thermal fluctuations of immature SOD1 lead to separate folding and misfolding pathways. *Elife* 4.

302. Fee JA (1973) Studies on the reconstitution of bovine erythrocyte superoxide dismutase. IV. Preparation and some properties of the enzyme in which Co(II) is substituted for Zn(II). *J Biol Chem* 248:4229–34.

303. Crow J, Sampson J, Zhuang Y, Thompson J, Beckman J (1997) Decreased zinc affinity of amyotrophic lateral sclerosis-associated superoxide dismutase mutants leads to enhanced catalysis of tyrosine nitration by peroxynitrite. *J Neurochem* 69:1936–1944.

304. Crow JP, Sampson JB, Zhuang Y, Thompson JA, Beckman JS (1997) Decreased zinc affinity of amyotrophic lateral sclerosis-associated superoxide dismutase mutants leads to enhanced catalysis of tyrosine nitration by peroxynitrite. *J Neurochem* 69:1936–44.

305. Doyle C (2014) A Refined Method for Quantitation of Divalent Metal Ions in Metalloproteins and Local Stability and Conformational Heterogeneity of Amyotrophic Lateral Sclerosis-Associated Cu , Zn Superoxide Dismutase.

306. Hunt JB, Neece SH, Ginsburg A (1985) The use of 4-(2-pyridylazo)resorcinol in studies of zinc release from Escherichia coli aspartate transcarbamoylase. *Anal Biochem* 146:150–7.

307. Davydov DR et al. (1995) High-pressure-induced transitions in microsomal cytochrome P450 2B4 in solution: evidence for conformational inhomogeneity in the oligomers. *Arch Biochem Biophys* 320:330–44.

308. Nobbmann U et al. (2007) Dynamic light scattering as a relative tool for assessing the molecular integrity and stability of monoclonal antibodies. *Biotechnol Genet Eng Rev* 24:117–28.

309. Inagaki S, Ghirlando R, Grisshammer R (2013) Biophysical characterization of membrane proteins in nanodiscs. *Methods* 59:287–300.

310. Formulation stability evaluation using light scattering techniques *Malvern Instruments Appl Note*. Available at: http://www.malvern.com/en/support/resource-center/application-notes/AN110627FormulationStabilityEvaluation.aspx [Accessed April 11, 2015].

311. Finsy R (1994) Particle sizing by quasi-elastic light scattering. *Adv Colloid Interface Sci* 52:79 – 143.

312. Koppel DE, Carlson C, Smilowitz H (1989) Analysis of heterogeneous fluorescence photobleaching by video kinetics imaging: the method of cumulants. *J Microsc* 155:199–206.

313. Pecora R (2000) Dynamic Light Scattering Measurement of Nanometer Particles in Liquids. *J Nanoparticle Res* 2:123–131.

314. Dynamic light scattering - common terms defined *Malvern Instruments Appl Note*. Available at: http://www.malvern.com/en/support/resource-center/Whitepapers/WP111214DLSTermsDefined.aspx [Accessed April 11, 2015].

315. Characterization of Ferritin *Malvern Instruments Appl Note*. Available at: http://www.malvern.com/en/support/resource-center/application-notes/AN101104CharacterizationFerritin.aspx [Accessed April 11, 2015].

316. Jiskoot W, Crommelin D (2005) *Methods for Structural Analysis of Protein Pharmaceuticals* (Springer Science & Business Media).

317. Willard L (2003) VADAR: a web server for quantitative evaluation of protein structure quality. *Nucleic Acids Res* 31:3316–3319.

318. Intensity - Volume - Number *Malvern Instruments Tech Note*. Available at: http://www.malvern.com/en/support/resource-center/technical-notes/TN101104IntensityVolumeNumber.aspx [Accessed April 11, 2015].

319. Number and volume size distributions *Malvern Instruments Appl Note*. Available at: http://www.malvern.com/en/support/resource-center/application-notes/AN140403NumberVolumeSizeDistributions.aspx [Accessed April 11, 2015].

320. Ferrone F (1999) Analysis of protein aggregation kinetics. *Methods Enzymol* 309:256–74.

321. Mathé C et al. (2013) Structural determinants for protein adsorption/non-adsorption to silica surface. *PLoS One* 8:e81346.

322. Campioni S et al. (2014) The presence of an air-water interface affects formation and elongation of α-Synuclein fibrils. *J Am Chem Soc* 136:2866–75.

323. Delahaije RJBM, Gruppen H, Giuseppin MLF, Wierenga PA (2014) Quantitative description of the parameters affecting the adsorption behaviour of globular proteins. *Colloids Surf B Biointerfaces* 123:199–206.

324. Schladitz C, Vieira EP, Hermel H, Möhwald H (1999) Amyloid-beta-sheet formation at the air-water interface. *Biophys J* 77:3305–10.

325. Soreghan B, Kosmoski J, Glabe C (1994) Surfactant properties of Alzheimer's A beta peptides and the mechanism of amyloid aggregation. *J Biol Chem* 269:28551–4.

326. Hoernke M, Falenski JA, Schwieger C, Koksch B, Brezesinski G (2011) Triggers for β-sheet formation at the hydrophobic-hydrophilic interface: high concentration, in-plane orientational order, and metal ion complexation. *Langmuir* 27:14218–31.

327. Moores B, Drolle E, Attwood SJ, Simons J, Leonenko Z (2011) Effect of surfaces on amyloid fibril formation. *PLoS One* 6:e25954.

328. Trigg BJ, Lee CF, Vaux DJ, Jean L (2013) The air-water interface determines the outcome of seeding during amyloidogenesis. *Biochem J* 456:67–80.

329. LeVine H (1993) Thioflavine T interaction with synthetic Alzheimer's disease beta-amyloid peptides: detection of amyloid aggregation in solution. *Protein Sci* 2:404–10.

330. Naiki H, Higuchi K, Hosokawa M, Takeda T (1989) Fluorometric determination of amyloid fibrils in vitro using the fluorescent dye, thioflavin T1. *Anal Biochem* 177:244–9.

331. Biancalana M, Koide S (2010) Molecular mechanism of Thioflavin-T binding to amyloid fibrils. *Biochim Biophys Acta* 1804:1405–12.

332. Krebs MRH, Bromley EHC, Donald AM (2005) The binding of thioflavin-T to amyloid fibrils: localisation and implications. *J Struct Biol* 149:30–7.

333. Wright CF, Teichmann SA, Clarke J, Dobson CM (2005) The importance of sequence diversity in the aggregation and evolution of proteins. *Nature* 438:878–81.

334. Ganesan A et al. (2014) Selectivity of Aggregation-Determining Interactions. *J Mol Biol* 427:236–47.

335. Chien P, DePace AH, Collins SR, Weissman JS (2003) Generation of prion transmission barriers by mutational control of amyloid conformations. *Nature* 424:948–51.

336. Morell M et al. (2008) Inclusion bodies: specificity in their aggregation process and amyloid-like structure. *Biochim Biophys Acta* 1783:1815–25.

337. Dubey K, Anand BG, Temgire MK, Kar K (2014) Evidence of rapid coaggregation of globular proteins during amyloid formation. *Biochemistry* 53:8001–4.

338. Ono K, Takahashi R, Ikeda T, Yamada M (2012) Cross-seeding effects of amyloid β-protein and α-synuclein. *J Neurochem* 122:883–90.

339. Xu J et al. (2011) Gain of function of mutant p53 by coaggregation with multiple tumor suppressors. *Nat Chem Biol* 7:285–95.

340. Weissgerber TL, Milic NM, Winham SJ, Garovic VD (2015) Beyond Bar and Line Graphs: Time for a New Data Presentation Paradigm. *PLOS Biol* 13:e1002128.

341. Waner MJ, Gilchrist M, Schindler M, Dantus M (1998) Imaging the Molecular Dimensions and Oligomerization of Proteins at Liquid/Solid Interfaces. *J Phys Chem B* 102:1649–1657.

342. Dzwolak W, Pecul M (2005) Chiral bias of amyloid fibrils revealed by the twisted conformation of Thioflavin T: an induced circular dichroism/DFT study. *FEBS Lett* 579:6601–3.

343. Wu C, Biancalana M, Koide S, Shea J-E (2009) Binding modes of thioflavin-T to the single-layer beta-sheet of the peptide self-assembly mimics. *J Mol Biol* 394:627–33.

344. Biancalana M, Makabe K, Koide A, Koide S (2009) Molecular mechanism of thioflavin-T binding to the surface of beta-rich peptide self-assemblies. *J Mol Biol* 385:1052–63.

345. Sabaté R, Lascu I, Saupe SJ (2008) On the binding of Thioflavin-T to HET-s amyloid fibrils assembled at pH 2. *J Struct Biol* 162:387–96.

346. Apetri MM, Maiti NC, Zagorski MG, Carey PR, Anderson VE (2006) Secondary structure of alpha-synuclein oligomers: characterization by raman and atomic force microscopy. *J Mol Biol* 355:63–71.

347. Williams AD et al. (2005) Structural properties of Abeta protofibrils stabilized by a small molecule. *Proc Natl Acad Sci U S A* 102:7115–20.

348. Majumdar R et al. (2013) Effects of salts from the Hofmeister series on the conformational stability, aggregation propensity, and local flexibility of an IgG1 monoclonal antibody. *Biochemistry* 52:3376–89.

349. Cacace MG, Landau EM, Ramsden JJ (1997) The Hofmeister series: salt and solvent effects on interfacial phenomena. *Q Rev Biophys* 30:241–77.

350. Baldwin RL (1996) How Hofmeister ion interactions affect protein stability. *Biophys J* 71:2056–63.

351. Zhang Y, Cremer PS (2006) Interactions between macromolecules and ions: The Hofmeister series. *Curr Opin Chem Biol* 10:658–63.

352. Bjellqvist B et al. (1993) The focusing positions of polypeptides in immobilized pH gradients can be predicted from their amino acid sequences. *Electrophoresis* 14:1023–31.

353. Bjellqvist B, Basse B, Olsen E, Celis JE (1994) Reference points for comparisons of two-dimensional maps of proteins from different human cell types defined in a pH scale where isoelectric points correlate with polypeptide compositions. *Electrophoresis* 15:529–39.

354. Mouat MF, Manchester KL (1998) The intracellular ionic strength of red cells and the influence of complex formation. *Comp Haematol Int* 8:58–60.

355. Jain S, Udgaonkar JB (2010) Salt-induced modulation of the pathway of amyloid fibril formation by the mouse prion protein. *Biochemistry* 49:7615–24.

356. Kodali R, Wetzel R (2007) Polymorphism in the intermediates and products of amyloid assembly. *Curr Opin Struct Biol* 17:48–57.

357. Sekhar A, Kay LE (2013) NMR paves the way for atomic level descriptions of sparsely populated, transiently formed biomolecular conformers. *Proc Natl Acad Sci U S A* 110:12867–74.

358. Vallurupalli P, Bouvignies G, Kay LE (2012) Studying “invisible” excited protein states in slow exchange with a major state conformation. *J Am Chem Soc* 134:8148–61.

359. Palmer AG, Kroenke CD, Loria JP (2001) Nuclear magnetic resonance methods for quantifying microsecond-to-millisecond motions in biological macromolecules. *Methods Enzymol* 339:204–38.

360. Ohhashi Y, Ito K, Toyama BH, Weissman JS, Tanaka M (2010) Differences in prion strain conformations result from non-native interactions in a nucleus. *Nat Chem Biol* 6:225–230.

361. Dominguez C, Boelens R, Bonvin AMJJ (2003) HADDOCK: a protein-protein docking approach based on biochemical or biophysical information. *J Am Chem Soc* 125:1731–7.

362. Takai E et al. (2014) Cysteine inhibits amyloid fibrillation of lysozyme and directs the formation of small worm-like aggregates through non-covalent interactions. *Biotechnol Prog* 30:470–8.

363. Jordens S, Adamcik J, Amar-Yuli I, Mezzenga R (2011) Disassembly and reassembly of amyloid fibrils in water-ethanol mixtures. *Biomacromolecules* 12:187–93.

364. Jain S, Udgaonkar JB (2011) Defining the pathway of worm-like amyloid fibril formation by the mouse prion protein by delineation of the productive and unproductive oligomerization reactions. *Biochemistry* 50:1153–61.

365. Klement K et al. (2007) Effect of different salt ions on the propensity of aggregation and on the structure of Alzheimer’s abeta(1-40) amyloid fibrils. *J Mol Biol* 373:1321–33.

366. Munishkina LA, Henriques J, Uversky VN, Fink AL (2004) Role of protein-water interactions and electrostatics in alpha-synuclein fibril formation. *Biochemistry* 43:3289–300.

367. Yeh V et al. (2010) The Hofmeister effect on amyloid formation using yeast prion protein. *Protein Sci* 19:47–56.

368. Raman B et al. (2005) Critical balance of electrostatic and hydrophobic interactions is required for beta 2-microglobulin amyloid fibril growth and stability. *Biochemistry* 44:1288–99.

369. Rubin J, Linden L, Coco WM, Bommarius AS, Behrens SH (2013) Salt-induced aggregation of a monoclonal human immunoglobulin G1. *J Pharm Sci* 102:377–86.

370. Rubin J et al. (2013) Ion-specific effects on prion nucleation and strain formation. *J Biol Chem* 288:30300–8.

371. Roberts CJ (2014) Protein aggregation and its impact on product quality. *Curr Opin Biotechnol* 30:211–7.

372. Pedersen JS, Andersen CB, Otzen DE (2010) Amyloid structure--one but not the same: the many levels of fibrillar polymorphism. *FEBS J* 277:4591–601.

373. Berryman JT, Radford SE, Harris SA (2011) Systematic examination of polymorphism in amyloid fibrils by molecular-dynamics simulation. *Biophys J* 100:2234–42.

374. Roberts HL, Brown DR (2015) Seeking a Mechanism for the Toxicity of Oligomeric α-Synuclein. *Biomolecules* 5:282–305.

375. Amin S, Barnett G V., Pathak JA, Roberts CJ, Sarangapani PS (2014) Protein aggregation, particle formation, characterization & rheology. *Curr Opin Colloid Interface Sci* 19:438–449.

376. Hörnberg A, Logan DT, Marklund SL, Oliveberg M (2007) The Coupling between Disulphide Status , Metallation and Dimer Interface Strength in Cu / Zn Superoxide Dismutase. *Interface*:333–342.

377. Ray SS, Lansbury PT (2004) A possible therapeutic target for Lou Gehrig's disease. *Proc Natl Acad Sci U S A* 101:5701–2.

378. Wright GS a, Antonyuk S V, Kershaw NM, Strange RW, Samar Hasnain S (2013) Ligand binding and aggregation of pathogenic SOD1. *Nat Commun* 4:1758.

379. Auclair JR, Boggio KJ, Petsko GA, Ringe D, Agar JN (2010) Strategies for stabilizing superoxide dismutase (SOD1), the protein destabilized in the most common form of familial amyotrophic lateral sclerosis. *Proc Natl Acad Sci U S A* 107:21394–9.

380. Nowak RJ, Cuny GD, Choi S, Lansbury PT, Ray SS (2010) Improving binding specificity of pharmacological chaperones that target mutant superoxide dismutase-1 linked to familial amyotrophic lateral sclerosis using computational methods. *J Med Chem* 53:2709–18.

381. Ray SS, Nowak RJ, Brown RH, Lansbury PT (2005) Small-molecule-mediated stabilization of familial amyotrophic lateral sclerosis-linked superoxide dismutase mutants against unfolding and aggregation. *Proc Natl Acad Sci U S A* 102:3639–44.

382. Rumfeldt JAO (2006) Thermodynamics, Kinetics, and Structural dynamics of Amyotrophic Lateral Sclerosis-Associated Mutant Copper-Zinc Superoxide Dismutases mutants. Dissertation (University of Waterloo).

383. Freire E, Obdiluo ML, Straume M (1990) Isothermal Titration Calorimetry. *Anal Chem* 62:950A–959A.

384. Duff MR, Grubbs J, Howell EE (2011) Isothermal titration calorimetry for measuring macromolecule-ligand affinity. *J Vis Exp*.

385. Wiseman T, Williston S, Brandts JF, Lin LN (1989) Rapid measurement of binding constants and heats of binding using a new titration calorimeter. *Anal Biochem* 179:131–7.

386. Potter SZ et al. (2007) Binding of a single zinc ion to one subunit of copper-zinc superoxide dismutase apoprotein substantially influences the structure and stability of the entire homodimeric protein. *J Am Chem Soc* 129:4575–83.

387. Pickles S et al. Mitochondrial dysfunction in Amyotrophic Lateral Sclerosis : A misfolded SOD1 conformer with preferential mitochondrial association. 10.

388. Cardamone M, Puri NK (1992) Spectrofluorimetric assessment of the surface hydrophobicity of proteins. *Biochem J* 282 (Pt 2:589–93.

389. Bosco DA et al. (2010) Wild-type and mutant SOD1 share an aberrant conformation and a common pathogenic pathway in ALS. *Nat Neurosci* 13:1396–403.